LORETA ANGELA MUSCARELLA

# STRAIN EFFECTS ON THE OPTICAL PROPERTIES OF LEAD-HALIDE PEROVSKITES



Ph.D. Thesis, University of Groningen, October 2021
Loreta Angela Muscarella

Ph.D. Examining committee:

Prof. M.A Loi
Prof. F.C Grozema
Prof. R.A.J Janssen
Prof. M. Tromp
Dr. J.V. Milić

The work described in this thesis was performed between January 2018 and September 2021 at AMOLF, Science Park 104, 1098 XG Amsterdam, The Netherlands and financed by the Netherlands Organization for Scientific Research (NWO).

Printed by IPSKAMP printing

Cover Design by Valerio Favale

Cover Image is a plot of an EBSD measurement of $MAPbI_3$ film

A digital version of this thesis can be downloaded at amolf.nl

ISSN: 1570-1530

university of groningen / faculty of science and engineering / zernike institute for advanced materials

# Strain effects on the optical properties of lead-halide perovskites

**PhD thesis**

to obtain the degree of PhD at the
University of Groningen
on the authority of the
Rector Magnificus Prof. C. Wijmenga
and in accordance with
the decision by the College of Deans.

This thesis will be defended in public on

18 January 2022 at 09:00 hours

by

**Loreta Angela Muscarella**

born on 15 January 1994
in Palermo, Italy

## Supervisors
Prof. B. Ehrler
Prof. A. Polman

## Assessment Committee
Prof. M.A. Loi
Prof. F.C. Grozema
Prof. R.A.J. Janssen

*To Valerio and my family who have always believed in me*
*And have supported me through these years with love and understanding*

*Gutta cavat lapidem non vi, sed saepe cadendo*
*- Lucretius*

# CONTENTS

# 1. Introduction & Background


In the last 10 years, lead halide perovskites have gathered significant attention for a plethora of applications such as solar cells, LEDs, thermoelectric materials, scintillators and sensors. This class of materials exhibits attractive physical and chemical properties which can be associated with its peculiar electronic and crystal structure. In this Chapter, we first introduce lead halide perovskites, their potential and challenges. We then focus on how the ionic-covalent bond dual nature in these solids is reflected in the mechanically soft and dynamically disordered lattice whose alteration affects the electronic landscape. External pressure can be used as a tool to induce structural modifications of the perovskite lattice and therefore to investigate the structure-properties relationship in these solids. We introduce the main techniques used throughout this thesis: Electron-Backscattered Diffraction (EBSD) to spatially resolve the crystal structure and grain orientation of perovskite thin films; femtosecond pressure-dependent transient absorption and pressure-dependent photoluminescence spectroscopy to correlate the structural variation with optical properties of such films.

# 1.1. Lead-Halide Perovskites

*Perovskites* refers to a group of materials with the same crystal structure as calcium titanium oxide ($CaTiO_3$) described by the formula $ABX_3$. Metal-halide perovskites (MHP) feature a monovalent cation such as the organic methylammonium ($MA^+$: $CH_3NH_3^+$), formamidinium ($FA^+$: $CH_2(NH_2)_2^+$) or the inorganic caesium ($Cs^+$). B is a divalent cation, usually lead ($Pb^{2+}$) or tin ($Sn^{2+}$), and X is the anion, *e.g.*, iodide ($I^-$), bromide ($Br^-$) or chloride ($Cl^-$). A representation of the cubic crystal structure of MHP is shown in **Figure 1.1a**. The crystal structure consists of corner-sharing $BX_6$ octahedra, with the A cation occupying the 12-fold coordination site in the middle of the cube of eight such octahedra and interacting with the $BX_3^-$ lattice mainly *via* ion-ion, ion-dipole, and hydrogen bonding interactions. The divalent B cation is located at the corner of the cube and surrounded by an octahedron of anions. Deviations from the $ABX_3$ stoichiometry are also possible when the A and B cations are replaced by a combination of cations having different valences but retaining an overall neutral charge balance (double or quadruple perovskites)[1,2].

Incorporation of larger organic cations that do not satisfy the tolerance factor criterium for the formation of the 3D perovskite can results in the formation of low-dimensional layered 2D metal-halide perovskite (LMH)[3,4], schematically represented in **Figure 1.1b**. This class of materials consists of infinite 2D slabs of the $ABX_3$ type structure which are separated by some organic spacers (S). Layered 2D perovskites are often classified into Ruddlesden-Popper (RP) and Dion-Jacobson (DJ) types. The RP perovskites can be described by the formula $S_2[A_{(n-1)}B_nX_{(3n+1)}]$ [5], where the spacer S consists of two monofunctional organic molecules, each of them binding a side of the perovskite slab, whereas van der Walls interactions dominate between the two spacers. In the DJ perovskites, described by the formula $S[A_{(n-1)}B_nX_{(3n+1)}]$ [6], the spacer consists of a bifunctional organic molecule directly binding the two side of the perovskite slab[7]. They are further classified based on the number of perovskites layers ($n$) which are separated by the organic spacer layer (*e.g.* $n$ = 1, 2, r, etc.). In layered 2D perovskites, charges are mostly confined to the inorganic framework as the organic spacers are mostly electronically insulating. This class of materials shows

a unique quantum well behaviour, where for low *n*, the bandgap decreases as a function of the reduced thickness of the perovskite slab because of the reduced quantum confinement (**Figure 1.1c**). The possibility to choose a larger variety of organic spacers with *ad hoc* functionalities, makes the tunability of the layered 2D perovskites higher in comparison with their 3D counterparts.

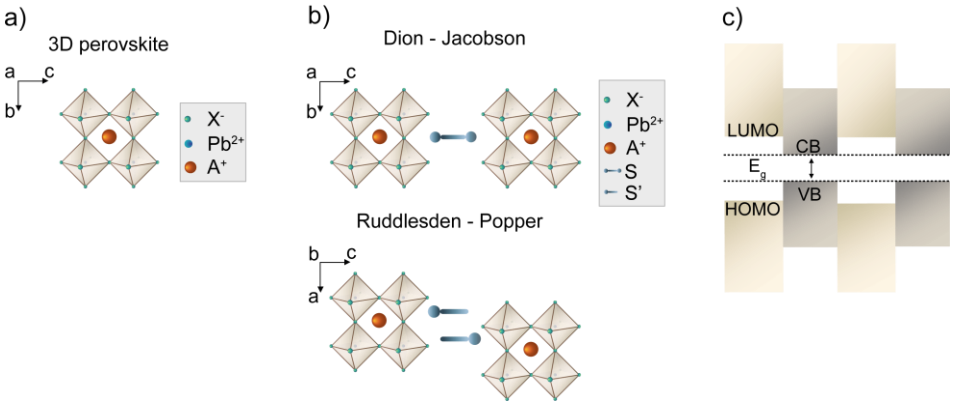


**Figure 1.1.** *From 3D to layered 2D perovskites.* A representation of **a)** the crystal structure of 3D MHP, **b)** layered 2D perovskites classified into Ruddlesden-Popper and Dion-Jacobson types, and **c)** their quantum well behaviour, with the energy bandgap ($E_g$) defined by conduction band (CB) and valence band (VB) edges and the highest occupied molecular orbital (HOMO) and the lowest occupied molecular orbital (LUMO) levels.

## 1.2. Promises and Challenges

Lead-halide perovskites have recently gathered significant attention due to the high efficiency of perovskite-based solar cells and other optoelectronic devices combined with the possibility for low-cost and simple solution or vapour-based fabrication methods[8,9]. Their bandgap tunability is one of the most exciting properties for lighting applications, displays and tandem solar cells where the possibility of choosing the bandgap of the material used is quintessential. The simplest and most studied perovskite is the methylammonium lead iodide ($MAPbI_3$). Any intermediate bandgap between the full iodide $MAPbI_3$ (1.65 eV)

and the full bromide $MAPbBr_3$ system (2.3 eV) can be obtained[10,11] by partially replacing the iodide species with bromide. Replacing iodide or bromide with chloride is also possible, opening the possibility to extend the bandgap tunability toward the UV [12]. To a minor extent, the bandgap tunability is also achieved by replacing the methylammonium $MA^+$ cation with a different monovalent $A^+$ cation with different properties (*e.g.* size[13], hydrogen bonding donor character[13]). Together with the bandgap tunability, the high photoluminescence quantum efficiency (PLQE) makes perovskites promising for solar cells and light-emitting diodes (LEDs). As a matter of fact, in solar cells the PLQE is directly related to the open-circuit voltage ($V_{oc}$)[14] and is an important metric to optimize the luminous efficiency of LEDs[15]. So far, despite the PLQE is reduced by the presence of defects[14,16–18], perovskites have demonstrated to be relatively defect tolerant[19,20] which partially relax the requirements for the fabrication strategies.

Another intriguing property of this class of materials is their low thermal conductivity[21,22] and the consequent slow heat transport. For instance, the thermal conductivity κ at room temperature of $CsPbBr_3$[23] and $MAPbI_3$[24] single crystals is found to be 1 and 0.5 W $m^{-1}$ $K^{-1}$, respectively. In contrast, GaAs[25] and silicon[26] exhibit a thermal conductivity κ of 52 and 150 W $m^{-1}$ $K^{-1}$, respectively. A significant difference in thermal conductivity is also found between rocksalt IV–VI materials (*e.g.* SnTe, $\kappa = 4$ W $m^{-1}$ $K^{-1}$ ) and zincblende III–V materials (*e.g.* InSb, $\kappa = 16$ W $m^{-1}$ $K^{-1}$) and often attributed to their different structural coordination, octahedral and tetrahedral, respectively. Compounds with octahedral coordination often exhibit low thermal conductivity in comparison with other structural coordination (*e.g.* tetrahedral) and this has been attributed to the reduced ability for an atom to vibrate given the larger number of neighbours[27]. However, vacancies[27], the phonon lifetime[28] and the phonon mean free path can also affect the overall thermal conductivity. Despite a full picture of what causes the low thermal conductivity in lead-halide perovskites is still missing, the polar nature of these semiconductors together with its structural disorder are key. Differences in thermal conductivity are also present within the class of lead-halide perovskites. Replacing the organic cation ($MA^+$) with an inorganic one ($Cs^+$) halves the density of states of accessible modes, resulting in higher thermal conductivity. Furthermore, the lower thermal conductivity of $MAPbI_3$ is

attributed to its particular crystal structure, involving the slow rotation of the $MA^+$ cation within the unit cell that changes the cation-lattice coupling[29,30]. This property opens up applications where slow heat transport is required, such as in thermoelectric devices[31]. Linked to the low thermal conductivity, a slow energy dissipation is also observed on the picosecond timescale. When semiconductors are photoexcited with a photon energy larger than their bandgap, hot carriers are generated (*i.e.*, high-energy electrons in the conduction band and high-energy holes in the valence band). In solar cells, the collection of these electrons (holes) is typically preceded by the loss of the excess of energy until they reach the minimum of the conduction band (maximum of the valence band). This process, known as *hot-carrier cooling*[32–34], occurs in the picosecond timescale when all the charges have reached a common temperature and start to interact with the lattice through carrier-phonon scattering to lose the excess of energy. The process is complete when the charges have reached the thermal equilibrium with the lattice. Manipulating this process is critical for many applications, from thermoelectric devices[31] where slow hot-carrier cooling is preferred to lasers[35] where short hot-carrier cooling time is desired for efficient radiative recombination[36]. These are only a few of the most interesting properties that perovskites exhibit, suggesting their versatility for several applications, not only as active absorber for PV applications.

## 1.3. The Key Role of the Lattice Softness

The bonding nature within the anionic inorganic framework in lead-halide perovskites exhibit a dual covalent and ionic nature[37] and electrostatic interactions dominate between ions with net charge making lead-halide perovskites polar semiconductors[38]. In addition, H-bonding interactions between the $A^+$ cation and the halide in the inorganic framework are present when the $A^+$ is organic[39]. This weaker bond nature compared to the purely covalent bond exhibited by silicon is reflected in the mechanically soft and dynamically disordered perovskite lattice whose alteration affects the electronic landscape of these solids. In addition, this class of materials tends to easily form vacancies and other defects in the lattice[40–42] that, in combination with the weak ionic bond

nature, unlocks the possibility for ions to migrate within the perovskites lattice or, in a solar cell stack, to drift toward the electrode of reverse polarity. This process is called *ion migration*[42–45] and has been identified as one of the main drivers for degradation[45–47] affecting the long-term stability of perovskite-based devices. In $MAPbI_3$, theoretical calculations and experiments show that both the $A^+$ cation and the $X^-$ anion can migrate with activation energies ranging from 0.46 to 1.12 eV, and 0.08 to 0.58 eV, for $MA^+$ and $I^-$ respectively[48–51]. The activation energy for the migration of $Pb^{2+}$ is found between 0.80 and 2.31 eV[48,51]. Thus, due to the high activation energy for the process, $Pb^{2+}$ is unlikely to migrate[48]. Ion migration is observed both in single-halide systems and in mixed-halide systems where the process is more evident under continuous illumination. In mixed-halide perovskites, the halide migration within the perovskite lattice results in a process known as *phase-segregation*[52–54]. In this process, halides migrate and form halide-rich domains which in turn affect the bandgap homogeneity (*i.e.* the bandgap of the mixed-halide perovskite is lost and domains of lower and higher bandgap are formed). The lattice softness of lead-halide perovskites also impacts their photodynamics. Several works suggested the formation of polarons (*i.e.* an electron/hole in an ionic crystal together with the induced polarization of the surrounding lattice) after photo-excitation to rationalize the early photophysics and carrier transport dynamics in these materials (*e.g.* slow hot-carrier cooling[55,56], low electron-hole recombination rate and long carrier lifetime[57], defect tolerance[58], ion migration and phase segregation[59–61]). Thus, a deep understanding of the perovskite lattice and strategies to modify it either by replacing its constitutive elements or by applying external stimuli is key for tuning the optoelectronic properties to access new properties that allow the development of new functional materials.

## 1.4. Pressure to Manipulate Optical Properties

The impact of the crystal structure on the optoelectronic landscape in perovskites has been discussed in the previous paragraph. Application of external stimuli (*e.g.* temperature, pressure, electric or magnetic field) is a direct way of tuning these properties[62–66]. Although temperature has been extensively used as a

tool for a better fundamental understanding of lead-halide perovskites in combination with several spectroscopic techniques[43,67–70], studies related to the pressure-induced effects and thus the structural properties of these materials are still scarce and mainly devoted to the high-pressure range (1-20 GPa)[71–74]. Pressure is a way to externally induce strain in a controlled way, while lattice mismatch during the crystal growth and lattice vibrations within the crystal can also lead to strain within the material. The effect of pressure on the optoelectronic properties of lead-halide perovskites can be understood from the diagram of bonding and antibonding orbitals of a representative $APbX_3$ that is responsible for the formation of the electronic bandgap as schematically shown in **Figure 1.2** (*left*). The valence band edge is formed by an antibonding combination of halogen *np orbitals* (Cl-3p, Br-4p or I-5p) and Pb *s orbitals* (Pb-6s), and the conduction band edge by an antibonding combination of Pb *p orbitals* (Pb-6p) with negligible coupling with of halogen *p orbitals* (Cl-3p, Br-4p or I-5p)[75–77]. The lead atomic orbitals contribute to 30-40% of the valence band and 70-90% of the conduction band[75,78]. Due to the antibonding character of the valence band edge, any change to the perovskite lattice that can increase (decrease) the overlap of the Pb *s orbitals* with the halide *p orbitals* will impact the energy of the valence band edge, moving it towards more positive (negative) potentials. Similarly, the conduction band has an antibonding character. Therefore, any change in the perovskite lattice that can increase (decrease) the overlap of the Pb *p orbitals* with the halide *p orbitals* will impact the energy of the conduction band minimum, moving it towards more positive (negative) potentials.

However, because of the poor coupling of the orbitals forming the conduction band, the changes in the energy level will occur to a minor extent in comparison to the one in the valence band. Although the $A^+$ cation does not play a major role in the formation of the electronic bandgap, it induces distortions in the inorganic framework through templating effects and thus plays a critical role in how the Pb and X orbitals overlap, determining many properties of this class of materials. Pressure – and therefore strain – can tune the extent of overlap of Pb orbitals with X orbitals. The main effects of pressure can be related to change in the metal coordination sphere such as bond lengths and interoctahedral tilting[79] as shown in **Figure 1.2**.

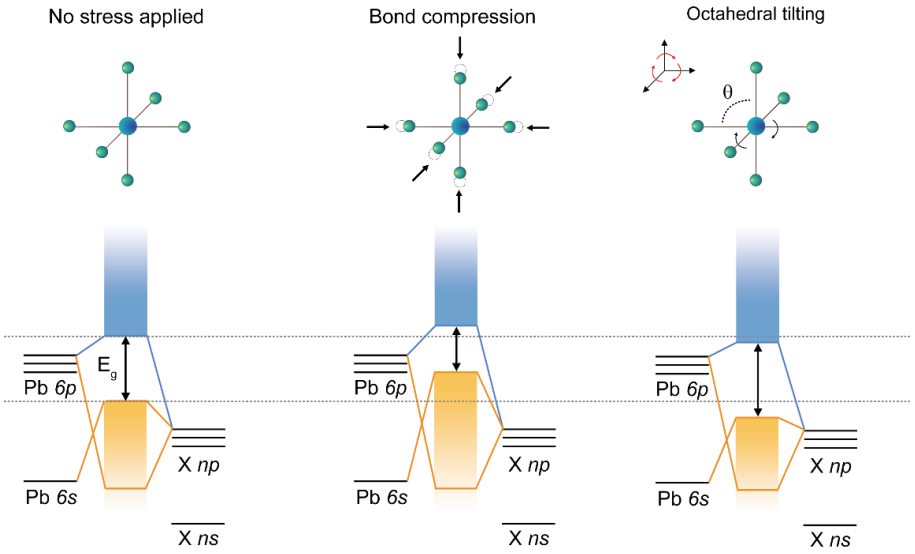


**Figure 1.2.** *External pressure can alter bond length and the octahedral tilting in lead-halide perovskites.* On the left, the schematic diagram of bonding and antibonding orbitals of $APbX_3$ showing the formation of VB and CB with no stress applied. In the middle, the result of external compression when the Pb–X bond length is reduced. The valence and conduction band edge are pushed toward higher energies to a different extent, reducing the bandgap energy. On the right, the band diagram shows the effect of external pressure when altering the octahedral tilting. When the Pb–X–Pb deviates from 180°, the valence band is pushed toward lower energies compared to the conduction band edge resulting in the enlargement of the bandgap energy.

In addition, in the case of layered 2D perovskite, the interlayer spacing distance and lattice packing arrangements are also affected by pressure. Compression of the Pb–X bonds results in higher overlap of the Pb *s orbitals* with the halide *p orbitals*, consequently reducing the bandgap energy. This pressure effect has been observed in many occasions at low pressure (<5 GPa) both in 3D and in layered 2D perovskites[71,80,81]. Further increasing pressure leads to the contraction of bonds, accompanied by a change in the bond angles which distorts the inorganic

framework[82,83]. Depending on the symmetry and orientation of orbitals within the inorganic framework, this can result in enlarged or reduced bandgap due to the change in the overlap between atomic orbitals. In layered 2D perovskites, pressure can affect the distance between inorganic sheets by compressing the organic interlayer spacing and thus enhancing the interlayer electronic interaction. This change leads to a relaxation of the confinement and hence a decrease in bandgap. Depending on the stiffness of the organic molecule[84–86] used to form the perovskite, pressure can induce a relatively large or small compression of the organic spacer.

On a macroscopic level, the Young's ($E$) and bulk modulus ($K$) in Eq. 1.1 and Eq.1.2 can be used as metric to evaluate the material's resistance to axial and uniform compression, respectively. The first is often used for layered 2D perovskites where the unit cell compression has been found to be anisotropic[81,83] and particularly pronounced along the *c-axis*, where the organic interlayer spacers sit. $K$ is often used for 3D perovskites and in layered 2D perovskites where the compression is found more isotropic[80].

The Young's modulus ($E$) is described by the equation

$$E = \frac{\sigma}{\varepsilon} = \frac{F}{A}\frac{L_0}{\Delta L} \tag{1.1}$$

where $\sigma$ is the uniaxial stress (force F per unit area A) and $\varepsilon$ is the axial strain (proportional deformation) in the linear elastic region, $L_0$ is the original length, $\Delta L$ is the change in length (negative under compression, positive when stretched). Soft elastic solids exhibit a low Young's modulus. For example, rubber has a Young's modulus between 0.01 and 0.1 GPa. Contrary, stiff or inelastic solids exhibit high Young's modulus. This is the case for steel that exhibit a Young's modulus between 190 and 215 GPa. Young's modulus always refers to a specific crystal direction and different crystal orientations can exhibit a different Young's modulus.

The bulk modulus ($K$) is described by the formula

$$K = -V\frac{dP}{dV} \quad (1.2)$$

Where $V$ is the final volume after load and $\frac{dP}{dV}$ is the partial derivative of pressure with respect to volume. For comparison, the bulk and Young's moduli of the most common 3D perovskites, layered 2D perovskites with $n$ = 1 and conventional semiconductors[87] are reported in **Table 1.1**.

**Table 1.1.** Bulk and Young's moduli for the most common conventional semiconductors, 3D and layered 2D lead-halide perovskites ($n$ = 1) with butylamine (BA) and phenethylamine (PEA) used as spacers. In brackets is the crystallographic direction to which the Young's modulus is referred.

| Material | Bulk Modulus (GPa) | Young's modulus (GPa) |
|---|---|---|
| Silicon | 105 [88] | 62 <100> [89] -188 <111> [90] |
| GaAs | 75 [91] | 84.4 <100> [92] |
| $MAPbI_3$ | 15 [93–95] | 10 [95] - 14 [94] <100> |
| $MAPbBr_3$ | 24 [93] | 19.2 <100>[96] |
| $MAPbCl_3$ | 45 [97] | 17.7 <100> [96] |
| $FAPbI_3$ | 14 [98] | 12.8 <110> [96] |
| $CsPbBr_3$ | 22[99] | 15.6 <101> [96] |
| $(BA)_2PbI_4$ | 6-8 [100] | 8-9 [100] <001> |
| $(PEA)_2PbI_4$ | 10[101] | 11 <001> [101] |

As can be seen in **Table 1.1**, both the Young's and Bulk moduli of III-V semiconductors and silicon are almost an order of magnitude higher than those of perovskites, confirming the softer nature of the perovskite lattice. Thus, their structure and consequently electronic states tend to be more affected by pressure. There are also larger differences among the perovskite compositions. In the 3D perovskites, when replacing iodine with bromine or chlorine in $MAPbX_3$ systems, the bulk modulus increases due to the stronger bond between Pb–X which makes the inorganic framework stiffer. In addition, the reduced unit cell volume induced by the replacement of a large halide with a small halide leads to stronger atomic interactions within the perovskite lattice and the overall softness of the material is reduced. The lattice stiffness is also affected by the change in the $A^+$ cation. For instance, replacing an organic cation with an inorganic one as caesium ($Cs^+$)

results in a stiffer lattice. In the layered 2D perovskites, a key role is played by the organic interlayer spacer. For this class of materials, the mechanical properties are not only related to the inorganic framework but also to the stiffness of the organic molecule used in the composition. The large parameter space of the organic molecules used as spacers allows for designing materials with different flexibility. It is worthwhile to mention that not only the spacer itself delineates the structural-optoelectronic properties relationship but also how the organic spacer packs in the crystal.

So far, studies in a relatively mild range of pressure (< 1 GPa) are rare. This means we are missing important information about the material's behaviour in a strain range that can be introduced during the manufacturing process or during operation (*e.g.* from polaron formation). In addition, these studies can pave the way toward new applications that exploit perovskite's mechanochromic properties expanding the perspective for their future applications[102–104]. No less important is investigating perovskite's properties under mild range of pressure for a deeper understanding of fundamental properties and mechanisms often overlooked when studying materials at high pressures. In turn, understanding of pressure-induced modifications is quintessential for a systematic implementation of this pressure through compositional engineering to permanently realize the effects of mechanical compression.

## 1.5. Electron Back-Scattered Diffraction

Despite the remarkable properties of halide perovskites due to the softer lattice in comparison with conventional semiconductors such as silicon and III-V semiconductors, the softness of the lattice is also responsible for reduced stability of the perovskites under some experimental conditions. In particular, lead-halide perovskites with an organic $A^+$ cation exhibit significant instability under electron beam irradiation[105,106] complicating the study of the microstructure with some of the most common scanning electron microscopy-based (SEM) techniques (*e.g.* cathodoluminescence, electron back-scattered diffraction). Given the profound relation between structural and optoelectronic properties of these materials, sensitive and less destructive techniques are required to probe their

microstructure. In metallurgy, geology, and in the ceramics sector, electron-back scattered diffraction (EBSD) is used as a powerful technique to identify the presence of different crystal phases with high spatial resolution, characterise the grain size and the strain among grains, discriminating compounds with similar crystal structures and the temperature response of crystal structures. Combining good spatial resolution, large scale coverage and the simple implementation in SEM-based tools, EBSD is one of the leading techniques for investigation of a material's microstructure[107,108]. In this paragraph, based on this reference[109], we expand on the working principle of EBSD together with its potential and limitations as a tool to investigate the microstructure of lead-halide perovskites. In addition, we discuss the importance of the image processing and the indexing procedure to extract crystallographic information from the diffraction patterns collected. EBSD is a SEM-based technique where the incident electron beam interacts with a crystalline material and diffracted backscattered electrons are collected forming the so-called Kikuchi patterns. Electrons from the electron beam penetrating in the sample are elastically and inelastically scattered. This results in a diverging source of electrons with a broad range of energies. Those electrons which have undergone elastic and quasi-elastic scatter events and thus lost only a small quantity of energy - in the range of a few eV – can escape from the specimen and if they satisfy Bragg's law they can diffract into cones (Kossel cones) with the cone axis normal to the diffraction plane normal. Then, the Kossel cones intersect with a planar detector (usually a phosphor screen) and the typical nearly straight Kikuchi lines appear. Those lines lie on a diffuse background generated by the inelastically scattered electrons having lower energies. The combination of Kikuchi lines provides a direct measurement of the crystallographic orientations of the specimen. A schematic representation of the technique, working principle and the typical Kikuchi pattern collected are shown in **Figure 1.3**.

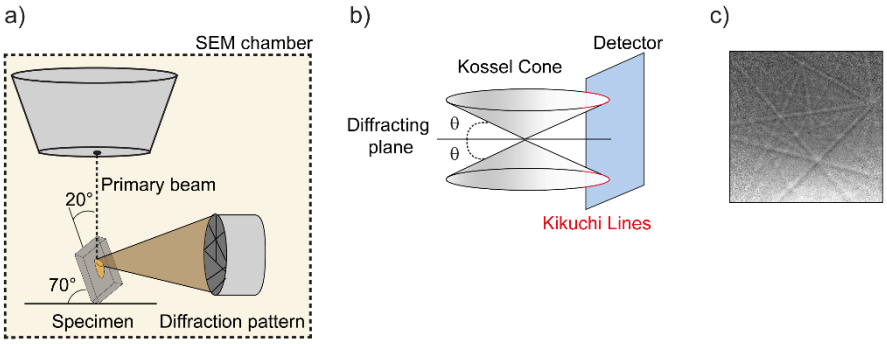


**Figure 1.3.** *EBSD for probing the material's microstructure.* **a)** Schematic representation of a typical EBSD setup[109], **b)** Kikuchi lines originating from a diffracting plane at the intersection of the Kossel cone and the detector and **c)** the experimental Kikuchi pattern obtained from $MAPbI_3$ thin film[109].

The EBSD system used in this thesis has an angular resolution of about 0.5°. The angular resolution of EBSD is related to the quality and sharpness of the diffraction patterns and therefore how well a Kikuchi pattern can be indexed. The depth resolution of the EBSD is limited by the excitation volume which is the interaction volume of the primary electrons within the sample from which electrons are backscattered, forming the typical diffraction patterns.
From a Monte Carlo-based simulation (CASINO[110]) where 15 keV is used as primary beam voltage, we estimate the 50% escape probability of electrons in the interaction volume to be from 35 nm below the surface for a 70° tilted sample. For a 0° tilted sample these electrons could escape from 260 nm below the surface as shown in **Figure 1.4**. Thus, tilting the sample makes EBSD a more surface sensitive technique. The spatial resolution depends on the sample volume where electrons undergo elastic scattering events. When the electron beam interacts with the tilted specimen, the largest electron density and the largest escape probability are both located close to the spot where the beam enters the sample (grey scale in **Figure 1.4**). The interaction volume is hence close to the beam size. In the example below for electrons with 50% escape probability is about 9 nm at 6 nm beam size, which then defines the lateral resolution.

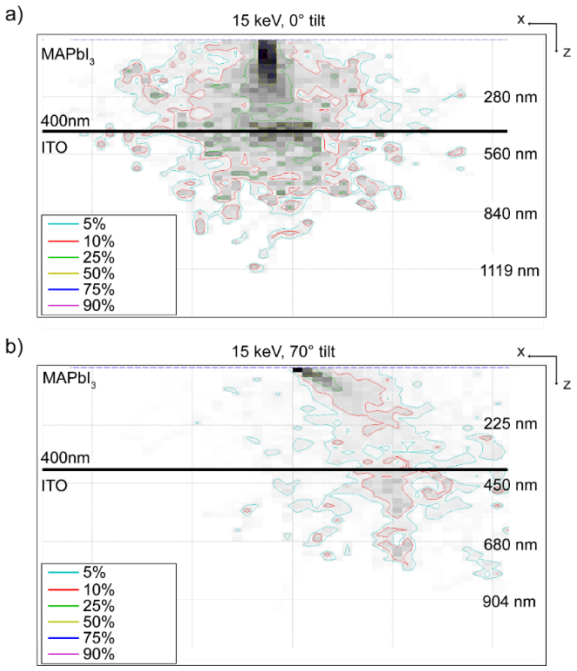


**Figure 1.4.** *Simulated interaction*[109] *volume between 15keV electron beam and 400nm $MAPbI_3$ perovskite on ITO obtained using a Monte Carlo simulator (CASINO).* **a)** Interaction volume in the X-Z plane of back-scattered electron beam at 0° (no tilt applied) and **b)** 70° tilt (EBSD configuration). The X direction (3 nm/pixel) is parallel to the surface and Z direction corresponds to the thickness of the sample. The percentages shown represent the escape probability of back-scattering electrons from different locations in the sample (*e.g.* 50% of escape probability represented by the yellow line).

The smallest reasonable step size is the lateral resolution. However, the choice of such small step size is impractical as the total number of collected points would be extremely large and would require many hours of collection with the risk of damaging the material. Using an extreme example, a 500 µm x 500 µm scan area with a 10 nm step size would result in $2.5\times10^8$ data points. If we consider 2s as typical exposure time per data point in a conventional EBSD system, the measurement will require 158 years. In practice, a step size small enough to resolve the desired features (*e.g.* grain size) is chosen. During the experiment, the

sample is mounted at 70° with respect to the horizontal to maximize the collection yield of the backscattered electrons, and the detector is placed horizontally on the side a few centimeters away from the specimen as shown in **Figure 1.5**. As mentioned earlier, Kossel cones intersect with a planar detector and the so-called Kikuchi lines emerge from a diffuse background generated by the inelastically scattered electrons forming characteristic Kikuchi patterns. The Kikuchi patterns can be described as a gnomonic projection of the crystal lattice on the flat screen where the angles between the projected planes correspond to the interplanar angles, the band crossings to zone axes of the crystal lattice, and the width of the bands is related to the interplanar spacing, $d_{hkl}$, as follows from Bragg's law. Kikuchi bands are converted into points by the mathematical Hough's transformation as they are easier to locate and fit automatically. To enhance the Kikuchi lines from the background, we use a Phyton script to average the background from at least 1000 Kikuchi patterns and divide the pattern from the measurement by this background to correct for spatial differences in collection efficiency. In addition, we apply brightness corrections to remove fluctuations of individual quadrant brightness from frame to frame (usually observed working at low beam current).

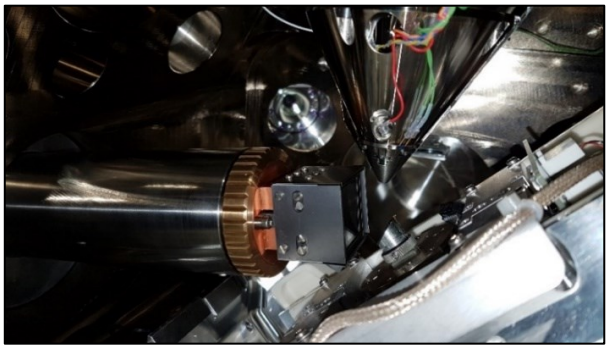

**Figure 1.5.** *Geometry of the EBSD setup used in this thesis*[109]. On the left, the direct-electron detector facing the sample mounted on a metallic stub and the sample is tilted by 70° with respect to the horizontal. Above the sample, the source of electrons is shown, operating at a few millimetres distance from the surface of the sample.

The result of our image processing is adapted from reference [111] and shown in **Figure 1.6**. We index the Kikuchi patterns using OIM Analysis™ from EDAX. The rotation of the probed crystal results in a rotation of the Kikuchi pattern, whereas a tilting of the crystal orientation results in a shift of the pattern. To index the Kikuchi patterns, it is necessary to input the correct crystal structure of the material and an accurate calibration.

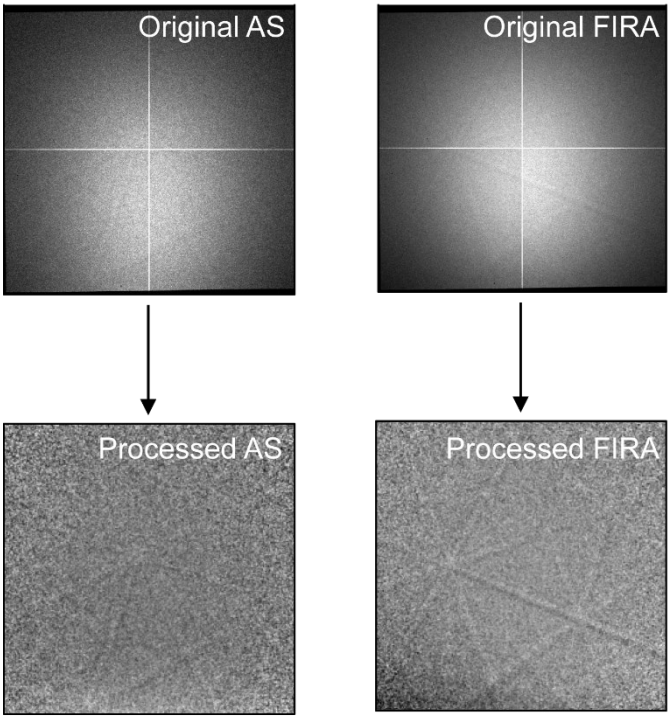


**Figure 1.6.** *Image processing routine.* Kikuchi patterns taken from reference[109] for $MAPbI_3$ thin films fabricated via two different strategies before and after image processing.

Calibration is fundamental to obtain reliable data. The goal of the calibration is to establish the geometry of the projection of the EBSD pattern onto the detector and therefore determine the geometrical relationship between the sample coordinates in the SEM chamber and the detector. To calibrate our system, we use a routine which define the calibration parameters using a high-

quality pattern from a known material at a specific working distance (*e.g.* Cu, Al or Si). Specifically, we have measured Kikuchi patterns of copper and silicon at working distances from 10 to 13mm. Then this calibration is applied to the perovskite Kikuchi patterns before indexing. Despite the power of this technique for probing microstructural information of crystalline solids, the detection with a phosphor screen requires high current for the collection of a sufficiently large signal-to-noise ratio due to presence of losses given by the optics present in the collection path. This is a limitation when investigating perovskite thin films, as the use of a current of a few nA can already be damaging to the material. Instead, in this thesis we use a direct-electron detector[112] (*i.e.* the phosphor screen is not used), which directly measures the incident electrons onto the detector. Therefore, this type of detector has higher sensitivity compared to the traditional detectors and crucial for probing perovskite's microstructure without altering or damaging the specimen while measuring[113]. Here, the current required to collect a sufficient large signal-to-noise ratio signal is in the order of a few pA. The other difference with the traditional EBSD detectors employing phosphor screens is the required accelerating voltage. The traditional one requires a voltage of 15-20 kV that also increases the probing depth. On the other hand, the direct-electron detector can probe the microstructure with adequate signal-to-noise ratio even at 5kV, making the technique more surface sensitive. In addition, the typical acquisition time per pixel necessary to obtain high quality patterns is significantly reduced from a few seconds to a few milliseconds when moving from a phosphor screen-based detector to a direct electron detector.

## 1.6. Pressure-dependent Spectroscopy

We have already discussed in **Chapter 1.3** and **Chapter 1.4** how the dual ionic-covalent nature of the bond in perovskites is reflected in the mechanically soft and dynamically disordered perovskite lattice. Alterations of the perovskite lattice provide a route to manipulate the electronic landscape of these solids. These alterations can be achieved by chemically replacing the elemental components of the perovskite lattice or by applying an external bias. The aim of this thesis is to investigate how changes in a specific perovskite lattice affects the

optical properties without altering the composition. Therefore, the first approach is here excluded. The second approach requires the application of an external bias able to induce a small and continuous change in the atomic structure in order to draw a correlation with a change in the perovskite properties. To date, how changes in temperature affect the perovskite structure are well known and heavily studied[62,68,114,115]. Changes in temperature include alterations in the crystal lattice constants together with modifications in the phonon distribution, carrier mobility, charges diffusion length. In sharp contrast, changes induced by pressure affect only the perovskite lattice constants and all the following modifications in the optoelectronic landscape can be linked to these structural changes without being affected by pressure in the first place.

Most of the pressure-dependent techniques are based on diamond anvil cell. Here, the sample is placed between small flat faces on the pointy ends of two diamonds and the pressure is generated by applying a force across the faces of the diamonds. One of the main advantages in the use of the diamond anvil cell over other pressure techniques is its transparency to many forms of radiations. The absence of windows between the sample and the radiation source allows the combination of this tool with various light sources. Therefore, X-Ray can be used to characterize the structure of the material, lasers of various wavelengths can be used to study absorption, photoluminescence or other processes in different range of energies. Nowadays, most of the high-pressure material properties known are the result of employing anvil cell-based techniques.

The application of the force across the faces of the diamonds results in a gradient of pressure within the sample, where the highest pressure is experienced in the centre of the sample and the lowest (1 atm) at the edges. Thus, the pressure applied is not isotropic but limited from the force exerted on the diamonds in a particular sample's direction. Since diamonds are inert, this technique is extremely versatile for a wide range of substances, and it works both for powders, films, or liquid provided that the diamonds are not damaged. Gasket and confining media (*e.g.* $N_2$, Ar, He, ethanol, methanol and NaCl) are also used to reduce the extreme shear stress within the sample and friction between the sample and the diamond face. However, despite their popularity for pressure-dependent structural and spectroscopic measurements, the pressure range accessible through

this type of pressure cell starts at high values, from gigapascals to hundreds of gigapascal. Lower ranges are difficult to access in a controlled way. Lower pressures in the order of $10^{-2}$-$10^{-1}$ GPa are an interesting range to investigate because it aligns with typical values reached during the manufacturing or through chemical and compositional engineering in semiconductor materials. For this reason, in this thesis, we use a hydrostatic pressure cell working in a lower range of pressure (0.05 – 0.4 GPa). The pressure cell consists of a metal housing with transparent windows as shown in **Figure 1.7a**. Depending on the transmission range needed, it is possible to use quartz (180-2000 nm), sapphire (250-5000 nm) or magnesium fluoride (150-6500 nm) as a material for the pressure cell windows, bearing in mind that different materials can handle a different value of maximum pressure. In this thesis, the windows used are quartz, allowing for pressure range from 0 GPa to 0.4 GPa. The pressure cell is filled with a transparent fluorinated mix of inert liquids that are perfluorohexane, dodecafluoro-n-pentane and decafluorobutane. In this thesis, the liquid is abbreviated with his commercial name, FC-72[116]. The liquid is thermally and chemically stable and compatible with all the perovskites studied in this thesis. Furthermore, it is not toxic and evaporates without leaving residuals on the sample. An important requirement for a liquid to be used as medium in the pressure cell is a negligible absorption in the range of energies used to investigate the material properties. All the measurements conducted in this thesis aim to investigate perovskite properties in the near ultraviolet and the visible. As shown in **Figure 1.7b**, the FC-72 has a flat optical response in this range, making it suitable for the scope of this thesis. However, extra care needs to be taken when measuring at pressure above 0.3 GPa as the liquid become translucent, increasing the scattering and therefore reducing the transmission through the liquid. This effect is due to the presence of $O_2$ in the liquid. To prevent a significant reduction in transmission when working at high pressure, the liquid is degassed with the *Freeze-Pump-Thaw cycling* in the Schlenk line through which dissolved gases are removed from the liquid. The liquid is first frozen by immersion of the flask in liquid $N_2$. When completely frozen, the flask is opened to the vacuum and pumped for 3 minutes with the flask still immersed in the liquid $N_2$. The vacuum is then closed, and the flask is warmed until the solvent has completely melted. This process is repeated for 3

times before to disconnect the flask from the Schlenk line and store it in the glovebox to prevent further incorporation of $O_2$. The pressure is generated by increasing the amount of the liquid in the pressure cell through a pump at a constant volume. An advantage of the use of this hydrostatic pressure cell is the possibility to probe a large area sample (a few $cm^2$) in comparison with the diamond anvil cells (powders or films with volume in the cubic micrometre range). It is worth mentioning that contrary to the diamond anvil cell, the hydrostatic pressure cell applies an isotropic pressure.

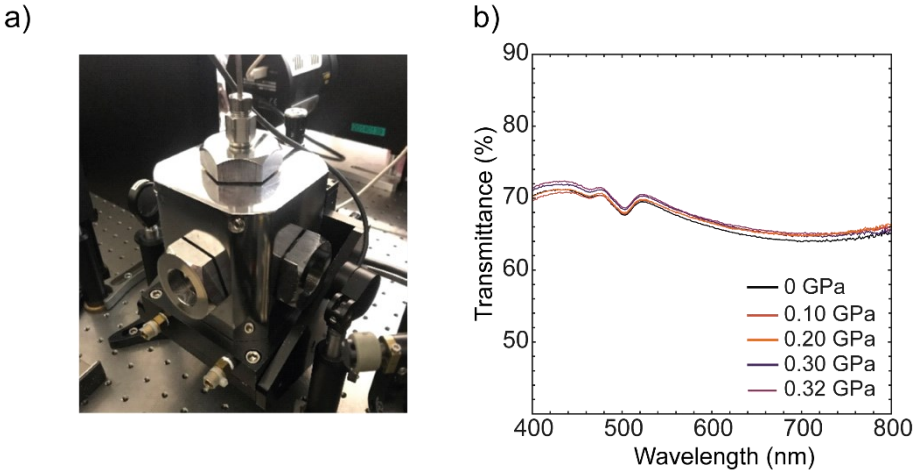


**Figure 1.7.** *Hydrostatic pressure cell used to compress the perovskite.* **a)** Hydrostatic pressure cell with quartz windows used in this thesis. The pressure cell is connected to a manual pump. **b)** Transmittance spectrum of the FC-72 shows a relatively flat response in the energy range used in this thesis.

Pressure-dependent optical absorption allows for monitoring the bandgap of materials as a function of the applied pressure. While the bandgap can also be measured using emission spectroscopy, absorption is not only useful in the case of compositions that do not show radiative band-edge transitions at a certain pressure, but also for compositions where several optical bandgaps are present, whereas the emission feature derives only from certain states. For example, this is the case of mixed-halide perovskites under illumination that exhibit phase segregation. During illumination of such materials, iodide- and bromide-rich

domains are formed. Thus, three bandgaps are present in the composition: one can be attributed to the original mixing ratio, one to the bromide-rich phase (high-energy bandgap) and one to the iodide-rich phase (low-energy bandgap). However, the radiative emission of these compositions originates only from the iodide-rich phase that is the low energy state into which charges funnel from the mixed-phase. Thus, the bandgap evolution obtained through pressure-dependent photoluminescence is not complete. In addition, the comparison between absorption and emission can reveal the evolution of the Stokes shift under pressure. Together with the steady-state optical absorption measurements, pressure-dependent transient absorption spectroscopy is a powerful tool to investigate the photogenerated excited state absorption energies and associated lifetimes of perovskites.

In this thesis, we use a femtosecond pressure-dependent transient absorption setup (fs-TAS) where we combine our hydrostatic pressure cell with a non-degenerate pump-probe configuration. The setup is schematically depicted in **Figure 1.8**. The laser source for the TA is a regenerative Ti:sapphire amplifier (Coherent) generating a fundamental beam characterized by 800-nm pulses at a 1-kHz repetition rate, with a pulse duration of 35 fs and a pulse energy of 6.5 mJ. The fundamental beam is split into two beams by a beam splitter. After chopping the beam in the pump path (using 500 Hz as the frequency), a 400-nm pulse pump is generated by doubling the 800-nm pulse with a beta barium borate (BBO) crystal. This beam is the *pump* and is responsible for the generation of the excited states.

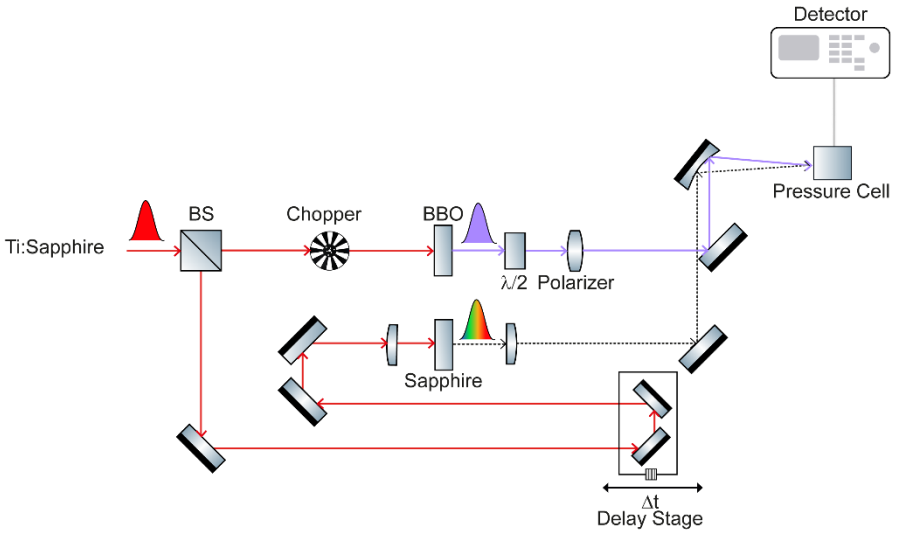


**Figure 1.8.** *Schematic representation of the pressure-dependent transient absorption spectroscopy setup used in this thesis.* The laser source (Ti:Sapphire) is split in two beams. The frequency of the first is doubled using a BBO crystal to generate the pump beam (3.1 eV). The second beam is used to generate white light using a sapphire plate. The pump-probe delay is controlled by a mechanical delay stage allowing for probing from 0.05 ps to 800 ps. Pump and probe are focussed on the sample sitting inside the pressure cell through a parabolic mirror.

A short-pass filter is placed after the BBO crystal in the pump path to remove 800-nm residue from the fundamental beam which might cause saturation of the detector during the acquisition and a falsehood of $\Delta T/T$ features in that wavelength range. The white light continuum *probe* pulse is generated by focusing the 800-nm femtosecond pulses through a 2-mm sapphire plate. To prevent two-photons absorption by the sample, which could be excited by the high-density probe, a reflective neutral density filter (OD 1) is placed in the probe path before the sample position.

A 50 cm mechanical delay stage is used to delay the arrival time of the probe with respect to the pump and thus follow the evolution of ultrafast processes as a function of time. The delay time accessible is from 0.05 ps to 800 ps.

Furthermore, it is possible to set a specific delay time and follow in real time (seconds or minutes) the evolution of the investigated system. This functionality will be used later in **Chapter 4** to investigate the phase segregation of mixed-halide perovskites during illumination as a function of real time (minutes) and at a specific delay time, after the hot-carrier cooling process and before charges recombination. The pump beam (3.1 eV) and the probe beam (white light) are overlapped inside the pressure cell during the measurement and the probe spot size was chosen to be smaller than the pump spot size to obtain homogenous excitation over the probed area.

The overlap of the pump and probe beam inside the pressure cell is crucial to collect the $\Delta T/T$ signal and the correct alignment is challenging. The alignment process in the pressure cell, compared to the case of a conventional sample holder in air, is limited by the size of the pressure cell windows whose aperture is 10 mm and the inability of looking directly at the sample while aligning. The first issue is tackled by focusing on the sample both the pump and probe with a parabolic mirror (*i.e.* avoiding two different focussing paths for the two beams). Aligning a parabolic mirror is not straightforward, and the two incoming beams must be parallel to be focussed at the same distance without elliptical distortion of the beam. The second issue is tackled by using a specific alignment strategy which consists of the use of a 3-axis translation stage where the pressure cell sits and a metallic plate of the same size of the sample characterised by a pinhole in the center of about 100 μm. This metallic plate is used as guide for a first rough alignment. First, we move the pressure cell along the $x$, $y$ and $z$ direction to make the probe beam passing through the pinhole in the metallic plate. This procedure has the scope of aligning the beam in a specific point of the sample. The goodness of the alignment is monitored by looking at the number of counts reaching the detector placed after the pressure cell. When the counts are optimised, the pump beam is moved toward the same position of the probe, this time without moving the pressure cell. When the pump spot is observed after the pressure cell, the first rough alignment is complete, and the metallic plate is replaced by the real specimen. At this stage, pump and probe overlap roughly at the same position. However, a fine tuning is done using the sample to monitor the overlap. When the sample is placed in the pressure cell, we move the mirror before the parabolic

mirror that controls the direction of the pump beam to increase the *ΔT/T* signal collected by the detector. When the signal is optimised, the sample is ready to be measured. It is worth note mentioning that this alignment procedure is done with the pressure cell liquid as the refractive index of the liquid is higher (1.25) than air (1.00), thus changing the focal point of the beam. The alignment of the pressure-dependent transient absorption setup is fine-tuned at each pressure from ambient to 0.35 GPa by moving the pump beam to optimize the number of counts collected by the detector.

The collected spectrum of the transient species is a measure of the change in the transmittance *ΔT* of the system after excitation with the pump pulse $T_{on}$ and before excitation $T_{off}$ when the system is in the ground state as in Eq. 1.3. The collected signal can be expressed also using the absorption.

$$\frac{\Delta T}{T} = \frac{T_{on} - T_{off}}{T_{off}} \tag{1.3}$$

The differential spectrum collected at different delay time between pump and probe can track the evolution of the ground and excited states of the material as a function of wavelength and time. **Figure 1.9** shows a simple case of a sample with a ground state (G) and, as example, two excited states (A and B). The differential transmittance spectrum contains much information of the system but in turn it results in a complex convolution of signals:

- *Ground-state bleach (GSB)*: in the unperturbed system (*pump off*), most of the charges are in the ground state (G). When the system is excited by the pump (*pump on*), some of these charges are promoted to the excited level A. Hence, the ground-state transmittance in the excited system is greater than the one in the non-excited system, resulting in a positive signal in the *ΔT/T* spectrum in the wavelength region of the ground state absorption as in **Figure 1.9**.
- *Stimulated emission to the ground-state bleach (SE)*: this process occurs when a photon from the probe passes through the excited volume of the sample and induces the emission of another photon from the excited state A of the sample to the ground-state G. The emitted photons have the same

direction of the probe and therefore collected by the detector. As a result, the transmitted light intensity at the detector position will be higher when the pump is on, and the *ΔT/T* signal will be positive as in **Figure 1.9**. The energy of the emitted photons roughly matches the photoluminescence spectrum of the sample.

- *Excited state absorption (ESA)*: the pump excitation may induce optical transition from the excited state A to a higher-lying excited state B in certain wavelength regions with a consequent absorption of the probe at these wavelengths. Thus, the transmittance at these wavelengths when the system is excited is lower than when the system is not excited due to the promotion of charges to those energy levels. Therefore, a negative signal in the *ΔT/T* spectrum will appear (**Figure 1.9**).

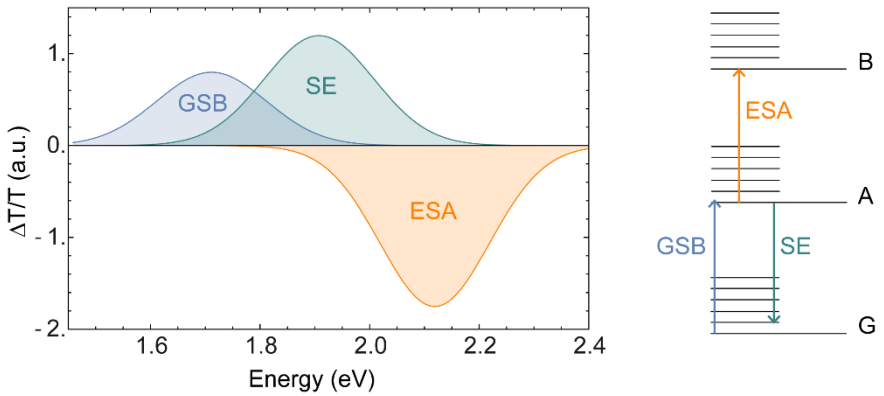


**Figure 1.9.** *Typical features expected in a ΔT/T spectrum.* Schematic representation of the deconvoluted signals observed after collection of TA spectra. On the right, the energy transition associated to the observed features.

A common artifact related to the use of a supercontinuum pulse is the chirp of the white light due to the temporal dispersion of the frequency of the probe. In other words, all the wavelengths of the white light do not reach the sample at the same time (**Figure 1.10a**), resulting in a different time zero (*i.e.* when pump and probe overlap in time) that distorts the *ΔT/T* spectrum. The kinetics at a specific wavelength is not affected by this artifact but to monitor precisely the

evolution in the picosecond timescale of all the *ΔT/T* features, a correction needs to be made. We extract the chirp measuring the arrival time of each wavelength on a bare quartz substrate, the same used as substrate to deposit the perovskites studied in this thesis. The measurement is done inside the pressure cell, with the same optics and in the same conditions as the real experiment. The chirp is not affected by pressure; thus, we use the correction calculated at ambient pressure (~3 ps) and the result is shown in **Figure 1.10b**.

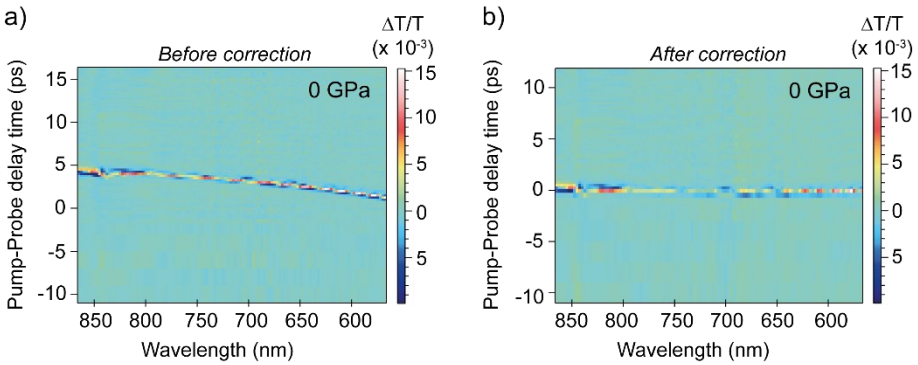


**Figure 1.10**. *Chirp of the white light continuum.* **a)** Common artifact when using supercontinuum probe light due to the temporal dispersion (chirp) of the frequency of the probe and **b)** its correction resulting at the same time zero for all the wavelengths of the light.

To date, a broad range of photoluminescence-based techniques have been used to characterise the properties of perovskite[114]. For instance, pressure- and temperature-dependent PL have been used to investigate phase transitions. Voltage-dependent PL has been used in complete solar cells or LEDs to study the interplay between radiative and non-radiative recombination[117]. Spatially resolved PL is used to characterise large areas in the perovskite thin films and quantify inhomogeneities relevant for devices[118]. For a more complete picture of the optical properties of a material, absorption measurements can be combined with pressure-dependent photoluminescence experiments as later discussed in **Chapter 5**. The setup used in this thesis is schematically represented in **Figure 1.11**.

In this thesis, we conduct pressure-dependent photoluminescence measurements using a 405 nm or 375 nm continuous laser (CW) as source of excitation. We then focus the laser on the sample sitting inside the pressure cell at 45° and the reflected signal is collected from a spectrometer operating in the visible. To avoid the saturation of the spectrometer, a 450 nm long pass filter is placed after the pressure cell to filter out the reflection of the laser. The alignment of the pressure-dependent photoluminescence setup is fine-tuned at each pressure from ambient to 0.35 GPa to compensate for slight deviation of the beam with respect to the spectrometer. Exposure time between 0.5 s and 10 s are used depending on the emissivity of the sample.

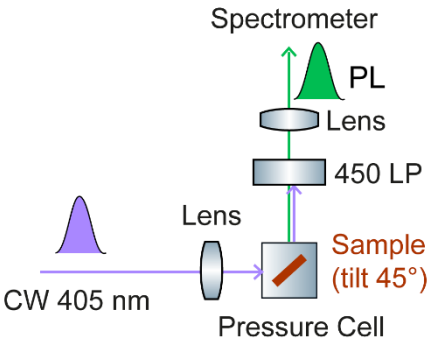


**Figure 1.11.** *Photoluminescence setup.* Schematic representation of the steady-state photoluminescence setup used in this thesis.

## 1.7. Outline of the thesis

In this thesis, we focus on investigating the structural response of perovskites to the exertion of external pressure. Due to the strong connection between structural and optoelectronic properties in these materials, external pressure and, more in general, strain, can be used to manipulate the optical properties of these materials targeting specific device applications.

In **Chapter 2** we study the microstructure of methylammonium lead iodide ($MAPbI_3$) thin films fabricated with the conventional antisolvent-dripping (AS) method and the novel flash-infrared annealing (FIRA) and how this affects

optoelectronic properties such as local photoluminescence (PL), charge carrier lifetimes, and mobilities. To probe the microstructure, we use electron back-scattered diffraction (EBSD), and we find that oftentimes domains observed in SEM are misidentified with crystallographic grains. Despite substantial differences in grain size between the two systems (~100s of nm for the AS and ~100s of μm for the FIRA), we find similar optoelectronic properties suggesting that the optoelectronic quality is not necessarily related to the orientation and size of crystalline domains.

In **Chapter 3** we move to investigate how structural changes in $MAPbI_3$ thin films induced by external pressure affect its photophysics in the femtosecond timescale. Here, we suggest pressure as a tool to manipulate the hot-carrier cooling for targeting specific applications as hot-carrier solar cells, lasers, thermoelectric devices. A combination of computational analysis and spectroscopic data reveal the role of pressure in the change of electron-phonon coupling which in turn affects the rate at which hot-carriers reach the lattice temperature. Applying compressive stress to the material favours fast hot-carrier cooling at high excitation density ($> 10^{18}$ photons/cm$^2$) which would be beneficial for light-emitting diodes (LEDs) and laser applications.

The effect of pressure is noticeable not only in the femtosecond timescale but also in the seconds-minutes timescale. In **Chapter 4** we investigate the phase segregation in mixed-halide perovskites, a detrimental process occurring when mixed-halide compositions are subjected to continuous illumination. This segregation occurs through halide migration, which is also observed in single-halide compositions, and whose control is thus essential to enhance the lifetime and long-term stability of devices. We use pressure-dependent transient absorption spectroscopy in combination with computational calculations to track the evolution of the mixed phase as well as the bromide- and iodide-rich phase in mixed-halide perovskites as a function of real time and pressure. We observe that phase segregation is almost suppressed at 0.3 GPa for several bromide-iodide mixing ratio and also the overall segregation rate is dramatically reduced. Our findings suggest that the process of phase segregation cannot be associated only to thermodynamics or kinetics but a combination of the two is the key towards a better understanding of this process. Furthermore, the pressure reveals itself as an

effective tool to reduce phase segregation. A similar compression of the unit cell volume can be achieved by chemical engineering, specifically replacing the $A^+$ cation with a smaller ion, exemplified by replacing $MA^+$ with $Cs^+$. Comparably to what obtained under hydrostatic pressure, the change induced by this "*chemical pressure*" reduces the phase segregation.

Layered 2D perovskites offer even a richer parameter space for property manipulations as they consist of an inorganic framework and organic spacer that can be tuned according to the required functionalities. Therefore, external mechanical stimuli, such as pressure, can be used to induce structural changes and investigate the effect on their optical properties. In **Chapter 5** we investigate the structure-property relationship in representative iodide- and bromide-based Ruddlesden-Popper and Dion-Jacobson 2D perovskites fabricated with comparable organic spacers, benzylammonium (BN) and 1,4-phenylenedimethylammonium (PDMA), respectively. By using pressure-dependent absorption and X-ray diffraction (synchrotron source), we probe the correlation between optical and structural properties in the range of 0-0.35 GPa, a pressure at which the observed effects might be comparable to the processes occurring in the optoelectronic devices (*e.g.* polaron induced strain, lattice mismatch, chemical strain) and during manufacturing. We find that Ruddlesden-Popper and Dion-Jacobson perovskites behave similarly under pressure, despite the different forces involved in connecting the two perovskites slabs and there is no difference in the pressure response between the iodide- and bromide-based systems. The only outlier is $(BN)_2PbBr_4$, where we find a larger redshift in the optical absorption under pressure (-54.9 meV). Pressure-dependent X-ray diffraction measurements in combination with density functional theory calculations reveal that the origin of this large shift is the presence of an isostructural phase transition. This phase transition is associated with a decrease in the octahedra tilting (*i.e.* angles closer to 180°) which leads to an increased penetration depth of the BN spacers into the inorganic framework.

# 1.8. References


(1) Bai, T.; Yang, B.; Chen, J.; Zheng, D.; Tang, Z.; Wang, X.; Zhao, Y.; Lu, R.; Han, K. Efficient Luminescent Halide Quadruple-Perovskite Nanocrystals via Trap-Engineering for Highly Sensitive Photodetectors. *Adv. Mater.* **2021**, *33* (8). https://doi.org/10.1002/ADMA.202007215.

(2) Wei, F.; Deng, Z.; Sun, S.; Xie, F.; Kieslich, G.; Evans, D. M.; Carpenter, M. A.; Bristowe, P. D.; Cheetham, A. K. The Synthesis, Structure and Electronic Properties of a Lead-Free Hybrid Inorganic–Organic Double Perovskite $(MA)_2KBiCl_6$. *Mater. Horizons* **2016**, *3* (4). https://doi.org/10.1039/C6MH00053C.

(3) Liang, K.; Mitzi, D. B.; Prikas, M. T. Synthesis and Characterization of Organic-Inorganic Perovskite Thin Films Prepared Using a Versatile Two-Step Dipping Technique. *Chem. Mater.* **1998**, *10* (1). https://doi.org/10.1021/cm970568f.

(4) Mitzi, D. B. Templating and Structural Engineering in Organic-Inorganic Perovskites. *J. Chem. Soc., Dalt. Trans* **2001**, *1* (12). https://doi.org/10.1039/b007070j.

(5) Mao, L.; Ke, W.; Pedesseau, L.; Wu, Y.; Katan, C.; Even, J.; Wasielewski, M. R.; Stoumpos, C. C.; Kanatzidis, M. G. Hybrid Dion−Jacobson 2D Lead Iodide Perovskites,. *J. Am. Chem. Soc* **2018**, *140*, 47. https://doi.org/10.1021/jacs.8b00542.

(6) Stoumpos, C. C.; Cao, D. H.; Clark, D. J.; Young, J.; Rondinelli, J. M.; Jang, J. I.; Hupp, J. T.; Kanatzidis, M. G. Ruddlesden − Popper Hybrid Lead Iodide Perovskite 2D Homologous Semiconductors. *Chem. Mater.* **2016**, *28*. https://doi.org/10.1021/acs.chemmater.6b00847.

(7) Kong, L.; Liu, G.; Gong, J.; Mao, L.; Chen, M.; Hu, Q.; Lü, X.; Yang, W.; Kanatzidis, M. G.; Mao, H. K. Highly Tunable Properties in Pressure-Treated Two-Dimensional Dion–Jacobson Perovskites. *Proc. Natl. Acad. Sci. U. S. A.* **2020**, *117* (28). https://doi.org/10.1073/pnas.2003561117.

(8) Chen, Y.; Zhang, L.; Zhang, Y.; Gao, H.; Yan, H. Large-Area Perovskite Solar Cells – a Review of Recent Progress and Issues. *RSC Adv.* **2018**, *8* (19). https://doi.org/10.1039/C8RA00384J.

(9) Nie, W. Y.; Tsai, H. H.; Asadpour, R.; Blancon, J.-C. C. J.-C. J.-C. C.; Neukirch, A. J.; Gupta, G.; Crochet, J. J.; Chhowalla, M.; Tretiak, S.; Alam, M. A.; et al. High-Efficiency Solution-Processed Perovskite Solar Cells with Millimeter-Scale Grains. *Science* **2015**, *347* (6221). https://doi.org/10.1126/science.aaa0472.

(10) Eperon, G. E.; Stranks, S. D.; Menelaou, C.; Johnston, M. B.; Herz, L. M.; Snaith, H. J. Formamidinium Lead Trihalide: A Broadly Tunable Perovskite for Efficient Planar Heterojunction Solar Cells. *Energy Environ. Sci.* **2014**, *7* (3). https://doi.org/10.1039/c3ee43822h.

(11) Noh, J. H.; Im, S. H.; Heo, J. H.; Mandal, T. N.; Seok, S. Il. Chemical Management for Colorful, Efficient, and Stable Inorganic-Organic Hybrid Nanostructured Solar Cells. *Nano Lett.* **2013**, *13* (4). https://doi.org/10.1021/nl400349b.

(12) Sadhanala, A.; Ahmad, S.; Zhao, B.; Giesbrecht, N.; Pearce, P. M.; Deschler, F.; Z Hoye, R. L.; Go, K. C.; Bein, T.; Docampo, P.; et al. Blue-Green Color Tunable Solution Processable Organolead Chloride−Bromide Mixed Halide Perovskites for Optoelectronic Applications. *Nano Lett* **2015**, *15* (6101). https://doi.org/10.1021/acs.nanolett.5b02369.

(13) Amat, A.; Mosconi, E.; Ronca, E.; Quarti, C.; Umari, P.; Nazeeruddin, M. K.; Grätzel, M.; De Angelis, F. Cation-Induced Band-Gap Tuning in Organohalide Perovskites: Interplay of Spin-Orbit Coupling and Octahedra Tilting. *Nano Lett.* **2014**, *14* (6). https://doi.org/10.1021/NL5012992.

(14) Pazos-Outón, L. M.; Xiao, T. P.; Yablonovitch, E. Fundamental Efficiency Limit of Lead Iodide Perovskite Solar Cells. *J. Phys. Chem. Lett.* **2018**, *9* (7). https://doi.org/10.1021/acs.jpclett.7b03054.

(15) Wang, Q.; Wang, X.; Yang, Z.; Zhou, N.; Deng, Y.; Zhao, J.; Xiao, X.; Rudd, P.; Moran, A.; Yan, Y.; et al. Efficient Sky-Blue Perovskite Light-Emitting Diodes via Photoluminescence Enhancement. *Nat. Commun. 2019 101* **2019**, *10* (1). https://doi.org/10.1038/s41467-019-13580-w.

(16) Sarritzu, V.; Sestu, N.; Marongiu, D.; Chang, X.; Masi, S.; Rizzo, A.; Colella, S.; Quochi, F.; Saba, M.; Mura, A.; et al. Optical Determination of Shockley-Read-Hall and Interface Recombination Currents in Hybrid Perovskites. *Sci. Rep.* **2017**, *7* (44629). https://doi.org/10.1002/adom.201700839.

(17) Ball, J. M.; Petrozza, A. Defects in Perovskite-Halides and Their Effects in Solar Cells. *Nat. Energy* **2016**, *1* (16149). https://doi.org/10.1038/nenergy.2016.149.

(18) Meggiolaro, D.; De Angelis, F. First-Principles Modeling of Defects in Lead Halide Perovskites: Best Practices and Open Issues. *ACS Energy Lett.* **2018**, *3* (9). https://doi.org/10.1021/acsenergylett.8b01212.

(19) Das, B.; Liu, Z.; Aguilera, I.; Rau, U.; Kirchartz, T. Defect Tolerant Device Geometries for Lead-Halide Perovskites. *Mater. Adv.* **2021**, *2* (11). https://doi.org/10.1039/d0ma00902d.

(20) Kim, G. W.; Petrozza, A. Defect Tolerance and Intolerance in Metal-Halide Perovskites. *Adv. Energy Mater.* **2020**, *10* (37). https://doi.org/10.1002/AENM.202001959.

(21) Pisoni, A.; Jaćimović, J.; Barišić, O. S.; Spina, M.; Gaál, R.; Forró, L.; Horváth, E. Ultra-Low Thermal Conductivity in Organic-Inorganic Hybrid Perovskite $CH_3NH_3PbI_3$. *J. Phys. Chem. Lett.* **2014**, *5* (14). https://doi.org/10.1021/jz5012109.

(22) Kovalsky, A.; Wang, L.; Marek, G. T.; Burda, C.; Dyck, J. S. Thermal Conductivity of $CH_3NH_3PbI_3$ and $CsPbI_3$: Measuring the Effect of the Methylammonium Ion on Phonon Scattering. *J. Phys. Chem. C* **2017**, *121* (6). https://doi.org/10.1021/acs.jpcc.6b12231.

(23) Kanak, A.; Lishchuk, P.; Kuryliuk, V.; Kuzmich, A.; Lacroix, D.; Khalavka, Y.; Isaiev, M. Thermal Conductivity of CsPbBr3 Halide Perovskite: Photoacoustic Measurements and Molecular Dynamics Analysis. *AIP Conf. Proc.* **2020**, *2305* (1). https://doi.org/10.1063/5.0033821.

(24) Pisoni, A.; Jaćimović, J.; Barišić, O. S.; Spina, M.; Gaál, R.; Forró, L.; Horváth, E. Ultra-Low Thermal Conductivity in Organic-Inorganic Hybrid Perovskite $CH_3NH_3PbI_3$. *J. Phys. Chem. Lett.* **2014**, *5* (14). https://doi.org/10.1021/jz5012109.

(25) Mei, S.; Knezevic, I. Thermal Conductivity of Ternary III-V Semiconductor Alloys: The Role of Mass Difference and Long-Range Order. *J. Appl. Phys.* **2018**, *123* (12). https://doi.org/10.1063/1.5008262.

(26) Leturcq, P.; Dorkel, J. M.; Napieralski, A.; Lachiver, E. A New Approach to Thermal Analysis of Power Devices. *IEEE Trans. Electron Devices* **1987**, *34* (5). https://doi.org/10.1109/T-ED.1987.23057.

(27) Spitzer, D. P. Lattice Thermal Conductivity of Semiconductors: A Chemical Bond Approach. *J. Phys. Chem. Solids* **1970**, *31* (1). https://doi.org/10.1016/0022-3697(70)90284-2.

(28) Gold-Parker, A.; Gehring, P. M.; Skelton, J. M.; Smith, I. C.; Parshall, D.; Frost, J. M.; Karunadasa, H. I.; Walsh, A.; Toney, M. F. Acoustic Phonon Lifetimes Limit Thermal Transport in Methylammonium Lead Iodide. *Proc. Natl. Acad. Sci. U. S. A.* **2018**, *115* (47). https://doi.org/10.1073/pnas.1812227115.

(29) Bakulin, A. A.; Selig, O.; Bakker, H. J.; Rezus, Y. L. A.; Müller, C.; Glaser, T.; Lovrincic, R.; Sun, Z.; Chen, Z.; Walsh, A.; et al. Real-Time Observation of Organic Cation Reorientation in Methylammonium Lead Iodide Perovskites. *J. Phys. Chem. Lett.* **2015**, *6* (18). https://doi.org/10.1021/ACS.JPCLETT.5B01555.

(30) Fabini, D. H.; Siaw, T. A.; Stoumpos, C. C.; Laurita, G.; Olds, D.; Page, K.; Hu, J. G.; Kanatzidis, M. G.; Han, S.; Seshadri, R. Universal Dynamics of Molecular Reorientation in Hybrid Lead Iodide Perovskites. *J. Am. Chem. Soc.* **2017**, *139* (46). https://doi.org/10.1021/JACS.7B09536.

(31) Haque, M. A.; Kee, S.; Villalva, D. R.; Ong, W. L.; Baran, D. Halide Perovskites: Thermal Transport and Prospects for Thermoelectricity. *Advanced Science*. **2020**, 7, (10). https://doi.org/10.1002/advs.201903389.

(32) Fu, J.; Xu, Q.; Han, G.; Wu, B.; Huan, C. H. A.; Leek, M. L.; Sum, T. C. Hot Carrier Cooling Mechanisms in Halide Perovskites. *Nat. Commun.*

**2017**, *8* (1). https://doi.org/10.1038/s41467-017-01360-3.

(33) Lim, J. W. M.; Giovanni, D.; Righetto, M.; Feng, M.; Mhaisalkar, S. G.; Mathews, N.; Sum, T. C. Hot Carriers in Halide Perovskites: How Hot Truly? *J. Phys. Chem. Lett.* **2020**, *11* (7). https://doi.org/10.1021/acs.jpclett.0c00504.

(34) Shen, Q.; Ripolles, T. S.; Even, J.; Ogomi, Y.; Nishinaka, K.; Izuishi, T.; Nakazawa, N.; Zhang, Y.; Ding, C.; Liu, F.; et al. Slow Hot Carrier Cooling in Cesium Lead Iodide Perovskites. *Appl. Phys. Lett.* **2017**, *111* (15). https://doi.org/10.1063/1.4991993.

(35) Fehse, R.; Tomić, S.; Adams, A. R.; Sweeney, S. J.; O'Reilly, E. P.; Andreev, A.; Riechert, H. A Quantitative Study of Radiative, Auger, and Defect Related Recombination Processes in 1.3-Mm GaInNAs-Based Quantum-Well Lasers. *IEEE J. Sel. Top. Quantum Electron.* **2002**, *8* (4). https://doi.org/10.1109/JSTQE.2002.801684.

(36) Righetto, M.; Lim, S. S.; Giovanni, D.; Lim, J. W. M.; Zhang, Q.; Ramesh, S.; Tay, Y. K. E.; Sum, T. C. Hot Carriers Perspective on the Nature of Traps in Perovskites. *Nat. Commun.* **2020**, *11* (1). https://doi.org/10.1038/s41467-020-16463-7.

(37) Walsh, A. Principles of Chemical Bonding and Band Gap Engineering in Hybrid Organic–Inorganic Halide Perovskites. *J. Phys. Chem. C* **2015**, *119* (11). https://doi.org/10.1021/jp512420b.

(38) Brivio, F.; Walker, A. B.; Walsh, A. Structural and Electronic Properties of Hybrid Perovskites for High-Efficiency Thin-Film Photovoltaics from First-Principles. *APL Mater.* **2013**, *1* (4). https://doi.org/10.1063/1.4824147.

(39) Lee, J. H.; Lee, J.-H.; Kong, E.-H.; Jang, H. M. The Nature of Hydrogen-Bonding Interaction in the Prototypic Hybrid Halide Perovskite, Tetragonal $CH_3NH_3PbI_3$. *Sci. Reports 2016 61* **2016**, *6* (1). https://doi.org/10.1038/srep21687.

(40) Walsh, A.; Scanlon, D. O.; Chen, S.; Gong, X. G.; Wei, S.-H. H. Self-Regulation Mechanism for Charged Point Defects in Hybrid Halide Perovskites. *Angew. Chemie Int. Ed.* **2015**, *54* (6). https://doi.org/10.1002/anie.201409740.

(41) Li, C.; Guerrero, A.; Huettner, S.; Bisquert, J. Unravelling the Role of Vacancies in Lead Halide Perovskite through Electrical Switching of Photoluminescence. *Nat. Commun.* **2018**, *9* (1). https://doi.org/10.1038/s41467-018-07571-6.

(42) Meggiolaro, D.; Mosconi, E.; Angelis, F. De. Formation of Surface Defects Dominates Ion Migration in Lead-Halide Perovskites. *ACS Energy Lett.* **2019**, *4* (3). https://doi.org/10.1021/ACSENERGYLETT.9B00247.

(43) Futscher, M. H.; Lee, J. M.; McGovern, L.; Muscarella, L. A.; Wang, T.; Haider, M. I.; Fakharuddin, A.; Schmidt-Mende, L.; Ehrler, B.

Quantification of Ion Migration in $CH_3NH_3PbI_3$ Perovskite Solar Cells by Transient Capacitance Measurements. *Mater. Horizons* **2019**, *6* (7). https://doi.org/10.1039/c9mh00445a.

(44) Lee, J. W.; Kim, S. G.; Yang, J. M.; Yang, Y.; Park, N. G. Verification and Mitigation of Ion Migration in Perovskite Solar Cells. *APL Mater.* **2019**, *7* (4). https://doi.org/10.1063/1.5085643.

(45) Yuan, H.; Debroye, E.; Janssen, K.; Naiki, H.; Steuwe, C.; Lu, G.; Moris, M.; Orgiu, E.; Uji-I, H.; De Schryver, F.; et al. Degradation of Methylammonium Lead Iodide Perovskite Structures through Light and Electron Beam Driven Ion Migration. *J. Phys. Chem. Lett.* **2016**, *7* (3). https://doi.org/10.1021/acs.jpclett.5b02828.

(46) Nandal, V.; Nair, P. R. Predictive Modeling of Ion Migration Induced Degradation in Perovskite Solar Cells. *ACS Nano* **2017**, *11* (11). https://doi.org/10.1021/ACSNANO.7B06294.

(47) Azpiroz, J. M.; Mosconi, E.; Bisquert, J.; De Angelis, F. Defects Migration in Methylammonium Lead Iodide and Their Role in Perovskite Solar Cells Operation. *Energy Environ. Sci.* **2015**, *8* (7). https://doi.org/10.1039/C5EE01265A.

(48) Eames, C.; Frost, J. M.; Barnes, P. R. F.; O'Regan, B. C.; Walsh, A.; Islam, M. S. Ionic Transport in Hybrid Lead Iodide Perovskite Solar Cells. *Nat. Commun. 2015 61* **2015**, *6* (1), 1–8. https://doi.org/10.1038/ncomms8497.

(49) Delugas, P.; Caddeo, C.; Filippetti, A.; Mattoni, A. Thermally Activated Point Defect Diffusion in Methylammonium Lead Trihalide: Anisotropic and Ultrahigh Mobility of Iodine. *J. Phys. Chem. Lett.* **2016**, *7* (13). https://doi.org/10.1021/ACS.JPCLETT.6B00963.

(50) Haruyama, J.; Sodeyama, K.; Han, L.; Tateyama, Y. First-Principles Study of Ion Diffusion in Perovskite Solar Cell Sensitizers. *J. Am. Chem. Soc.* **2015**, *137* (32). https://doi.org/10.1021/JACS.5B03615.

(51) Meloni, S.; Moehl, T.; Tress, W.; Franckeviius, M.; Saliba, M.; Lee, Y. H.; Gao, P.; Nazeeruddin, M. K.; Zakeeruddin, S. M.; Rothlisberger, U.; et al. Ionic Polarization-Induced Current-Voltage Hysteresis in $CH_3NH_3PbX_3$ Perovskite Solar Cells. *Nat. Commun.* **2016**, *7* (1). https://doi.org/10.1038/ncomms10334.

(52) Slotcavage, D. J.; Karunadasa, H. I.; McGehee, M. D. Light-Induced Phase Segregation in Halide-Perovskite Absorbers. *ACS Energy Letters*. **2016**, *1* (6). https://doi.org/10.1021/acsenergylett.6b00495.

(53) Hoke, E. T.; Slotcavage, D. J.; Dohner, E. R.; Bowring, A. R.; Karunadasa, H. I.; McGehee, M. D. Reversible Photo-Induced Trap Formation in Mixed-Halide Hybrid Perovskites for Photovoltaics. *Chem. Sci.* **2015**, *6* (1). https://doi.org/10.1039/c4sc03141e.

(54) Tang, X.; van den Berg, M.; Gu, E.; Horneber, A.; J. Matt, G.; Osvet, A.; J. Meixner, A.; Zhang, D.; J. Brabec, C. Local Observation of Phase

Segregation in Mixed-Halide Perovskite. *Nano Lett.* **2018**, *18* (3). https://doi.org/10.1021/acs.nanolett.8b00505.

(55) Frost, J. M.; Whalley, L. D.; Walsh, A. Slow Cooling of Hot Polarons in Halide Perovskite Solar Cells. *ACS Energy Lett.* **2017**, *2* (12). https://doi.org/10.1021/acsenergylett.7b00862.

(56) Bretschneider, S. A.; Ivanov, I.; Wang, H. I.; Miyata, K.; Zhu, X.; Bonn, M. Quantifying Polaron Formation and Charge Carrier Cooling in Lead-Iodide Perovskites. *Adv. Mater.* **2018**, *30* (29). https://doi.org/10.1002/adma.201707312.

(57) Zhu, X. Y.; Podzorov, V. Charge Carriers in Hybrid Organic-Inorganic Lead Halide Perovskites Might Be Protected as Large Polarons. *J. Phys. Chem. Lett.* **2015**, *6* (23). https://doi.org/10.1021/acs.jpclett.5b02462.

(58) Tan, H.; Che, F.; Wei, M.; Zhao, Y.; Saidaminov, M. I.; Todorović, P.; Broberg, D.; Walters, G.; Tan, F.; Zhuang, T.; et al. Dipolar Cations Confer Defect Tolerance in Wide-Bandgap Metal Halide Perovskites. *Nat. Commun. 2018 91* **2018**, *9* (1). https://doi.org/10.1038/s41467-018-05531-8.

(59) Bischak, C. G.; Hetherington, C. L.; Wu, H.; Aloni, S.; Ogletree, D. F.; Limmer, D. T.; Ginsberg, N. S. Origin of Reversible Photoinduced Phase Separation in Hybrid Perovskites. *Nano Lett.* **2017**, *17* (2). https://doi.org/10.1021/acs.nanolett.6b04453.

(60) Rehman, W.; McMeekin, D. P.; Patel, J. B.; Milot, R. L.; Johnston, M. B.; Snaith, H. J.; Herz, L. M. Photovoltaic Mixed-Cation Lead Mixed-Halide Perovskites: Links between Crystallinity, Photo-Stability and Electronic Properties. *Energy Environ. Sci.* **2017**, *10* (1). https://doi.org/10.1039/c6ee03014a.

(61) Bischak, C. G. G.; Wong, A. B.; Lin, E.; Limmer, D. T.; Yang, P.; Ginsberg, N. S. Tunable Polaron Distortions Control the Extent of Halide Demixing in Lead Halide Perovskites. *J. Phys. Chem. Lett.* **2018**, *9* (14). https://doi.org/10.1021/acs.jpclett.8b01512.

(62) Lioliou, G.; Meng, X.; Ng, J. S.; Barnett, A. M. Temperature Dependent Characterization of Gallium Arsenide X-Ray Mesa p-i-n Photodiodes. *J. Appl. Phys.* **2016**, *119* (12). https://doi.org/10.1063/1.4944892.

(63) Navarro-Urrios, D.; Colombano, M. F.; Maire, J.; Chávez-Ángel, E.; Arregui, G.; Capuj, N. E.; Devos, A.; Griol, A.; Bellieres, L.; Martínez, A.; et al. Properties of Nanocrystalline Silicon Probed by Optomechanics. *Nanophotonics* **2020**, *9* (16). https://doi.org/10.1515/NANOPH-2020-0489.

(64) Ono, S.; Kikegawa, T. Phase Transformation of GaAs at High Pressures and Temperatures. *J. Phys. Chem. Solids* **2018**, *113*. https://doi.org/10.1016/J.JPCS.2017.10.005.

(65) Brennan, K. F.; Brown, A. S. Magnetic Field Effects in Semiconductors. *Theory Mod. Electron. Semicond. Devices* **2003**.

https://doi.org/10.1002/0471224618.CH9.

(66) Chang, K.; Xia, J.-B. The Effects of Electric Field on the Electronic Structure of a Semiconductor Quantum Dot. *J. Appl. Phys.* **1998**, *84* (3). https://doi.org/10.1063/1.368207.

(67) Hutter, E. M.; Savenije, T. J. Thermally Activated Second-Order Recombination Hints toward Indirect Recombination in Fully Inorganic CsPbI3 Perovskites. *ACS Energy Lett.* **2018**, *3* (9). https://doi.org/10.1021/ACSENERGYLETT.8B01106.

(68) Hutter, E. M.; Gélvez-Rueda, M. C.; Osherov, A.; Bulović, V.; Grozema, F. C.; Stranks, S. D.; Savenije, T. J. Direct-Indirect Character of the Bandgap in Methylammonium Lead Iodide Perovskite. *Nat. Mater.* **2017**, *16* (1). https://doi.org/10.1038/nmat4765.

(69) Thouin, F.; Valverde-Chávez, D. A.; Quarti, C.; Cortecchia, D.; Bargigia, I.; Beljonne, D.; Petrozza, A.; Silva, C.; Srimath Kandada, A. R. Phonon Coherences Reveal the Polaronic Character of Excitons in Two-Dimensional Lead Halide Perovskites. *Nat. Mater. 2019 184* **2019**, *18* (4). https://doi.org/10.1038/s41563-018-0262-7.

(70) Mauck, C. M.; France-Lanord, A.; Oendra, A. C. H.; Dahod, N. S.; Grossman, J. C.; Tisdale, W. A. Inorganic Cage Motion Dominates Excited-State Dynamics in 2D-Layered Perovskites $(C_xH_{2x+1}NH_3)_2PbI_4$ (x = 4–9). *J. Phys. Chem. C* **2019,** *123* (45). https://doi.org/10.1021/ACS.JPCC.9B07933.

(71) Francisco-López, A.; Charles, B.; Weber, O. J.; Alonso, M. I.; Garriga, M.; Campoy-Quiles, M.; Weller, M. T.; Goñi, A. R. Pressure-Induced Locking of Methylammonium Cations versus Amorphization in Hybrid Lead Iodide Perovskites. *J. Phys. Chem. C* **2018**, *122* (38). https://doi.org/10.1021/acs.jpcc.8b05188.

(72) Jaffe, A.; Lin, Y.; L. Mao, W.; I. Karunadasa, H. Pressure-Induced Conductivity and Yellow-to-Black Piezochromism in a Layered Cu–Cl Hybrid Perovskite. *J. Am. Chem. Soc.* **2015**, *137* (4). https://doi.org/10.1021/ja512396m.

(73) Yin, T.; Liu, B.; Yan, J.; Fang, Y.; Chen, M.; Chong, W. K.; Jiang, S.; Kuo, J. L.; Fang, J.; Liang, P.; et al. Pressure-Engineered Structural and Optical Properties of Two-Dimensional $(C_4H_9NH_3)_2PbI_4$ Perovskite Exfoliated Nm-Thin Flakes. *J. Am. Chem. Soc.* **2019**, *141* (3). https://doi.org/10.1021/jacs.8b07765.

(74) Liu, S.; Sun, S.; Kwan Gan, C.; Granados del Águila, A.; Fang, Y.; Xing, J.; Thu Ha Do, T.; White, T. J.; Li, H.; Huang, W.; et al. Manipulating Efficient Light Emission in Two-Dimensional Perovskite Crystals by Pressure-Induced Anisotropic Deformation. *Sci. Adv.* **2019**, *5* (7). https://doi.org/10.1126/sciadv.aav9445.

(75) Meloni, S.; Palermo, G.; Ashari-Astani, N.; Grätzel, M.; Rothlisberger, U. Valence and Conduction Band Tuning in Halide Perovskites for Solar Cell

Applications. *J. Mater. Chem. A* **2016**, *4* (41). https://doi.org/10.1039/c6ta04949d.

(76) Pazoki, M.; Jacobsson, T. J.; Hagfeldt, A.; Boschloo, G.; Edvinsson, T. Effect of Metal Cation Replacement on the Electronic Structure of Metalorganic Halide Perovskites: Replacement of Lead with Alkaline-Earth Metals. *Phys. Rev. B* **2016**, *93* (14). https://doi.org/10.1103/PhysRevB.93.144105.

(77) Butler, K. T.; Frost, J. M.; Walsh, A. Band Alignment of the Hybrid Halide Perovskites $CH_3NH_3PbCl_3$, $CH_3NH_3PbBr_3$ and $CH_3NH_3PbI_3$. *Mater. Horizons* **2015**, *2* (2). https://doi.org/10.1039/C4MH00174E.

(78) Yin, W.-J.; Shi, T.; Yan, Y. Unusual Defect Physics in CH 3 NH 3 PbI 3 Perovskite Solar Cell Absorber, *Appl. Phys. Lett*., **2014**, *104* (6). https://doi.org/10.1063/1.4864778.

(79) Lee, J. H.; Bristowe, N. C.; Lee, J. H.; Lee, S. H.; Bristowe, P. D.; Cheetham, A. K.; Jang, H. M. Resolving the Physical Origin of Octahedral Tilting in Halide Perovskites. *Chem. Mater.* **2016**, *28* (12). https://doi.org/10.1021/acs.chemmater.6b00968.

(80) Jaffe, A.; Lin, Y.; Beavers, C. M.; Voss, J.; Mao, W. L.; Karunadasa, H. I. High-Pressure Single-Crystal Structures of 3D Lead-Halide Hybrid Perovskites and Pressure Effects on Their Electronic and Optical Properties. *ACS Cent. Sci.* **2016**, *2* (4). https://doi.org/10.1021/acscentsci.6b00055.

(81) Liu, G.; Gong, J.; Kong, L.; Schaller, R. D.; Hu, Q.; Liu, Z.; Yan, S.; Yang, W.; Stoumpos, C. C.; Kanatzidis, M. G.; et al. Isothermal Pressure-Derived Metastable States in 2D Hybrid Perovskites Showing Enduring Bandgap Narrowing. *Proc. Natl. Acad. Sci. U. S. A.* **2018**, *115* (32). https://doi.org/10.1073/pnas.1809167115.

(82) Jaffe, A.; Lin, Y.; Karunadasa, H. I. Halide Perovskites under Pressure: Accessing New Properties through Lattice Compression. *ACS Energy Lett.* **2017**, *2* (7). https://doi.org/10.1021/acsenergylett.7b00284.

(83) Liu, S.; Sun, S.; Gan, C. K.; Del Águila, A. G.; Fang, Y.; Xing, J.; Thu Ha Do, T.; White, T. J.; Li, H.; Huang, W.; et al. Manipulating Efficient Light Emission in Two-Dimensional Perovskite Crystals by Pressure-Induced Anisotropic Deformation. *Sci. Adv.* **2019**, *5* (7). https://doi.org/10.1126/sciadv.aav9445.

(84) Tu, Q.; Spanopoulos, I.; Vasileiadou, E. S.; Li, X.; Kanatzidis, M. G.; Shekhawat, G. S.; Dravid, V. P. Exploring the Factors Affecting the Mechanical Properties of 2D Hybrid Organic-Inorganic Perovskites. *ACS Appl. Mater. Interfaces* **2020**, *12* (18). https://doi.org/10.1021/acsami.0c02313.

(85) Tu, Q.; Spanopoulos, I.; Hao, S.; Wolverton, C.; Kanatzidis, M. G.; Shekhawat, G. S.; Dravid, V. P. Out-of-Plane Mechanical Properties of 2D Hybrid Organic-Inorganic Perovskites by Nanoindentation. *ACS Appl.*

*Mater. Interfaces* **2018**, *10* (26). https://doi.org/10.1021/acsami.8b05138.
(86) Gao, H.; Wei, W.; Li, L.; Tan, Y.; Tang, Y. Mechanical Properties of a 2D Lead-Halide Perovskite, $(C_6H_5CH_2NH_3)_2PbCl_4$ by Nanoindentation and First-Principles Calculations. *J. Phys. Chem. C* **2020**, *124* (35). https://doi.org/10.1021/acs.jpcc.0c04283.
(87) Xu, B.; Wang, Q.; Tian, Y. Bulk Modulus for Polar Covalent Crystals. **2013**, *3*. https://doi.org/10.1038/srep03068.
(88) Kamran, S.; Chen, K.; Chen, L. Semiempirical Formulae for Elastic Moduli and Brittleness of Diamondlike and Zinc-Blende Covalent Crystals, Appl. Phys. Lett, **2008**, *77* (9). https://doi.org/10.1103/PhysRevB.77.094109.
(89) Menčík, J.; Munz, D.; Quandt, E.; Weppelmann, E. R.; Swain, M. V. Determination of Elastic Modulus of Thin Layers Using Nanoindentation. *J. Mater. Res.* **1997**, *12* (9). https://doi.org/10.1557/JMR.1997.0327.
(90) Kim, M. T. Influence of Substrates on the Elastic Reaction of Films for the Microindentation Tests. *Thin Solid Films* **1996**, *283* (1–2). https://doi.org/10.1016/0040-6090(95)08498-3.
(91) Ahmed, R.; Javad Hashemifar, S.; Akbarzadeh, H.; Ahmed, M.; Fazal-e-Aleem. Ab Initio Study of Structural and Electronic Properties of III-Arsenide Binary Compounds. *Comput. Mater. Sci.* **2007**, *39* (3). https://doi.org/10.1016/J.COMMATSCI.2006.08.014.
(92) S. M. SZE. Semiconductor Devices Physics and Technology 3rd Edition.
(93) Ferreira, A. C.; Létoublon, A.; Paofai, S.; Raymond, S.; Ecolivet, C.; Rufflé, B.; Cordier, S.; Katan, C.; Saidaminov, M. I.; Zhumekenov, A. A.; et al. Elastic Softness of Hybrid Lead Halide Perovskites. *Phys. Rev. Lett.* **2018**, *121* (8). https://doi.org/10.1103/PhysRevLett.121.085502.
(94) Rakita, Y.; Cohen, S. R.; Kedem, N. K.; Hodes, G.; Cahen, D. Mechanical Properties of APbX3 (A = Cs or $CH_3NH_3$; X = i or Br) Perovskite Single Crystals. *MRS Commun.* **2015**, *5* (4). https://doi.org/10.1557/mrc.2015.69.
(95) Sun, S.; Fang, Y.; Kieslich, G.; White, T. J.; Cheetham, A. K. Mechanical Properties of Organic–Inorganic Halide Perovskites, CH3NH3PbX3 (X = I, Br and Cl), by Nanoindentation. *J. Mater. Chem. A* **2015**, *3* (36). https://doi.org/10.1039/C5TA03331D.
(96) Ma, L.; Li, W.; Yang, K.; Bi, J.; Feng, J.; Zhang, J.; Yan, Z.; Zhou, X.; Liu, C.; Ji, Y.; et al. A- or X-Site Mixture on Mechanical Properties of APbX3 Perovskite Single Crystals. *APL Mater.* **2021**, *9* (4). https://doi.org/10.1063/5.0015569.
(97) Giorgi, G.; Fujisawa, J.-I.; Segawa, H.; Yamashita, K. Cation Role in Structural and Electronic Properties of 3D Organic− Inorganic Halide Perovskites: A DFT Analysis. *J. Phys. Chem. C* **2014**, *118*, 41. https://doi.org/10.1021/jp504479c.
(98) Zhu, H.; Cai, T.; Que, M.; Song, J.-P.; Rubenstein, B. M.; Wang, Z.; Chen,

O. Pressure-Induced Phase Transformation and Band-Gap Engineering of Formamidinium Lead Iodide Perovskite Nanocrystals. *J. Phys. Chem. Lett* **2018**, *9*, 42. https://doi.org/10.1021/acs.jpclett.8b01852.

(99) Ghaithan, H. M.; Alahmed, Z. A.; Qaid, S. M. H.; Hezam, M.; Aldwayyan, A. S. Density Functional Study of Cubic, Tetragonal, and Orthorhombic CsPbBr 3 Perovskite. *Cite This ACS Omega* **2020**, *5* (13), 7480. https://doi.org/10.1021/acsomega.0c00197.

(100) Gupta, Y.; Rathore, S.; Singh, A.; Kumar, A. Mechanical Response of Butylamine Based Ruddlesden Popper Organic-Inorganic Lead Halide Perovskites. **2021**, arXiv:2106.04960

(101) Reyes-Martinez, M. A.; Tan, P.; Kakekhani, A.; Banerjee, S.; Zhumekenov, A. A.; Peng, W.; Bakr, O. M.; Rappe, A. M.; Loo, Y.-L. Unraveling the Elastic Properties of (Quasi)Two-Dimensional Hybrid Perovskites: A Joint Experimental and Theoretical Study. *Cite This ACS Appl. Mater. Interfaces* **2020**, *12*. https://doi.org/10.1021/acsami.0c02327.

(102) Zhang, W.; Ye, H.-Y.; Graf, R.; Spiess, H. W.; Yao, Y.-F.; Zhu, R.-Q.; Xiong, R.-G. Tunable and Switchable Dielectric Constant in an Amphidynamic Crystal. *J. Am. Chem. Soc* **2013**, *135*, 7. https://doi.org/10.1021/ja3110335.

(103) Al-Qatatsheh, A.; Morsi, Y.; Zavabeti, A.; Zolfagharian, A.; Salim, N.; Kouzani, A. Z.; Mosadegh, B.; Gharaie, S.; Au, A. Z. K. Blood Pressure Sensors: Materials, Fabrication Methods, Performance Evaluations and Future Perspectives, *Sensors*, **2020**, 20 (16) https://doi.org/10.3390/s20164484.

(104) Cho, S.; Kang, S.; Pandya, A.; Shanker, R.; Khan, Z.; Lee, Y.; Park, J.; Craig, S. L.; Ko, H. Large-Area Cross-Aligned Silver Nanowire Electrodes for Flexible, Transparent, and Force-Sensitive Mechanochromic Touch Screens. *ACS Nano* **2017**, *11*, 7. https://doi.org/10.1021/acsnano.7b01714.

(105) Dang, Z.; Shamsi, J.; Palazon, F.; Imran, M.; Akkerman, Q. A.; Park, S.; Bertoni, G.; Prato, M.; Brescia, R.; Manna, L. In Situ Transmission Electron Microscopy Study of Electron Beam-Induced Transformations in Colloidal Cesium Lead Halide Perovskite Nanocrystals. *ACS Nano* **2017**, *11* (2). https://doi.org/10.1021/acsnano.6b08324.

(106) Dang, Z.; Shamsi, J.; Akkerman, Q. A.; Imran, M.; Bertoni, G.; Brescia, R.; Manna, L. Low-Temperature Electron Beam-Induced Transformations of Cesium Lead Halide Perovskite Nanocrystals. *ACS Omega* **2017**, *2* (9). https://doi.org/10.1021/acsomega.7b01009.

(107) Ryde, L. Application of EBSD to Analysis of Microstructures in Commercial Steels. *Mater. Sci. Technol.* **2006**, *22* (11). https://doi.org/10.1179/174328406X130948.

(108) Kamaya, M.; da Fonseca, J. Q.; Li, L. M.; Preuss, M. Local Plastic Strain

Measurement by EBSD. In *Advances in Experimental Mechanics V*; *Applied Mechanics and Materials*, **2007**, *7* (8). https://doi.org/10.4028/www.scientific.net/AMM.7-8.173.

(109) Muscarella, L. A.; Hutter, E. M.; Sanchez, S.; Dieleman, C. D.; Savenije, T. J.; Hagfeldt, A.; Saliba, M.; Ehrler, B. Crystal Orientation and Grain Size: Do They Determine Optoelectronic Properties of MAPbI3 Perovskite? *J. Phys. Chem. Lett.* **2019**, *10* (20). https://doi.org/10.1021/acs.jpclett.9b02757.

(110) Demers, H.; Poirier-Demers, N.; Couture, A. R.; Joly, D.; Guilmain, M.; de Jonge, N.; Drouin, D. Three-Dimensional Electron Microscopy Simulation with the CASINO Monte Carlo Software. *Scanning* **2011**, *33* (3). https://doi.org/10.1002/sca.20262.

(111) Muscarella, L. A.; Hutter, E. M.; Sanchez, S.; Dieleman, C. D.; Savenije, T. J.; Hagfeldt, A.; Saliba, M.; Ehrler, B. Crystal Orientation and Grain Size: Do They Determine Optoelectronic Properties of $MAPbI_3$ Perovskite? *J. Phys. Chem. Lett.* **2019**, *10* (20). https://doi.org/10.1021/acs.jpclett.9b02757.

(112) Levin, B. D. A. Direct Detectors and Their Applications in Electron Microscopy for Materials Science. *J. Phys. Mater.* **2021**, *4* (4). https://doi.org/10.1088/2515-7639/AC0FF9.

(113) Sun, H.; Adhyaksa, G. W. P.; Garnett, E. C. The Application of Electron Backscatter Diffraction on Halide Perovskite Materials. *Adv. Energy Mater.* **2020**, *10* (26). https://doi.org/10.1002/AENM.202000364.

(114) Kirchartz, T.; Márquez, J. A.; Stolterfoht, M.; Unold, T. Photoluminescence-Based Characterization of Halide Perovskites for Photovoltaics. *Adv. Energy Mater.* **2020**, *10* (26). https://doi.org/10.1002/aenm.201904134.

(115) Futscher, M. H.; Gangishetty, M. K.; Congreve, D. N.; Ehrler, B. Quantifying Mobile Ions and Electronic Defects in Perovskite-Based Devices with Temperature-Dependent Capacitance Measurements: Frequency vs Time Domain. *J. Chem. Phys.* **2020**, *152* (4). https://doi.org/10.1063/1.5132754.

(116) 3M™ Fluorinert™ Elektronicavloeistof FC-72 | 3M Nederland

(117) Stolterfoht, M.; Corre, V. M. Le; Feuerstein, M.; Caprioglio, P.; Koster, L. J. A.; Neher, D. Voltage-Dependent Photoluminescence and How It Correlates with the Fill Factor and Open-Circuit Voltage in Perovskite Solar Cells. *ACS Energy Lett.* **2019**, *4* (12). https://doi.org/10.1021/ACSENERGYLETT.9B02262.

(118) El-Hajje, G.; Momblona, C.; Gil-Escrig, L.; Ávila, J.; Guillemot, T.; Guillemoles, J.-F.; Sessolo, M.; Bolink, H. J.; Lombez, L. Quantification of Spatial Inhomogeneity in Perovskite Solar Cells by Hyperspectral Luminescence Imaging. *Energy Environ. Sci.* **2016**, *9* (7). https://doi.org/10.1039/C6EE00462H.

# 2. Effects of Grain Size and Orientation on Optical Properties

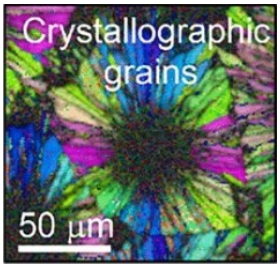


Growing large, oriented grains of perovskite often leads to efficient devices, but it is unclear if properties of the grains are responsible for the efficiency. Domains observed in SEM are commonly misidentified with crystallographic grains, but SEM images do not provide diffraction information. We study methylammonium lead iodide ($MAPbI_3$) films fabricated via flash-infrared annealing (FIRA) and the conventional antisolvent (AS) method by measuring grain size and orientation using electron back-scattered diffraction (EBSD) and studying how these affect optoelectronic properties such as local photoluminescence (PL), charge carrier lifetimes, and mobilities. We observe a local enhancement and shift of the PL emission at different regions of the FIRA clusters, but we observe no effect of crystal orientation on the optoelectronic properties. Additionally, despite substantial differences in grain size between the two systems, we find similar optoelectronic properties. These findings show that optoelectronic quality is not necessarily related to the orientation and size of crystalline domains.

*This chapter is based on the following publication:*
L.A. Muscarella, E.M. Hutter, S. Sanchez, C.D. Dieleman, T. J. Savenije, A. Hagfeldt, M. Saliba, B. Ehrler, Crystal Orientation and Grain Size: Do They determine Optoelectronic Properties of $MAPbI_3$ Perovskite?, *The Journal of Physical Chemistry Letters*, 2019, 10 (20), 6010-6018

# 2.1 Introduction

As discussed in **Chapter 1**, lead-halide perovskites have recently gathered significant attention due to the high efficiency of perovskite-based solar cells and other optoelectronic devices[1,2]. One of the most surprising properties of these materials is that the performance is very tolerant to different methods of fabrication[3–5], different compositions[6,7], and chemical treatments[8–10]. This robustness is reflected in high photoluminescence quantum efficiencies (PLQEs)[11,12], which is a measure of the fraction of radiative versus non-radiative decay, and therefore a direct measurement of the optical quality. In solar cells, the PLQE, for example, is directly related to the open-circuit voltage[13]. In practice, PLQE is reduced by the presence of defects[13,14] which are often related to chemical impurities such as interstitials, vacancies, dangling bonds[15,16] or defects on the surface and grain boundaries[17–19]. Both bulk and surface defects have been extensively studied in perovskites[20–23], and efficient passivation strategies are now routinely employed to achieve high LED and solar cell efficiencies[24–26]. In addition, chemical methods (*e.g.* Lewis bases[21] or chloride-based additives[6,27]) in the perovskite precursor are often applied to grow larger grains which has been thought to suppress non-radiative recombination pathways by reducing the number of grain boundaries[28–30]. Furthermore, these changes in the synthesis route affect the crystal growth and therefore the preferred crystallographic orientations[8,31,32].

However, it is unclear if the changes in grain size and orientation obtained by these treatments cause the improved optoelectronic properties, or if these are mainly related to passivation effects from the additives. Crystallographic orientation and their relation to the photoluminescence and other properties have not been studied in thin films so far because spatial resolution of the crystallographic parameters was lacking. Furthermore, the morphological “grain” observed in SEM images does not necessarily correspond to a crystallographic grain; so additional information is needed in order to relate the grain size with optoelectronic properties.

In this chapter, we use EBSD based on a direct-electron detection as described in **Chapter 1.5** to measure size, orientation, and rotation of

crystallographic grains in polycrystalline $MAPbI_3$ films with high spatial resolution. We study a $MAPbI_3$ thin film where crystallization is induced by FIRA, a low cost and rapid synthesis method[33,34]. These films exhibit large grains (tens of micrometers) highly oriented along the (112) and (400) planes in the direction parallel to the substrate. We find that the growth is spherulitic, *i.e.* starting from needle-like arrays, yielding ~100 micrometer sized clusters that consist of radially grown grains. With EBSD mapping we find two crystal orientations in the FIRA films that are well-separated in pairs in the large clusters of grains. We compare the PL from these clusters and find that PL intensity and spectrum is the same for the two crystal orientations. These results suggest that the two crystallographic orientations found do not govern the optical quality of perovskite thin films. Similarly, we find comparable emission in the interior part of the grain and at the grain boundaries (GBs) but we find enhanced emission and a red-shift at the cluster boundaries (CBs) and at the nucleation sites, which we attribute to favourable light-outcoupling and self-absorption. Finally, we compare the FIRA sample to one where crystallization is induced by the conventional AS dripping method, from the same precursor solution. This method produces sub-micron grains with random orientation. In our case, both samples show comparable charge carrier mobility and lifetime demonstrating that these properties are not necessarily determined by the grain size, at least for grains above a few hundred nanometers.

## 2.2. Fabrication-dependent Microstructure

To study the relation between the perovskite crystal orientation and its optoelectronic properties we first synthesize $MAPbI_3$ on ITO *via* FIRA wherein the spin-coated perovskite film is annealed using a short (1.2 second), highly intense infrared illumination to induce nucleation, as previously reported[33]. For comparison we also fabricate a sample by the AS method where chlorobenzene is rapidly poured onto the liquid precursor while spin coating. Both the FIRA and AS sample were fabricated from the same precursors under identical conditions, and thus the only difference is the crystallization process. Details on the fabrication are reported in the **Experimental Methods 2.5**. We probe the

morphology of both samples using scanning electron microscopy (SEM) as shown in **Figure 2.1a,b** and **Figure A2.1**. SEM images show a dramatic difference in cluster size from the AS method (100 nm - 2 µm) compared to FIRA (~100 µm). The differentiation between morphological grains (or clusters) observed in the SEM and real crystallographic grains is still largely misunderstood[35,36] and often, these clusters seen in SEM images are assigned to grains. In crystallography, the term "grain" is defined by a coherently diffracting domain of solid-state matter which has the same structure as a single crystal[37]. Therefore, from SEM images alone it is not possible to define the apparent domains as crystallographic grains because diffraction information is not measured. For this reason, we use "clusters" to describe the large perovskite domains shown in SEM images. We analyse the bulk crystal structure of the two systems deposited on ITO using X-ray diffraction (XRD). The AS sample shows a tetragonal XRD pattern where peaks from (110), (112), (220), (310) planes arise from the background[38,39].

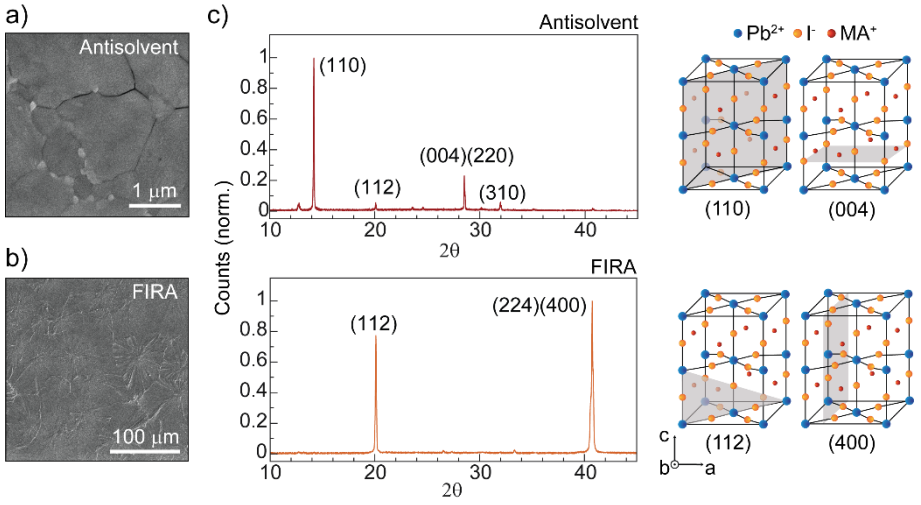


**Figure 2.1.** *Morphology and crystal orientation of AS and FIRA sample deposited on ITO.* SEM image of $MAPbI_3$ crystallized with **a)** AS and **b)** FIRA, **c)** XRD pattern of AS and FIRA $MAPbI_3$ with the corresponding unit cell cut along the (110) and (004) planes for the AS sample and along (112) and (400) for the FIRA sample.

In contrast, the FIRA sample shows a strong preferential orientation along the (112) and (400) planes (**Figure 2.1c**). A cut-off of the primitive tetragonal cell with the planes which show the highest diffraction peaks is shown next to the diffraction patterns. To investigate the crystal growth of the FIRA sample, we apply infrared annealing with varying pulse duration (**Figure 2.2a**). After 0.2 s of annealing, we observe a needle-like crystal morphology. After 0.5 s the crystals have grown in a space-filling manner by branching from the parental needle until each domain impinges with neighbouring domains resulting in straight boundaries. Optical microscopy of the final films (**Figure 2.2b**) shows large perovskite clusters in agreement with the SEM images.

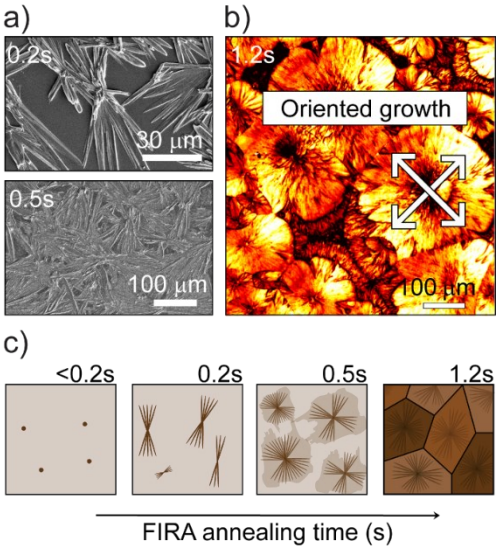


**Figure 2.2.** *Spherulitic growth mechanism of $MAPbI_3$ results in paired oriented domains.* **a)** SEM of FIRA film after 0.2s and 0.5s of infrared annealing, **b)** Polarized microscopy image of the final FIRA film showing paired oriented perovskite domains, **c)** Schematic spherulitic growth of perovskite films after 0.2, 0.5, 1, and 1.2 s of FIRA annealing.

We use polarized light microscopy to find how the two orientations observed in the XRD are spatially distributed. **Figure 2.2b** shows the presence of paired oriented domains within FIRA films for all the clusters (see also **Figure A2.2**) originated by the change in polarization of the incident polarized light caused by the two different refractive indices in the different crystal directions. This is a

indication of spherulitic growth (schematically shown in **Figure 2.2c**) *via* non-crystallographic branching[40] typical for many polymeric materials[41] and inorganic salts[42]. Interestingly, there also seems to be a common direction to all clusters, suggesting a global effect from temperature or strain gradient. In general, spherulitic growth requires the use of a saturated solution, high viscosity, and slow crystallization. This growth is also catalysed by the presence of impurities[40] or strain in the material. In this case, $MAPbI_3$ and the ITO (or quartz) show a substantial difference in the thermal expansion coefficient ($\alpha_{MAPbI3}$ =6.1 × $10^{-5}$ $K^{-1}$, $\alpha_{ITO}$ = 0.85 × $10^{-5}$ $K^{-1}$, $\alpha_{quartz}$ = 0.37 × $10^{-5}$ $K^{-1}$ [43]), which has been shown to be the origin of strain during the cooling process after the thermal annealing[44]. Thus, strain can be considered as a factor inducing spherulitic growth in our system.

Recently, Adhyaksa et al.[48] have pioneered the application of EBSD for $MAPbBr_3$ using a direct electron detector which allows for low accelerating voltage of 5 kV instead of 30 kV, and low sample currents of pA instead of nA in conventional systems. We use the same detection system to collect the Kikuchi patterns from our $MAPbI_3$ films. The obtained Kikuchi patterns allow for the identification of grains, their size and shape and the boundaries between them. By fitting the patterns, we can identify crystal phase, grain orientation and rotation, as previously described in **Chapter 1.5**. Importantly, since with EBSD diffraction information is measured, we can distinguish clusters from grains and define the crystallographic grain size of $MAPbI_3$ fabricated via FIRA and AS. Furthermore, being a spatially resolved technique, it allows the direct comparison of a specific crystallographic orientation or a specific grain size with other spatially resolved optoelectronic techniques. **Figure 2.3b,c** shows an overlay of the image quality (*brightness*, IQ) with inverse pole figure (*color*, IPF) of the AS and FIRA system along the *z-axis* (parallel to the substrate). The IQ maps the sharpness of the Kikuchi lines obtained from the EBSD measurement which gives qualitative indications about the crystallinity of the material, topographic effects (*e.g.* roughness), strain of the microstructure and grain boundaries. The IPF map represents the crystal orientation obtained from fitting the Kikuchi patterns to each pixel of the image with respect to a reference axis. Along the *z-axis* (parallel to the substrate), the AS sample (**Figure 2.3b**) shows randomly oriented grains

of hundreds of nanometers. On the contrary, in the FIRA sample (**Figure 2.3c**), all grains are aligned along [100] and [112] direction (green and purple color) and the two orientations are paired in larger regions, in agreement with XRD and polarized microscopy measurements. The distribution of orientations for the two samples clearly shows the mostly random orientation for the AS sample, and the bipolar distribution of orientations for the FIRA sample (**Figure 2.3d**). Consistent with XRD (**Figure 2.1c**), we observe significant orientation along both the [100] and [112] direction, but locally the ratio can vary as shown for another FIRA cluster in **Figure A2.3**. Orientation maps along *x*- and *y-axis* (perpendicular to the substrate) show random grain orientations for the AS sample (see **Figure A2.4**) and highly oriented and paired grains for the FIRA sample (**Figure 2.3e,f**)**.** Distribution plots of the crystallographic orientations along *x*- and *y*- are also shown in **Figure A2.5** clearly identifying the difference in the crystallization for the FIRA and AS systems along the *x*- and *y-axis*. In **Figure 2.3e,f**, grain boundaries within the FIRA cluster and the nucleation site are shown in dark gray (low IQ value). As previously discussed, this can be attributed to the roughness of the area, lower crystallinity but also due to the large step size used during the measurement in comparison with the grain size of that region. A grain, by definition, has the same orientation in all three directions. More than 90% of the grains we measure are smaller than 1 $\mu m^2$ for the AS sample, while the FIRA samples shows 83% of the grains having an area between 0-30 $\mu m^2$ as we report in **Figure A2.6**. While the FIRA grains are large, they are smaller than the size of the clusters shown in SEM **Figure 2.3g**).

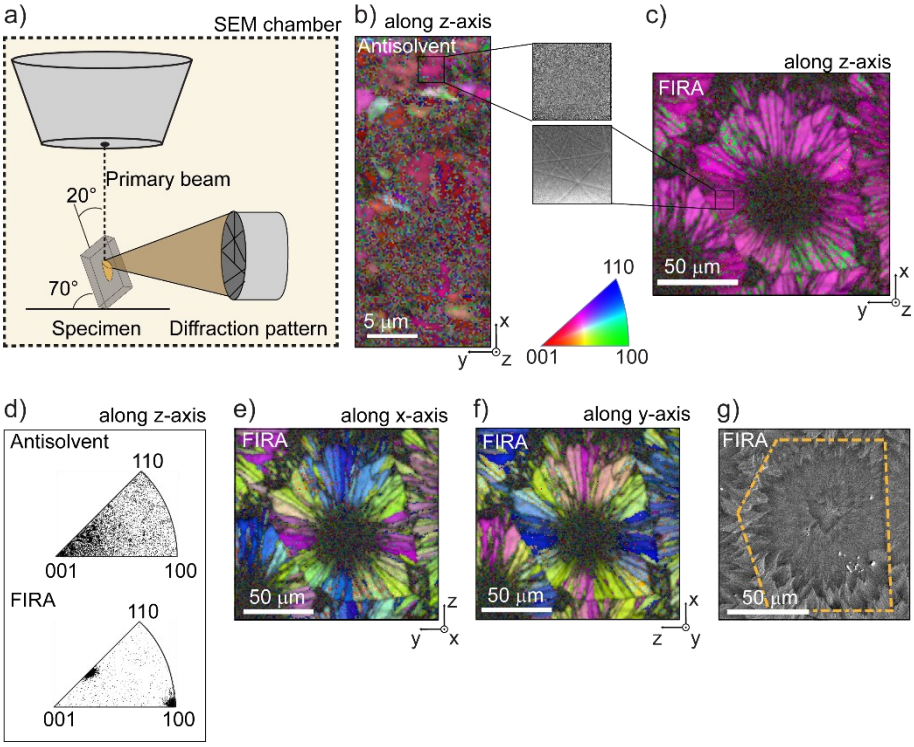


**Figure 2.3.** *EBSD maps reveal the crystal orientation and grain size of the two systems*. **a)** EBSD setup. **b)** IQ (brightness) overlay with IPF (color) map of AS sample showing crystallographic orientation along *z-axis*. Inset, a magnification of the typical Kikuchi patterns recorded from the sample. **c)** IQ (brightness) overlay with IPF (color) map of FIRA sample showing crystallographic orientation along *z-axis*. Inset, a magnification of the typical Kikuchi patterns recorded from the sample. **d)** Distribution of orientation for the two samples along z-axis. IQ (brightness) overlays with IPF (color) map of FIRA sample showing crystallographic orientation along **e)** *x*- and **f)** *y-axis*. **g)** SEM image showing the apparent grain size of a FIRA cluster. The cluster measured with EBSD is highlighted with a dashed line.

$MAPbI_3$ has an anisotropic tetragonal crystal structure and properties like trap-state density have been shown to be dependent upon crystal orientation[49,50]. In the following, we study the optoelectronic properties of the two well-characterized and spatially separated orientations shown by FIRA sample using

spatially resolved photoluminescence. Often, enlargement and preferential orientation of grains are achieved by introducing chemical additives which often also passivate the perovskite grains, prolonging lifetime and enhancing the photoluminescence. To avoid misleading attribution of the effects of additives to the grain size effects, here we compare the highly oriented FIRA and the AS samples fabricated without additives and from the same precursor solution.

## 2.3. Optoelectronic Properties

We measure the PL intensity using a confocal imaging microscope using 405nm laser as excitation source with a power density of 0.23 W/cm$^2$. As the two orientations on the sample are spatially well-separated, we can map any difference in PL emission between them. We measure a large area of the FIRA and AS samples including a whole FIRA cluster as shown in **Figure 2.4a** and **Figure A2.7** for a larger area. In the AS sample the PL intensity is relatively homogeneously distributed across the measured region, varying from cluster to cluster, consistent with many other works[51,52]. For the FIRA sample, we find comparable photoluminescence between the interior of the grain and the GBs. Previously grain boundaries were reported to cause either enhancement or reduction[29,48,53] of the emission intensity, mostly caused by ambiguities of assigning these boundaries. In our case, GBs do not lower the emission of the film. In contrast, the FIRA sample shows an enhancement in intensity of two to six-fold at the CBs and at the nucleation site where the spherulitic growth is started. To investigate the role of grain size on the PL intensity we compare the PL from the interior of the FIRA sample to the AS sample. In **Figure 2.4b** we plot PL spectra from five random regions of the two samples. Here we show that the interior region of the FIRA cluster shows a comparable PL intensity with the AS sample (FIRA Point 2&3), despite much larger size of the FIRA grains. This comparison shows that the PL emission is not solely determined by the grain size (at least for grains > 400 nm). Furthermore, we see no difference in wavelength or intensity for the regions that correspond to the two different, well-defined crystal orientations. Hence, the variation in PL emission intensity and wavelength are not related to the crystallographic orientations for the samples studied here.

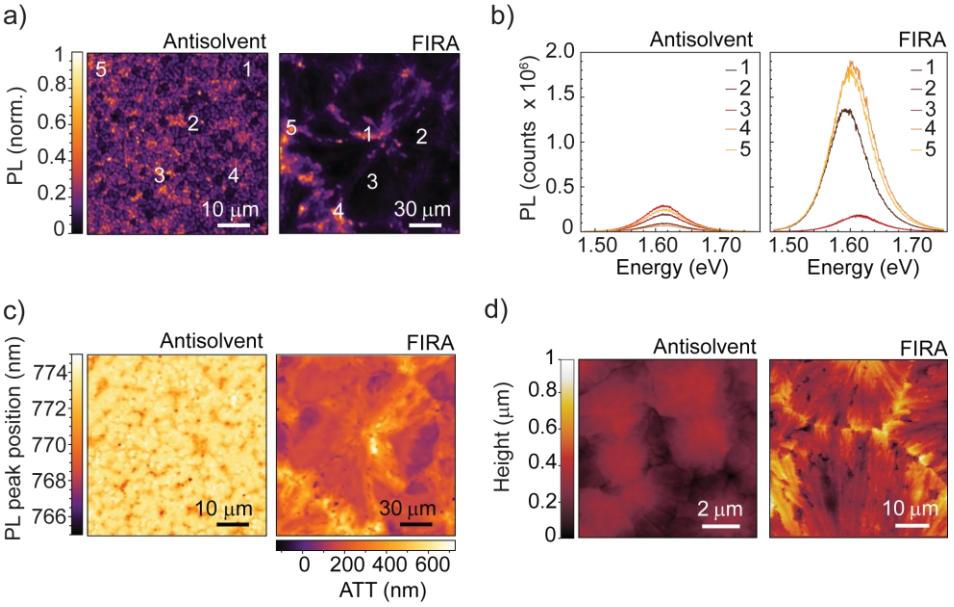


**Figure 2.4.** *Emission properties of $MAPbI_3$ varying crystal orientation and grain size.* **a)** Spatially resolved PL maps of AS and FIRA sample and corresponding **b)** PL spectra extracted from five random regions indicated in figure (a). **c)** Emission wavelength map of the same region as in figure (a) for the AS and FIRA samples. For the FIRA sample, the emission wavelength is converted into the additional travelled thickness ATT (on the horizontal scale bar) the light has been through before it is emitted and **d)** AFM image of AS and FIRA sample highlighting the CBs region in the FIRA sample.

The map of the PL peak position of the AS sample (**Figure 2.4c**) shows identical emission wavelength for every grain. In contrast, the FIRA sample shows a variation in emission wavelengths at distinct locations. The PL peak position at the CBs and nucleation point is red shifted compared to the interior of the cluster (**Figure 2.4c**). We also observe an asymmetric shape of the peak for the FIRA sample as shown in **Figure A2.8**. This shape, in combination with the red shift of the peak has been assigned to self-absorption when light travels through the perovskite layers before being emitted.[54] To validate this assignment we calculate the emission spectra expected from the light passing through different thicknesses of $MAPbI_3$ before being emitted. We calculate the red-shift

at the CBs and nucleation points we observe corresponds to light that has been travelling through 400nm – 800nm excess material as compared to the cluster interior region before being emitted (additional travelled thickness (ATT) on horizontal scale bar in **Figure 2.4c**). The calculation is reported in the **Appendix 2.6.2**. This is in good agreement with the observed thickness variation between the two regions in the AFM. From AFM measurements, the AS sample shows only minor height variation between the center and the rest of the grain (RMS roughness 70.5±7.5 nm, **Figure 2.4d**). On the contrary, the FIRA sample shows significant height variation at the CBs and at the nucleation point as shown in **Figure 2.4d** and in **Figure A2.9**. In these regions the film is around 400 nm to 1000 nm thicker compared to the interior of the cluster leading to a much larger roughness (RMS roughness is estimated 26.8±14.5 nm in the interior of the cluster, 175±47 nm at the nucleation site and 75.3±21 nm at the CBs).

The rough nature of the boundary observed in **Figure 2.4d** can favour light-outcoupling, as shown on patterned perovskite surfaces[55]. We hence tentatively assign the higher PL intensity in the CBs and nucleation site to better light-outcoupling at these rough surfaces. We corroborate the assignment of self-absorption and outcoupling differences by measuring PL lifetime maps of the FIRA sample. We observe a bi-exponential decay, with a fast and a slow component. The effect of reabsorption and photon recycling have been shown to affect the recombination dynamics by lengthening the slow lifetime component[55–58]. The lifetime of the FIRA sample at the CBs and at the nucleation site shows the same fast lifetime component, but a prolonged slow decay component compared to the interior of the cluster ($\tau_1 = 10.1 \pm 0.9$ and $\tau_2 = 49.2 \pm 2.0$ for the darker PL region in the grain interior and $\tau_1 = 12.9 \pm 0.9$ and $\tau_2 = 75.1 \pm 1.1$ for the brighter PL region at the CBs as reported in **Figure 2.5a,b**. The ratio of the slow-to-fast lifetime component (1.5 in our case) depends on the thickness and the likelihood of the light-outcoupling events[56]. The increased thickness increases the likelihood of re-absorption and increases the ratio, and better light-outcoupling decreases the lifetime ratio. Accounting only for difference in thickness at the CBs compared to the cluster interior, the lifetime ratio is overestimated. However, outcoupling is also most likely at rougher regions such as the CBs. Thus, the change in lifetime can be explained taking both the larger

thickness and outcoupling into account, consistent with the shift in PL spectrum. A semi-quantitative analysis is reported in **Appendix 2.6.3**. Similarly, no significant difference in lifetime is observed between the interior of the grain and the GBs within the FIRA cluster. We also do not observe a trend across the cluster that would correspond to the two different grain orientations. Thus, we do not find direct correlation between the crystal orientation and the PL intensity.

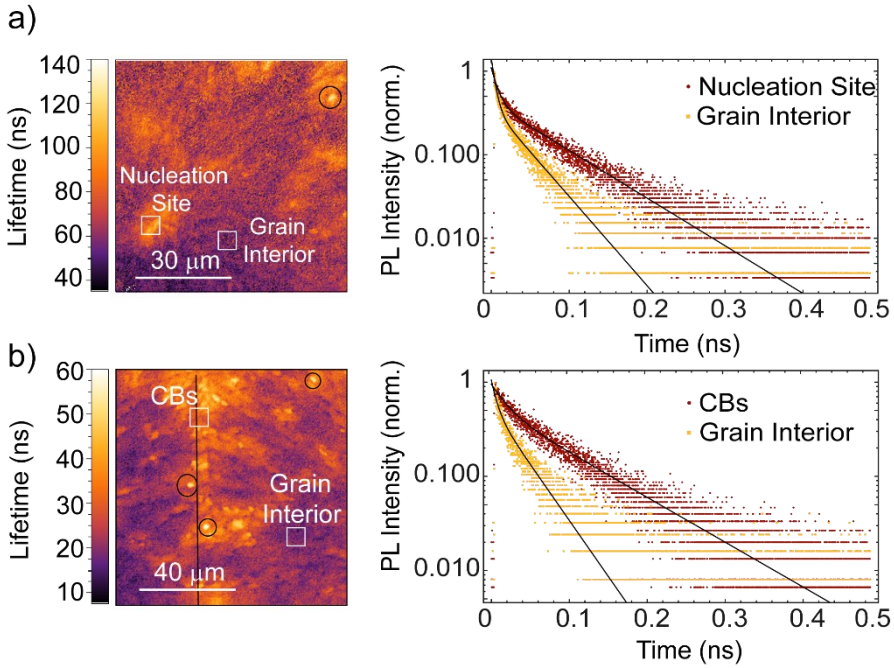


**Figure 2.5.** *Extended charge lifetime at the rough regions in the FIRA sample.* Lifetime maps of FIRA sample of the **a)** nucleation site and the **b)** CBs and corresponding decay curves of grain interior (darker) and CBs/nucleation site regions (brighter). Throughout the cluster the lifetime is comparable and neither shortening nor lengthening of lifetime is observed at the GBs within the FIRA cluster, while we observe longer slow component at the CBs and some long-lived hotspots. Lines represent the cluster boundaries and the long-lived hotspots are circled in black.

Next to the optical properties, the electronic properties have been shown to depend on grain size in some cases[59]. To investigate the mobility and recombination dynamics of photoexcited charge carriers in our two systems we

use the time-resolved microwave conductivity (TRMC) technique. The FIRA and AS samples were excited with 485 nm excitation wavelength. **Figure 2.6** shows the photoconductance ΔG as a function of time after pulsed excitation of AS and FIRA sample, respectively. The product of the yield of free charges φ and their mobility Σμ (sum of electron and hole mobility) is derived from the maximum signal height ($\Delta G_{max}$) which was divided by the fraction of absorbed photons for the two samples to take into account the difference in absorption.

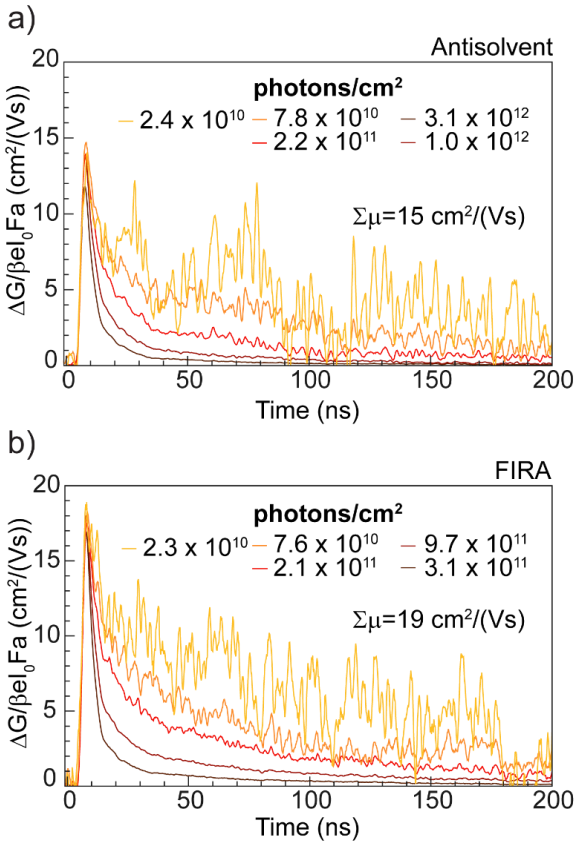


**Figure 2.6.** *Mobility and lifetime varying the grain size.* Time-resolved microwave conductivity (TRMC) traces measured at different carrier density for the **a)** AS and **b)** FIRA sample deposited on quartz.

We find a mobility of (15±3) $cm^2/(Vs)$ for the AS and (19±4) $cm^2/(Vs)$ for the FIRA sample, the difference of which is comparable to sample-to-sample

variation. The charge carrier lifetime is obtained from the photoconductance decay. The decay of the photoconductance represents the immobilization of free charges due to trapping or recombination. For both systems, we find that the lifetime of charges is in the order of a few hundred nanoseconds. We observe a slight increase of the effective mobility in the FIRA sample compared to the AS sample likely related to the enlarged grain size[59]. This difference is relatively small, despite the difference in grain size between the FIRA (tens of microns) and the AS sample (hundreds of nanometers). This shows that grain size alone does not dominate charge carrier transport properties. We note that the TRMC measurement mostly probes the local conductivity (~50 nm, more details about the probing length are reported in **Appendix 2.6.4**). Inter-grain transport across larger distances may show larger differences in crystallographically different systems. This finding is consistent with the similar device performances that have been reported for both FIRA and AS showing similar $J_{sc}$, $V_{oc}$, FF and PCE[33]. Practically, FIRA could allow a lower cost, environmentally friendly fabrication route to produce large scale, reproducible and more stable (**Figure A2.10**) perovskite compared to the AS method[33].

# 2.4. Conclusion

We have shown that the crystallographic orientation of $MAPbI_3$ grains does not determine the optical and local electronic properties. We study a $MAPbI_3$ thin film where crystallization is induced by FIRA. We apply EBSD to extract information about the microstructure of the perovskite thin film with high spatial resolution. The large FIRA clusters consist of grains that are tens of micrometer in size, highly oriented perpendicularly and in parallel to the substrate with a preferential orientation along the [112] and [100] direction along the *z-axis*. In comparison, a conventional sample fabricated via AS shows grains of hundreds of nanometers in size, randomly oriented in the three directions. We find increased PL intensity and a spectral shift in the FIRA sample at the CBs compared to the interior part of the FIRA cluster, which can be explained by roughness and thickness variations favoring light-outcoupling and self-absorption, respectively. No difference in PL between the grain and the GBs is

observed in the FIRA sample, leading us to the conclusion that in the grain boundaries are not detrimental to the PL in our system. Finally, we investigate charge carrier dynamics and find comparable lifetime and a slight increase in effective mobility in the FIRA and AS samples. We hence conclude that in our case, neither the grain size (when larger than a few hundred nm) nor the grain orientation are the dominant factor determining the optoelectronic properties of perovskite thin films. This finding implies that efforts towards a more efficient perovskite device may need to focus on reducing defects within the bulk and at the interface as well as impurities within the materials rather than growing large, oriented grains.

## 2.5. Experimental Methods

### Sample Preparation

The precursor solution used to fabricate $MAPbI_3$ thin films is prepared at a concentration of 1M by mixing 1 M solutions of $PbI_2$ and MAI in a 1:1 ratio. The solutions are prepared in anhydrous 3 v/v DMF:1 v/v DMSO. For the AS film, the perovskite solution is spin-coated in two steps at 1000 and 6000 rpm for 10 and 20 s, respectively. During the second step, 100 µL of chlorobenzene is poured onto the substrate 5 s before the end of the spin coating program. Finally, the substrates are annealed at 100 °C for 1 h. The FIRA films are made by using the same precursor solution as described above. The spin-coating program consists of a single step at 4000 rpm for 10 s. Right after the spin coating, the substrates are irradiated with a 1.2 s short pulse of IR light to induce the crystallization of the perovskite.

### X-Ray Diffraction

The X-Ray diffraction pattern of perovskite films deposited on ITO was measured using an X-ray diffractometer, Bruker D2 Phaser, with Cu Kα 1.5406 Å as X-Ray source, 0.002° (2θ) as step size, 0.150 s as exposure time. A FEI Verios 460 instrument was used to obtain SEM images. Atomic force microscopy (AFM) measurements were performed on a Veeco Dimension 3100 (Bruker) in tapping mode.

### Optical Microscopy

Optical microscope (Zeiss, AxioCam ICc 5) equipped with a 10x/0.2 objective EC Epiplan, polarizer and analyzer set at different angles was used for polarized optical microscopy imaging. We combine the optical microscope in reflection mode with two polarizers, one placed in the light path before the specimen, and a second one, called analyzer, between the objective lenses and eyepieces.

### Steady-State Photoluminescence

Steady-state PL of samples deposited on quartz was measured with a home-built setup equipped with a 640 nm continuous-wave laser as source of excitation (PicoQuant LDH-D-C-640) at a power output of 1 mW. Two Thorlabs filters, a long pass, ET655LP, and a notch, ZET642NF, were used to remove the excitation laser from the signal. The PL was coupled into a fiber connected to an OceanOptics USB4000 spectrometer. An integration time of 300 ms was used for each measurement.

### Electron Back-Scattered Diffraction

The samples were prepared and kept in a nitrogen-filled glovebox to prevent degradation from moisture exposure before the measurement. Samples were deposited on ITO to avoid charging effects during the experiment. Samples were glued on a metallic stub with silver paste and left degassing for at least 2 hours in a humidity-controlled environment (<5%). Since the perovskite is a soft material, no additional mechanical treatments (e.g. mechanical polishing, grinding, electropolishing, ion milling) were applied before the measurement. The detector used is a direct electron detector based on the Timepix sensor from Amsterdam Scientific Instruments (ASI). The best parameters for the scans were found to be 15 keV as acceleration voltage, 100 pA as beam current, 100 ms as exposure time and working distances between 12 mm and 10.1 mm. This translates to the application of 10 nA per ms per pixel which is around $10^3$ times lower compared conventional measurement reducing sample damage. The step size was chosen depending on the cluster size shown by the specific sample, 200 nm and 1 μm for the AS and FIRA sample, respectively. EBSD data were collected using EDAX OIM software and a Python script was used for image processing. The resulting Kikuchi patterns were indexed using tetragonal symmetry, *I*4/*mcm*, using 1-3° as degree of tolerance.

### Spatially-resolved Photoluminescence

Spatially resolved PL maps were measured using a confocal imaging microscope (WITec alpha300 SR). A 405 nm laser diode (Thorlabs S1FC405) was used as excitation source where the PL intensity of the two $MAPbI_3$ films

was collected in reflection mode through a NA 0.9 objective using a spectrometer (UHTC 300 VIS, WITec) leading to a spatial resolution of 0.33 µm. The intensity was measured within the 700 to 840 nm emission wavelength range. A 488 nm LP filter was used to remove the excitation laser from the signal. The light collection was done from the same sample side as the excitation. The PL spectra were converted to the energy scale using a Jacobian transformation[60].

### Time-Resolved Microwave Conductivity

Time-Resolved Microwave Conductivity (TRMC) was measured on AS and FIRA sample deposited on quartz. The thin films were placed in a sealed resonance cavity inside a nitrogen-filled glovebox to avoid degradation due to air exposure. The samples were excited at 485 nm using a pulsed excitation (10 Hz) and the photoconductance probed at different excitation densities. Neutral density filters were used to vary the intensity of the incident light. The ΔG signal rise is limited by the width of the laser pulse (3.5 ns FWHM) and the response time of the microwave system (18 ns). The slow repetition rate of the laser of 10 Hz ensures full relaxation of all photo-induced charges to the ground state before the next laser pulse hits the sample. The mobility $\sum \mu$ which is the sum of the electrons and holes mobility ($\mu_e + \mu_h$) is derived by the maximum signal height by the following equation[61],

$$\varphi \Sigma \mu = \frac{\Delta G_{max}}{\beta e I_0 F_A} \tag{2.1}$$

where $I_0$ is the number of photons per unit area per pulse, $\beta$ a geometric factor related to the microwave cell, $e$ is the elementary charge, $\varphi$ is the charge carrier generation yield and $F_A$ the fraction of the light absorbed by the sample at the excitation wavelength used. We assume $\varphi$ to be unitary for the low exciton binding energy of the material.

### Photoluminescence decay

Time-correlated single photon counting (TCSPC) measurements were performed with a home-built setup equipped with PicoQuant PDL 828 ‘‘Sepia

II'' and a PicoQuant HydraHarp 400 multichannel picosecond event timer and TCSPC module. A 640 nm pulsed laser (PicoQuant LDH-D-C-640) with a repetition rate of 2 MHz was used to excite the sample. A Thorlabs FEL-700 long-pass filter was used to remove the excitation laser.

# 2.6. Appendix

## 2.6.1. Additional Figures

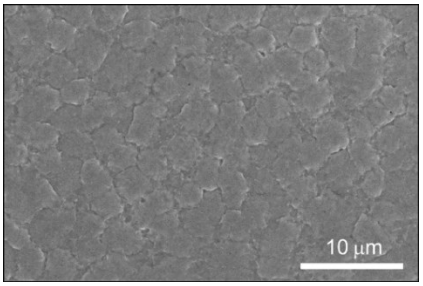


**Figure A2.1.** SEM images of $MAPbI_3$ fabricated via antisolvent dripping at lower magnification. SEM shows perovskite domains of (sub-)micron size.

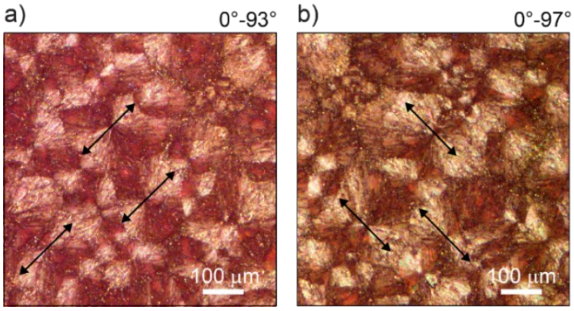


**Figure A2.2.** Polarized light microscopy of the same area of FIRA sample deposited on quartz. Analyser and polarizer are set at **a)** 0° and 93° and **b)** 0° and 97° degree, respectively. The perovskite shows a birefringent behaviour typical of spherulitic crystals.

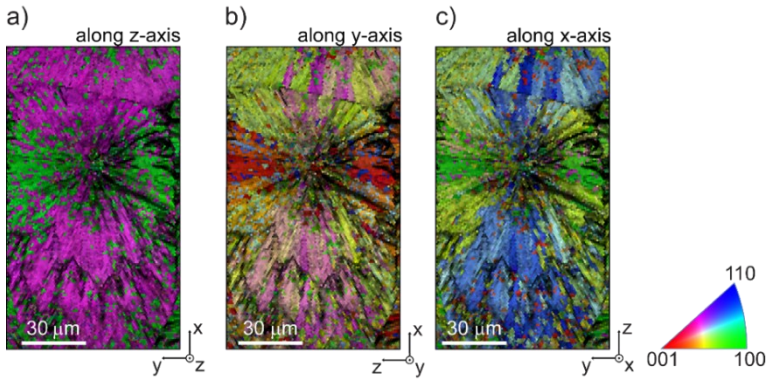


**Figure A2.3.** Image Quality (IQ) overlay with Inverse Pole Figure (IPF) map of the FIRA sample showing crystallographic orientation along **a)** z-direction, **b)** y-direction and **c)** x-direction. The perovskite domains that show homogeneous orientation along all three directions correspond to a crystallographic grain.

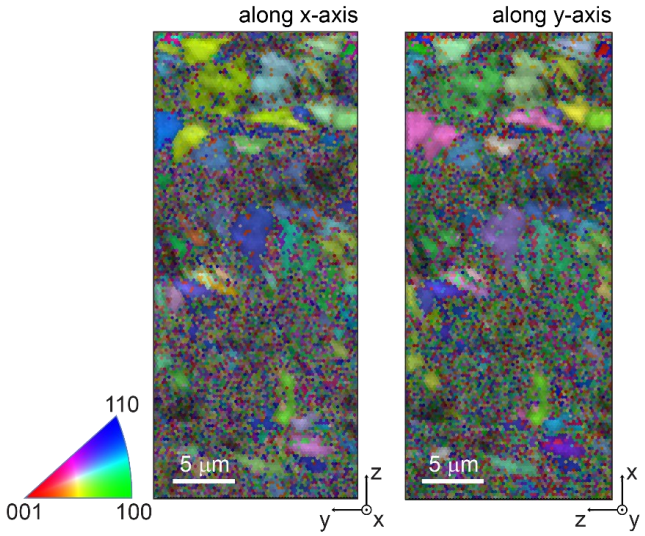


**Figure A2.4.** Image Quality (IQ, brightness) overlay with Inverse Pole Figure (IPF) map of AS sample showing crystallographic orientation along x-direction and y-direction. The perovskite domains that show homogeneous orientation along x-, y-, and z-direction correspond to a crystallographic grain.

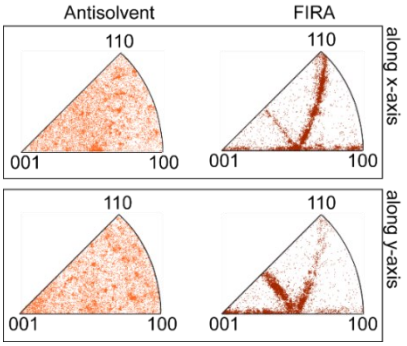


**Figure A2.5.** Crystal orientation distribution along x-, y- and z-axis for AS and FIRA system. The AS system shows almost random orientation long the three directions while the FIRA system shows preferential orientation.

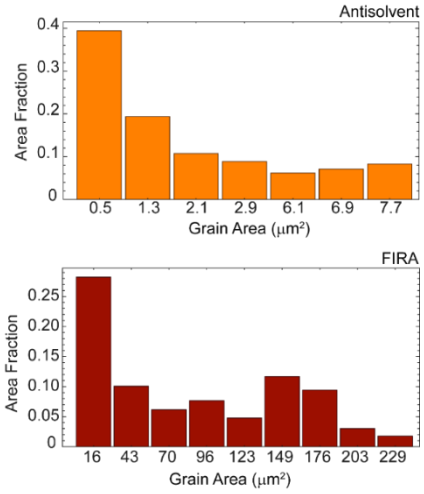


**Figure A2.6.** Grain area obtained from EBSD measurements in the AS and FIRA system. For the AS sample the binning in the histogram is 1 $\mu m^2$ and for the FIRA sample is 10 $\mu m^2$.

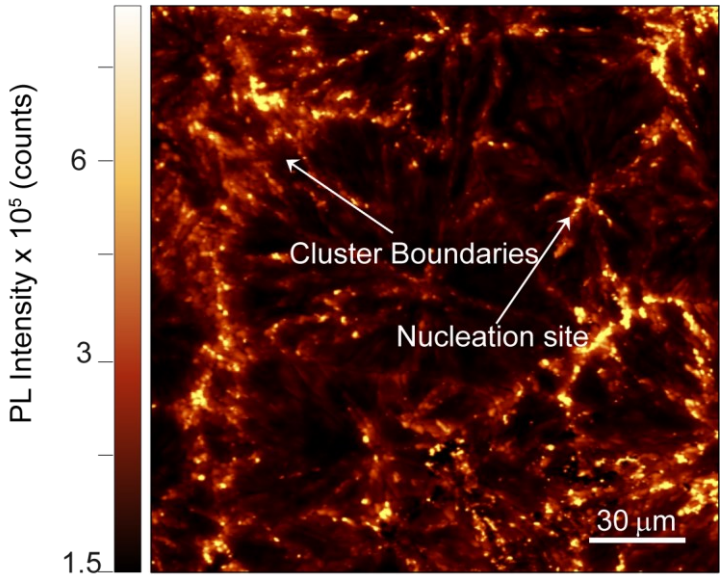


**Figure A2.7.** Spatially resolved PL of a bigger region of the FIRA sample including several clusters with a resolution of 0.33 μm per pixel. This map shows the enhancement in PL at the CBs and nucleation site for all the clusters. The enhancement varies from 4 to 6 times.

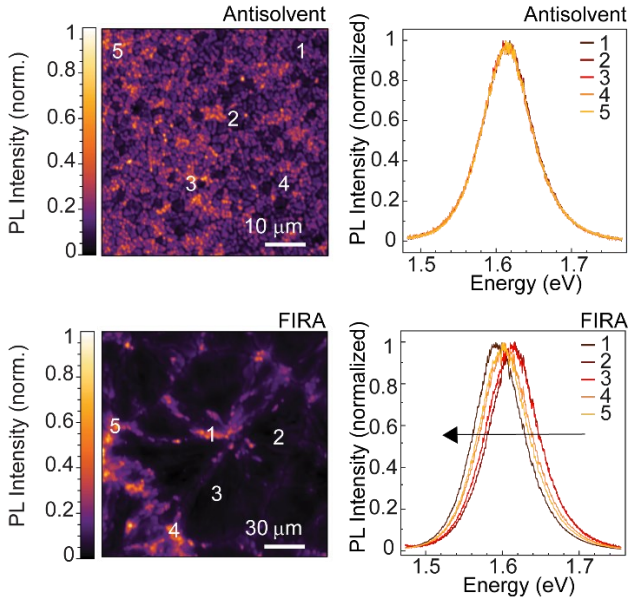


**Figure A2.8.** Normalized PL of the five regions highlighted in the main text for the AS and FIRA sample. The peak position in the AS sample remains constant in different regions showing no asymmetry in the emission peak, whereas in the FIRA sample the PL peak is red-shifted and more asymmetric moving from the interior region of the cluster (Point 2&3) to the CBs (Point 4&5) to the nucleation site (Point 1).

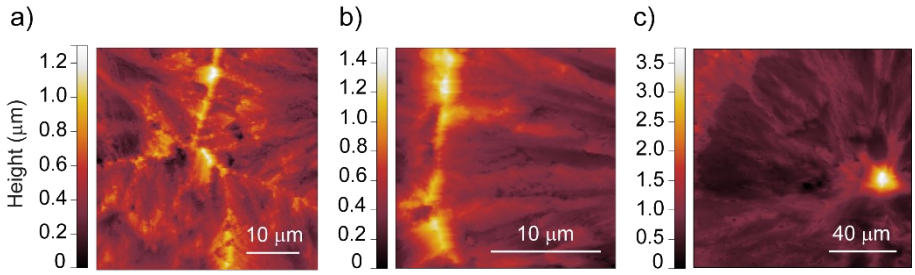


**Figure A2.9.** AFM images of FIRA sample at two different regions at a,b) the CBs and at c) the nucleation site

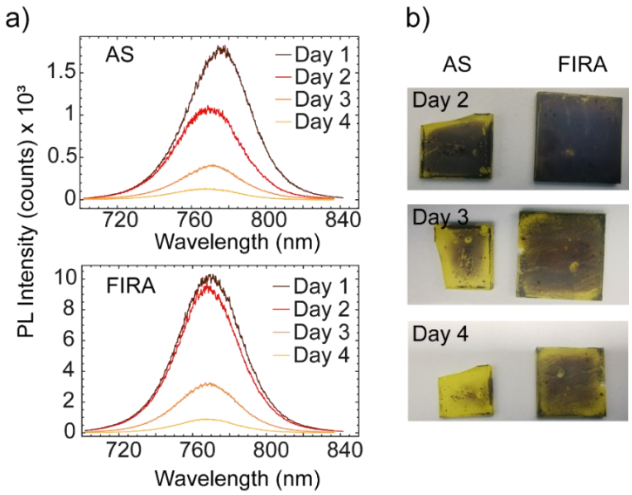


**Figure A2.10.** PL spectra of **a)** AS and FIRA measured after fabrication and up to 4 days of exposure to ambient conditions (with relative humidity of 22±4 RH% and temperature of 21±2 °C). **b)** Images of AS and FIRA films after 2, 3 and 4 days of air exposure.

### 2.6.2. Additional Thickness Travelled by Light

We simulate the expected PL spectra as a function of the additional travelled thickness (ATT) by the light before being emitted using the model following[54]

$$I_{emission}(d;\lambda) = I_{emission}(d_0;\lambda)e^{-\alpha(\lambda)d} \tag{2.2}$$

where $I_{emission}(0;\lambda)$ is the PL spectrum of the interior region of the cluster used as reference, $d$ is the thickness by which light is transmitted within the perovskite, $\alpha(\lambda)$ is the absorption coefficient obtained from absorption, A(λ), as follows

$$\alpha(\lambda) = \frac{2.303\ A(\lambda)}{d_0} \tag{2.3}$$

The model takes in account only the attenuation of the emitted light due to self-absorption events. In **Figure A2.11a**, we show the agreement of the simulated PL spectrum with the experimentally measured spectrum when the ATT is 250 nm. We convert the additional thickness transmitted by the light through the perovskite into the expected PL peak position using equation (2.1). Therefore, we fit a second order polynomial to find the relation between the PL peak position and the ATT (**Figure A2.11b**). Then the experimental emission wavelengths of the FIRA cluster shown in **Figure 2.4c** are converted using the relation obtained.

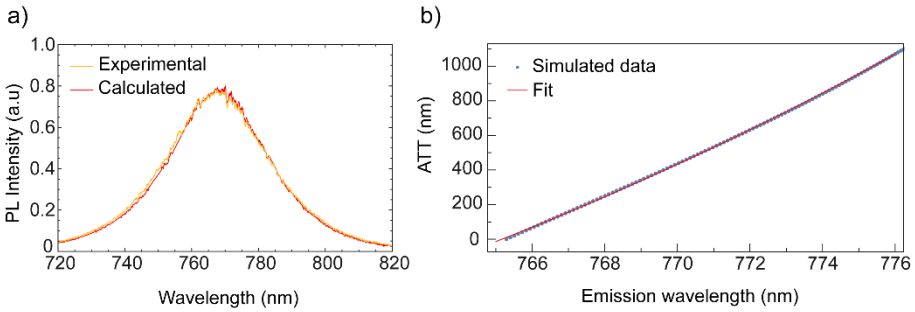


**Figure A2.11. a)** Experimental and simulated PL spectrum for additional transmitted thickness (ATT) of 250 nm. **b)** Relation between the PL peak position and the ATT before light being emitted

### 2.6.3. Thickness and Roughness Effect on Lifetimes

The elongation of the radiative decay component due to photon recycling events has been observed in earlier works[55–57]. From Staub et al.,[56] the externally observed bimolecular component ratio is given by

$$k_{ratio}^{ext} = \frac{1 - p_{r,0}k}{1 - p_{r,CB}k} \tag{2.4}$$

Where $k$ is the radiative fraction, $p_{r,0}$ and $p_{r,CB}$ is the probability for a photon to be reabsorbed in the layer before being emitted at the interior of the grain and at the cluster boundaries (CB), respectively. This term can be described as

$$p_r = 1 - p_e - p_p \tag{2.5}$$

and $p_e$ is the probability for a photon to be emitted without reabsorption events which depends on the escape cone Ω, and $p_p$ is parasitic absorption into the substrate. Assuming the radiative fraction $k$ and $p_p$ are constant, the radiative lifetime ratio at the grain interior and at the grain boundaries would only depend on the sample thickness and the escape cone

$$\frac{\tau_0}{\tau_{CB}} \approx \frac{1 - \left(\frac{p_{e,0}}{d_0} d\Omega_0 + \frac{p_{a,0}}{d_{CB}}\right)k}{1 - \left(\frac{p_{e,CB}}{d_{CB}} d\Omega_{CB} + \frac{p_{a,0}}{d_{CB}}\right)k} \tag{2.6}$$

where $d_0$ and $d_{CB}$ are the thickness at the grain interior and at the cluster boundaries, respectively. $d\Omega_0$ and $d\Omega_{CB}$ are the escape cone at the grain and at the cluster boundaries. Experimentally we find the lifetime ratio to be 1.5. Accounting only for differences in thickness, the value obtained from calculation is 2.5, overestimating the one observed experimentally.

Light-outcoupling is favored by the difference in roughness of the surfaces. On average the grain interior and the cluster boundary regions show RMS roughness

of 26.8±14.5 nm and 75.3±21 nm, respectively. Thus, for the CBs, the $d\Omega_{CB}$ is increased and the lifetime ratio decreases in accordance with the experiments.

## 2.6.4. Probing Length in Tr-Microwave Conductivity

The distance crossed by the charges is limited by the charge carrier diffusion coefficient and half the oscillation period ν (8.5 GHz), and the probing length *P* is given by:

$$P = \sqrt{\mu(k_B T/e)\frac{1}{2}\upsilon^{-1}} \tag{2.7}$$

**Figure A2.12** shows the probing length at room temperature as function of mobility for different measurement frequencies.[4] If we now assume a 300 nm-sized grain in which the charges are homogeneously distributed, then ~83% of the charges will be generated within the TRMC probing length of 68 nm of a grain boundary. For a grain size of 10 µm, this would be less than 5%. Hence, the similar lifetimes of mobile charges for the different grain sizes means that the recombination is not significantly affected by the surface.

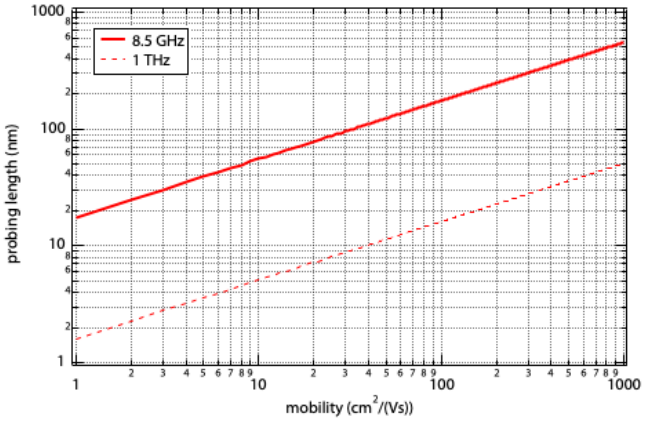


**Figure A2.12.** Probing length as function of mobility for photoconductivity measurements conducted at a frequency of 8.5 GHz (solid line, TRMC technique). This shows that the mobilities of 15 $cm^2/(Vs)$ and 19 $cm^2/(Vs)$ correspond to probing lengths of 68 nm and 76 nm, respectively. The probing length at 1 THz (dotted line, THz).

# 2.7. References


(1) Chen, Y.; Zhang, L.; Zhang, Y.; Gao, H.; Yan, H. Large-Area Perovskite Solar Cells – a Review of Recent Progress and Issues. *RSC Adv.* **2018**, *8* (19). https://doi.org/10.1039/C8RA00384J.

(2) Nie, W. Y.; Tsai, H. H.; Asadpour, R.; Blancon, J.-C. C.; Neukirch, A. J.; Gupta, G.; Crochet, J. J.; Chhowalla, M.; Tretiak, S.; Alam, M. A.; et al. High-Efficiency Solution-Processed Perovskite Solar Cells with Millimeter-Scale Grains. *Science* **2015**, *347* (6221). https://doi.org/10.1126/science.aaa0472.

(3) Howard, I. A.; Abzieher, T.; Hossain, I. M.; Eggers, H.; Schackmar, F.; Ternes, S.; Richards, B. S.; Lemmer, U.; Paetzold, U. W. Coated and Printed Perovskites for Photovoltaic Applications. *Adv. Mater.* **2019**, *31* (26). https://doi.org/10.1002/adma.201806702.

(4) Ren, Y.-K.; Shi, X.-Q.; Ding, X.-H.; Zhu, J.; Hayat, T.; Alsaedi, A.; Li, Z.-Q.; Xu, X.-X.; Yang, S.-F.; Dai, S.-Y. Facile Fabrication of Perovskite Layers with Large Grains through a Solvent Exchange Approach. *Inorg. Chem. Front.* **2018**, *5* (2). https://doi.org/10.1039/C7QI00685C.

(5) Whitaker, J. B.; Kim, D. H.; Larson, B. W.; Zhang, F.; Berry, J. J.; van Hest, M. F. A. M.; Zhu, K. Scalable Slot-Die Coating of High Performance Perovskite Solar Cells. *Sustain. Energy Fuels* **2018**, *2* (11). https://doi.org/10.1039/C8SE00368H.

(6) Jin, J.; Li, H.; Chen, C.; Zhang, B.; Xu, L.; Dong, B.; Song, H.; Dai, Q. Enhanced Performance of Perovskite Solar Cells with Zinc Chloride Additives. *ACS Appl. Mater. Interfaces* **2017**, *9* (49). https://doi.org/10.1021/acsami.7b15310.

(7) Saliba, M. Polyelemental, Multicomponent Perovskite Semiconductor Libraries through Combinatorial Screening. *Adv. Energy Mater.* **2019**, *9* (25). https://doi.org/10.1002/aenm.201803754.

(8) Huang, Y.; Wu, S.; Chen, R.; Fang, S.; Zhang, S.; Wang, G.; Chen, W. Efficient Methylamine-Containing Antisolvent Strategy to Fabricate High-Efficiency and Stable FA0.85Cs0.15Pb(Br0.15I2.85) Perovskite Solar Cells. *ACS Appl. Mater. Interfaces* **2019**, *11* (20). https://doi.org/10.1021/acsami.9b03323.

(9) Klug, M. T.; Osherov, A.; Haghighirad, A. A.; Stranks, S. D.; Brown, P. R.; Bai, S.; Wang, J. T.-W.; Dang, X.; Bulovic, V.; Snaith, H. J.; et al. Tailoring Metal Halide Perovskites through Metal Substitution: Influence on Photovoltaic and Material Properties. *Energy Environ. Sci.* **2017**, *10* (1). https://doi.org/10.1039/C6EE03201J.

(10) Mojtaba, A.; Ibrahim, D. M.; Aditya, S.; P., S. S.; Marius, F.; Neha, A.; Yuanyuan, H.; Khaja, N. M.; M., Z. S.; Michael, G.; et al. Impact of

Monovalent Cation Halide Additives on the Structural and Optoelectronic Properties of $CH_3NH_3PbI_3$ Perovskite. *Adv. Energy Mater.* **2016**, *6* (10). https://doi.org/10.1002/aenm.201502472.

(11) Abdi-Jalebi, M.; Andaji-Garmaroudi, Z.; Cacovich, S.; Stavrakas, C.; Philippe, B.; Richter, J. M.; Alsari, M.; Booker, E. P.; Hutter, E. M.; Pearson, A. J.; et al. Maximizing and Stabilizing Luminescence from Halide Perovskites with Potassium Passivation. *Nature* **2018**, *555* (497). https://doi.org/10.1038/nature25989.

(12) Halder, A.; Chulliyil, R.; Subbiah, A. S.; Khan, T.; Chattoraj, S.; Chowdhury, A.; Sarkar, S. K. Pseudohalide (SCN–)-Doped MAPbI3 Perovskites: A Few Surprises. *J. Phys. Chem. Lett.* **2015**, *6* (17). https://doi.org/10.1021/acs.jpclett.5b01327.

(13) Pazos-Outón, L. M.; Xiao, T. P.; Yablonovitch, E. Fundamental Efficiency Limit of Lead Iodide Perovskite Solar Cells. *J. Phys. Chem. Lett.* **2018**, *9* (7). https://doi.org/10.1021/acs.jpclett.7b03054.

(14) Sarritzu, V.; Sestu, N.; Marongiu, D.; Chang, X.; Masi, S.; Rizzo, A.; Colella, S.; Quochi, F.; Saba, M.; Mura, A.; et al. Optical Determination of Shockley-Read-Hall and Interface Recombination Currents in Hybrid Perovskites. *Sci. Rep.* **2017**, *7* (44629). https://doi.org/10.1038/srep44629.

(15) Meggiolaro, D.; De Angelis, F. First-Principles Modeling of Defects in Lead Halide Perovskites: Best Practices and Open Issues. *ACS Energy Lett.* **2018**, *3* (9). https://doi.org/10.1021/acsenergylett.8b01212.

(16) Ball, J. M.; Petrozza, A. Defects in Perovskite-Halides and Their Effects in Solar Cells. *Nat. Energy* **2016**, *1* (16149). https://doi.org/10.1038/nenergy.2016.149.

(17) Wang, J.; Fu, W.; Jariwala, S.; Sinha, I.; Jen, A. K.-Y.; Ginger, D. S. Reducing Surface Recombination Velocities at the Electrical Contacts Will Improve Perovskite Photovoltaics. *ACS Energy Lett.* **2019**, *4* (1),. https://doi.org/10.1021/acsenergylett.8b02058.

(18) Sherkar, T. S.; Momblona, C.; Gil-Escrig, L.; Ávila, J.; Sessolo, M.; Bolink, H. J.; Koster, L. J. A. Recombination in Perovskite Solar Cells: Significance of Grain Boundaries, Interface Traps, and Defect Ions. *ACS Energy Lett.* **2017**, *2* (5). https://doi.org/10.1021/acsenergylett.7b00236.

(19) Fassl, P.; Zakharko, Y.; Falk, L. M.; Goetz, K. P.; Paulus, F.; Taylor, A. D.; Zaumseil, J.; Vaynzof, Y. Effect of Density of Surface Defects on Photoluminescence Properties in MAPbI3 Perovskite Films. *J. Mater. Chem. C* **2019**, *7* (18). https://doi.org/10.1039/c8tc05998e.

(20) Uratani, H.; Yamashita, K. Charge Carrier Trapping at Surface Defects of Perovskite Solar Cell Absorbers: A First-Principles Study. *J. Phys. Chem. Lett.* **2017**, *8* (4). https://doi.org/10.1021/acs.jpclett.7b00055.

(21) Zhu, L.; Xu, Y.; Zhang, P.; Shi, J.; Zhao, Y.; Zhang, H.; Wu, J.; Luo, Y.; Li, D.; Meng, Q. Investigation on the Role of Lewis Bases in the Ripening Process of Perovskite Films for Highly Efficient Perovskite Solar Cells.

*J. Mater. Chem. A* **2017**, *5* (39). https://doi.org/10.1039/C7TA05378A.

(22) Stavrakas, C.; Zhumekenov, A. A.; Brenes, R.; Abdi-Jalebi, M.; Bulović, V.; Bakr, O. M.; Barnard, E. S.; Stranks, S. D. Probing Buried Recombination Pathways in Perovskite Structures Using 3D Photoluminescence Tomography. *Energy Environ. Sci.* **2018**, *11* (10). https://doi.org/10.1039/C8EE00928G.

(23) Staub, F.; Hempel, H.; Hebig, J.-C.; Mock, J.; Paetzold, U. W.; Rau, U.; Unold, T.; Kirchartz, T. Beyond Bulk Lifetimes: Insights into Lead Halide Perovskite Films from Time-Resolved Photoluminescence. *Phys. Rev. Appl.* **2016**, *6* (4). https://doi.org/10.1103/PhysRevApplied.6.044017.

(24) Lee, D. S.; Yun, J. S.; Kim, J.; Soufiani, A. M.; Chen, S.; Cho, Y.; Deng, X.; Seidel, J.; Lim, S.; Huang, S.; et al. Passivation of Grain Boundaries by Phenethylammonium in Formamidinium-Methylammonium Lead Halide Perovskite Solar Cells. *ACS Energy Lett.* **2018**, *3* (3). https://doi.org/10.1021/acsenergylett.8b00121.

(25) Zhang, H.; Wu, Y.; Shen, C.; Li, E.; Yan, C.; Zhang, W.; Tian, H.; Han, L.; Zhu, W. H. Efficient and Stable Chemical Passivation on Perovskite Surface via Bidentate Anchoring. *Adv. Energy Mater.* **2019**, *9* (13). https://doi.org/10.1002/aenm.201803573.

(26) Guo, Q.; Yuan, F.; Zhang, B.; Zhou, S.; Zhang, J.; Bai, Y.; Fan, L.; Hayat, T.; Alsaedi, A.; Tan, Z. Passivation of the Grain Boundaries of $CH_3NH_3PbI_3$ Using Carbon Quantum Dots for Highly Efficient Perovskite Solar Cells with Excellent Environmental Stability. *Nanoscale* **2019**, *11* (1). https://doi.org/10.1039/C8NR08295B.

(27) Zhang, W.; Saliba, M.; Moore, D. T.; Pathak, S. K.; Hörantner, M. T.; Stergiopoulos, T.; Stranks, S. D.; Eperon, G. E.; Alexander-Webber, J. A.; Abate, A.; et al. Ultrasmooth Organic–Inorganic Perovskite Thin-Film Formation and Crystallization for Efficient Planar Heterojunction Solar Cells. *Nat. Commun.* **2015**, *6* (6142). https://doi.org/10.1038/ncomms7142.

(28) Yang, Y.; Peng, H.; Liu, C.; Arain, Z.; Ding, Y.; Ma, S.; Liu, X.; Hayat, T.; Alsaedi, A.; Dai, S. Bi-Functional Additive Engineering for High-Performance Perovskite Solar Cells with Reduced Trap Density. *J. Mater. Chem. A* **2019**, *7* (11). https://doi.org/10.1039/C8TA11925B.

(29) Yang, M.; Zeng, Y.; Li, Z.; Kim, D. H.; Jiang, C.-S.; van de Lagemaat, J.; Zhu, K. Do Grain Boundaries Dominate Non-Radiative Recombination in $CH_3NH_3PbI_3$ Perovskite Thin Films? *Phys. Chem. Chem. Phys.* **2017**, *19* (7). https://doi.org/10.1039/C6CP08770A.

(30) Gedamu, D.; Asuo, I. M.; Benetti, D.; Basti, M.; Ka, I.; Cloutier, S. G.; Rosei, F.; Nechache, R. Solvent-Antisolvent Ambient Processed Large Grain Size Perovskite Thin Films for High-Performance Solar Cells. *Sci. Rep.* **2018**, *8* (1). https://doi.org/10.1038/s41598-018-31184-0.

(31) Foley, B. J.; Girard, J.; Sorenson, B. A.; Chen, A. Z.; Scott Niezgoda, J.;

Alpert, M. R.; Harper, A. F.; Smilgies, D.-M.; Clancy, P.; Saidi, W. A.; et al. Controlling Nucleation, Growth, and Orientation of Metal Halide Perovskite Thin Films with Rationally Selected Additives. *J. Mater. Chem. A* **2017**, *5* (1). https://doi.org/10.1039/C6TA07671H.

(32) Rong, Y.; Hou, X.; Hu, Y.; Mei, A.; Liu, L.; Wang, P.; Han, H. Synergy of Ammonium Chloride and Moisture on Perovskite Crystallization for Efficient Printable Mesoscopic Solar Cells. *Nat. Commun.* **2017**, *8* (14555). https://doi.org/10.1038/ncomms14555.

(33) Sanchez, S.; Hua, X.; Phung, N.; Steiner, U.; Abate, A. Flash Infrared Annealing for Antisolvent-Free Highly Efficient Perovskite Solar Cells. *Adv. Energy Mater.* **2018**, *8* (12). https://doi.org/10.1002/aenm.201702915.

(34) Sánchez, S.; Vallés-Pelarda, M.; Alberola-Borràs, J.-A.; Vidal, R.; Jerónimo-Rendón, J. J.; Saliba, M.; Boix, P. P.; Mora-Seró, I. Flash Infrared Annealing as a Cost-Effective and Low Environmental Impact Processing Method for Planar Perovskite Solar Cells. *Mater. Today* **2019,** *31*. https://doi.org/https://doi.org/10.1016/j.mattod.2019.04.021.

(35) Han, L.; Cong, S.; Yang, H.; Lou, Y.; Wang, H.; Huang, J.; Zhu, J.; Wu, Y.; Chen, Q.; Zhang, B.; et al. Environmental-Friendly Urea Additive Induced Large Perovskite Grains for High Performance Inverted Solar Cells. *Sol. RRL* **2018**, *2* (7). https://doi.org/10.1002/solr.201800054.

(36) Feng, J.; Zhu, X.; Yang, Z.; Zhang, X.; Niu, J.; Wang, Z.; Zuo, S.; Priya, S.; Liu, S. (Frank); Yang, D. Record Efficiency Stable Flexible Perovskite Solar Cell Using Effective Additive Assistant Strategy. *Adv. Mater.* **2018**, *30* (35). https://doi.org/10.1002/adma.201801418.

(37) Nalwa, H. S. *Handbook of Nanostructured Materials and Nanotechnology, Five-Volume Set*; Elsevier Science, **1999**.

(38) Zhou, Y.; Yang, M.; Vasiliev, A. L.; Garces, H. F.; Zhao, Y.; Wang, D.; Pang, S.; Zhu, K.; Padture, N. P. Growth Control of Compact $CH_3NH_3PbI_3$ Thin Films via Enhanced Solid-State Precursor Reaction for Efficient Planar Perovskite Solar Cells. *J. Mater. Chem. A* **2015**, *3* (17). https://doi.org/10.1039/C4TA07036D.

(39) Mali, S. S.; Hong, C. K.; Inamdar, A. I.; Im, H.; Shim, S. E. Efficient Planar N-i-p Type Heterojunction Flexible Perovskite Solar Cells with Sputtered TiO2 Electron Transporting Layers. *Nanoscale* **2017**, *9* (9). https://doi.org/10.1039/C6NR09032J.

(40) Shtukenberg, A. G.; Punin, Y. O.; Gunn, E.; Kahr, B. Spherulites. *Chem. Rev.* **2012**, *112* (3). https://doi.org/10.1021/cr200297f.

(41) Marentette, J. M.; Brown, G. R. Polymer Spherulites: I. Birefringence and Morphology. *J. Chem. Educ.* **1993**, *70* (6). https://doi.org/10.1021/ed070p435.

(42) Fu, W.; Vaughan, J.; Gillespie, A. Effects of Inorganic Anions on the Morphology of Sodium Oxalate Crystallized from Highly Alkaline

Solutions. *Cryst. Growth Des.* **2014**, *14* (4). https://doi.org/10.1021/cg5000952.

(43) Craciun, V.; Craciun, D.; Wang, X.; Anderson, T. J.; Singh, R. K. Transparent and Conducting Indium Tin Oxide Thin Films Grown by Pulsed Laser Deposition at Low Temperatures. *Thin Films Solid.* **2004**, *453*. https://doi.org/10.1016/j.tsf.2003.11.132.

(44) Zhao, J.; Deng, Y.; Wei, H.; Zheng, X.; Yu, Z.; Shao, Y.; Shield, J. E.; Huang, J. Strained Hybrid Perovskite Thin Films and Their Impact on the Intrinsic Stability of Perovskite Solar Cells. *Sci. Adv.* **2017**, *3* (11). https://doi.org/10.1126/sciadv.aao5616.

(45) Ryde, L. Application of EBSD to Analysis of Microstructures in Commercial Steels. *Mater. Sci. Technol.* **2006**, *22* (11). https://doi.org/10.1179/174328406X130948.

(46) Kamaya, M.; Quinta Da Fonseca, J.; Li, L. M.; Preuss, M. Local Plastic Strain Measurement by EBSD. *Applied Mechanics and Materials* **2007**, *7* (8). https://doi.org/10.4028/www.scientific.net/AMM.7-8.173.

(47) Rohrer, G. S.; Li, J.; Lee, S.; Rollett, A. D.; Groeber, M.; Uchic, M. D. Deriving Grain Boundary Character Distributions and Relative Grain Boundary Energies from Three-Dimensional EBSD Data. *Mater. Sci. Technol.* **2010**, *26* (6). https://doi.org/10.1179/026708309X12468927349370.

(48) Adhyaksa, G. W. P.; Brittman, S.; Āboliņš, H.; Lof, A.; Li, X.; Keelor, J. D.; Luo, Y.; Duevski, T.; Heeren, R. M. A.; Ellis, S. R.; et al. Understanding Detrimental and Beneficial Grain Boundary Effects in Halide Perovskites. *Adv. Mater.* **2018**, *30* (52). https://doi.org/10.1002/adma.201804792.

(49) Zhang, T.; Long, M.; Yan, K.; Zeng, X.; Zhou, F.; Chen, Z.; Wan, X.; Chen, K.; Liu, P.; Li, F.; et al. Facet-Dependent Property of Sequentially Deposited Perovskite Thin Films: Chemical Origin and Self-Annihilation. *ACS Appl. Mater. Interfaces* **2016**, *8* (47). https://doi.org/10.1021/acsami.6b11986.

(50) Leblebici, S. Y.; Leppert, L.; Li, Y.; Reyes-Lillo, S. E.; Wickenburg, S.; Wong, E.; Lee, J.; Melli, M.; Ziegler, D.; Angell, D. K.; et al. Facet-Dependent Photovoltaic Efficiency Variations in Single Grains of Hybrid Halide Perovskite. *Nat. Energy* **2016**, *1* (16093). https://doi.org/10.1038/nenergy.2016.93.

(51) Moerman, D.; Eperon, G. E.; Precht, J. T.; Ginger, D. S. Correlating Photoluminescence Heterogeneity with Local Electronic Properties in Methylammonium Lead Tribromide Perovskite Thin Films. *Chem. Mater.* **2017**, *29* (13). https://doi.org/10.1021/acs.chemmater.7b00235.

(52) de Quilettes, D. W.; Vorpahl, S. M.; Stranks, S. D.; Nagaoka, H.; Eperon, G. E.; Ziffer, M. E.; Snaith, H. J.; Ginger, D. S. Impact of Microstructure on Local Carrier Lifetime in Perovskite Solar Cells. *Science* **2015**, *348*

(6235). https://doi.org/10.1126/science.aaa5333.
(53) Castro-Méndez, A.-F.; Hidalgo, J.; Correa-Baena, J.-P. The Role of Grain Boundaries in Perovskite Solar Cells. *Adv. Energy Mater.* **2019**, *9* (38), 1901489. https://doi.org/10.1002/aenm.201901489.
(54) Mohan, V.; Jain, P. K. Spectral Heterogeneity of Hybrid Lead Halide Perovskites Demystified by Spatially Resolved Emission. *J. Phys. Chem. C* **2017**, *121* (35). https://doi.org/10.1021/acs.jpcc.7b08005.
(55) Richter, J. M.; Abdi-Jalebi, M.; Sadhanala, A.; Tabachnyk, M.; Rivett, J. P. H.; Pazos-Outón, L. M.; Gödel, K. C.; Price, M.; Deschler, F.; Friend, R. H. Enhancing Photoluminescence Yields in Lead Halide Perovskites by Photon Recycling and Light Out-Coupling. *Nat. Commun.* **2016**, *7* (13941). https://doi.org/10.1038/ncomms13941.
(56) Staub, F.; Kirchartz, T.; Bittkau, K.; Rau, U. Manipulating the Net Radiative Recombination Rate in Lead Halide Perovskite Films by Modification of Light Outcoupling. *J. Phys. Chem. Lett.* **2017**, *8* (20). https://doi.org/10.1021/acs.jpclett.7b02224.
(57) W. Crothers, T.; L. Milot, R.; B. Patel, J.; S. Parrott, E.; Schlipf, J.; Müller-Buschbaum, P.; B. Johnston, M.; M. Herz, L. Photon Reabsorption Masks Intrinsic Bimolecular Charge-Carrier Recombination in CH3NH3PbI3 Perovskite. *Nano Lett.* **2017**, *17* (9). https://doi.org/10.1021/acs.nanolett.7b02834.
(58) Diab, H.; Arnold, C.; Lédée, F.; Trippé-Allard, G.; Delport, G.; Vilar, C.; Bretenaker, F.; Barjon, J.; Lauret, J.-S. S.; Deleporte, E.; et al. Impact of Reabsorption on the Emission Spectra and Recombination Dynamics of Hybrid Perovskite Single Crystals. *J. Phys. Chem. Lett.* **2017**, *8* (13). https://doi.org/10.1021/acs.jpclett.7b00998.
(59) Reid, O. G.; Yang, M.; Kopidakis, N.; Zhu, K.; Rumbles, G. Grain-Size-Limited Mobility in Methylammonium Lead Iodide Perovskite Thin Films. *ACS Energy Lett.* **2016**, *1* (3). https://doi.org/10.1021/acsenergylett.6b00288.
(60) Mooney, J.; Kambhampati, P. Get the Basics Right: Jacobian Conversion of Wavelength and Energy Scales for Quantitative Analysis of Emission Spectra. *J. Phys. Chem. Lett.* **2013**, *4* (19). https://doi.org/10.1021/jz401508t.
(61) Savenije, T. J.; Ferguson, A. J.; Kopidakis, N.; Rumbles, G. Revealing the Dynamics of Charge Carriers in Polymer:Fullerene Blends Using Photoinduced Time-Resolved Microwave Conductivity. *J. Phys. Chem. C* **2013**, *117* (46). https://doi.org/10.1021/jp406706u.

# 3. Pressure Effects on the Hot-Carrier Cooling

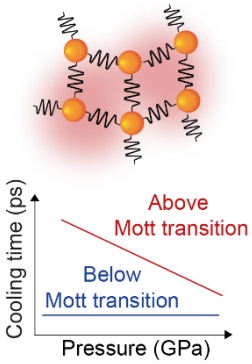


Hot-carrier cooling (HCC) in metal halide perovskites is significantly slower compared to conventional semiconductors above the Mott transition. This effect is commonly attributed to a hot-phonon bottleneck but the influence of the lattice properties on the HCC behaviour is poorly understood. Using pressure-dependent femtosecond transient absorption spectroscopy (fs-TAS) we find that at an excitation density below Mott transition, pressure does not affect the HCC. On the contrary, above Mott transition, HCC in methylammonium lead iodide ($MAPbI_3$) is around two – three times as fast at 0.3 GPa compared to ambient pressure. Our electron-phonon coupling calculations reveal about two times stronger electron-phonon coupling for the inorganic cage mode at 0.3 GPa. However, our experiments reveal that pressure promotes faster HCC only above Mott transition. Altogether, these findings suggest a change in the nature of excited carriers above the Mott transition threshold, providing insights on the electronic behavior of devices operating at such high charge-carrier density.

*This chapter is based on the following publication:*
L. A. Muscarella, E. M. Hutter, J. M. Frost, G. G. Grimaldi, H. Bakker, B. Ehrler, Accelerated Hot-Carrier Cooling in MAPbI3 Perovskite by Pressure-Induced Lattice Compression, *The Journal of Physical Chemistry Letters*, 2021, 12 (17), 4118-4124.

# 3.1. Introduction

In **Chapter 1.2**, we have briefly introduced the concept of hot-carrier cooling occurring when a semiconductor is excited with a photon energy larger than its bandgap. This high-energy excitation results in the formation of a non-thermal distribution of "hot charge-carriers" (*i.e.* high-energy electrons in the conduction band and high-energy holes in the valence band). In semiconductor solar cells, these charges relax to the conduction (and valence) band edge before they are collected. The first step of this process is the thermalization[1,2], occurring within a few hundred femtoseconds, where the generated hot-carriers interact with each other through carrier-carrier scattering until they reach a common quasi-Fermi temperature, usually much higher than the lattice temperature. Subsequently, HCC occurs though carrier-phonon or carrier-impurity scattering until a thermal equilibrium with the local lattice is reached, usually on picosecond timescales[1,3,4]. In this step, heat is dissipated in the lattice through acoustic phonons. In solar cells, 33% of the energy of sunlight is lost as heat[5,6] during the thermalization and cooling processes. Slow HCC is desired for thermoelectric devices[7], and hot carrier solar cells[8] where extracting carriers before they have cooled could enables circumventing the thermodynamic limit for single-junction solar cells. Emissive applications such as lasers[9], single-photon sources[10] and optical modulators[11] require short HCC time for efficient radiative recombination and to prevent carrier trapping. In particular for lasers, it is quintessential to understand the electronic properties at the high-carrier density required to obtain lasing.

In metal halide perovskites, the HCC timescale was found to be significantly slower[3,12–14] than in conventional semiconductors like InN[15] or GaAs[12] under the same (high) excitation density conditions and upon increasing excitation density[3,16,17]. This slower cooling has been explained from an effect that is commonly known as hot-phonon bottleneck. The origin of this phenomenon is still under debate, but it has been attributed to several mechanisms such as the accumulation of optical phonons that cannot be easily dissipated[12,18,3], optical-acoustic phonon up-conversion[14] and polaron formation[19–21]. Metal halide perovskites are polar semiconductors, and thus their electronic properties are

expected to be strongly coupled with the lattice vibrations. Applying external pressure directly affects the lattice dynamics, and therefore can be used to tune properties that are strongly dependent on the lattice vibrations, such as the electron-phonon coupling and the phonon lifetimes. Changes in one or both of these quantities can affect the HCC. Increasing the electron-phonon coupling is expected to lead to faster HCC. For example, replacing iodide with a lighter halide increases the frequency of the longitudinal optical phonon mode ($\omega_{LO}$)[22] and thus shortens the HCC time measured under the same excess of energy and excitation density conditions[23,24,3]. In $MAPbI_3$, the acoustic phonon lifetime, responsible for heat transport, has been found in the range of a few ps[25,26], two orders of magnitude shorter than in conventional semiconductors[27]. Thus, the thermal transport at room temperature in $MAPbI_3$ is highly inefficient if no thermal management strategy is applied. If the acoustic phonon lifetime increases, the HCC is expected to become faster. Understanding how lattice properties relate with HCC provides insights on the electronic behaviour of devices operating at various charge-carrier densities. For some devices such as hot carrier solar cells, slow cooling is desired, while for lasing applications fast cooling is preferred. Thus, an effective strategy to manipulate *ad hoc* the HCC time is required to design devices with a specific application operating in a certain charge-carrier density regime.

In this Chapter, we combine pressure-dependent femtosecond transient absorption spectroscopy (fs-TAS) previously discussed in **Chapter 1.6** and electron-phonon coupling calculations to elucidate the effect of lattice compression on the factors that influence the HCC. We experimentally probe the HCC time in $MAPbI_3$ at room temperature at pressures ranging from 0 to 0.3 GPa at varying light excitation densities. At low excitation density ($7 \times 10^{17}$ photons/cm$^3$), the HCC time is fast (0.3 - 0.5 ps) and independent of pressure. High excitation density triggers a Mott transition, previously calculated to occur at an excitation density above $7 \times 10^{17}$ photons/cm$^3$ [21]. Here, we refer to "*Mott transition*" as a change in electronic species from isolated polarons acting independently to an electron-hole plasma where the thermal energy is shared between overlapping polarons. At an excitation density above the Mott transition threshold ($5.9 \times 10^{18}$ photons/cm$^3$), the HCC is significantly slower (2-3 ps) at

ambient pressure but accelerates by a factor 2-3 upon increasing the pressure to 0.3 GPa. Electron-phonon calculations reveal that the phonon mode at ~27 $cm^{-1}$ (0.8 THz), associated with the lead-iodide octahedral twist shows a significant and approximately linear increase as a function of pressure. In solar cells and optoelectronic devices operating above the Mott transition (> $10^{18}$ photons/$cm^3$), faster HCC timescale may allow for a faster dissipation of heat and therefore a lower operating temperature.

## 3.2. Pressure-dependent Cooling

Solution-processed $MAPbI_3$ thin films were deposited by spin coating onto quartz substrates as reported in the **Experimental Methods 3.5.** Absorption measurements as a function of pressure and X-Ray diffraction measurements were performed on the sample to confirm the bandgap energy and the high crystallinity of the sample as shown in **Figure A3.1**. Pressure-dependent transient absorption measurements were performed inside a hydrostatic pressure cell filled with the inert hydraulic liquid tetradecafluorohexane as schematically depicted in **Figure 3.1a**.

A 100-fs pulsed pump beam with an energy of 3.1 eV is used for photoexciting the sample and a 100-fs pulsed probe beam (white light) is used to probe the excitation-induced change in transmission of $MAPbI_3$ on a picosecond timescale. The two beams are overlapped on the sample inside the pressure cell, and the arrival time of the two pulses is controlled with a delay stage. To ensure the absence of any non-linear effects, we investigated the HCC process at excitation densities above Mott transition, but where the $\Delta T/T$ still shows a linear behavior with the pump fluence (**Figure A3.2**).

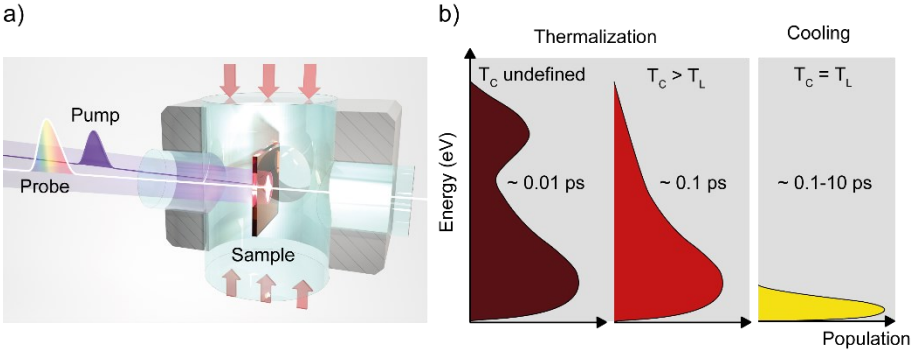


**Figure 3.1.** *Pressure-dependent transient absorption spectroscopy to probe the hot-carrier cooling.* **a)** Schematic representation of the pressure-dependent fs-TA setup showing the generation of hot-carriers (white spot on the sample) and **b)** HCC mechanism following photoexcitation.

Photoexcitation with a photon energy larger than the $MAPbI_3$ bandgap lead to a population of high-energy carriers (electrons and holes) with no common temperature (**Figure 3.1b**, dark red curve) that undergo rapid (~ 85 fs[1]) thermalization, faster than our temporal resolution. This thermalization process results from carrier-carrier scattering. The resulting hot-carrier population can be approximated to a quasi-Fermi distribution. Once the hot-carrier population reaches a common temperature $T_c$ (**Figure 3.1b**, red curve), higher than the lattice temperature $T_L$, carrier-phonon interactions dominate the HCC until $T_c$ is in equilibrium with $T_L$ (**Figure 3.1b**, yellow curve). **Figure 3.2** show representative pseudo-color TA plots of $MAPbI_3$ at 0 and 0.3 GPa as a function of the pump-probe delay and probe energy. $MAPbI_3$ is photoexcited at 3.1 eV (bandgap 1.7 eV) with an initial carrier density $n_0$ of $7.0 \times 10^{17}$ photons/cm$^3$ (**Figure 3.2a,b**) and $5.9 \times 10^{18}$ photons/cm$^3$ (**Figure 3.2c,d**) at ambient pressure and at 0.3 GPa, respectively. The carrier density is calculated as described in **Appendix 3.6.2**. Importantly, no degradation is observed at high excitation density as demonstrated in **Figure A3.3** from the stability of the TA signal over the course of the measurement.

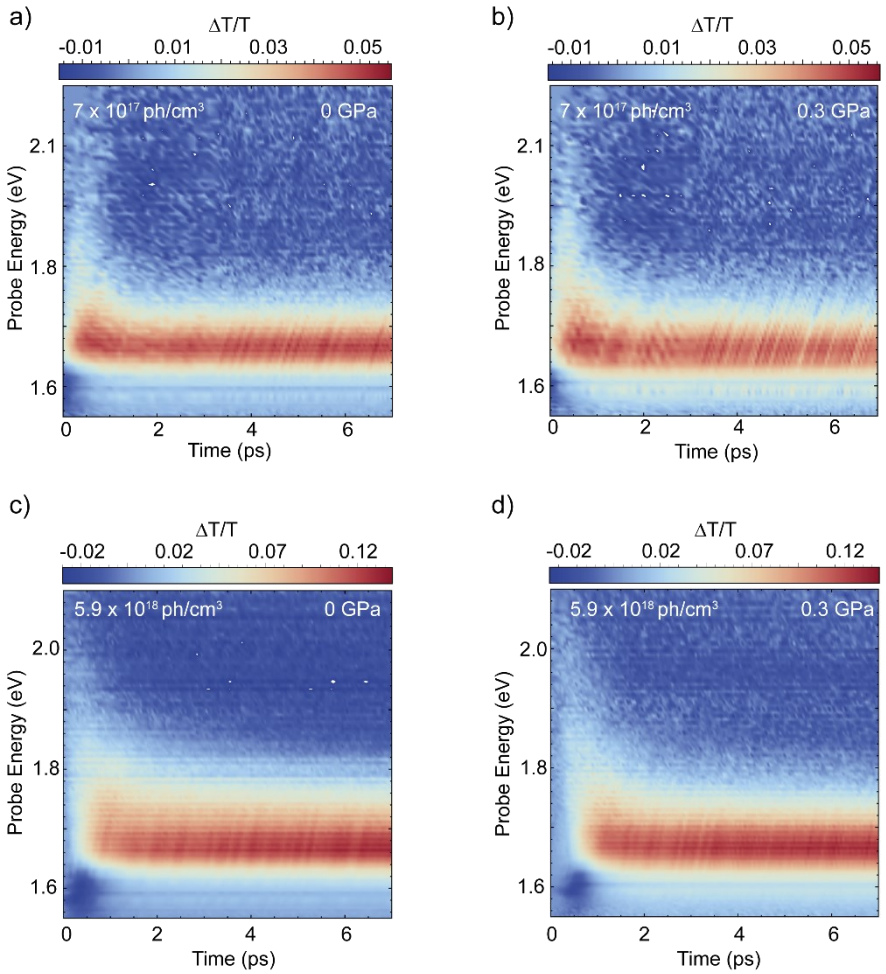


**Figure 3.2.** *2D plot of ΔT/T collected for $MAPbI_3$ at low and high pressure.* **a)** 2D plot of Δ*T*/*T* as a function of the probe energy and time excited in the low-density regime ($7 \times 10^{17}$ photons/cm$^3$) at 0 GPa and **b)** 0.3 GPa and **c)** in the high-density regime ($5.9 \times 10^{18}$ photons/cm$^3$) at 0 GPa and **d)** 0.3 GPa. The evolution of the high-energy tail represents the hot carriers.

The pseudo-color Δ*T*/*T* plots show three features: (*i*) a positive Δ*T*/*T* centred at the bandgap energy of ~1.67 eV corresponding to the ground state bleach (GSB) signal that results from the band filling effect; (*ii*) a negative Δ*T*/*T* feature at energies below the bandgap (< 1.67 eV) at early times resulting from the bandgap decrease induced by the high-energy carriers.[2]; (*iii*) a negative and

broad $\Delta T/T$ signal at energies above the bandgap (> ~1.7 eV) resulting from light absorption of the photo-generated carriers. The corresponding $\Delta T/T$ traces are reported for 0.3 to 5 ps delay time in **Figure 3.3a-d**.

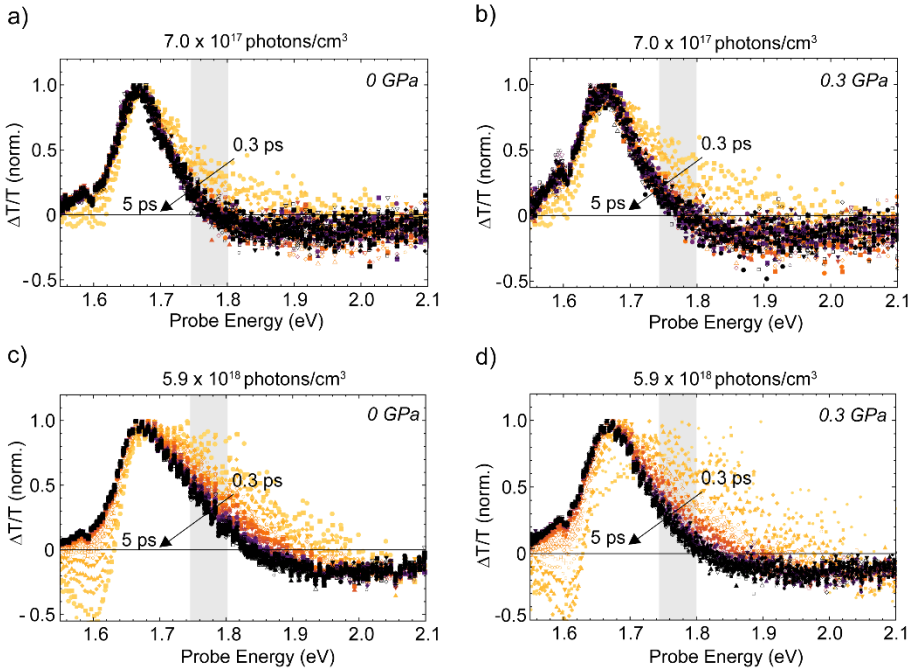


**Figure 3.3**. *Charge carrier cooling as a function of applied pressure from 0.3 ps to 5 ps in step of 1 ps*. **a)** *ΔT/T* traces of $MAPbI_3$ with $n_0$ of $7.0 \times 10^{17}$ photons/cm$^3$ at ambient pressure and **b)** at 0.3 GPa. **c)** *ΔT/T* traces of $MAPbI_3$ with $n_0$ of $5.9 \times 10^{18}$ photons/cm$^3$ at ambient pressure and **d)** at 0.3 GPa.

Here, the hot-carrier population is evident from the width of the initial GSB signal, which shrinks over the course of the measurement (picosecond timescale) as the hot carriers cool down to the lattice temperature. This feature represents an average of the hot electron and hot hole temperatures given the effective masses are very similar[28]. A comprehensive model to obtain the HCC time and temperature from the transient absorption measurements has still to be developed but several methods are commonly used[13,16,29]. We use two fitting strategies to obtain the trend of the HCC time as a function of pressure and excitation density. Both strategies yield a comparable HCC time upon increasing

the pressure and for both excitation densities. The first method consists of integrating the $\Delta T/T$ signal in the region of the high-energy GSB tail from 1.75 – 1.80 eV and plotting the result as a function of delay time. The integrated range is highlighted in grey in **Figure 3.3**. We plot the integrated traces for the low and high-density regime in **Figure 3.4a,b**.

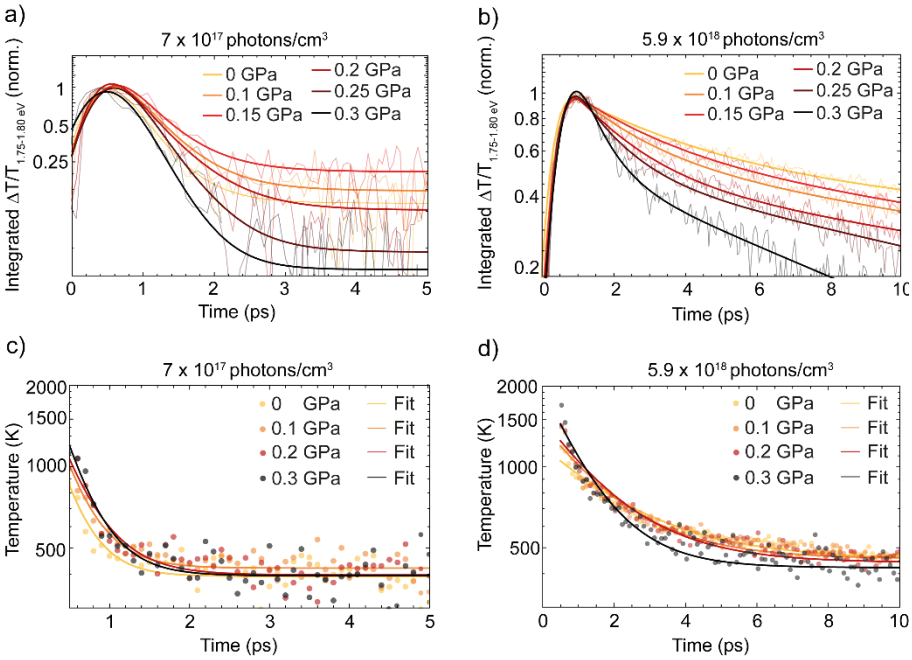


**Figure 3.4.** *Two fitting strategies for determining the HCC time as a function of pressure.* **a)** Normalized $\Delta T/T$ integrated in the range of 1.75-1.80 eV in the GSB tail as a function of time, and delay time for excitation density of $7 \times 10^{17}$ photons/cm$^3$ and **b)** $5.9 \times 10^{18}$ photons/cm$^3$ at different applied pressures. The decay of the GSB tail becomes faster upon increasing pressure in the high-density regime. **c)** Carrier temperature obtained by fitting the high-energy tail of the GSB with a Maxwell-Boltzmann distribution, as a function of delay time for high excitation density of $7 \times 10^{17}$ photons/cm$^3$ and **d)** $5.9 \times 10^{18}$ photons/cm$^3$ at different applied pressures.

We fit the traces at fluences below and above Mott transition with a convolution of the instrument response function (IRF) and an exponential decay function as

reported in **Appendix 3.6.3** and shown in **Figure A3.7.** Below the Mott transition threshold ($7 \times 10^{17}$ photons/cm$^3$), no pressure dependency is observed, showing fast (~ 0.3 ps) HCC at all pressures investigated (**Figure 3.5a**, blue). Above the Mott transition threshold, the decay comprises a fast component with a time constant of a few picoseconds (attributed to the HCC) and a slow component with a time constant in the order of tens of picoseconds. The presence of an additional slower process above the Mott transition has been shown previously and its origin is still under debate[13,14,30,31], therefore we compare the two fast components at the two excitation density used. The time constant for the short-lived component above the Mott transition is plotted in **Figure 3.5a** (red).

This experiment, contrary to the one below the Mott transition threshold, shows almost three times faster HCC (time constant ~1 ps) at 0.3 GPa compared to ambient pressure (~3 ps). To make sure the extracted trend of the HCC time with pressure is not affected by the energy range integrated, we performed the same fit but integrating $\Delta T/T$ in various energy ranges of the broad tail (**Figure A3.4** and **Figure A3.5** above and below the Mott transition threshold, respectively). The absolute values of the HCC time constants vary slightly, but the trend as a function of pressure is consistent. To make sure the fitting method does not influence our result, we test a second method to obtain the HCC time. It consists of approximating the high-energy tail of the GSB and the negative PIA[14] with a modified Maxwell–Boltzmann distribution function[13,32,33] as shown in **Appendix 3.6.4**. The fit yields the carrier temperatures which we show in **Figure 3.4c,d** as a function of delay time for ambient and three representative high-pressure conditions.

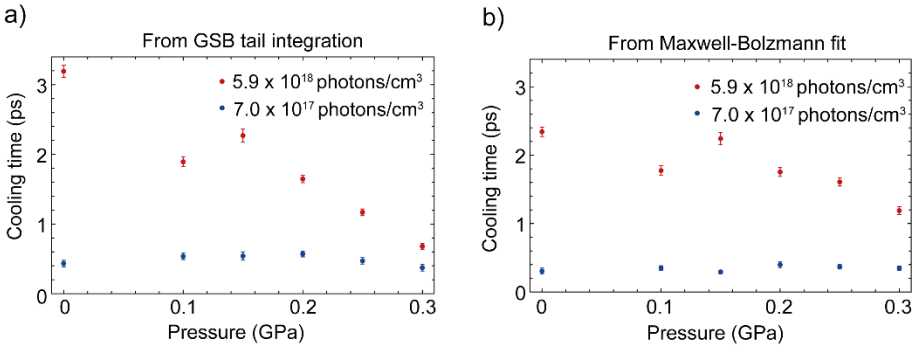


**Figure 3.5.** *Hot-carrier cooling time obtained from two fitting strategies.* HCC time extracted from **a)** the fit of the GSB tail decay and **b)** from the fit of the temperature decay as a function of pressure above (red) and below the Mott transition threshold (blue).

The initial temperature depends on the excess energy of the photoinduced carriers, and the excitation density. This is the temperature reached by the carriers directly after the thermalization. Interestingly, we observe a higher initial hot-carrier temperature upon increasing the pressure both in the low and high-density regime. The slight redshift in the bandgap energy (7 meV, **Figure A3.6**) when we increase the pressure cannot account for this effect. We thus conclude that pressure may have an effect on the thermalization process as well, but because this process is faster than our temporal resolution, we cannot further investigate this effect. The cooling time plotted in **Figure 3.5b** for the regime below and above Mott transition (in blue and red, respectively) is obtained by fitting an exponential decay function to the curve in **Figure 3.4c,d** taking into account the temperature errors of each datapoint. As with the first fitting routine, the HCC at ambient pressure and above the Mott transition is much slower than at high pressure, as reflected in a longer HCC time. The absolute values obtained by this fitting procedure for the cooling time are slightly lower than those obtained with the integration method shown in **Figure 3.5a**. As before, below the Mott transition threshold, HCC is fast, and there is no variation within the experimental error. Thus, in both regimes, the results by both fitting routines match qualitatively, and to a large extent quantitatively show the same result.

The HCC time depends on experimental parameters like the ambient temperature, the excess of excitation energy compared to the bandgap of the material, and the excitation density[3,20,34]. To exclude that the change in the HCC time observed as a function of pressure is determined by the change of one of these factors, we now discuss each of them. The temperature of the sample is kept constant (room temperature) during the experiment for all the pressure measured, and possible minor fluctuations cannot explain the change in cooling time as a function of pressure. The energy used to excite the perovskite is 3.1 eV, resulting in an excess energy of 1.42 eV compared to the $MAPbI_3$ bandgap at ambient pressure. As a function of pressure, we observe a redshift of the $MAPbI_3$ bandgap equal to 7 meV (**Figure A3.6**). A change in the excess energy can change the HCC time, however, to obtain a 2× faster hot carrier cooling, the excess of energy would have to be around 1 eV lower[20] (*i.e.* the excitation energy should be ≈ 2.1 eV). Therefore, we can exclude the change in the bandgap and the excess of energy as the reason of the faster HCC observed. The excitation density calculated as a function of pressure is dependent on the fraction of absorbed photons (**Appendix 3.6.2**) by the material at the excitation energy used. This quantity increases 1.8% as a function of pressure and this should result in the same increase of the excitation density. If such a small increase in excitation density would affect HCC, the expected time constant should be longer upon increasing pressure but not shorter as found experimentally. Thus, we can exclude the slight change in excitation density as origin for the shorter HCC. Finally, the pressure applied is below the threshold to induce a crystallographic phase transition (> 0.35 GPa[35]) that may cause a significant change the thermal properties of the material. Since we can exclude significative changes in these parameters upon changing the pressure, we can attribute the pressure-dependent trend observed solely to changes in the material properties following compression. In particular, we focus on the electron-phonon coupling.

## 3.3. Electron-Phonon Calculation

In order to understand the processes occurring in the microscopic scale within the material as a function of pressure, we calculate the electron-phonon coupling for all the phonon modes. The results of the relevant phonon modes are shown in **Figure 3.6a**. In these calculations we uniformly increase the pressure in a semi-local DFT electronic structure calculation (see **Experimental Methods 3.5**), starting with an ambient pressure pseudo-cubic $MAPbI_3$ structure[36]. The number of the phonon modes shown in **Figure 3.6a** is indexed in ascending energy order. The modes 1-3 represent the acoustic modes, that play a negligible role in the initial HCC where charge carriers strongly couple to optical modes though Fröhlich interactions. Modes 4-6 and 7-9 with frequencies ranging from 19 to 35 $cm^{-1}$ (0.5-1 THz) represent octahedral twist and distortion, respectively. These phonon modes generally preserve the bond length and have limited coupling with the organic cation, in contrast to the phonon modes with frequencies above 65 $cm^{-1}$ (~ 2 THz), from mode 10 onwards. For these latter modes, the change in bond length leads to collisions with the $A^+$-site ion, inducing coupling with the tumbling $MA^+$ [37]. Modes 10-16 are coupled motions of the organic cation with the inorganic sub-lattice and rotational vibration of the cation around the nitrogen or the carbon atom. Modes 17-36 are related to intramolecular vibration of the organic cation, and not relevant in the context of HCC as the electronic modes are localized mostly on the inorganic cage. A detailed assignment and description of the phonon modes can be found also in Leguy et al.[38] Previous works[39,40] have shown that the dominant phonon mode coupled to the excited state dynamics observed by fs-TAS in $MAPbI_3$ has a frequency around 27 $cm^{-1}$ (~ 0.8 THz), and that there is a somewhat less strongly coupled mode at higher frequencies. For this reason, we confine our discussion to phonon modes 4-9 representing octahedral twist and distortion, as these are the most relevant for the coupling with the electrons at the conduction band minimum. Whereas most of phonon modes show no clear trend with pressure, the electron-phonon coupling of mode 5 (~27 $cm^{-1}$, ~ 0.8 THz) associated with the octahedral twist, highlighted in grey in **Figure 3.6a**, shows a significant and approximately

linear increase (**Figure 3.6b**) when pressure rises from ambient to 1 GPa, with two times enhancement at 0.3 GPa compared to ambient pressure.

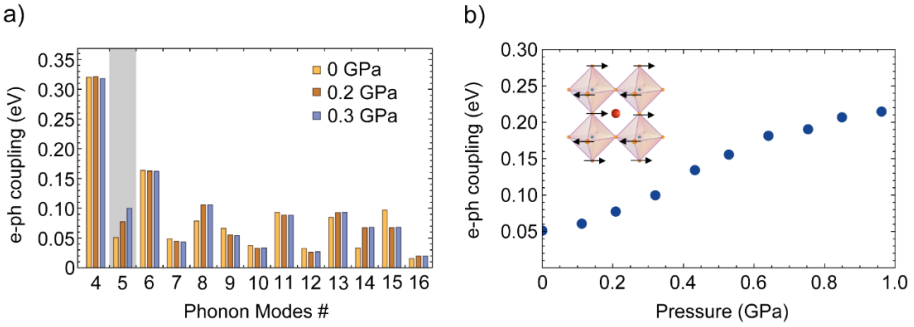


**Figure 3.6.** *Calculated electron-phonon coupling as a function of pressure.* **a)** Electron-phonon coupling strength of the $MAPbI_3$ phonon modes to the conduction band minimum (CBM) at the gamma point in the Brillouin zone in a 2×2×2 supercell, listed in ascending phonon energy. Highlighted in grey is the phonon mode 5 (~27 $cm^{-1}$, ~0.8 THz), affected most strongly by pressure. **b)** Electron-phonon coupling of the mode 5 (~27 $cm^{-1}$, ~0.8 THz) as a function of pressure. *Inset*: atomic motions related to the phonon mode 5 (octahedral twist).

A quantitative prediction of HCC (a phenomenological quantity) from the calculation of microscopic electron-phonon coupling matrix elements requires a mechanistic model of the cooling processes, and a detailed consideration of the electron-phonon interaction across the double electron and phonon Brillouin zones and goes beyond the scope of this work.

One would anticipate that the greater electron-phonon coupling at higher pressure would result in faster HCC, both below and above the Mott transition. However, we only observe a dependence on pressure above the Mott transition threshold. Below that, HCC is fast (0.3-0.5 ps) and independent of pressure. In a polar material, the dielectric electron-phonon coupling dominates because it is long-range[41], and will provide the main channel by which electrons photo-excited above bandgap will lose their energy. This coupling involves the interaction of the charge of the carriers with the transition dipole moment of the surrounding phonon modes. The variational polaron method predicts a polaron relaxation time constant of ~ 0.1 ps[42] for this material, which is consistent with our observation

of a very short HCC time. This long-range dielectric coupling is not expected to be significantly affected by pressure[43], in agreement with our observations. Above the threshold for the Mott transition, we propose that this dielectric coupling is screened, and instead the HCC proceeds via the weaker local electron-phonon coupling. We calculate that this local electron-phonon coupling is proportional to pressure over the pressure range 0-0.3 GPa (in fact we find a linear trend up until 1.0 GPa), and so the HCC above the Mott transition becomes faster with pressure. This result is related to what has been found by Mohanan et al.[44] who attributed the presence of a hot-phonon bottleneck to the deposition of a large portion of the initial energy on the optical modes at 27 $cm^{-1}$ (~0.8 THz). These do not efficiently dissipate the excess energy as they are isolated from the rest of the lattice. Our findings thus reveal that the pressure enhancement of the electron-phonon coupling can be used to manipulate HCC at densities above the Mott transition density, while having no effect in the regime below, where the long-range dielectric electron-phonon coupling dominates. The excitation density that we assign for the Mott transition comes from considering the polaron size. An alternative interpretation of the observed pressure-dependence of the cooling time could be that this Mott transition is being pushed to a higher density under pressure. This change would require that the polarons are more localised at higher pressure. In turn, within the Fröhlich theory, this would require a considerably larger dielectric electron-phonon coupling, or a considerably larger effective mass. However, we are cautious with this interpretation as the vibrational and optical properties do not change significantly over this pressure range. The hot-phonon bottleneck in $MAPbI_3$ perovskite has also been attributed to the extremely short acoustic phonon lifetime[45] of this material, which also causes its low thermal conductivity[46]. A short acoustic phonon lifetime can thus be responsible for the suppression of heat dissipation, as this energy could be reabsorbed by optical phonons and thus create a hot-phonon bottleneck that slows down the cooling of the hot electron-phonon plasma. Although this mechanism occurs in the second stage of the cooling (tens of picosecond), it might have some minor influence on the first cooling stage as well. To determine to what extent the faster HCC results only from the enhanced electron-phonon coupling or from a

combination with a longer acoustic phonon lifetime would require an expensive computation that is beyond the scope of this work.

## 3.4. Conclusion

We used pressure-dependent fs-TAS to investigate the effect of external pressure on hot-carrier cooling in $MAPbI_3$ thin films. We found that below the Mott transition threshold, the HCC time is not affected by pressure, whereas it becomes two to three times faster above Mott transition. Our calculations reveal a twofold enhancement of the electron-phonon coupling for the mode related to the octahedral twist when the pressure is increased from ambient pressure to 0.3 GPa. These findings, together with the observed difference in the behaviour in the low and high-density regime, suggest the presence of two different mechanisms dominating HCC at the two excitation densities explored. Below the Mott transition threshold, where polarons do not overlap, the long-range dielectric electron-phonon coupling dominates. Above the Mott transition threshold, this contribution is suppressed as the polarisation fields of the polarons overlap forming an electron-hole plasma and the HCC occurs via local electron-phonon coupling. This local contribution is significantly weaker at ambient pressure leading to slow HCC but increases linearly over the 0.3 GPa pressure range studied. These findings contribute to the understanding of how applied stress can be used to control the HCC time in halide-perovskite devices for emissive applications such as lasers and single-photon sources.

# 3.5. Experimental Methods

### Sample Preparation

$MAPbI_3$ precursor solution (1.05 M) is prepared by mixing MAI (TCI, >99%) and lead iodide (TCI, 99.99%, trace metals basis) in N,N-dimethylformamide (DMF, Sigma Aldrich anhydrous, ≥99%) in a 1:1 ratio. Thin films are prepared by spin coating the precursor solution at 9000rpm for 30s and the antisolvent (Chlorobenzene, Sigma Aldrich, anhydrous, ≥99%) dripped after 15s on quartz. Films are subsequentially annealed at 100 °C for 1 hour. The precursor solution preparation and spin coating are conducted in a nitrogen-filled glovebox.

### X-Ray Diffraction

The XRD pattern of perovskite films deposited on quartz was measured using an X-ray diffractometer, Bruker D2 Phaser, with Cu Kα (λ = 1.541 Å) as X-ray source, 0.01° (2θ) as the step size, and 0.100 s as the exposure time.

### Steady-State Absorption

Absorption spectra of $MAPbI_3$ films on quartz as a function of pressure were measured in a pressure cell (ISS Inc.) with a LAMBDA 750 UV/Vis/NIR Spectrophotometer (Perkin Elmer) from 550 nm to 850 nm.

### Pressure-dependent Transient Absorption

Hydrostatic pressure was generated inside a pressure cell (ISS Inc.) increasing the volume of an inert liquid (FC-72, 3M) using a manual pump. Prior using, the liquid was degassed in a Schlenk line to remove oxygen which causes, from 0.3 GPa onwards, scattering of a fraction of light and therefore a reduction of the transmitted signal from the sample. The pressure was applied from 0.3 GPa to ambient pressure in steps of 0.050 GPa. The error in the pressure reading is estimated to be 0.020 GPa. We wait 7 minutes after applying the pressures before the measurement for equilibration of the material under pressure. The transient absorption (TA) setup used for pressure-dependent measurements has been previously described in Hutter et al.[47] In addition, a reflective neutral density filter

(OD 1) is placed in the probe path, before the sample, to reduce the 800 nm residue. To avoid polarization effects, the relative polarization of the probe and pump pulses was set to the magic angle (54.6°). The pump beam (3.1 eV) and the probe beam (white light) are overlapped inside the pressure cell during the measurement and the probe spot size was chosen to be smaller than the pump spot size to obtain homogenous excitation over the probed area. A mechanical delay stage is used to change the pump-probe overlap time to follow the evolution of the hot-carrier cooling from 0.05 ps to 30 ps with a step size of 0.05 ps. To correct all spectra for the chirp of the white light, we extract the chirp from the cross-correlation measured on a bare quartz substrate, inside the pressure cell and in the same conditions as the experiments with $MAPbI_3$.

### Electron-Phonon Coupling Calculation

The reference structures at pressures 0 GPa to 1 GPa were generated with a Limited-memory Broyden–Fletcher–Goldfarb–Shanno (LBFGS) optimisation, using Perdew–Burke–Ernzerhof (PBE) exchange correlation functional with a plane-wave basis of 700 eV cut-off and a 6x6x6 Brillouin-zone integration grid. Pressure was applied in increments of 0.1 GPa. Electron-phonon couplings were then calculated by a linear combination of atomic orbitals (LCAO) method with a double-zeta basis set, in a 2x2x2 supercell of the pressurised realisations, with the PBE functional. All calculations were in Grade Point Average Weighted (GPAW)[48,49] using the Atomic Simulation Environment (ASE)[50] interface.

# 3.6. Appendix

## 3.6.1. Additional Figures

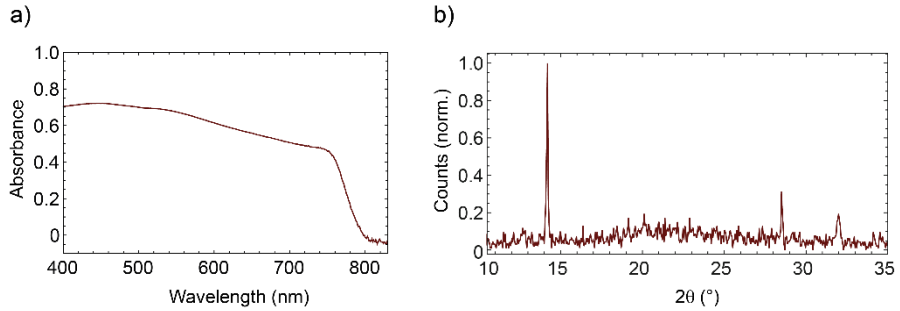


**Figure A3.1. a)** UV-Vis absorption spectrum and **b)** XRD pattern of tetragonal $MAPbI_3$ thin films

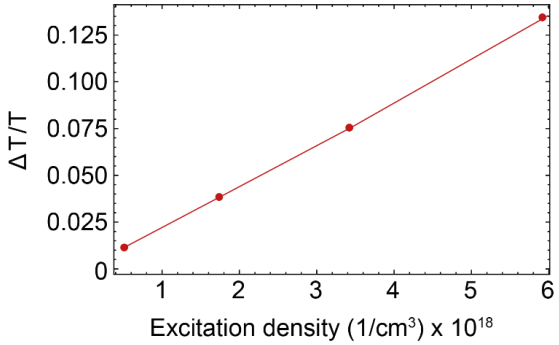


**Figure A3.2.** Δ*T*/*T* as a function of the pump excitation density confirms the investigation of the HCC mechanism in the linear regime.

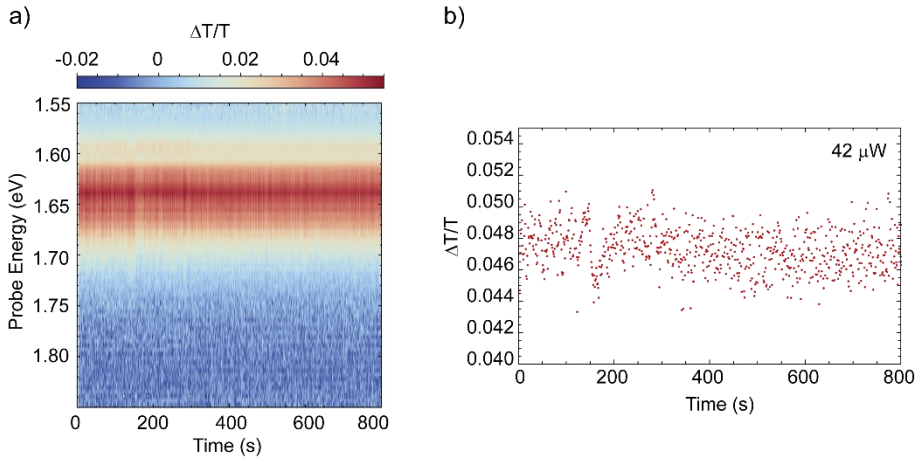


**Figure A3.3. a)** $\Delta T/T$ as a function of the probe energy at 15 ps (delay stage position) and real time for $MAPbI_3$ at ambient pressure excited at the band-edge with a fluence comparable to the high excitation density shown in main text and **b)** a cross-cut of the ground state bleach signal at 15 ps as a function of real time showing that no degradation is observed at the high excitation density used.

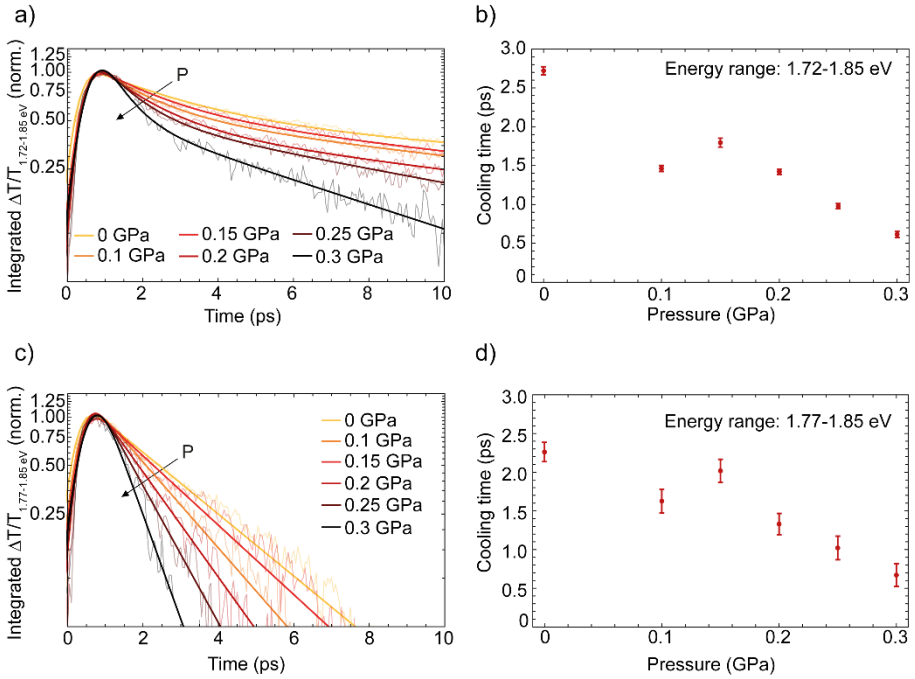


**Figure A3.4.** Normalized *ΔT/T* integrated in the range **a)** 1.72-1.85 eV and **c)** 1.77-1.85 eV in the ground state bleach tail as a function of time and pressure applied in the high-density regime. The decay of the ground state bleach tail is faster upon increasing pressure. **b)** HCC time extracted from the fit of the tail decay in the 1.72-1.85 eV and **d)** 1.77-1.85 eV energy range as a function of pressure. Changing the integrated energy range may change the absolute decay time but the trend with pressure is consistent.

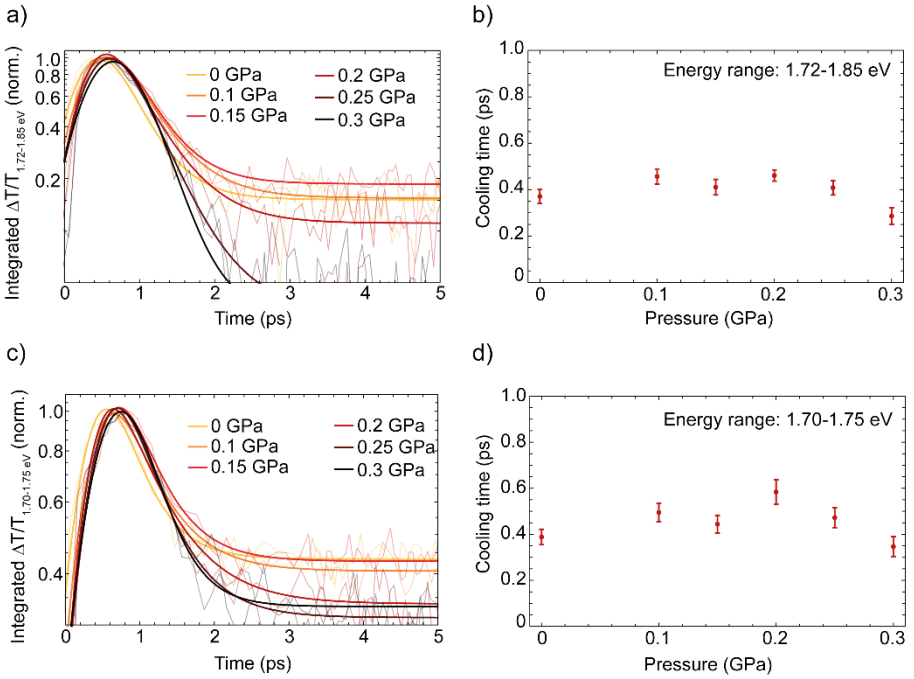


**Figure A3.5.** Normalized *ΔT/T* integrated in the range **a)** 1.72-1.85 eV and **c)** 1.70-1.75 eV in the ground state bleach tail as a function of time and pressure applied in the low-density regime. No appreciable change is observed. **b)** HCC time extracted from the fit of the tail decay in the 1.72-1.85 eV and **d)** 1.70-1.75 eV energy range. Changing the integrated energy range may change the absolute value but the trend is consistent.

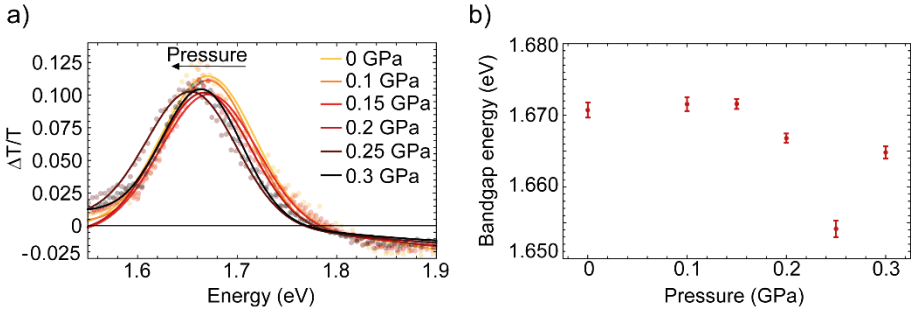


**Figure A3.6. a)** Averaged Δ*T/T* in the range of 35-38 ps as a function of the probe energy and pressure for $MAPbI_3$ and **b)** the extracted band gap from the ground state bleach as a function of pressure.

### 3.6.2. ESTIMATION OF THE CARRIER DENSITY

The pump fluence of each pulse was calculated by using the following formula

$$\#photons = \frac{P}{f \times E_{pump}} \tag{3.1}$$

Where $P$ is the pump power in Watt, $f$ is the frequency of the chopper in Herz, $E_{pump}$ is the energy of a single pump photon in Joule. The number of photons is then converted into carrier density by using the following formula

$$n_0 = \frac{\#photons \times F_A}{Area_{pump} \times d} \tag{3.2}$$

Where $F_A$ is the fraction of absorbed photons by the sample at the pump energy measured by absorption measurements, $Area_{pump}$ is the area of the pump beam in cm$^2$ and $d$ is the thickness of the film as measured by SEM cross-section in cm. The only parameter that could change as a function of pressure is $F_A$ as both the pump energy and the beam area are kept constant during the experiment. However, as reported in **Table 3.1**, the $F_A$ at the pump energy measured is constant to a value of 0.65 and therefore the excitation density as a function of pressure is constant.

**Table 3.1.** Fraction of absorbed photons calculated from pressure-dependent absorption (assuming constant reflectance increasing pressure).

| Pressure (GPa) | $F_A$ |
|---|---|
| 0 | 0.64 |
| 0.10 | 0.65 |
| 0.15 | 0.65 |
| 0.20 | 0.66 |
| 0.25 | 0.66 |
| 0.30 | 0.65 |

### 3.6.3. IRF FUNCTION AT 800 NM

The TA signal can be described by the convolution of the Instrument Response Function (IRF)

$$f_{IRF}(x) = \frac{1}{\sqrt{2\pi\sigma^2}} e^{-\frac{x^2}{2\sigma^2}} \tag{3.3}$$

and the function describing the change of the TA signal after excitation,

$$f_{ex}(x) = A\theta(x)e^{-\frac{x}{\tau}} + A_2\theta(x) \tag{3.4}$$

where $\theta$ is the Heaviside theta function. Equation 3.4 describes a signal whose height switches instantaneously from 0 to $A + A_2$ at time 0 and that then decays exponentially to the value $A_2$ with a time constant $\tau$ representing the HCC time. The convolution integral of the IRF function and an exponential decay after a step function can be written as

$$\begin{aligned}(f_{IRF} * f_{ex})(y) = \frac{A}{2} e^{\frac{\sigma^2}{2\tau^2} - \frac{y}{\tau}} \left[1 + \operatorname{erf}\left(\frac{y}{\sqrt{2}\sigma} - \frac{\sigma}{\sqrt{2}\tau}\right)\right] \\ + \frac{1}{2}\left(1 + \operatorname{erf}\left(\frac{y}{\sqrt{2}\sigma}\right)\right) A_2\end{aligned} \tag{3.5}$$

We obtain the standard deviation $\sigma$ of the IRF by fitting the time-dependence of the band-edge signal for resonantly excited $MAPbI_3$, where no carrier cooling is expected, and the rise time is limited by the IRF. To fit the below-bandgap signal we neglect any HCC effect. The $\sigma$ obtained is shown in **Figure A3.7** and does not change significantly as a function of pressure. We then fixed $\sigma$ to the value obtained for resonant excitation and fitted the TA curves of $MAPbI_3$ excited with 3.1 eV in the low- and high-density regime, optimizing the fit for HCC time $\tau$.

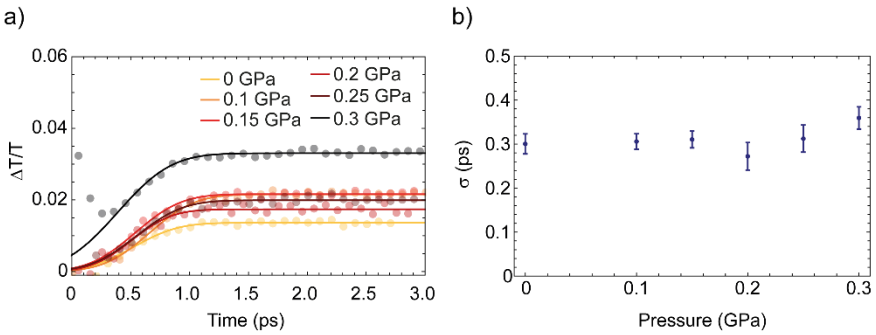


**Figure A3.7. a)** *ΔT/T* traces at 1.59 eV (below bandgap) as a function of pressure and **b)** the resulting IRF extracted by fitting a rise function, $\frac{1}{2}\mathrm{A}\left(1+\mathrm{erf}\left[\frac{\mathrm{t0}+x}{\sqrt{2}\sigma}\right]\right)$, to the curves.

### 3.6.4. MAXWELL-BOLTZMANN FIT FUNCTION

Following Yang et al.[12], the modified Maxwell–Boltzmann distribution function used for the second fitting strategy is

$$f_{MB}(x) = \frac{A_1}{x}\sqrt{x - E_g}\, Exp^{\left(-\frac{x-E_f}{2\,k\,T_c}\right)} + \frac{A_2}{\sqrt{x - E_g}} \tag{3.6}$$

Here, $A_1$ and $A_2$ represent the amplitudes of the band-filling and bandgap renormalization components, $k$ is the Boltzmann constant, $E_g$ is the bandgap energy as calculated from the fit of the GSB as a function of pressure at later times when the HCC is completed (**Figure A3.6**), $E_f$ is the electron (and holes) quasi-Fermi level, and $x$ is the energy. We approximate $E_f$ as $E_g$ and obtain the values of $A_1$, $A_2$ and $T_c$ from the fit. The second term of this fitting function is included to fit the negative feature originating from hot carrier induced bandgap reduction. We perform this fitting method on the same data. To probe the same population of hot carriers at all pressures conditions, the selected starting energy of the fit is the one corresponding to 1/2 of the maximum bleach. To ensure to probe the hot-carrier population after thermalization (but before HCC is finished), we only consider the data starting from 0.5 ps after photoexcitation.

# 3.7. References


(1) Richter, J. M.; Branchi, F.; Valduga de Almeida Camargo, F.; Zhao, B.; Friend, R. H.; Cerullo, G.; Deschler, F. Ultrafast Carrier Thermalization in Lead Iodide Perovskite Probed with Two-Dimensional Electronic Spectroscopy. *Nat. Commun.* **2017**, *8* (1), 376. https://doi.org/10.1038/s41467-017-00546-z.

(2) Shah, J. *Ultrafast Spectroscopy of Semiconductors and Semiconductor Nanostructures*; **1999**, Springer.

(3) Fu, J.; Xu, Q.; Han, G.; Wu, B.; Huan, C. H. A.; Leek, M. L.; Sum, T. C. Hot Carrier Cooling Mechanisms in Halide Perovskites. *Nat. Commun.* **2017**, *8* (1). https://doi.org/10.1038/s41467-017-01360-3.

(4) Ziaja, B.; Medvedev, N.; Tkachenko, V.; Maltezopoulos, T.; Wurth, W. Time-Resolved Observation of Band-Gap Shrinking and Electron-Lattice Thermalization within X-Ray Excited Gallium Arsenide. *Sci. Rep.* **2015**, *5* (18068). https://doi.org/10.1038/srep18068.

(5) Polman, A.; Atwater, H. A. Photonic Design Principles for Ultrahigh-Efficiency Photovoltaics. *Nat. Mater.* **2012**, *11* (174). https://doi.org/10.1038/nmat3263.

(6) Alharbi, F. H.; Kais, S. Theoretical Limits of Photovoltaics Efficiency and Possible Improvements by Intuitive Approaches Learned from Photosynthesis and Quantum Coherence. *Renewable and Sustainable Energy Reviews*. **2015**, 43. https://doi.org/10.1016/j.rser.2014.11.101.

(7) Haque, M. A.; Kee, S.; Villalva, D. R.; Ong, W. L.; Baran, D. Halide Perovskites: Thermal Transport and Prospects for Thermoelectricity. *Advanced Science*. **2020**, *7*. https://doi.org/10.1002/advs.201903389.

(8) Kahmann, S.; Loi, M. A. Hot Carrier Solar Cells and the Potential of Perovskites for Breaking the Shockley-Queisser Limit. *Journal of Materials Chemistry C*. **2019**, *7*. https://doi.org/10.1039/c8tc04641g.

(9) Fehse, R.; Tomić, S.; Adams, A. R.; Sweeney, S. J.; O'Reilly, E. P.; Andreev, A.; Riechert, H. A Quantitative Study of Radiative, Auger, and Defect Related Recombination Processes in 1.3-Mm GaInNAs-Based Quantum-Well Lasers. *IEEE J. Sel. Top. Quantum Electron.* **2002**, *8* (4). https://doi.org/10.1109/JSTQE.2002.801684.

(10) Kim, J. H.; Ko, Y. H.; Gong, S. H.; Ko, S. M.; Cho, Y. H. Ultrafast Single Photon Emitting Quantum Photonic Structures Based on a Nano-Obelisk. *Sci. Rep.* **2013**, *3*. https://doi.org/10.1038/srep02150.

(11) Wang, C. Y.; Liu, M.; Feng, M.; Holonyak, N. Microwave Extraction Method of Radiative Recombination and Photon Lifetimes up to 85 °C on 50 Gb/s Oxide-Vertical Cavity Surface Emitting Laser. *J. Appl. Phys.* **2016**. https://doi.org/10.1063/1.4971978.

(12) Yang, Y.; Ostrowski, D. P.; France, R. M.; Zhu, K.; Van De Lagemaat, J.; Luther, J. M.; Beard, M. C. Observation of a Hot-Phonon Bottleneck in

Lead-Iodide Perovskites. *Nat. Photonics.* **2016**, *10*. https://doi.org/10.1038/nphoton.2015.213.

(13) Verma, S. D.; Gu, Q.; Sadhanala, A.; Venugopalan, V.; Rao, A. Slow Carrier Cooling in Hybrid Pb-Sn Halide Perovskites. *ACS Energy Lett.* **2019**, *4* (3). https://doi.org/10.1021/acsenergylett.9b00251.

(14) Yang, J.; Wen, X.; Xia, H.; Sheng, R.; Ma, Q.; Kim, J.; Tapping, P.; Harada, T.; Kee, T. W.; Huang, F.; et al. Acoustic-Optical Phonon up-Conversion and Hot-Phonon Bottleneck in Lead-Halide Perovskites. *Nat. Commun.* **2017**, *8* (1). https://doi.org/10.1038/ncomms14120.

(15) Wen, Y. C.; Chen, C. Y.; Shen, C. H.; Gwo, S.; Sun, C. K. Ultrafast Carrier Thermalization in InN. *Appl. Phys. Lett.* **2006**, *89*. https://doi.org/10.1063/1.2402899.

(16) Price, M. B.; Butkus, J.; Jellicoe, T. C.; Sadhanala, A.; Briane, A.; Halpert, J. E.; Broch, K.; Hodgkiss, J. M.; Friend, R. H.; Deschler, F. Hot-Carrier Cooling and Photoinduced Refractive Index Changes in Organic-Inorganic Lead Halide Perovskites. *Nat. Commun.* **2015**, *6* (8420). https://doi.org/10.1038/ncomms9420.

(17) Chen, J.; E. Messing, M.; Zheng, K.; Pullerits, T. Cation-Dependent Hot Carrier Cooling in Halide Perovskite Nanocrystals. *J. Am. Chem. Soc.* **2019**, *141* (8). https://doi.org/10.1021/jacs.8b11867.

(18) Shi, H.; Zhang, X.; Sun, X.; Zhang, X. Strong Hot-Phonon Bottleneck Effect in All-Inorganic Perovskite Nanocrystals. *Appl. Phys. Lett.* **2020**, *116* (15). https://doi.org/10.1063/1.5145261.

(19) Hopper, T. R.; Gorodetsky, A.; M. Frost, J.; Müller, C.; Lovrincic, R.; A. Bakulin, A. Ultrafast Intraband Spectroscopy of Hot-Carrier Cooling in Lead-Halide Perovskites. *ACS Energy Lett.* **2018**, *3* (9). https://doi.org/10.1021/acsenergylett.8b01227.

(20) Bretschneider, S. A.; Ivanov, I.; Wang, H. I.; Miyata, K.; Zhu, X.; Bonn, M. Quantifying Polaron Formation and Charge Carrier Cooling in Lead-Iodide Perovskites. *Adv. Mater.* **2018**, *30* (29). https://doi.org/10.1002/adma.201707312.

(21) Frost, J. M.; Whalley, L. D.; Walsh, A. Slow Cooling of Hot Polarons in Halide Perovskite Solar Cells. *ACS Energy Lett.* **2017**, *2* (12). https://doi.org/10.1021/acsenergylett.7b00862.

(22) Sendner, M.; Nayak, P. K.; Egger, D. A.; Beck, S.; Müller, C.; Epding, B.; Kowalsky, W.; Kronik, L.; Snaith, H. J.; Pucci, A.; et al. Optical Phonons in Methylammonium Lead Halide Perovskites and Implications for Charge Transport. *Mater. Horiz.* **2016**, *3* (6). https://doi.org/10.1039/c6mh00275g.

(23) Price, M. B.; Butkus, J.; Jellicoe, T. C.; Sadhanala, A.; Briane, A.; Halpert, J. E.; Broch, K.; Hodgkiss, J. M.; Friend, R. H.; Deschler, F. Hot-Carrier Cooling and Photoinduced Refractive Index Changes in Organic-Inorganic Lead Halide Perovskites. *Nat. Commun.* **2015**, *6*.

https://doi.org/10.1038/ncomms9420.

(24) Li, M.; Bhaumik, S.; Goh, T. W.; Kumar, M. S.; Yantara, N.; Grätzel, M.; Mhaisalkar, S.; Mathews, N.; Sum, T. C. Slow Cooling and Highly Efficient Extraction of Hot Carriers in Colloidal Perovskite Nanocrystals. *Nat. Commun.* **2017**, *8* (1). https://doi.org/10.1038/ncomms14350.

(25) Li, B.; Kawakita, Y.; Liu, Y.; Wang, M.; Matsuura, M.; Shibata, K.; Ohira-Kawamura, S.; Yamada, T.; Lin, S.; Nakajima, K.; et al. Polar Rotor Scattering as Atomic-Level Origin of Low Mobility and Thermal Conductivity of Perovskite $CH_3NH_3PbI_3$. *Nat. Commun.* **2017**, *8*. https://doi.org/10.1038/ncomms16086.

(26) Beecher, A. N.; Semonin, O. E.; Skelton, J. M.; Frost, J. M.; Terban, M. W.; Zhai, H.; Alatas, A.; Owen, J. S.; Walsh, A.; Billinge, S. J. L. Direct Observation of Dynamic Symmetry Breaking above Room Temperature in Methylammonium Lead Iodide Perovskite. *ACS Energy Lett* .**2016**, *1* (4). https://doi.org/10.1021/acsenergylett.6b00381.

(27) Nolas, G. S.; Goldsmid, H. J. Thermal Conductivity of Semiconductors. *Thermal Conductivity*; **2006**. https://doi.org/10.1007/0-387-26017-x_4.

(28) Giorgi, G.; Fujisawa, J. I.; Segawa, H.; Yamashita, K. Small Photocarrier Effective Masses Featuring Ambipolar Transport in Methylammonium Lead Iodide Perovskite: A Density Functional Analysis. *J. Phys. Chem. Lett.* **2013**, *4* (24). https://doi.org/10.1021/jz4023865.

(29) Lim, J. W. M.; Giovanni, D.; Righetto, M.; Feng, M.; Mhaisalkar, S. G.; Mathews, N.; Sum, T. C. Hot Carriers in Halide Perovskites: How Hot Truly? *J. Phys. Chem. Lett.* **2020**, *11* (7). https://doi.org/10.1021/acs.jpclett.0c00504.

(30) Senellart, P.; Solomon, G.; White, A. High-Performance Semiconductor Quantum-Dot Single-Photon Sources. *Nature Nanotechnology*. **2017**, *12*. https://doi.org/10.1038/nnano.2017.218.

(31) Savill, K. J.; Klug, M. T.; Milot, R. L.; Snaith, H. J.; Herz, L. M. Charge-Carrier Cooling and Polarization Memory Loss in Formamidinium Tin Triiodide. *J. Phys. Chem. Lett.* **2019**, *10* (20). https://doi.org/10.1021/acs.jpclett.9b02353.

(32) Von Der Linde, D.; Lambrich, R. Direct Measurement of Hot-Electron Relaxation by Picosecond Spectroscopy. *Phys. Rev. Lett.* **1979**, *42*. https://doi.org/10.1103/PhysRevLett.42.1090.

(33) Zanato, D.; Balkan, N.; Ridley, B. K.; Hill, G.; Schaff, W. J. Hot Electron Cooling Rates via the Emission of LO-Phonons in InN. *Semicond. Sci. Technol.* **2004**, *19*. https://doi.org/10.1088/0268-1242/19/8/013.

(34) Kawai, H.; Giorgi, G.; Marini, A.; Yamashita, K. The Mechanism of Slow Hot-Hole Cooling in Lead-Iodide Perovskite: First-Principles Calculation on Carrier Lifetime from Electron–Phonon Interaction. *Nano Lett.* **2015**, *15* (5). https://doi.org/10.1021/acs.nanolett.5b00109.

(35) Szafrański, M.; Katrusiak, A. Mechanism of Pressure-Induced Phase

Transitions, Amorphization, and Absorption-Edge Shift in Photovoltaic Methylammonium Lead Iodide. *J. Phys. Chem. Lett.* **2016**, *7* (17). https://doi.org/10.1021/acs.jpclett.6b01648.

(36) Walsh, A.; Brivio, F.; Frost, J. M. WMD-Group/Hybrid-Perovskites. **2019**. https://doi.org/10.5281/ZENODO.2641358.

(37) Pérez-Osorio, M. A.; Milot, R. L.; Filip, M. R.; Patel, J. B.; Herz, L. M.; Johnston, M. B.; Giustino, F. Vibrational Properties of the Organic-Inorganic Halide Perovskite $CH_3NH_3PbI_3$ from Theory and Experiment: Factor Group Analysis, First-Principles Calculations, and Low-Temperature Infrared Spectra. *J. Phys. Chem. C* **2015**, *119* (46). https://doi.org/10.1021/acs.jpcc.5b07432.

(38) Leguy, A. M. A.; Goñi, A. R.; Frost, J. M.; Skelton, J.; Brivio, F.; Rodríguez-Martínez, X.; Weber, O. J.; Pallipurath, A.; Alonso, M. I.; Campoy-Quiles, M.; et al. Dynamic Disorder, Phonon Lifetimes, and the Assignment of Modes to the Vibrational Spectra of Methylammonium Lead Halide Perovskites. *Phys. Chem. Chem. Phys.* **2016**, *18* (39). https://doi.org/10.1039/c6cp03474h.

(39) Guo, P.; Xia, Y.; Gong, J.; Cao, D. H.; Li, X.; Li, X.; Zhang, Q.; Stoumpos, C. C.; Kirschner, M. S.; Wen, H.; et al. Direct Observation of Bandgap Oscillations Induced by Optical Phonons in Hybrid Lead Iodide Perovskites. *Adv. Funct. Mater.* **2020**, *30* (22). https://doi.org/10.1002/adfm.201907982.

(40) Park, M.; Neukirch, A. J.; Reyes-Lillo, S. E.; Lai, M.; Ellis, S. R.; Dietze, D.; Neaton, J. B.; Yang, P.; Tretiak, S.; Mathies, R. A. Excited-State Vibrational Dynamics toward the Polaron in Methylammonium Lead Iodide Perovskite. *Nat. Commun.* **2018**, *9* (1). https://doi.org/10.1038/s41467-018-04946-7.

(41) Giustino, F. Electron-Phonon Interactions from First Principles. *Rev. Mod. Phys.* **2017**. *89* (1). https://doi.org/10.1103/RevModPhys.89.015003.

(42) Frost, J. M. Calculating Polaron Mobility in Halide Perovskites. *Phys. Rev. B* **2017**, *96* (19). https://doi.org/10.1103/PhysRevB.96.195202.

(43) Francisco-López, A.; Charles, B.; Weber, O. J.; Alonso, M. I.; Garriga, M.; Campoy-Quiles, M.; Weller, M. T.; Goñi, A. R. Pressure-Induced Locking of Methylammonium Cations versus Amorphization in Hybrid Lead Iodide Perovskites. *J. Phys. Chem. C* **2018**, *122* (38). https://doi.org/10.1021/acs.jpcc.8b05188.

(44) Monahan, D. M.; Guo, L.; Lin, J.; Dou, L.; Yang, P.; Fleming, G. R. Room-Temperature Coherent Optical Phonon in 2D Electronic Spectra of CH3NH3PbI3 Perovskite as a Possible Cooling Bottleneck. *J. Phys. Chem. Lett.* **2017**, *8* (14). https://doi.org/10.1021/acs.jpclett.7b01357.

(45) Gold-Parker, A.; Gehring, P. M.; Skelton, J. M.; Smith, I. C.; Parshall, D.; Frost, J. M.; Karunadasa, H. I.; Walsh, A.; Toney, M. F. Acoustic Phonon

Lifetimes Limit Thermal Transport in Methylammonium Lead Iodide. *Proc. Natl. Acad. Sci. U. S. A.* **2018**, *115* (47). https://doi.org/10.1073/pnas.1812227115.

(46) Pisoni, A.; Jaćimović, J.; Barišić, O. S.; Spina, M.; Gaál, R.; Forró, L.; Horváth, E. Ultra-Low Thermal Conductivity in Organic-Inorganic Hybrid Perovskite $CH_3NH_3PbI_3$. *J. Phys. Chem. Lett.* **2014**, *5* (14). https://doi.org/10.1021/jz5012109.

(47) Hutter, E. M.; Muscarella, L. A.; Wittmann, F.; Versluis, J.; McGovern, L.; Bakker, H. J.; Woo, Y.-W.; Jung, Y.-K.; Walsh, A.; Ehrler, B. Thermodynamic Stabilization of Mixed-Halide Perovskites against Phase Segregation. *Cell Reports Phys. Sci.* **2020**. https://doi.org/10.1016/j.xcrp.2020.100120.

(48) Mortensen, J. J.; Hansen, L. B.; Jacobsen, K. W. Real-Space Grid Implementation of the Projector Augmented Wave Method. *Phys. Rev. B. Condens. Matter Mater. Phys.* **2005**, *71* (3). https://doi.org/10.1103/PhysRevB.71.035109.

(49) Enkovaara, J.; Rostgaard, C.; Mortensen, J. J.; Chen, J.; Dułak, M.; Ferrighi, L.; Gavnholt, J.; Glinsvad, C.; Haikola, V.; Hansen, H. A.; et al. Electronic Structure Calculations with GPAW: A Real-Space Implementation of the Projector Augmented-Wave Method. *Journal of Physics Condensed Matter*. **2010**, *22*. https://doi.org/10.1088/0953-8984/22/25/253202.

(50) Hjorth Larsen, A.; JØrgen Mortensen, J.; Blomqvist, J.; Castelli, I. E.; Christensen, R.; Dułak, M.; Friis, J.; Groves, M. N.; Hammer, B.; Hargus, C.; et al. The Atomic Simulation Environment - A Python Library for Working with Atoms. *Journal of Physics Condensed Matter*. **2017**, *29*. https://doi.org/10.1088/1361-648X/aa680e.

# 4. Pressure-dependent Manipulation of Phase Segregation

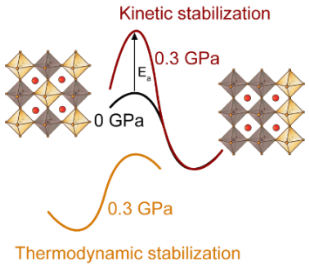


The easy bandgap tunability of mixed-halide perovskites makes them promising candidates for LEDs and tandem solar cells. However, illuminating mixed-halide perovskites leads to the formation of segregated phases enriched in a single-halide. This segregation occurs through ion migration and its control is essential for the long-term stability of the devices. Using pressure-dependent transient absorption spectroscopy, we find that the formation rates of both iodide- and bromide-rich phases in $MAPb(Br_xI_{1-x})_3$ ($x$ = 0.25, 0.5, 0.7) reduce by 2 orders of magnitude upon increasing the pressure to 0.3 GPa. At high pressure, we find that the segregation is also almost suppressed, as indicated by the energy of the final phase that is very similar to the mixed phase. A similar mechanism occurs when the unit cell volume is reduced by incorporating a smaller cation (*e.g.* $Cs^+$). These findings reveal that external pressure can manipulate both the kinetics and thermodynamics of the phase segregation and this stability with respect to halide segregation can be achieved either physically through compressive stress or chemically through compositional engineering.

*This chapter is based on the following publications:*

L.A. Muscarella, E.M. Hutter, F. Wittmann, Y.W. Woo, Y.-K. Jung, L. McGovern, J. Versluis, A. Walsh, H.J. Bakker and B. Ehrler, Lattice Compression Increases the Activation Barrier for Phase Segregation in Mixed-Halide Perovskites, *ACS Energy Letters*, 2020, 5 (10), 3152-3158

E.M. Hutter, L.A. Muscarella, F. Wittmann, J. Versluis, L. McGovern, H.J. Bakker, Y.W. Woo, Y.-K. Jung, A. Walsh and B. Ehrler, Thermodynamic Stabilization of Mixed-Halide Perovskites against Phase Segregation, *Cell Rep. Phys. Sci.,* 2020, 1 (8), 100120, 1-11

# 4.1. Introduction

In **Chapter 1.3** we have discussed the characteristic softness of the perovskite lattice and how the relatively weak covalent-ionic bond nature can cause the so-called *ion migration* process. This process consists in the migration of the halide or the organic cation species within the perovskite lattice compromising the long-term stability of the associated devices[1]. For mixed-halide perovskites, halide migration[2] during continuous light exposure[3] or applied bias[4] leads to *phase segregation* where domains enriched in one of the halides are formed.

The bandgap of mixed-halide perovskites can easily be tuned by mixing halides in different ratio[5]. For instance, mixing iodide and bromide in $MAPb(Br_xI_{1-x})_3$ (with MA = methylammonium, $CH_3NH_3^+$) results in bandgaps in between that of full iodide ($x = 0$, 1.6 eV) and full bromide perovskites ($x = 1$, 2.3 eV).[6,7] The easy fabrication of compositions with the desired bandgap makes the mixed-halide perovskites promising candidates for light emitting diodes (LEDs)[8,9] and tandem solar cells[10]. However, methylammonium(MA)-based mixed-halide perovskites, $MAPb(Br_xI_{1-x})_3$, with $x > 0.20$ lack long-term bandgap stability under standard solar cell operating conditions[11] because these compositions have been shown to suffer from phase segregation[2]. As a result of continuous light exposure, low- and high-bandgap phases are formed within the mixed composition. The low- and high-bandgap phases correspond to iodide-rich and bromide-rich domains[2]. Phase segregation affects the homogeneity of the bandgap required for many applications such as lighting and displays as the photogenerated charges transfer into the low-bandgap iodide-rich domains, where they recombine.

The activation energies reported for halide migration in single-halide systems[12,13] and in mixed-halide systems[2,13] are comparable, suggesting a similar transport mechanism in both cases. Therefore, both single- and mixed-halide perovskites would benefit from increasing the activation energies for ion migration, as this would slow down the degradation rate and hence increase the lifetime of the corresponding device. For commercial purposes, a long-term stability of 20 years may not be possible with kinetic stabilization only, as this would require a five order of magnitude lower segregation rate[14] or an order of

magnitude higher activation energy. Therefore, understanding how to manipulate the segregation rate to a substantial extent and push toward a thermodynamic stabilization route would be the key to obtain long-term stability in devices.

Phase segregation has been shown to depend on various factors such as light intensity[13,15,16], duty cycle[17], and film quality and thickness[16,18]. Reducing the halide vacancy concentrations[19] and passivating electron traps[20] whose electric field has been proposed to initiate halide migration by accumulating holes, have been suggested as ways to reduce the rate of phase segregation. Slower phase segregation rate has also been achieved by partial replacement of the organic cation with the smaller $Cs^+$ in the mixed-perovskite[21–24].

In this Chapter, we investigate how the kinetics and thermodynamics of phase segregation can be manipulated upon compressing the unit cell volume by increasing physical pressure in mixed-halide perovskite $MAPb(Br_xI_{1-x})_3$. We use pressure-dependent transient absorption spectroscopy, previously introduced in **Chapter 1.6**. The measurements are performed at hydrostatic pressures ranging from 0 (ambient pressure) to 0.3 GPa using an additional light beam to induce phase segregation. We find that phase segregation is substantially slower at high pressure for all $MAPb(Br_xI_{1-x})_3$ mixing ratios ($x$ = 0.25, 0.5 and 0.7). We explain this reduction in the phase segregation rate by the increase of the activation energy ($E_a$, in light) for halide migration upon compression of the unit cell volume. Theoretical calculations corroborate this interpretation, revealing an increase in the energy barrier required for a halide species to diffuse into a vacancy under pressure. In addition, we find that the reduction of the unit cell volume at ambient pressure by partial replacement of the $MA^+$ cation with the smaller $Cs^+$, (*e.g.* $MA_{0.7}Cs_{0.3}Pb(Br_{0.5}I_{0.5})_3$ and $CsPb(Br_{0.5}I_{0.5})_3$), also leads to slower segregation, in a similar manner to the reduced segregation rate of $MAPb(Br_{0.5}I_{0.5})_3$ under high-pressure conditions. Surprisingly, we find that increasing pressure, the final mixing ratio of the segregated phases is closer to the one of the initial mixed-phase ratio, suggesting that pressure changes the thermodynamic landscape for phase segregation. This finding can be understood from a change in the thermodynamics (Gibbs free energy) as a function of pressure, paving a route to obtain mixed-halide perovskites stable against phase segregation regardless of their initial halide mixing ratio. Altogether, these

findings suggest that the reduction of the unit cell volume, achieved through compositional engineering or physical pressure, can be effectively used to delay halide migration by increasing the activation barrier of the halide migration process and push toward a thermodynamic stabilization.

## 4.2. Pressure-dependent Phase Segregation

MAPb($Br_xI_{1-x}$)$_3$ thin films with $x$ = 0, 0.25, 0.5, 0.7 and 1 were prepared by spin coating the precursor solutions onto quartz substrates as reported in the **Experimental Methods 4.6**. Absorption measurements and X-ray diffraction patterns are collected to confirm the successful fabrication of mixed-halide perovskites film as reported in **Figure A4.1**. To further confirm whether the desired halide mixing ratio was achieved after the fabrication, we performed elemental analysis using SEM/EDS and the results are reported in **Table 4.1**. The EDS analysis show a slight deficit of bromide in the case of the $x$ = 0.5 sample and a slight excess of bromide for the $x$ = 0.7. Overall, the real composition slightly differs from the stoichiometric one. We use the stoichiometric composition to label our samples throughout the entire chapter.

**Table 4.1.** Stoichiometric Br fraction $x$ compared to the real Br fraction incorporated in the mixed-halide films after fabrication.

| Stoichiometric $Br^-$ fraction ($x$) | Real $Br^-$ fraction (EDS) |
|---|---|
| 0.25 | 0.25±0.02 |
| 0.50 | 0.45±0.03 |
| 0.70 | 0.74±0.03 |

Transient absorption spectroscopy (TAS) allows us to probe the excited state of MAPb($Br_xI_{1-x}$)$_3$ by recording absorption spectra of the probed area at each delay time (from 0.05 ps to 800 ps) following a pulsed pump excitation (400 nm, with excitation density of ~$10^{18}$ absorbed photons/$cm^3$ corrected for the fraction of absorbed photons by each composition). **Figure 4.1a** shows a 2D plot of the $\Delta T/T$ signal of MAPb($Br_{0.5}I_{0.5}$)$_3$ as a function of the delay time between pump and probe and the probe pulse energy. In absence of an additional light-source,

$MAPb(Br_{0.5}I_{0.5})_3$ shows a ground state bleach at (2.08±0.01) eV in agreement with the onset obtained from steady-state absorption measurements reported in **Figure A4.1** at ambient pressure. We then focus a continuous wave (CW) light source ($\lambda$ = 405 nm, $I = 2.37 \times 10^3$ mW/cm$^2$) on the pump spot to induce phase segregation. In **Figure 4.1b** we show the 2D plot of $MAPb(Br_{0.5}I_{0.5})_3$ after 20 minutes of light-soaking, when the phase segregation is complete.

Here, we observe two bleaching signals, one at (1.88 ± 0.01) eV and one at higher energy (2.12 ± 0.003) eV compared to the initial bleach attributed to the mixed phase. These two features can be assigned to iodide- and bromide-rich domains, respectively. At later times, the bleaching signal from the bromide-rich phase decays, indicating the transfer of photogenerated charges into the iodide-rich phase. To investigate the phase segregation in $MAPb(Br_{0.5}I_{0.5})_3$ during light-soaking, we fixed the delay stage position at 15 ps, after most of the hot charge carriers induced by the high-energy pump have cooled[25,26] to the band edges of the high- and low-energy phases.

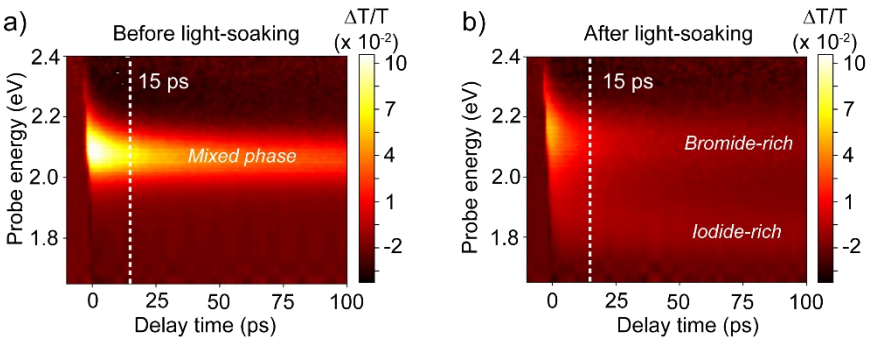


**Figure 4.1.** *Transient absorption to probe the segregated domains at ambient pressure.* **a)** $\Delta T/T$ as a function of the probe energy and delay time between the pump and probe pulse for $MAPb(Br_{0.5}I_{0.5})_3$ before light-soaking where only the bleach from the mixed-halide composition ($x$ = 0.5) is observed and **b)** after 20 minutes of light-soaking with a CW-laser where a bleach from two phases peaking at 1.88 eV and 2.12 eV are observed, indicative of halide segregation. The measurements are performed at ambient pressure. The dashed lines indicate the delay time chosen to study the evolution of phase segregation.

In **Chapter 3**, the hot-carrier cooling time at an excitation density of ~$10^{18}$ photons/$cm^3$ was found to be ~ 3ps for $MAPbI_3$. $MAPbI_3$ is the composition with the largest excess of energy generated after photo-excitation at 400 nm, thus we expect a faster cooling time for mixed-halide compositions where the excess of energy is lower. An important advantage of TAS with respect to time-resolved photoluminescence (TRPL) is the ability to track the excited population from both the iodide- and bromide-rich phase[15], whereas TRPL mainly probes the emissive low-energy phase.

We record $\Delta T/T$ spectra every second for 20 minutes. When only the pump excitation is present, we do not observe any phase segregation (see **Figure A4.2**) and the positive GSB feature peaking at (2.08±0.01) eV corresponds to the ground state bleach of the mixed iodide-bromide perovskite phase. When the mixed-halide perovskite film is irradiated by a CW laser at ambient pressure, we observe the appearance of a second feature at lower energy peaking at (1.88 ± 0.01) eV almost immediately, which subsequently grows in amplitude.

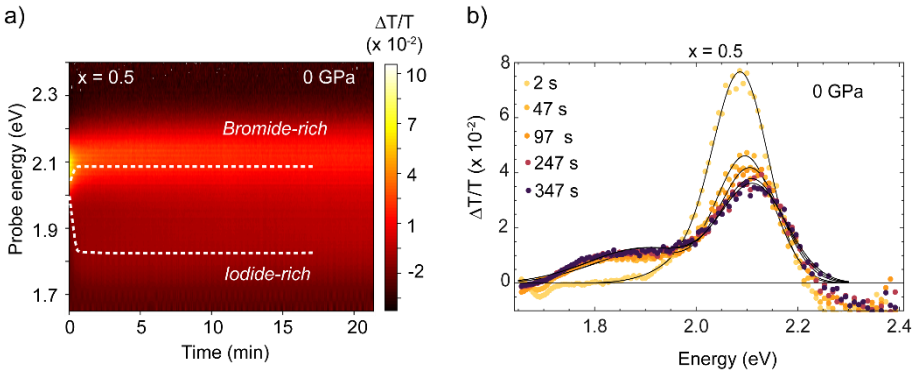


**Figure 4.2.** *Transient absorption in real time to probe phase segregation.* **a)** *ΔT/T* as a function of the probe energy and real time (minutes) at a pump-probe delay of 15 ps for $MAPb(Br_{0.5}I_{0.5})_3$ during light-soaking where both the iodide- and the bromide-rich domains is visible from early times after illumination. **b)** Cross-cut of the measured *ΔT/T* at 2, 47, 97, 247 and 347 s (from light to dark color) showing the reduction and the blue-shift of the initial peak attributed to the mixed-halide phase and the growth of the iodide-rich peak.

At the same time, the initial bleach shifts to higher energy peaking at (2.12 ± 0.003) eV and reduces in amplitude. The evolution of the ΔT/T as a function of time in minutes at ambient pressure is shown in **Figure 4.2a** as 2D plot and the growth of the amplitude of the low-energy peak is highlighted in the cross-cut at different times in **Figure 4.2b**. When the light-soaking is complete, two positive features are present in the *ΔT/T* spectrum, indicating the presence of an iodide-rich and bromide-rich domain with bandgaps of 1.88 and 2.12 eV, respectively. Subsequently, we investigated the phase segregation as a function of compressive stress induced by external pressure which reduces the unit cell size. We first calculate the change in the unit cell volume for each composition by fitting the pressure-dependent unit cell volume extracted from Jaffe et al.[27] for $x = 0$, 0.2 0.6 and 1 (**Figure 4.3a-d**) to the second-order Birch-Murnaghan[28] equation as following

$$P = \frac{3}{2} K_{T0} \left[ \left( \frac{V_0}{V} \right)^{\frac{7}{3}} - \left( \frac{V_0}{V} \right)^{\frac{5}{3}} \right] \tag{4.1}$$

where $K_{T0}$ is the isothermal bulk modulus at standard temperature, $V_0$ is the initial volume, $V$ is the volume at pressure $P$. Then, the bulk moduli for the mixed-halide perovskites $B(x)$ are calculated according[29] to

$$B(x) = \frac{(1-x) a_I B_I + (x) a_{Br} B_{Br}}{a_x} \tag{4.2}$$

where $a_I$ and $a_{Br}$ are the lattice parameters and $B_I$ and $B_{Br}$ the bulk moduli of $MAPbI_3$ and $MAPbBr_3$, respectively. The lattice parameter as function of $x$ is determined from the XRD measurements shown in **Figure A4.1b**. The calculated bulk moduli are shown in **Figure 4.3e**. From ambient pressure to 0.3 GPa, the unit cell volume change is about 3% for $x = 0.25$, 2.5% for $x = 0.5$ and 2.2% for $x = 0.7$ indicating higher compressibility for compositions with higher content of iodide.

In addition, **Figure 4.3f** shows that the lattice mismatch between the full $MAPbI_3$ and $MAPbBr_3$ decreases with pressure.

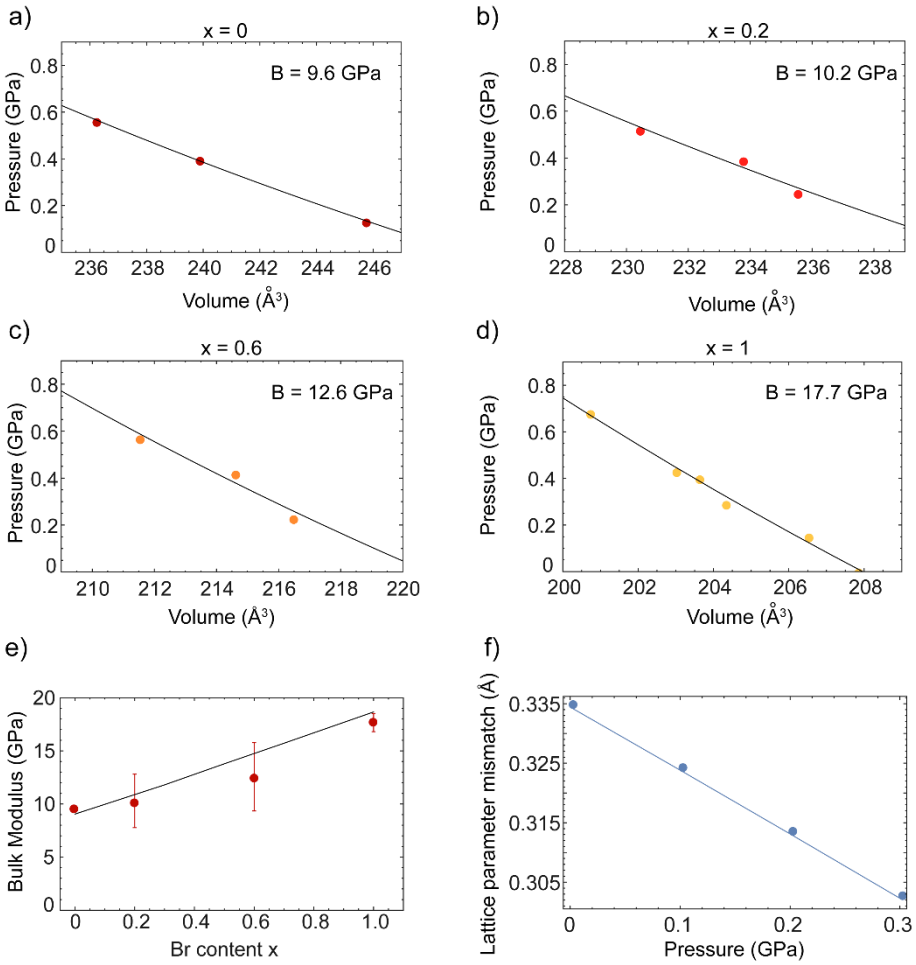


**Figure 4.3.** *Bulk moduli in mixed-halide perovskites*. **a-d)** *P-V* relation as a function of pressure adapted from Jaffe et al.[27] and the resulting bulk moduli obtained from the second-order Birch-Murnaghan equation in the inset. The error on the fit is displayed in (e). **e)** Fit to obtain the bulk moduli for the mixed-halide perovskites as a function of *x*. **f)** Lattice parameter mismatch between pure $MAPbI_3$ and $MAPbBr_3$ as a function of pressure.

Now that the change in the unit cell volume induced by external pressure is known, we perform pressure-dependent transient absorption measurement of the

sample with $x = 0.5$ inside a hydrostatic pressure cell filled with inert liquid (FC-72, see **Experimental Methods 4.6**). The change in hydrostatic pressure is achieved by increasing the amount of inert liquid through a manual pump, with a resulting pressure ranging from 0 (ambient pressure) to 0.3 GPa.

In **Figure 4.4**, after 20 minutes of light-soaking, we observe that the features attributed to the iodide- and bromide-rich domains change in energy as a function of the applied pressure. The narrower energy difference between the iodide and bromide phase is related to thermodynamic changes in the system and further discussed in **Chapter 4.3**. In addition, we observe a change in the rate at which the phase segregation occurs as a function of the increased pressure that can be related to a change in the kinetics behaviour of the system, further discussed in **Chapter 4.4**. The same behaviour under pressure as described above is observed for the composition with $x = 0.7$ shown in **Figure A4.3** and **Figure A4.4**. The 2D $\Delta T/T$ plot in **Figure A4.4** shows that, for the composition $x = 0.25$, closer to the threshold where the phase segregation does not occur, a complete suppression of phase segregation occurs already at 0.1 GPa and no clear iodide-rich or bromide-rich phase is observed. For $x = 0.5$ and 0.7, the phase segregation also becomes less visible. At 0.3 GPa, the phase segregation only leads to a broadening of the initial mixed-halide peak, and no clear separate iodide-rich phase is observed. In the following sections, we investigate how the composition of the segregated phase changes and how the dynamics of the formation rate of halide-rich domains is affected by the external pressure.

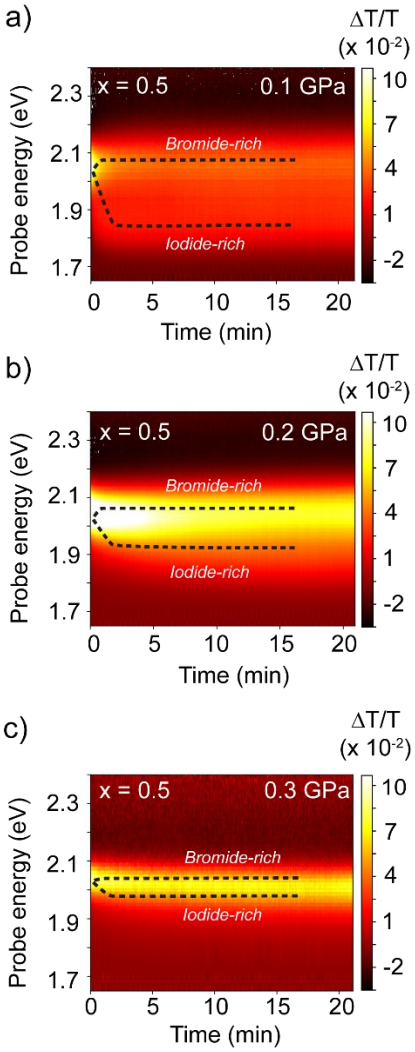


**Figure 4.4.** P*hase segregation as a function of pressure. ΔT/T* as a function of the probe energy and real time (minutes) for $MAPb(Br_{0.5}I_{0.5})_3$ under light-soaking at **a)** 0.1 GPa, **b)** 0.2 GPa and **c)** 0.3 GPa. The dashed lines are a guide for the eye to highlight the iodide- and bromide-rich phase.

# 4.3. Thermodynamics Changes under Pressure

**Figure 4.5a** shows cross-cuts of $\Delta T/T$ traces after different amounts of time (2 - 347 seconds) of light-soaking at ambient pressure for mixed-halide perovskites with $x = 0.5$. At ambient pressure, the initial bleach attributed to the mixed phase peak at (2.08±0.01) eV for $x = 0.5$ in agreement with steady-state absorption measurements shown in **Figure A4.1a**. After 20 minutes light-soaking, when the phase-segregation process is complete, the sample with composition $x = 0.5$ shows two features at an energy of (1.88 ± 0.01) eV and (2.12 ± 0.003) eV attributed to the iodide- and bromide-rich phase, respectively. By using the position of the initial bleach for $x = 0$, 1, 0.25, 0.5 and 0.7 at a pump-probe delay of 15 ps, we calculate the relation to convert the peak energy associated with the iodide- and bromide-segregated phase to the fraction of bromide in the segregated domains ($x_{s,Br}$ and $x_{s,I}$) after the phase segregation is complete (**Figure A4.6**). The energies reported above for the segregated phase in $x = 0.5$ correspond to a composition $x_{s,I}$ of 0.28 ± 0.02 for the iodide-rich phase, and $x_{s,Br} = 0.63 \pm 0.01$ for the bromide-rich phase. Upon increasing pressure at 0.3 GPa (**Figure 4.5b**), we find that the segregated iodide-rich phase has a different energy, much closer to the energy of the initial mixing ratio.

In fact, light soaking the same mixed-halide perovskite at high pressure (0.3 GPa) does not lead to the formation of distinct iodide and bromide phases. Instead, only a small side peak appears corresponding to $x_{s,I} = 0.41 \pm 0.03$, next to the initial $\Delta T/T$ peak ($x_{s,Br} = 0.51 \pm 0.04$). This observation shows that halide segregation is substantially suppressed at high pressure. For $x = 0.25$ (**Figure A4.6**), we find that this composition is entirely stable against phase segregation already at 0.2 GPa and no significant shift of the main peak is observed. For $x = 0.7$ (**Figure 4.5c**), the initial bleach at ambient pressure has an energy of (2.19 ± 0.01) eV. After 20 minutes light soaking at ambient pressure, we observe two features at (1.83 ± 0.01) eV and (2.26 ± 0.02) eV, attributed to the iodide- and bromide-rich phase. The corresponding composition are $x_{s,I} = 0.29 \pm 0.02$ and $x_{s,Br} = 0.81 \pm 0.05$. At high pressure, $x = 0.7$ remains mostly stable (**Figure 4.5d**) showing no iodide-rich or bromide-rich feature.

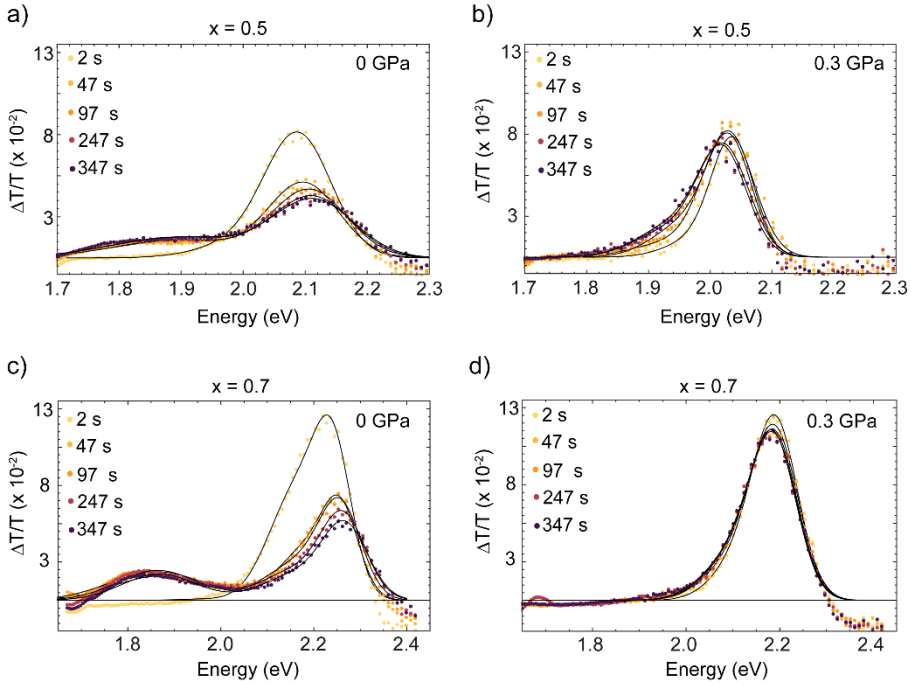


**Figure 4.5.** *Pressure-induced suppression of phase segregation in mixed-halide perovskites.* ΔT/T traces at different time for **a,b)** $x$ = 0.5, **c,d)** $x$ = 0.7 at 0 GPa and 0.3 GPa

We observe that whereas the iodide-rich phase has the same final composition independent of initial composition (at ambient pressure), the bromide-rich phase changes substantially with $x$, as indicated by the different positions of the high-energy peaks in **Figure 4.5a-d** after light-soaking. **Table 4.2** summarizes for each composition ($x$ = 0.25, 0.5 and 0.7, stoichiometric fraction) the values of the peak energy of the mixed phase before light soaking at different pressures $E_{mixed}$ and the corresponding composition $x_{mixed}$, the peak energy attributed to the iodide- and bromide-rich phase after light soaking together with the corresponding bromide fraction. Previously, it has been proposed[30,31] that the onset of the phase segregation matches with the bromide fraction at which the phase transition in the mixed-halide perovskites occurs ($x > 0.2$). When $x < 0.2$, the mixed-halide compositions show a tetragonal crystal structure, while when $x > 0.2$, the crystal structure adopted by the perovskite is cubic. In other words, the cubic phase was considered unstable under light and thus the origin of the immiscibility of iodide

and bromide in mixed-halide under illumination. However, our observation that the composition of the segregated phase $x_s$ does vary with $x$ at high pressure indicates that $x_s$ is not determined by the cubic-to-tetragonal phase transition. As found by Jaffe et al.[27], $x$ = 0.2 and $x$ = 0.4 are still cubic at 0.3 GPa and thus the pressure-dependent terminal $x$ cannot be explained with the cubic-to-tetragonal phase transition.

**Table 4.2.** Peak energy of the mixed phase for $x$ = 0.25, 0.5 and 0.7 before light soaking $E_{mixed}$ at different pressures and the corresponding composition $x_{mixed}$, the peak energy corresponding to the iodide- and bromide-rich phase after light soaking, $E_{x,I}$ and $E_{x,Br}$, respectively, and the corresponding bromide fraction.

| $x$ | P (GPa) | $E_{mixed}$ (eV) | $x_{mixed}$ | $E_{x,I}$ (eV) | $E_{x,Br}$ (eV) | $x_{s,I}$ | $x_{s,Br}$ |
|---|---|---|---|---|---|---|---|
| **0.25** | 0 | 1.79±0.01 | 0.22±0.01 | 1.76±0.03 | - | 0.19±0.02 | - |
| | 0.1 | 1.77±0.02 | 0.22±0.01 | 1.76±0.01 | - | 0.21±0.02 | - |
| | 0.2 | 1.78±0.01 | 0.21±0.01 | 1.77±0.01 | - | 0.21±0.02 | - |
| | 0.3 | 1.79±0.01 | 0.23±0.01 | 1.77±0.01 | - | 0.21±0.02 | - |
| **0.5** | 0 | 2.08±0.01 | 0.59±0.01 | 1.84±0.01 | 2.10±0.01 | 0.28± 0.02 | 0.63±0.05 |
| | 0.1 | 2.07±0.01 | 0.60±0.01 | 1.83±0.01 | 2.04±0.02 | 0.30± 0.02 | 0.56±0.04 |
| | 0.2 | 2.07±0.01 | 0.59±0.01 | 1.89±0.03 | 2.03±0.02 | 0.36± 0.03 | 0.54±0.03 |
| | 0.3 | 2.07±0.01 | 0.59±0.01 | 1.93±0.03 | 2.00±0.01 | 0.41± 0.03 | 0.51±0.04 |
| **0.7** | 0 | 2.19±0.01 | 0.75±0.01 | 1.83±0.01 | 2.26±0.02 | 0.29± 0.02 | 0.81±0.05 |
| | 0.1 | 2.19±0.01 | 0.75±0.01 | 1.89±0.01 | 2.19±0.02 | 0.37± 0.02 | 0.75±0.04 |
| | 0.2 | 2.19±0.02 | 0.74±0.01 | 2.00±0.01 | 2.18±0.02 | 0.50± 0.03 | 0.74±0.02 |
| | 0.3 | 2.18±0.01 | 0.75±0.01 | 2.09±0.03 | 2.18±0.01 | 0.63± 0.03 | 0.74±0.03 |

As origin of the phase segregation, we propose an alternative explanation for the suppression of the phase segregation process at high pressure that considers the mechanical effects associated with the less compressible and smaller unit cell volume for samples with higher bromide content. In **Figure 4.6a** we plot the composition of the segregated phase $x_s$ for $x$ = 0.25, 0.5 and 0.7 as a function of the unit cell volume calculated in **Figure 4.3e** and we observe that the final iodide-rich composition significantly shifts with the changes in the unit cell volume induced by the external pressure applied. In other words, the smaller the unit cell volume, the closer the composition of the segregated phase is to the original mixing ratio. At ambient pressure, the positive mixing enthalpy for $MAPb(Br_xI_{1-x})_3$ drives photo-induced segregation at $x > 0.2$[32,33]. For high pressure

and thus smaller unit cell volumes, the mixing enthalpy is reduced so that the entropy dominates for a larger range of mixing ratios.

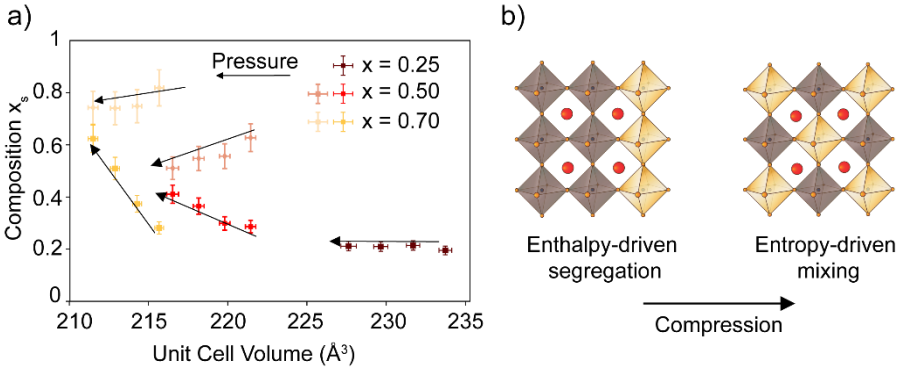


**Figure 4.6.** *Smaller unit cell volumes result in a more stable mixed-halide composition regardless from the initial mixing ratio.* **a)** Composition of the segregated phase $x_s$ as a function of the unit cell volume calculated using the bulk moduli. The larger volumes correspond to ambient pressure conditions, whereas smaller volumes result from compression at 0.3 GPa. **b)** Schematic representation of the suppression of segregation by compressing the mixed-halide perovskite.

$MAPb(Br_xI_{1-x})_3$ is a pseudo-binary mixture (or solid solution) and its accessible solubility range at a certain temperature $T$ is determined by the free energy of mixing $\Delta G(x)$, *i.e.* the free energy of the mixed phase with respect to the phase-separated iodide ($x = 0$) and bromide ($x = 1$) compounds assuming that $\Delta U = 0$. The free energy of mixing holds an enthalpic and entropic term, $\Delta H(x)$ and $\Delta S(x)$, respectively. Both depend on the material's composition $x$.

$$\Delta G(x) = \Delta H(x) - T\Delta S(x) \tag{4.3}$$

First-principles calculations of Eq. 4.3 confirm a positive enthalpic term $\Delta H(x = 0.5) \sim 2$ kJ/mol due to chemical strain in the mixed $MAPb(I_{1-x}Br_x)_3$ perovskite,[33] originating from the ionic size mismatch of $I^-$ (2.22 Å) and $Br^-$ (1.96 Å). This enthalpic cost of straining the bonding environment is offset by the gain in configurational entropy ($T\Delta S$).[33] For a binary mixture, the entropy $\Delta S(x)$ reaches a maximum at $x = 0.5$ with a value of also ~ 2 kJ/mol (0.7 $k_BT$ at $T = 300$ K).

Analysis of $\Delta G(x)$ shows two minima (at $x \sim 0.2$ and at 0.75) under ambient pressure conditions. The region in between these minima represents the miscibility gap (*i.e.* the range of compositions that are thermodynamically unstable). We propose that the externally applied pressure changes the $P\Delta V$ term contained in the enthalpic term $\Delta H$, whereas $\Delta S$ is unchanged under the mild pressure we apply, because the regular perovskite structure is maintained. For most solid semiconductors, the $P\Delta V$ term is often neglected due to a large resistance to compression under pressure. However, lead-halide perovskites are polar semiconductors and their bulk modulus is smaller than that of other conventional semiconductors (*e.g.* Si = 105 GPa, GaAs = 75 GPa) as discussed previously in **Chapter 1.4** and as reported in **Table 1.1**. Thus, manipulating the $\Delta H$ by inducing a change in the $P\Delta V$ term can be used as an additional lever to control and extend the stability range of mixed-halide compositions. Combining a pressure of 0.3 GPa for a composition $x = 0.5$ results in $\Delta V = 5 Å^3$, and $P\Delta V =$ 1 kJ/mol. Given that the magnitude of $T\Delta S$ is limited to 2 kJ/mol, this represents a substantial contribution. Furthermore, because the bulk modulus of the iodide perovskite (9 GPa for $MAPbI_3$) is much smaller than that of the bromide perovskite (18 GPa for $MAPbBr_3$), the iodide-rich regions undergo a larger volume change and pay a larger enthalpic penalty. As previously shown in **Figure 4.3f**, the compositions with a larger fraction of iodide are more compressible than the composition where a larger fraction of bromide is present. Therefore, upon increasing pressure the ionic size mismatch is reduced and so is the microscopic strain, which allows $T\Delta S$ to dominate and stabilize the mixture for larger values of $x$ as schematically depicted in **Figure 4.6b**. Local inhomogeneities in halide distribution may result in low-bandgap regions (already present in the dark),[34] which act as traps to photo-excited holes. The bandgap difference $\Delta E_g$ between the high- and low-bandgap domains then provides the driving force for the light-induced phase segregation process.[32] We note that this electronic term in the phase diagram is expected not to change significantly with pressure, as the bandgaps of both the iodide- and bromide compounds, and their mixtures, show a similar pressure dependence as reported in **Table 4.2**. These observations show that the unit cell volume is an important factor determining the $x$-values at which mixed-halide perovskites are stable. Another strategy to tune the unit cell volume

is by compositional engineering, *i.e.* replacing the $MA^+$ cation with a smaller cation, for instance $Cs^+$ as schematically depicted in **Figure 4.7a**. Indeed, we find that chemically reducing the unit cell volume of $x = 0.5$ by replacing 30% of MA with smaller Cs cations reduces the halide segregation roughly to the same extent as applying 0.2 GPa external pressure to the pure MA cation perovskite, as shown in **Figure 4.7b**. Note that the Cs-based perovskites have larger bandgaps than MA-based perovskites,[35] so that the absolute peak energies cannot be compared.

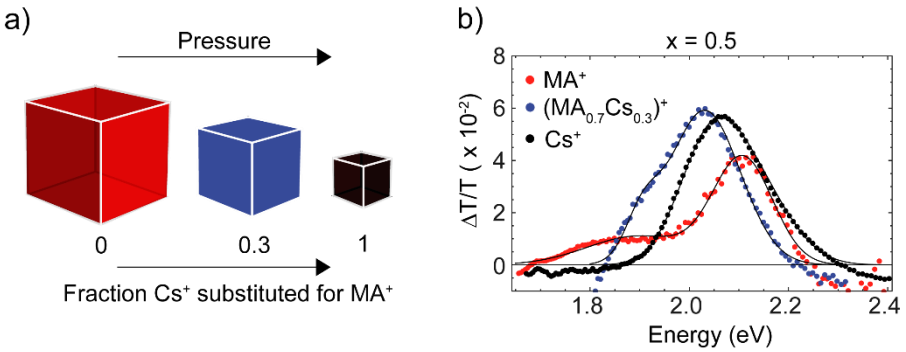


**Figure 4.7.** *Suppression of phase segregation in compositions where the unit cell volume is reduced by Cs incorporation*. **a)** Schematic representation of the unit cell volume reduction when the organic $MA^+$ is replaced by the smaller inorganic $Cs^+$. **b)** *ΔT/T* traces after 20 minutes of light soaking of composition with $x = 0.5$ where the cation $MA^+$ (red trace) is partially (blue trace) or fully replaced by $Cs^+$ (black trace).

When the $MA^+$ cation is fully replaced by $Cs^+$, the phase segregation is almost suppressed with the energy difference between the two peaks of only ~ 100 meV, similar to applying 0.3 GPa to the MA-based perovskite. While the pressure-dependent measurements on $MAPb(Br_xI_{1-x})_3$ allowed us to isolate the effect of pressure, reducing the unit cell by replacing $MA^+$ with $Cs^+$ may lead to changes in the defect density or the halide ratio. Therefore, a direct comparison between the physical and chemical pressure should not be made. However, the qualitative observation that phase stability in general can be improved on decreasing the unit cell volume, either physically or chemically, may explain the previously reported

absence of segregation in $CsPb(Br_xI_{1-x})_3$ for $x < 0.4$ (compared to $x < 0.2$ for MA analogues).[36]

## 4.4. Kinetics Changes under Pressure

Not only the composition of the segregated phase $x_s$ is affected by pressure but also the segregation rate, *i.e.* the formation rate of the iodide- and bromide-rich domains. The dynamic ingrowth of the iodide- and bromide-rich phases during light-soaking is shown in **Figure 4.8a**. As pressure increases, we observe a substantially slower phase segregation. This observation holds true for all $MAPb(Br_xI_{1-x})_3$ compositions studied, $x = 0.25$ (which barely segregates from 0.1 GPa onward), $x = 0.5$ and $x = 0.7$, as reported in **Figure A4.7**. To extract the segregation rate as a function of pressure, Gaussian profiles are fitted to the ground state bleaches of the low- and high-energy peaks position, and we monitor the peak energies of these Gaussians as a function of the light-soaking time. All kinetic traces are characterized by a continuous change in the ground state bleach energy, due to a change in composition, followed by saturation at a certain energy when segregation is complete. We observe that the time at which this final composition is reached changes substantially with pressure. The traces were fitted with mono-exponential curves, $Ae^{k_{seg}t} + c$ (eV, offset), to determine the segregation rate $k_{seg}$. Our rates at ambient pressure are comparable to previous work calculated under comparable light-soaking conditions[15,37]. Under pressure, the iodide-rich phase formation rate decreases by almost two orders of magnitude. For $x = 0.5$, $k_{seg}$ decreases from $(0.08 \pm 0.01)$ $s^{-1}$ at ambient pressure to $(0.003 \pm 0.001)$ $s^{-1}$ at 0.3 GPa. At 0.3 GPa the difference between the initial and final energies is much smaller than at ambient pressure[38]. However, still the time constant associated with the evolution towards the terminal $x_s$-value is much longer, indicating that segregation is substantially slower at 0.3 GPa. A similar trend is observed for $x = 0.7$ and $x = 0.25$, where the segregation rate decreases from $(0.1 \pm 0.03)$ $s^{-1}$ at ambient pressure to $(0.003 \pm 0.001)$ $s^{-1}$ at 0.3 GPa, and from $(0.028 \pm 0.002)$ $s^{-1}$ to $(0.004 \pm 0.001)$ $s^{-1}$, respectively. For $x = 0.25$, there was no detectable change in the mixed peak position within our resolution. For the other compositions, the formation rate of the bromide-rich phase is slower and less

affected by pressure compared to the iodide-rich one (**Figure 4.8b**). This observation will be discussed in more detail later.

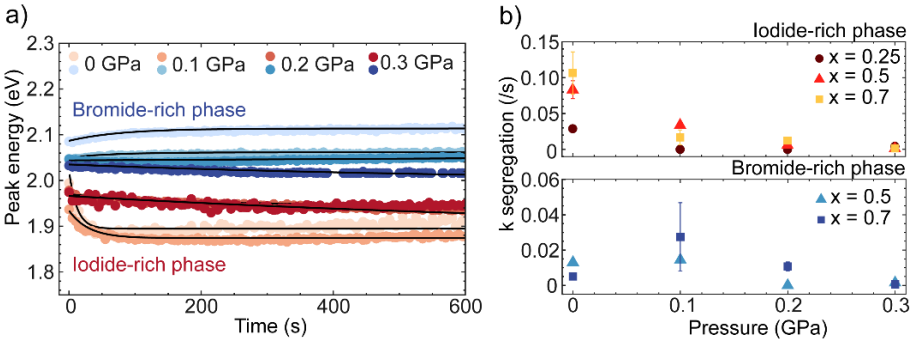


**Figure 4.8.** *Peak energy evolution of the iodide- and bromide-rich phase.* **a)** Dynamic evolution of the low-energy iodide-rich phase (red) and high-energy bromide-rich phase (blue) from ambient pressure to 0.3 GPa. **b)** Segregation rates for the iodide- and bromide-rich phases as function of pressure for all the $MAPb(Br_xI_{1-x})_3$ compositions ($x = 0.25$, $x = 0.5$ and $x = 0.7$).

We explain the diminution of the segregation rate upon increasing pressure from an increase of the activation energy associated with the migration of halide ions, consequently delaying the accumulation of ions in the low-energy phase. Density functional theory calculations on the model systems $CsPbI_3$ and $CsPbBr_3$ in **Figure 4.9a** show the energy barrier associated with vacancy-assisted halide diffusion. The potential energy surface for ion diffusion is calculated, and the saddle point is identified, as a function of applied pressure. The transition state increases in energy as the cell volume decreases (see **Figure A4.8**). As a result, the energy barrier increases with pressure for both materials, with a change of 0.134 eV ($I^-$) and 0.138 eV ($Br^-$) when the pressure is increased from 0 to 2 GPa.

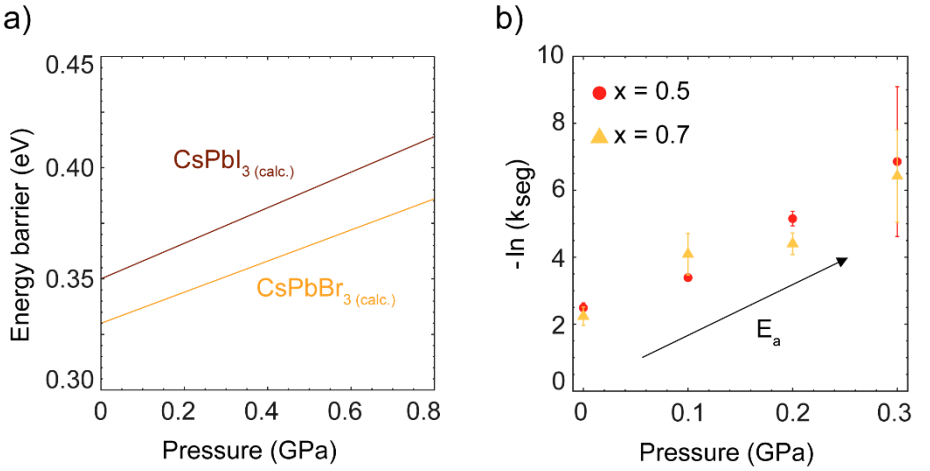


**Figure 4.9.** *Calculated and observed activation energy for halide migration of perovskites under pressure.* **a)** Calculated (DFT/PBEsol) activation energy for iodide and bromide diffusion in $CsPbI_3$ and $CsPbBr_3$ as a function of unit cell volume. **b)** $-ln(k_{seg})$ (which is proportional to the activation energy for phase segregation), plotted against the external physical pressure applied for $x = 0.5$ and $x = 0.7$

To derive the relation between the segregation rate and the activation energy for the halides migration we use the definition of the diffusion coefficient[39] (see **Appendix 4.7.2** for the full derivation)

$$k_{migration} = \frac{q^2 N \nu_0 d^2}{6\,\epsilon_0 \epsilon_{pero} k_B T} exp\left(\frac{\Delta^{\ddagger} S^{\circ}}{k_B}\right) exp\left(-\frac{E_a}{k_B T}\right) \qquad (4.4)$$

Where $\Delta^{\ddagger}S^{\circ}$ is the entropy change between the initial state and the activated state, as opposed to the entropy difference between reactant and product, $k_B$ is the Boltzmann constant, $\upsilon_0$ is the attempt frequency for an ion to hop, $d$ is the ionic hopping distance, $E_a$ is the activation energy, $q$ is the elementary charge, $\epsilon_{pero}$ is the permittivity of the perovskite, $\epsilon_0$ is the permittivity in vacuum and $N$ is the doping density. The attempt-to-escape frequency has been commonly attributed to the frequency of an attempt to break or loosen a bond. For ion migration in halide-based perovskites, the vibrational frequency relevant for halide migration

is determined by the Raman frequency of the $[PbI_6]^{4-}$ cage (10-50 $cm^{-1}$)[40]. As a function of pressure, this term has been found constant for $MAPbI_3$[41] and temperature-dependent Raman[42] shows similar results for $MAPbX_3$ (X=$Br^-$,$Cl^-$) below their phase transition, therefore we assume that this term remains relatively constant in the range of pressures we studied. At such mild pressure, we do not expect a change in the mechanism of halide migration and hence we can assume the $\Delta^{\ddagger}S^{\circ}$ to be constant in the range of pressure used. Similarly, we expect only small changes in the remainder of the pre-factor $\frac{q^2 N \nu_0 d^2}{6\,\epsilon_0 \epsilon_{pero} k_B T}$ under pressure. The jump distance $d$ can change as a function of pressure similarly as the strain (2-3%) as it depends on the lattice parameter of the unit cell. $\epsilon_{pero}$ and $N$ may both change proportionally to the volume change, which will be well below 5% at the mild pressures applied. Hence, the pre-factor cannot account for the large change in the migration rate. As a consequence of the discussion above, it follows that the natural logarithm of the migration rate is largely proportional to the activation energy for the migration process

$$-\ln\left(k_{migration}\right) \propto E_a \tag{4.5}$$

For simplicity, we define the experimental $-\ln\left(k_{seg}\right)$ as the effective activation energy $E_a^*$. Typical activation energies for halide migration in these perovskites are in the order of 100-200 meV (see transient ion drift (TID) measurements below)[13,37,43]. The experimental $E_a^*$ plotted as a function of physical pressure applied increases by a factor three upon increasing pressure to 0.3 GPa for all the compositions (**Figure 4.9b**).

Interestingly, we show in **Figure 4.10a** that similarly to what was observed in **Chapter 4.3**, the reduction in unit cell volume by partial or complete replacement of $MA^+$ with the smaller cation $Cs^+$ results in a similar kinetic behaviour as under high pressure. This observation suggests that slower ion migration is a phenomenon that is more generally linked to a reduction of the unit cell volume, independent of how this reduction is achieved (see **Figure A4.9** for $E_a^*$ as a function of unit cell volume change induced by chemical and physical pressure). We note here again that partial replacement of $MA^+$ with the smaller $Cs^+$ may

result in different defect densities, crystallinity and strain which will also affect the absolute segregation rate. As local stoichiometric variations could also play a role in establishing the absolute rates of phase segregation, further investigations on single crystals would be useful as they show less stoichiometric variations compared to thin films[44]. By applying external physical pressure, we essentially vary only one parameter while moving from $MA^+$ to $Cs^+$ may also change other parameters. However, the similarity in the trends observed in **Figure 4.9b** and **Figure 4.10b** indicates that the unit cell volume plays a key factor in the phase segregation rate.

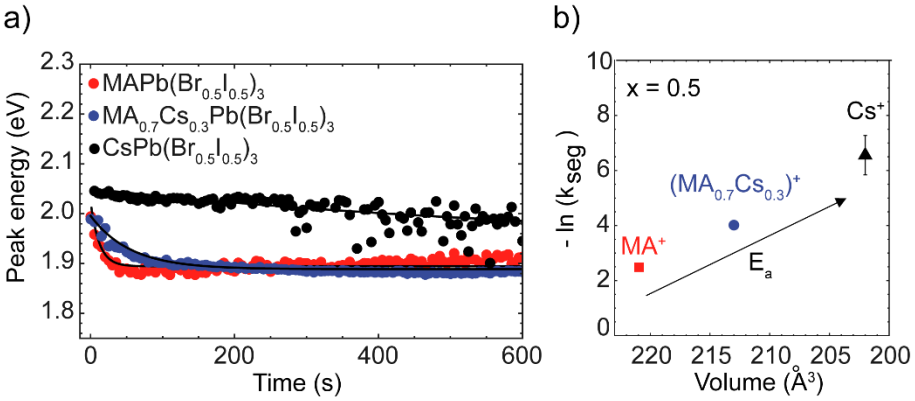


**Figure 4.10.** *Chemical modification to reduce the phase segregation rate.* **a)** Dynamic evolution of the low-energy iodide-rich phase measured by pressure-dependent TAS during light-soaking for compositions where the A cation is $MA^+$ (red trace), $MA^+$ : $Cs^+$ in 0.7 : 0.3 ratio (blue trace) and $Cs^+$ only (black trace). Corresponding **b)** $-ln(k_{seg})$ plotted against the unit cell volume. We observe that $-ln(k_{seg})$ follows the same trend as when the pressure is varied.

Ion migration plays a large role in the degradation of perovskite thin films, and the effect of strain shimmers through many observations related to perovskite stability. Under tensile strain, the inorganic $[PbX_6]^{4-}$ framework is distorted resulting in longer and weaker Pb−X bonds and less strongly tilted octahedra[45]. This strain results in a decreased formation energy for defects and a lower activation energy for ion migration[46]. A source of tensile strain which lowers the activation energy for ion migration[46,47,48] is the presence of light during

light-soaking, which has been shown to lead to thermal expansion in MA-based mixed halide perovskite unit cells[49]. We also find a lower activation energy under light exposure than under dark conditions, which we measured using TID on an $x = 0.20$ sample, the composition with the highest mixing ratio which does not segregate under light-soaking. We found two negatively charged species migrating with comparable activation energy in dark, namely (0.15 ± 0.03) eV and (0.14 ± 0.01) eV. In single-halide composition only one negative species was observed[12] so it is likely that the two species found in the mixed-halide compositions represent both iodide and bromide. In light, the activation energy of the former species is reduced to (0.09 ± 0.01) eV, whereas the latter remains constant at (0.13 ± 0.02) eV. The decrease in activation energy in light is consistent with the observation that light-induced tensile strain leads to increased ion migration. We note that some of the change in activation energy could be due to heating but it cannot explain the full magnitude[50]. Since light changes the activation energy of only one of the two halide migration processes, we propose that the process with the lower activation energy in light may be mainly responsible for phase segregation (see **Appendix 4.7.3** and **Figure A4.12** for TID traces and details on the fitting method).

Our observation that the rate of phase segregation strongly depends on the physical pressure demonstrates the large role that strain plays for ion migration. We hypothesize that pressure-induced compressive stress counteracts the effect of thermal expansion induced by light. Therefore, by strengthening the Pb−X bonds, pressure mitigates the reduction of the activation energy for halide migration. A scheme of the proposed mechanism at the microscopic and macroscopic level is shown in **Figure 4.11a-b**.

A similar reduction of phase segregation can be obtained at ambient pressure by inducing strain *via* either regulating strain in the perovskite film through charge-transport layers as recently reported by Xue et al.[51] or through compositional engineering, by partial replacement of $MA^+$ with smaller cations. As a consequence, $Cs^+$ incorporation further slows down phase segregation in MA-based mixed halide perovskites[52]. Ferdani et al.[53] have also reported increased ion migration activation energy in dark also when $MA^+$ is partially replaced by larger cation. In fact, strain can also play a key role in mixed-cation

mixed-halide perovskite compositions which are reported to be less sensitive to light-induced thermal expansion[50] and phase segregation[22,23,24].

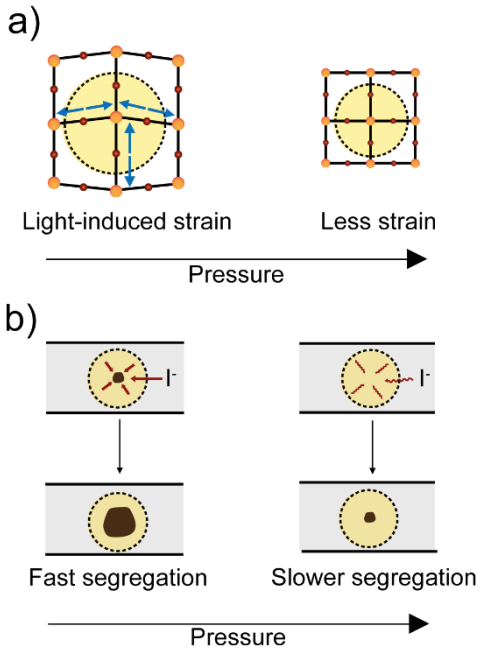


**Figure 4.11.** *Schemes of the proposed mechanism to kinetically stabilize phase segregation by external physical pressure*. **a)** Light induces thermal expansion strain and decreases the energy barrier for halide migration by weakening the Pb−X bonds. At high pressure, the compressive strain counteracts the light-induced strain and increases the activation energy for halide migration. **b)** At ambient pressure, mainly the iodide ions move to the illuminated areas (dashed circle) to increase the volume of quickly formed iodide-rich islands, increasing their volume. At high pressure, halide ions move slower given the higher activation energy, leading to slower phase segregation.

From our measurements the formation rate of the low-energy iodide-rich phase appears to be faster than the high-energy bromide-rich phase for all the compositions and pressures explored. The total mixing ratio before light-soaking at ambient conditions calculated from the area and the energy position of the bleach is 0.531 ± 0.001 for $x$ = 0.5. Now that we know the $x$-values of the

segregated phases calculated from the bleach energy positions, and their relative peak areas, we can calculate whether the total mixing ratio has changed during the segregation. After 20 minutes of light-soaking, the mixing ratio is 0.46 ± 0.01, suggesting iodide-enrichment of the illuminated area. Although most of the halide ions move within the illuminated area, the decrease in the total mixing ratio suggests that some iodide ions have moved from outside the illuminated region. At high pressure, a similar trend is observed ($x$ = 0.47± 0.01 after light-soaking). This similarity in total mixing ratio suggests that despite the changes in segregation rate and final composition, the total number of iodides moving into the probed area does not change with pressure. Furthermore, while both the segregation rate and the final composition of the iodide-rich phase are heavily affected by physical pressure[38], the bromide-rich phase does not show a clear trend with pressure. As an additional observation, the rate of evolution of the area of the bleach of the low-energy phase (roughly proportional to the volume fraction) is slower as compared to the rate obtained by the peak energy position in time, whereas the high-energy phase shows the same rate for the peak energy and peak area decay as shown in **Figure A4.10**. We speculate that all these observations could be explained by the formation of local, small iodide-rich islands (low-energy phase) with a well-defined composition from a small portion of the film which does not substantially affect the high-energy phase. Then, once those islands are formed, the bulk of the halides segregate via the migration of iodide ions into the initially-formed islands, growing the volume of these domains[32]. It is important to note that the different rates extracted from the areas can also be the result of different dynamics before 15 ps for the low- and high-energy phase. Therefore, the interpretation is not trivial. In addition, we observe that during halide segregation, the total area of the two bleaches changes over time at low pressure (see **Figure A 4.11**). Finally, given that the halide migration likely occurs *via* a similar vacancy-mediated mechanism both in mixed- and single-halide compositions, we propose that unit cell size is equally important for halide migration in single-halide systems, and that a similar chemical approach as in mixed-halide compositions could be used to reduce the rate of halide migration in single-halide compositions, *e.g.* $MAPbI_3$.

# 4.5. Conclusion

We used pressure-dependent transient absorption to investigate the evolution of the phase segregation in several mixed-halide perovskites, $MAPb(Br_xI_{1-x})_3$ ($x$ = 0.25, 0.5 and 0.7) by tracking the iodide- and bromide-rich phase formation over time. We have shown that the segregation threshold ($x_s$ ~ 0.2 at ambient pressure) is substantially shifted with pressure, reaching $x_s$ ~ 0.6 at 0.3 GPa for an initial mixing ratio of $x$ = 0.7. We propose that the external pressure applied alters the Gibbs free energy via the previously overlooked $P\Delta V$ term. This term, often neglected in conventional semiconductors due to the stiffness of their lattice in comparison with the perovskite one, supplies a lever to extend the range of thermodynamically stable mixed-halide compositions by increasing the pressure or decreasing the volume. This suggests that, in principle, any iodide-bromide mixing ratio could be thermodynamically stabilized against halide segregation by tuning the crystal volume and compressibility. We also found that the phase segregation rate is reduced by the external pressure applied. We attribute the reduced segregation rate to a pressure-induced increase in the effective activation energy for the halide migration process. First-principle calculations support this explanation. We show that a similar thermodynamic and kinetic manipulation can be achieved by reducing the unit cell volume achieved *via* partial or complete replacement of the $MA^+$ cation by the smaller $Cs^+$ cation. Hence, chemically tuning the unit cell at ambient conditions (instead of applying physical pressure) may be used to manipulate ion migration/phase segregation. These findings will help in understanding the key factors affecting the rate of halide migration and to develop an effective strategy that combine thermodynamic and kinetic manipulation to suppress halide migration for the lifetime of the perovskite-based devices.

# 4.6. Experimental Methods

### Sample fabrication

Quartz substrates were sonicated with deionized water, acetone, and isopropanol sequentially for 15 minutes, followed by an oxygen plasma treatment for 20 minutes at 100 W. The solvents N,N-dimethylformamide (DMF, Sigma Aldrich anhydrous, ≥ 99%) and dimethylsulfoxide (DMSO, Sigma Aldrich anhydrous, ≥ 99.9%) were mixed in a 4:1 (DMF:DMSO) volume ratio. The solvent mixtures were used to prepare stock solutions of lead iodide (TCI, 99.99%, trace metals basis), $CH_3NH_3I$ (MAI, TCI, >99%), lead bromide (Sigma Aldrich, trace metals basis) and $CH_3NH_3Br$ (MABr, TCI, >98%) by dissolving these precursors at 1.1 M concentration. $MAPbI_3$ and $MAPbBr_3$ solutions were prepared by mixing the MAI with $PbI_2$ and MABr with $PbBr_2$ stock solutions at 1:1 molar stoichiometric ratios (*i.e.* 1:1 v:v). Similarly, $CsPbI_3$ (0.4 M) and $CsPbBr_3$ (0.4 M) stock solutions were prepared in a nitrogen-filled glovebox mixing CsI (99.999% trace metals basis), CsBr (99.999% trace metals basis), $PbI_2$ and $PbBr_2$ in DMSO. Note that CsBr is soluble in DMSO only at smaller molar concentration compared to the MA equivalent. Stock solutions were mixed to obtain the desired halide and cation ratios. The MA-based mixed-halide solutions were spin coated on quartz at 9000 rpm for 30 s and anti-solvent of chlorobenzene was dropped 15 s after the start of spin coating. The films were annealed at 100 °C for 1 hour. For Cs-based compositions, no antisolvent was used and the annealing was done at 65°C for 15 minutes.

### X-Ray Diffraction

The XRD pattern of perovskite films deposited on quartz was measured using an X-ray diffractometer, Bruker D2 Phaser, with Cu Kα (λ = 1.541 Å) as X-ray source, 0.01° (2θ) as the step size, and 0.100 s as the exposure time.

### Steady-State Absorption

Absorption spectra of $MAPbI_3$ films on quartz were measured with a LAMBDA 750 UV/Vis/NIR Spectrophotometer (Perkin Elmer) from 550 nm to 850 nm.

### Elemental analysis

Elemental analysis was performed using a FEI Verios 460 field emission scanning electron microscope (SEM) combined with an energy-dispersive X-ray detector operating at 10 kV.

### First-principles defect diffusion

Activation energies were calculated for vacancy-assisted halide migration in both the cubic phases of $CsPbI_3$ and $CsPbBr_3$. These were performed within density functional theory and the PBEsol[54] exchange-correlation functional as implemented in VASP[55,56]. Scalar-relativistic projector-augmented wave pseudopotentials were combined with a plane-wave kinetic energy cutoff of 700 eV and a *k*-point sampling of 4×4×4. To begin, the volume of the $CsPbX_3$ (X = Br, I) unit cell was optimized in each case to obtain the equilibrium lattice constant *a* ($CsPbI_3$ = 6.25 Å, $CsPbBr_3$ = 5.87 Å) and bulk modulus B ($CsPbI_3$ = 17.34 GPa, $CsPbBr_3$ = 21.70 GPa). In the optimization procedure, the calculated energy-volume data was fit using the Birch–Murnaghan equation of state. Point defect calculations were then performed for a positively charged halide vacancy in a 4×4×4 supercell. In the cubic phase, all nearest-neighbour ion diffusion pathways are equivalent, so we chose one pathway in a (100) plane and mapped the ion diffusion on a real-space 41×41 2D grid. This provides direct access to the activation energy. These defect migration calculations were repeated as a function of the supercell volume, which was converted to pressure using the calculated bulk moduli.

### Pressure-dependent transient absorption spectroscopy

The setup in use is described extensively in **Chapter 1.6**. During the measurement, the sample is kept inside the pressure cell filled with FC-72 previously degassed in a Schlenk line. The range of pressures applied is from ambient pressure (0 GPa) to 0.3 GPa in steps of 0.1 GPa. We wait 7 minutes for equilibration of the material under pressure prior to the measurement. The pump fluence used during the experiment was ~$10^{18}$ photons/$cm^3$. To induce the phase segregation, we focus a 405 nm continuous wave (CW) light beam in the pressure

cell. The spot size of the light-soaking beam used was 243 μm in diameter with an intensity of $2.37 \times 10^3$ mW/cm$^2$ (~24 sun).

### Transient ion drift spectroscopy (TID)

TID is measured using a commercially available DLTS system from Semetrol. The sample is loaded into a Janis VPF-100 liquid nitrogen cryostat where the temperature is swept from 210 K to 330 K in steps of 3 K, with a temperature accuracy of 0.2 K. To ensure thermal equilibrium, the sample is held at 210 K for 30 minutes before starting the measurement. The cryostat is further linked to a turbo pump which maintains the pressure below $2 \times 10^{-6}$ mbar. TID relies on the application of a voltage pulse close to the built-in voltage, here 1.5 V for 2 seconds. Measurements under light are taken using a 405 nm continuous wave (CW) single-mode fibre-coupled laser source (Thorlabs), equivalent to the one used as the third light source in the pressure-dependent transient absorption spectroscopy experiments.

# 4.7. Appendix

## 4.7.1. Additional Figures

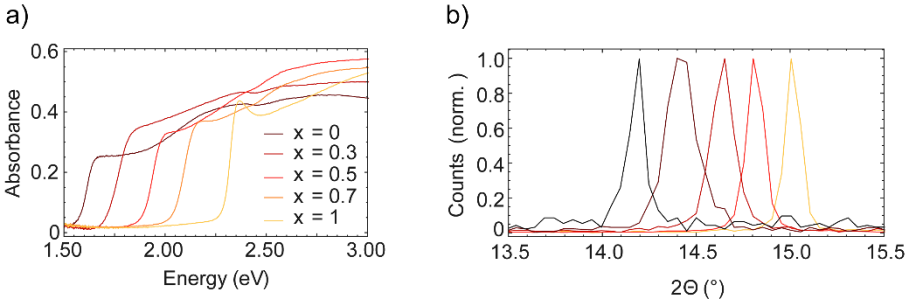


**Figure A4.1. a)** UV-VIS absorption spectrum and **b)** X-Ray Diffraction pattern of $MAPb(Br_xI_{1-x})_3$, showing that on a macroscopic level, the halides are homogeneously mixed and both the bandgap and unit cell size scale with $x$. For simplicity, only the diffraction peak corresponding to the (100) reflection is shown.

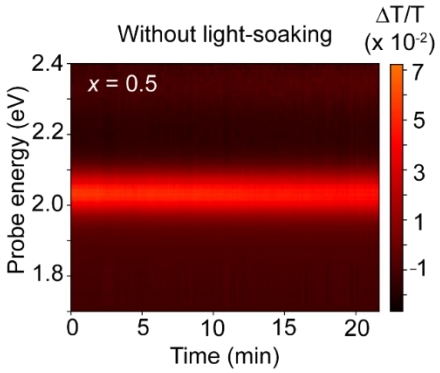


**Figure A4.2.** $\Delta T/T$ as a function of the probe energy and real time at a pump-probe delay of 15 ps for $MAPb(Br_{0.5}I_{0.5})_3$ at ambient pressure without CW light-soaking source, showing that the pulsed pump and probe used in the TA measurements do not induce phase segregation. The bleach of $x = 0.5$ is stable at (2.08±0.01) eV during the whole measurement and no second peak related to the formation of the iodide-rich phase is observed.

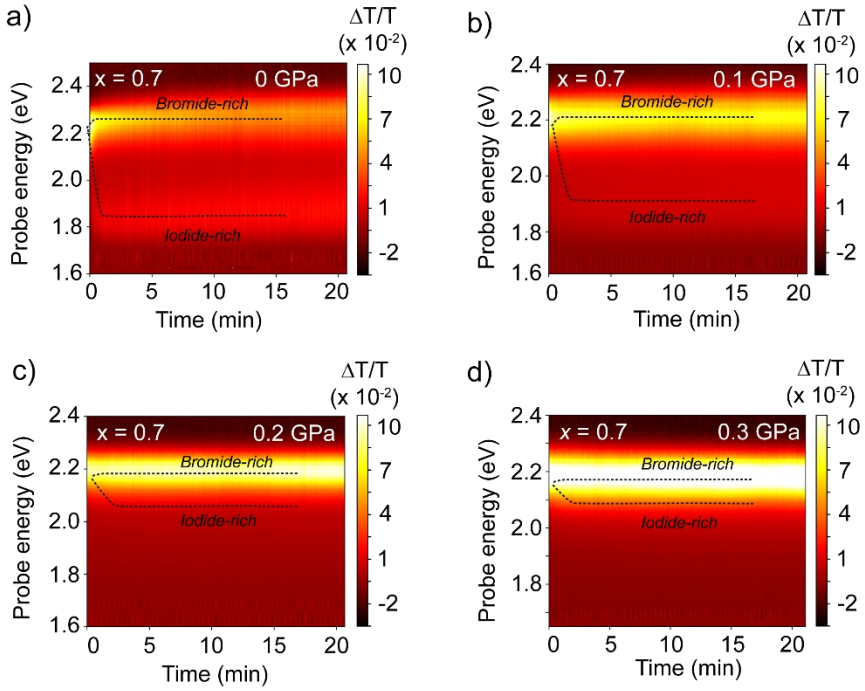


**Figure A4.3.** *ΔT/T* 2D plot as a function of the probe energy and real time (minutes) at a pump-probe delay of 15 ps for $x = 0.7$ during light-soaking at **a)** 0 GPa, **b)** 0.1 GPa, **c)** 0.2 GPa and **d)** 0.3 GPa. Dashed lines are used as a guide for the eye to highlight the iodide- and bromide-rich phase.

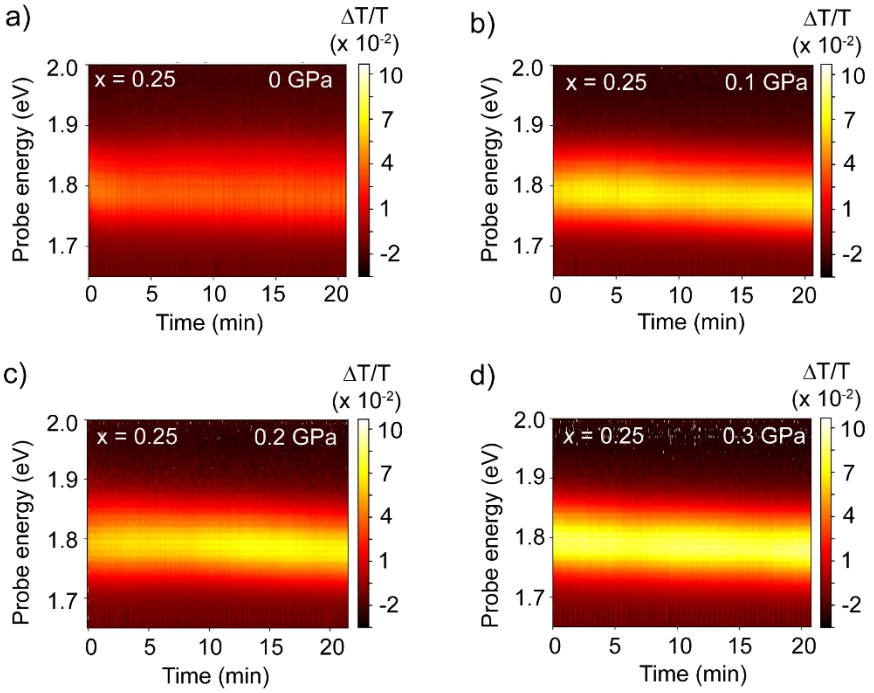


**Figure A4.4.** *ΔT/T* 2D plot as a function of the probe energy and real time (minutes) at a pump-probe delay of 15 ps for $x = 0.25$ during light-soaking at **a)** 0 GPa, **b)** 0.1 GPa, **c)** 0.2 GPa and **d)** 0.3 GPa.

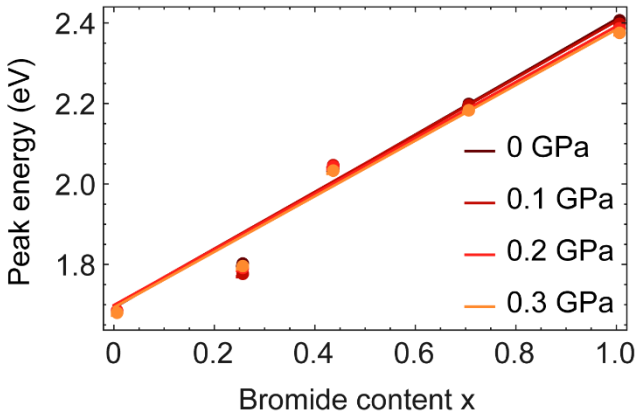


**Figure A4.5.** Bromide content determined with SEM-EDX elemental analysis for $x$ = 0, 1, 0.25, 0.5, 0.7 plotted against the energy (eV) of the bleach before segregation determined from fitting Gaussians to the $\Delta T/T$ spectra at a delay time of 15 ps at pressures of 0, 0.1,0.2 and 0.3 GPa. The lines represent the following fits $E_g = 0.79x + 1.61$ (0 GPa), $E_g = 0.80x + 1.59$ (0.1 GPa), $E_g = 0.78x + 1.61$ (0.2 GPa), $E_g = 0.76x + 1.61$ (0.3 GPa). These functions are used to convert the energy peak associated with the formation of iodide- and bromide-rich phase at the end phase segregation to the bromide fraction present in the segregated phase.

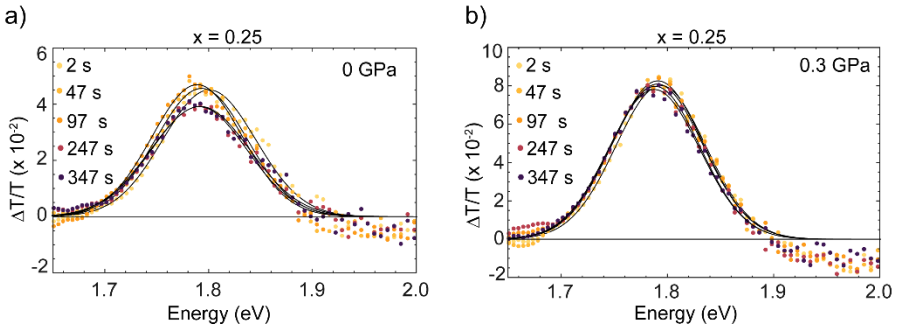


**Figure A4.6.** $\Delta T/T$ traces at different time for **a)** $x$ = 0.25 at ambient pressure and **b)** at 0.3 GPa.

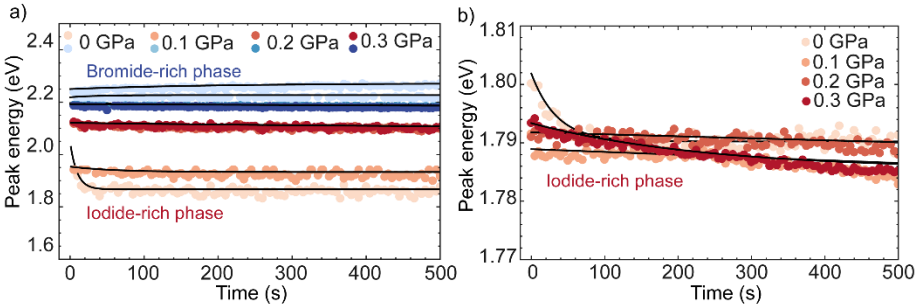


**Figure A4.7.** Dynamic evolution of the low-energy iodide-rich phase (red) and high-energy bromide-rich phase (blue) phase for **a)** $x$ = 0.7 and **b)** $x$ = 0.25 measured by pressure dependent TA during light-soaking with the CW-laser from ambient pressure (light color) to 0.3 GPa (dark color).

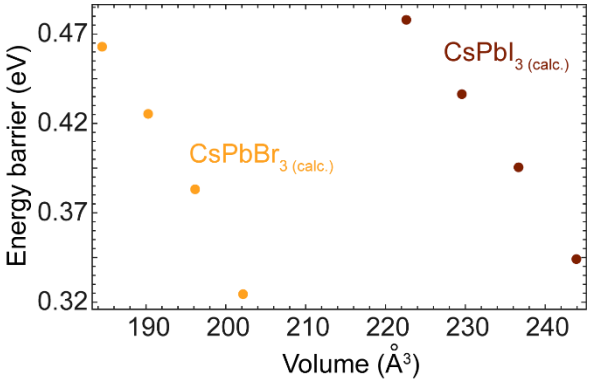


**Figure A4.8.** Calculated (DFT/PBEsol) activation energy for iodide and bromide diffusion in $CsPbI_3$ and $CsPbBr_3$ as a function the unit cell volume.

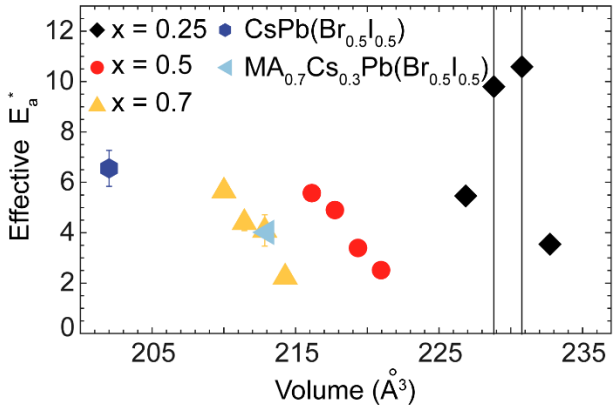


**Figure A4.9.** Effective activation energy $E_a^*$ as a function of unit cell volume change induced by physical pressure (for $x$ = 0.25, 0.5 and 0.7) and chemical pressure ($Cs^+$ incorporation). The unit cell volume at ambient pressure is calculated from XRD, whereas the one resulting from external physical pressure is calculated from the bulk moduli of the perovskite compositions.

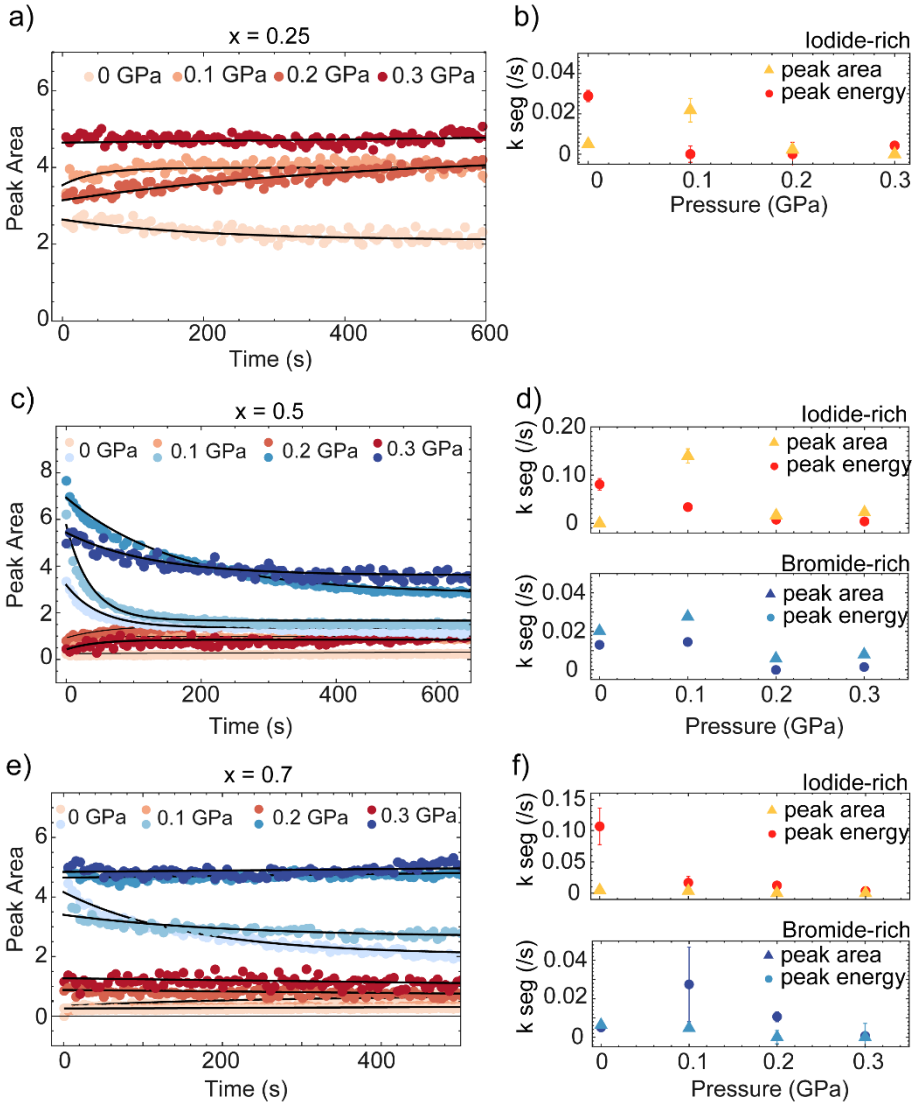


**Figure A4.10**. Dynamic evolution of the area of low-energy iodide-rich phase (red) and high-energy bromide-rich phase (blue) and corresponding rate for **a,b)** $x = 0.25$, **c,d)** $x = 0.5$ and **e,f)** $x = 0.7$

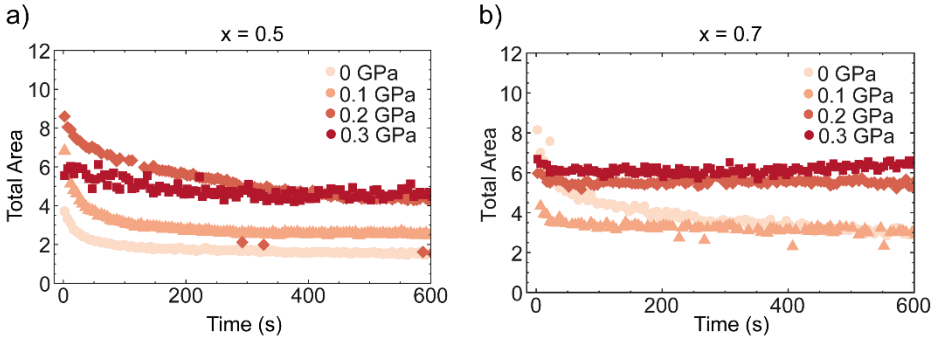


**Figure A 4.11.** Total area calculated as ( $A_{br} + A_I$) in time for **a)** $x = 0.5$ and **b)** $x = 0.7$ as a function of pressure. The total area decreases over time at low- and remains almost constant at high-pressure

## 4.7.2. Relation Between the Segregation Rate and The Activation Energy for Halide Migration

To derive the relation between the segregation rate and the activation energy for ion migration we use the definition of the diffusion coefficient[39]

$$k_{migration} = \frac{1}{\tau} = \frac{l^2}{D} \tag{4.6}$$

where $l$ is the ion diffusion length which is assumed to correspond to the Debye length $\frac{\epsilon_0 \epsilon_{pero} k_B T}{q^2 N}$ and the diffusion coefficient D can be expressed as $\frac{\nu_0 d^2}{6} exp\left(\frac{\Delta^{\ddagger} S^{\circ}}{k_B}\right) \exp\left(-\frac{\Delta^{\ddagger} H^{\circ}}{k_B T}\right)$. Combining these expressions, the migration rate can be written as

$$\begin{aligned} k_{migration} &= \frac{q^2 N \nu_0 d^2}{6\, \epsilon_0 \epsilon_{pero} k_B T} \exp\left(\frac{\Delta^{\ddagger} S^{\circ}}{k_B}\right) exp\left(-\frac{\Delta^{\ddagger} H^{\circ}}{k_B T}\right) \\ &= \frac{q^2 N \nu_0 d^2}{6\, \epsilon_0 \epsilon_{pero} k_B T} \exp\left(\frac{\Delta^{\ddagger} S^{\circ}}{k_B}\right) exp\left(-\frac{E_a}{k_B T}\right) \end{aligned} \tag{4.7}$$

where $\Delta^{\ddagger} H^{\circ}$ and $\Delta^{\ddagger} S^{\circ}$ are the changes in enthalpy and entropy of a single ion migration step, $k_B$ is the Boltzmann constant, $\upsilon_0$ is the attempt-to-escape frequency, $d$ is the ionic jump distance, $E_a$ is the activation energy, $q$ is the elementary charge, $\epsilon_{pero}$ is the permittivity of the perovskite, $\epsilon_0$ is the permittivity in vacuum and $N$ is the doping density. We refer to the change in Gibbs free enthalpy as the activation energy $E_a$[39].

### 4.7.3. Quantification of Halide Migration Using TID

To determine the activation energy of halide migration in MA-based mixed-halide perovskites, we use $MAPb(I_{1-x}Br_x)_3$ with $x$ = 0.2, *i.e.* the highest mixing ratio which does not segregate under light. Our measurement would be impossible with a device that segregates because the timescale of the measurement is much longer than the segregation time. In dark we notice that the capacitance transients decrease with time until they reach a plateau after ~200 ms, while in light, the capacitance transients decrease in the first 200 ms before they start increasing in the remaining time window (see **Figure A4.12**).
A detailed discussion of the TID technique can be found elsewhere[4]. In TID of p-type semiconductors, negative peaks are associated to anion migration, *i.e.* in the case of mixed-halide perovskites, to halide migration. We choose to focus on the halide migration process, as it is the relevant process when studying phase segregation. The fitting procedure goes as follows. To obtain the time constants for ion migration, the capacitance transients measured in dark are fitted with a function containing two exponential decay components, and the capacitance transients in light with a function containing three exponential decay components. In our case we are interested only in the two negative contributions originating from halide migration. We obtain the lifetime of the halide migration processes, τ, for each temperature. Finally, we analyse these lifetimes in an Arrhenius plot, as shown in **Figure A4.12**. The results for activation energy, $E_a$, diffusion coefficient, $D_0$, and concentration of the mobile halide ions, $N_{ion}$, are shown in **Table 4.3**. $N_{ion}$ is measured by using the following equation for mobile ion density

$$\Delta C = C(\infty) - C_0 = C(\infty)\frac{N_{ion}}{2N_A} \tag{4.9}$$

where $\Delta C$ is the magnitude of the transient, $C(\infty)$ is the capacitance at steady-state, $C_0$ is the initial capacitance at time $t$ = 0 after releasing the voltage pulse and $N_A$ is the electronic doping density. In the case of the light measurement, we use the minimum capacitance $C_{min}$ instead of $C(\infty)$, to avoid accounting for the cation concentration.

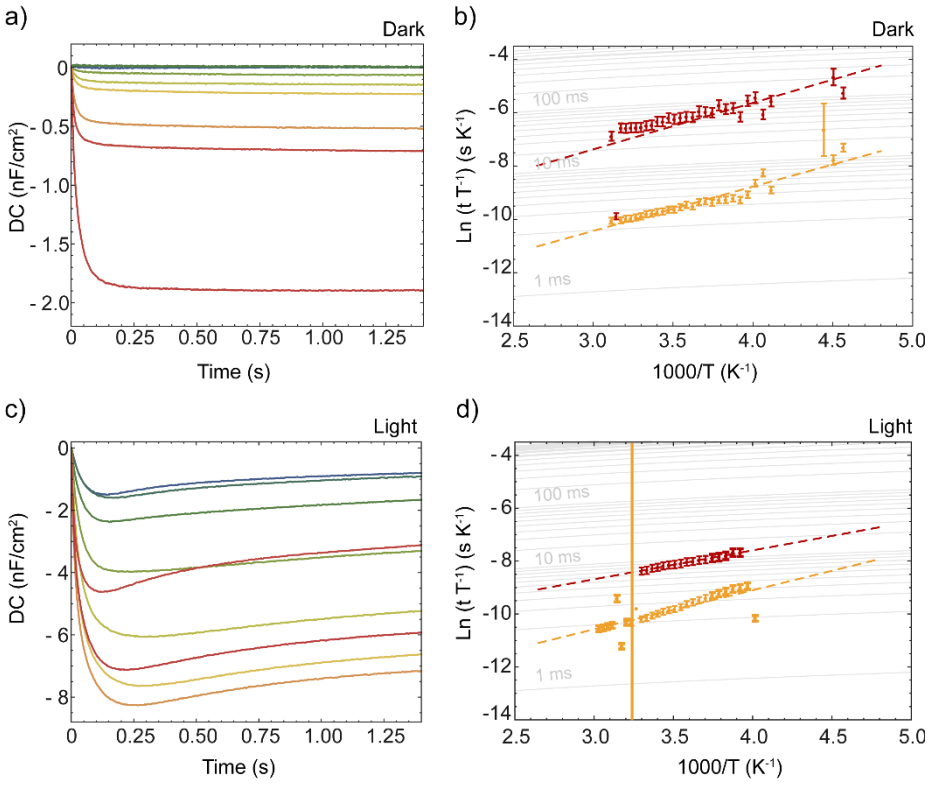


**Figure A4.12.** Relative difference in the capacitance transients $\Delta C = C(t) - C_0$ of a $MAPb(I_{0.8}Br_{0.2})_3$ solar cell (ITO/$NiO_x$/Perovskite/$C_{60}$/BCP/Ag) measured with a DC voltage of 0 V and an AC voltage of 20 mV at 10 kHz, after applying a pulse of 1.5 V for 2 seconds, between 210 K (blue) and 330 K (red) **a)** in dark, and **b)** in light. **c)** Arrhenius plots of the same composition in dark and **d)** in light. In both conditions, the negative transient corresponding to halide migration is decomposed into two contributions, shown here in red and orange.

**Table 4.3.** Characteristics of mobile halide ions in $MAPb(Br_{0.2}I_{0.8})_3$, under light-soaking and dark conditions

| | $E_a$ (eV) | D at 300 K ($cm^2s^{-1}$) | $N_{ion}$ ($cm^{-3}$) |
|---|---|---|---|
| **Dark** | $0.15 \pm 0.03$<br>$0.14 \pm 0.01$ | $(8.5 \pm 22) \times 10^{-12}$<br>$(1.9 \pm 1.5) \times 10^{-10}$ | $(1.2 \pm 0.3) \times 10^{16}$ |
| **Light** | $0.09 \pm 0.01$<br>$0.13 \pm 0.02$ | $(3.9 \pm 0.8) \times 10^{-11}$<br>$(2.3 \pm 3.6) \times 10^{-10}$ | $(4.3 \pm 1.3) \times 10^{16}$ |

# 4.8. References


(1) Yuan, H.; Debroye, E.; Janssen, K.; Naiki, H.; Steuwe, C.; Lu, G.; Moris, M.; Orgiu, E.; Uji-I, H.; De Schryver, F.; et al. Degradation of Methylammonium Lead Iodide Perovskite Structures through Light and Electron Beam Driven Ion Migration. *J. Phys. Chem. Lett.* **2016**, *7* (3). https://doi.org/10.1021/acs.jpclett.5b02828.

(2) Hoke, E. T.; Slotcavage, D. J.; Dohner, E. R.; Bowring, A. R.; Karunadasa, H. I.; McGehee, M. D. Reversible Photo-Induced Trap Formation in Mixed-Halide Hybrid Perovskites for Photovoltaics. *Chem. Sci.* **2015**, *6* (1). https://doi.org/10.1039/c4sc03141e.

(3) Slotcavage, D. J.; Karunadasa, H. I.; McGehee, M. D. Light-Induced Phase Segregation in Halide-Perovskite Absorbers. *ACS Energy Letters*. **2016**, *1* (6). https://doi.org/10.1021/acsenergylett.6b00495.

(4) Razera, R. A. Z.; Jacobs, D. A.; Fu, F.; Fiala, P.; Dussouillez, M.; Sahli, F.; Yang, T. C. J.; Ding, L.; Walter, A.; Feil, A. F.; et al. Instability of P-i-n Perovskite Solar Cells under Reverse Bias. *J. Mater. Chem. A* **2020**, *8* (1). https://doi.org/10.1039/c9ta12032g.

(5) Eperon, G. E.; Stranks, S. D.; Menelaou, C.; Johnston, M. B.; Herz, L. M.; Snaith, H. J. Formamidinium Lead Trihalide: A Broadly Tunable Perovskite for Efficient Planar Heterojunction Solar Cells. *Energy Environ. Sci.* **2014**, *7* (3). https://doi.org/10.1039/c3ee43822h.

(6) Jeon, N. J.; Noh, J. H.; Yang, W. S.; Kim, Y. C.; Ryu, S.; Seo, J.; Seok, S. Il. Compositional Engineering of Perovskite Materials for High-Performance Solar Cells. *Nature* **2015**, *517* (7535). https://doi.org/10.1038/nature14133.

(7) Noh, J. H.; Im, S. H.; Heo, J. H.; Mandal, T. N.; Seok, S. Il. Chemical Management for Colorful, Efficient, and Stable Inorganic-Organic Hybrid Nanostructured Solar Cells. *Nano Lett.* **2013**, *13* (4). https://doi.org/10.1021/nl400349b.

(8) Zhang, F.; Zhong, H.; Chen, C.; Wu, X.; Hu, X.; Huang, H.; Han, J.; Zou, B.; Dong, Y. Brightly Luminescent and Color-Tunable Colloidal $CH_3NH_3PbX_3$ (X = Br, I, Cl) Quantum Dots: Potential Alternatives for Display Technology. *ACS Nano* **2015**, *9* (4). https://doi.org/10.1021/acsnano.5b01154.

(9) Adjokatse, S.; Fang, H. H.; Loi, M. A. Broadly Tunable Metal Halide Perovskites for Solid-State Light-Emission Applications. *Materials Today*. **2017**, *20* (8). https://doi.org/10.1016/j.mattod.2017.03.021.

(10) McMeekin, D. P.; Sadoughi, G.; Rehman, W.; Eperon, G. E.; Saliba, M.; Hörantner, M. T.; Haghighirad, A.; Sakai, N.; Korte, L.; Rech, B.; et al. A Mixed-Cation Lead Mixed-Halide Perovskite Absorber for Tandem Solar Cells. *Science* **2016**, *351* (6269). https://doi.org/10.1126/science.aad5845.

(11) Christians, J. A.; Habisreutinger, S. N.; Berry, J. J.; Luther, J. M. Stability in Perovskite Photovoltaics: A Paradigm for Newfangled Technologies. *ACS Energy Letters*. **2018**, *3* (9). https://doi.org/10.1021/acsenergylett.8b00914.

(12) Futscher, M. H.; Lee, J. M.; McGovern, L.; Muscarella, L. A.; Wang, T.; Haider, M. I.; Fakharuddin, A.; Schmidt-Mende, L.; Ehrler, B. Quantification of Ion Migration in $CH_3NH_3PbI_3$ Perovskite Solar Cells by Transient Capacitance Measurements. *Mater. Horiz.* **2019**, *6* (7). https://doi.org/10.1039/C9MH00445A.

(13) Elmelund, T.; Seger, B.; Kuno, M.; Kamat, P. V. How Interplay between Photo and Thermal Activation Dictates Halide Ion Segregation in Mixed Halide Perovskites. *ACS Energy Lett.* **2020**, *5* (1). https://doi.org/10.1021/acsenergylett.9b02265.

(14) Ehrler, B.; Hutter, E. M. Routes toward Long-Term Stability of Mixed-Halide Perovskites. *Matter* **2020**, *2* (4). https://doi.org/10.1016/j.matt.2020.03.005.

(15) Joon Yoon, S.; Draguta, S.; S. Manser, J.; Sharia, O.; F. Schneider, W.; Kuno, M.; V. Kamat, P. Tracking Iodide and Bromide Ion Segregation in Mixed Halide Lead Perovskites during Photoirradiation. *ACS Energy Lett.* **2016**, *1* (1). https://doi.org/10.1021/acsenergylett.6b00158.

(16) Barker, A. J.; Sadhanala, A.; Deschler, F.; Gandini, M.; Senanayak, S. P.; Pearce, P. M.; Mosconi, E.; Pearson, A. J.; Wu, Y.; Srimath Kandada, A. R.; et al. Defect-Assisted Photoinduced Halide Segregation in Mixed-Halide Perovskite Thin Films. *ACS Energy Lett.* **2017**, *2* (6). https://doi.org/10.1021/acsenergylett.7b00282.

(17) Yang, X.; Yan, X.; Wang, W.; Zhu, X.; Li, H.; Ma, W.; Sheng, C. X. Light Induced Metastable Modification of Optical Properties in CH3NH3PbI3-XBrx Perovskite Films: Two-Step Mechanism. *Org. Electron.* **2016**, *34*. https://doi.org/10.1016/j.orgel.2016.04.020.

(18) Hu, M.; Bi, C.; Yuan, Y.; Bai, Y.; Huang, J. Stabilized Wide Bandgap $MAPbBr_xI_{3-x}$ Perovskite by Enhanced Grain Size and Improved Crystallinity. *Adv. Sci.* **2015**, *3* (6). https://doi.org/10.1002/advs.201500301.

(19) Ruth, A.; Brennan, M. C.; Draguta, S.; Morozov, Y. V.; Zhukovskyi, M.; Janko, B.; Zapol, P.; Kuno, M. Vacancy-Mediated Anion Photosegregation Kinetics in Mixed Halide Hybrid Perovskites: Coupled Kinetic Monte Carlo and Optical Measurements. *ACS Energy Lett.* **2018**, *3* (10). https://doi.org/10.1021/acsenergylett.8b01369.

(20) Knight, A. J.; Wright, A. D.; Patel, J. B.; McMeekin, D. P.; Snaith, H. J.; Johnston, M. B.; Herz, L. M. Electronic Traps and Phase Segregation in Lead Mixed-Halide Perovskite. *ACS Energy Lett.* **2019**, *4* (1). https://doi.org/10.1021/acsenergylett.8b02002.

(21) Beal, R. E.; Hagström, N. Z.; Barrier, J.; Gold-Parker, A.; Prasanna, R.;

Bush, K. A.; Passarello, D.; Schelhas, L. T.; Brüning, K.; Tassone, C. J.; et al. Structural Origins of Light-Induced Phase Segregation in Organic-Inorganic Halide Perovskite Photovoltaic Materials. *Matter* **2020**, *2* (1). https://doi.org/10.1016/j.matt.2019.11.001.

(22) Dang, H. X.; Wang, K.; Ghasemi, M.; Tang, M. C.; De Bastiani, M.; Aydin, E.; Dauzon, E.; Barrit, D.; Peng, J.; Smilgies, D. M.; et al. Multi-Cation Synergy Suppresses Phase Segregation in Mixed-Halide Perovskites. *Joule* **2019**, *3* (7). https://doi.org/10.1016/j.joule.2019.05.016.

(23) Xu, J.; Boyd, C. C.; Yu, Z. J.; Palmstrom, A. F.; Witter, D. J.; Larson, B. W.; France, R. M.; Werner, J.; Harvey, S. P.; Wolf, E. J.; et al. Triple-Halide Wide-Band Gap Perovskites with Suppressed Phase Segregation for Efficient Tandems. *Science* **2020**, *367* (6482). https://doi.org/10.1126/science.aaz4639.

(24) Rehman, W.; McMeekin, D. P.; Patel, J. B.; Milot, R. L.; Johnston, M. B.; Snaith, H. J.; Herz, L. M. Photovoltaic Mixed-Cation Lead Mixed-Halide Perovskites: Links between Crystallinity, Photo-Stability and Electronic Properties. *Energy Environ. Sci.* **2017**, *10* (1). https://doi.org/10.1039/c6ee03014a.

(25) Hopper, T. R.; Gorodetsky, A.; M. Frost, J.; Müller, C.; Lovrincic, R.; A. Bakulin, A. Ultrafast Intraband Spectroscopy of Hot-Carrier Cooling in Lead-Halide Perovskites. *ACS Energy Lett.* **2018**, *3* (9). https://doi.org/10.1021/acsenergylett.8b01227.

(26) Muscarella, L. A.; Hutter, E. M.; Frost, J. M.; Grimaldi, G. G.; Versluis, J.; Bakker, H. J.; Ehrler, B. Accelerated Hot-Carrier Cooling in $MAPbI_3$ perovskite by Pressure-Induced Lattice Compression. *J. Phys. Chem. Lett.* **2021**, *12* (17). https://doi.org/10.1021/acs.jpclett.1c00676.

(27) Jaffe, A.; Lin, Y.; Beavers, C. M.; Voss, J.; Mao, W. L.; Karunadasa, H. I. High-Pressure Single-Crystal Structures of 3D Lead-Halide Hybrid Perovskites and Pressure Effects on Their Electronic and Optical Properties. *ACS Cent. Sci.* **2016**, *2* (4). https://doi.org/10.1021/acscentsci.6b00055.

(28) Katsura, T.; Tange, Y. A Simple Derivation of the Birch–Murnaghan Equations of State (EOSs) and Comparison with EOSs Derived from Other Definitions of Finite Strain. *Minerals* **2019**, *9* (12). https://doi.org/10.3390/min9120745.

(29) Li, C.; Wu, P. Correlation of Bulk Modulus and the Constituent Element Properties of Binary Intermetallic Compounds. *Chem. Mater.* **2001**, *34*. https://doi.org/10.1021/cm0104203.

(30) Brennan, M. C.; Draguta, S.; V. Kamat, P.; Kuno, M. Light-Induced Anion Phase Segregation in Mixed Halide Perovskites. *ACS Energy Lett.* **2017**, *3* (1). https://doi.org/10.1021/acsenergylett.7b01151.

(31) Unger, E. L.; Kegelmann, L.; Suchan, K.; Sörell, D.; Korte, L.; Albrecht,

S. Roadmap and Roadblocks for the Band Gap Tunability of Metal Halide Perovskites. *J. Mater. Chem. A* **2017**, *5* (23). https://doi.org/10.1039/c7ta00404d.

(32) Draguta, S.; Sharia, O.; Yoon, S. J.; Brennan, M. C.; Morozov, Y. V.; Manser, J. M.; Kamat, P. V.; Schneider, W. F.; Kuno, M. Rationalizing the Light-Induced Phase Separation of Mixed Halide Organic-Inorganic Perovskites. *Nat. Commun.* **2017**, *8* (1). https://doi.org/10.1038/s41467-017-00284-2.

(33) Brivio, F.; Caetano, C.; Walsh, A. Thermodynamic Origin of Photoinstability in the $CH_3NH_3Pb(I_{1-X}Br_x)_3$ Hybrid Halide Perovskite Alloy. *J. Phys. Chem. Lett.* **2016**, *7* (6). https://doi.org/10.1021/acs.jpclett.6b00226.

(34) Feldmann, S.; Macpherson, S.; Senanayak, S. P.; Abdi-jalebi, M.; Rivett, J. P. H.; Nan, G.; Tainter, G. D.; Doherty, T. A. S.; Frohna, K.; Ringe, E.; et al. Photodoping through Local Charge Carrier Accumulation in Alloyed Hybrid Perovskites for Highly Efficient Luminescence. *Nat. Photonics* **2019**, *14* (2). https://doi.org/10.1038/s41566-019-0546-8.

(35) Eperon, G. E.; Paterno, G. M.; Sutton, R. J.; Zampetti, A.; Haghighirad, A. A.; Cacialli, F.; Snaith, H. J. Inorganic Caesium Lead Iodide Perovskite Solar Cells. *J. Mater. Chem. A* **2015**, *3* (39). https://doi.org/10.1039/C5TA06398A.

(36) Beal, R. E.; Slotcavage, D. J.; Leijtens, T.; Bowring, A. R.; Belisle, R. A.; Nguyen, W. H.; Burkhard, G. F.; Hoke, E. T.; McGehee, M. D. Fully Inorganic Cesium Lead Halide Perovskites with Improved Stability for Tandem Solar Cells. *2017 IEEE 44th Photovolt. Spec. Conf. PVSC 2017* **2017**, *7*. https://doi.org/10.1109/PVSC.2017.8366206.

(37) Yoon, S. J.; Kuno, M.; Kamat, P. V. Shift Happens. How Halide Ion Defects Influence Photoinduced Segregation in Mixed Halide Perovskites. *ACS Energy Lett.* **2017**, *2* (7). https://doi.org/10.1021/acsenergylett.7b00357.

(38) Hutter, E. M.; Muscarella, L. A.; Wittmann, F.; Versluis, J.; McGovern, L.; Bakker, H. J.; Woo, Y.-W.; Jung, Y.-K.; Walsh, A.; Ehrler, B. Thermodynamic Stabilization of Mixed-Halide Perovskites against Phase Segregation. *Cell Reports Phys. Sci.* **2020**, *1* (8). https://doi.org/10.1016/j.xcrp.2020.100120.

(39) Futscher, M. H.; Gangishetty, M. K.; Congreve, D. N.; Ehrler, B. Quantifying Mobile Ions and Electronic Defects in Perovskite-Based Devices with Temperature-Dependent Capacitance Measurements: Frequency vs Time Domain. *J. Chem. Phys.* **2020**, *152* (4). https://doi.org/10.1063/1.5132754.

(40) Pérez-Osorio, M. A.; Lin, Q.; Phillips, R. T.; Milot, R. L.; Herz, L. M.; Johnston, M. B.; Giustino, F. Raman Spectrum of the Organic-Inorganic Halide Perovskite $CH_3NH_3PbI_3$ from First Principles and High-Resolution

Low-Temperature Raman Measurements. *J. Phys. Chem. C* **2018**, *122* (38). https://doi.org/10.1021/acs.jpcc.8b04669.

(41) Francisco-López, A.; Charles, B.; J. Weber, O.; Isabel Alonso, M.; Garriga, M.; Campoy-Quiles, M.; T. Weller, M.; R. Goñi, A. Pressure-Induced Locking of Methylammonium Cations versus Amorphization in Hybrid Lead Iodide Perovskites. *J. Phys. Chem. C* **2018**, *122* (38). https://doi.org/10.1021/acs.jpcc.8b05188.

(42) Leguy, A. M. A.; Goñi, A. R.; Frost, J. M.; Skelton, J.; Brivio, F.; Rodríguez-Martínez, X.; Weber, O. J.; Pallipurath, A.; Alonso, M. I.; Campoy-Quiles, M.; et al. Dynamic Disorder, Phonon Lifetimes, and the Assignment of Modes to the Vibrational Spectra of Methylammonium Lead Halide Perovskites. *Phys. Chem. Chem. Phys.* **2016**, *18* (39). https://doi.org/10.1039/c6cp03474h.

(43) Futscher, M. H.; Lee, J. M.; McGovern, L.; Muscarella, L. A.; Wang, T.; Haider, M. I.; Fakharuddin, A.; Schmidt-Mende, L.; Ehrler, B. Quantification of Ion Migration in $CH_3NH_3PbI_3$ Perovskite Solar Cells by Transient Capacitance Measurements, *Mater. Horizons* **2019**, *6* (7). https://doi.org/10.1039/c9mh00445a.

(44) Groeneveld, B. G. H. M.; Adjokatse, S.; Nazarenko, O.; Fang, H. H.; Blake, G. R.; Portale, G.; Duim, H.; ten Brink, G. H.; Kovalenko, M. V.; Loi, M. A. Stable Cesium Formamidinium Lead Halide Perovskites: A Comparison of Photophysics and Phase Purity in Thin Films and Single Crystals. *Energy Technol.* **2020**, *8* (4). https://doi.org/10.1002/ente.201901041.

(45) Ghosh, D.; Acharya, D.; Zhou, L.; Nie, W.; Prezhdo, O. V.; Tretiak, S.; Neukirch, A. J. Lattice Expansion in Hybrid Perovskites: Effect on Optoelectronic Properties and Charge Carrier Dynamics. *J. Phys. Chem. Lett.* **2019**, *10* (17). https://doi.org/10.1021/acs.jpclett.9b02020.

(46) Zhao, J.; Deng, Y.; Wei, H.; Zheng, X.; Yu, Z.; Shao, Y.; Shield, J. E.; Huang, J. Strained Hybrid Perovskite Thin Films and Their Impact on the Intrinsic Stability of Perovskite Solar Cells. *Sci. Adv.* **2017**, *3* (11). https://doi.org/10.1126/sciadv.aao5616.

(47) Zhao, Y. C.; Zhou, W. K.; Zhou, X.; Liu, K. H.; Yu, D. P.; Zhao, Q. Quantification of Light-Enhanced Ionic Transport in Lead Iodide Perovskite Thin Films and Its Solar Cell Applications. *Light Sci. Appl.* **2017**, *6* (5). https://doi.org/10.1038/lsa.2016.243.

(48) Lee, J. W.; Kim, S. G.; Yang, J. M.; Yang, Y.; Park, N. G. Verification and Mitigation of Ion Migration in Perovskite Solar Cells. *APL Mater.* **2019**, *7* (4). https://doi.org/10.1063/1.5085643.

(49) Feng, J. Mechanical Properties of Hybrid Organic-Inorganic $CH_3NH_3BX_3$ (B = Sn, Pb; X = Br, I) Perovskites for Solar Cell Absorbers. *APL Mater.* **2014**, *2* (8). https://doi.org/10.1063/1.4885256.

(50) Rolston, N.; Bennett-Kennett, R.; Schelhas, L. T.; Luther, J. M.;

Christians, J. A.; Berry, J. J.; Dauskardt, R. H. Comment on "Light-Induced Lattice Expansion Leads to High-Efficiency Perovskite Solar Cells." *Science* **2020**, *368* (6488). https://doi.org/10.1126/science.aay8691.

(51) Xue, D. J.; Hou, Y.; Liu, S. C.; Wei, M.; Chen, B.; Huang, Z.; Li, Z.; Sun, B.; Proppe, A. H.; Dong, Y.; et al. Regulating Strain in Perovskite Thin Films through Charge-Transport Layers. *Nat. Commun.* **2020**, *11* (1). https://doi.org/10.1038/s41467-020-15338-1.

(52) Mathew, P. S.; Mathew, P. S.; Samu, G. F.; Samu, G. F.; Janáky, C.; Kamat, P. V.; Kamat, P. V.; Kamat, P. V. Iodine (I) Expulsion at Photoirradiated Mixed Halide Perovskite Interface. Should i Stay or Should i Go? *ACS Energy Lett.* **2020**, *5* (6). https://doi.org/10.1021/acsenergylett.0c00925.

(53) Ferdani, D. W.; Pering, S. R.; Ghosh, D.; Kubiak, P.; Walker, A. B.; Lewis, S. E.; Johnson, A. L.; Baker, P. J.; Islam, M. S.; Cameron, P. J. Partial Cation Substitution Reduces Iodide Ion Transport in Lead Iodide Perovskite Solar Cells. *Energy Environ. Sci.* **2019**, *12* (7). https://doi.org/10.1039/c9ee00476a.

(54) Perdew, J. P.; Ruzsinszky, A.; Csonka, G. I.; Vydrov, O. A.; Scuseria, G. E.; Constantin, L. A.; Zhou, X.; Burke, K. Restoring the Density-Gradient Expansion for Exchange in Solids and Surfaces. *Phys. Rev. Lett.* **2008**, *100* (13). https://doi.org/10.1103/PhysRevLett.100.136406.

(55) Kresse, G.; Furthmüller, J. Efficient Iterative Schemes for Ab Initio Total-Energy Calculations Using a Plane-Wave Basis Set. *Phys. Rev. B - Condens. Matter Mater. Phys.* **1996**, *54* (16). https://doi.org/10.1103/PhysRevB.54.11169.

(56) Kresse, G.; Furthmüller, J. Efficiency of Ab-Initio Total Energy Calculations for Metals and Semiconductors Using a Plane-Wave Basis Set. *Comput. Mater. Sci.* **1996**, *6* (1). https://doi.org/10.1016/0927-0256(96)00008-0.

# 5. PRESSURE EFFECTS ON 2D PEROVSKITES

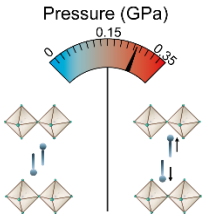


Layered 2D Dion-Jacobson (DJ) and Ruddlesden-Popper (RP) hybrid perovskite are promising materials for optoelectronic applications due to their modular structure. To fully exploit their functionality, mechanical external stimuli could be used to control their properties without changing the composition. However, the responsiveness of these systems to pressure compatible with practical applications (< 1 GPa) remains underexplored. We use hydrostatic pressure to investigate the structure-property relationships in representative iodide and bromide DJ and RP 2D perovskites based on 1,4-phenylenedimethylammonium (PDMA) and benzylammonium (BN) spacers in the 0–0.35 GPa pressure range. Pressure-dependent X-ray diffraction measurements reveal that lattices of these compositions monotonically shrink and DFT calculations provide insights into the structural changes within the organic spacer layer. These structural changes significantly affect the optical properties; the most significant shift in the optical absorption is observed in $(BN)_2PbBr_4$ under 0.35 GPa pressure, which is attributed to an isostructural phase transition. Surprisingly, the RP and DJ perovskites behave similarly under pressure, despite the different binding mode of the spacer molecules. This study provides important insights into understanding how the manipulation of the crystal structure affects the optical properties of such materials, whereas the reversibility of their response expands the perspectives for future applications.

*This chapter is based on the following work:*

L. A. Muscarella, A. Dučinskas, M. Dankl, M. Andrzejewski, N. P. M. Casati, U. Rothlisberger, D. Moia, J. Maier, M. Graetzel, B. Ehrler, J. Milic, Reversible Pressure-Dependent Mechanochromism of Dion-Jacobson and Ruddlesden-Popper Layered Hybrid Perovskites, *submitted*

# 5.1. Introduction

Layered two-dimensional (2D) hybrid perovskites have been briefly introduced in **Chapter 1.1**. These materials have attracted considerable interest due to their unique optoelectronic properties and highly modular structure that can be tailored by altering both organic and inorganic components.[1–4] These materials are composed of organic spacer (S) layers connecting adjacent perovskite slabs consisting of n layers of 3D perovskite based on the $S_xA_{n-1}M_nX_{3n+1}$ formula that involves a central (A) cation (*e.g.* $Cs^+$, methylammonium ($MA^+$), formamidinium ($FA^+$), etc.) embedded in the $\{MX_6\}$ octahedral metal-halide framework based on divalent metal ions ($Pb^{2+}$ or $Sn^{2+}$) and halide ($X^-$) anions ($I^-$, $Br^-$, or $Cl^-$). They are often broadly classified into Ruddlesden-Popper (RP)[5] and Dion-Jacobson (DJ) phases.[6] In the case of RP perovskites, the perovskite layers are displaced by half the length of the unit cell vectors along the in-plane direction (*a,b-axis*), which mostly involves monofunctional spacers ($x$ = 2),[3] whereas DJ perovskites attain the alignment in the structure without relative displacement and are commonly based on bifunctional spacer molecules ($x$ = 1; **Figure 5.1a**).[7] They are further classified based on the number of perovskites layers ($n$) which are separated by the organic spacer layer (*e.g.,* $n$ = 1, 2, 3, etc.).[2,3,8] Since the organic spacers are mostly electronically insulating, the charge carriers in these materials are predominantly confined to the inorganic slabs, resulting in natural quantum well (QW) behaviour (**Figure 5.1b**), where optical bandgaps decrease with the width of the QW because of reduced quantum confinement.[9] This implies that their optical properties can be modulated by changing the number of hybrid perovskite layers ($n$). The QW width and the potential barrier properties, which can be controlled by the spacer size, further affect the optical properties of layered perovskite materials.[10,11]

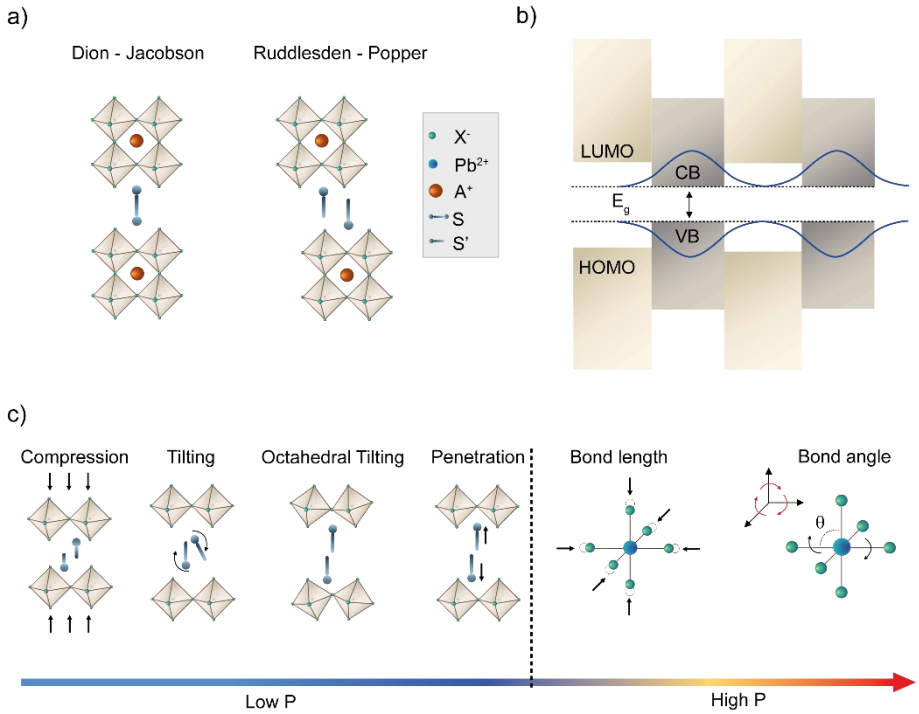


**Figure 5.1.** *Layered 2D perovskites and effect of pressure.* Schematic representation of **a)** Ruddlesden-Popper and Dion-Jacobson phases and **b)** their quantum well behaviour, with the energy bandgap ($E_g$) defined by conduction band (CB) and valence band (VB) edges of the inorganic slabs and the highest occupied (HOMO) and lowest unoccupied (LUMO) molecular orbitals of the organic spacer layer. In blue, the electronic wavefunction sitting mostly in the inorganic framework and leaking into the organic layers **c)** Illustration of the different structural changes that control the optoelectronic properties of layered hybrid perovskites by external pressure: at low pressures, the main effect is reflected in changes in the organic spacer and octahedral tilting, whereas at high pressures an additional effect on the bond length and angle is expected.

It would be of interest to control these effects on the potential barrier width without changing the perovskite composition, which can be achieved by relying on their mechanical properties and responsiveness to external stimuli, such as pressure.[12,13] Thus, understanding the structure-properties relationship in such

layered perovskites can serve as a guide to design materials with specific optical properties. Simultaneously, knowing the pressure response of these materials opens opportunities for sensing applications, and is important for other applications such as flexible solar cells where strain might be induced during operation.

The relatively low bulk modulus (*K*) of hybrid perovskites (of the order of 10s of GPa) renders them soft materials that are more easily compressible across different pressure ranges, demonstrating mechanochromic behaviour.[14–18] For comparison, halide perovskites show at least a five times smaller bulk modulus than their oxide analogues (> 100 GPa).[19,20] For 2D hybrid halide perovskites, the bulk modulus might not be an appropriate descriptor of their mechanical properties since compression in these materials is mostly anisotropic.[21,22] Alternatively, their mechanical properties can be better described by in-plane or out-of-plane Young's modulus (*E*),[23] which is more commonly used for layered perovskites as it defines the material's ability to deform along a given axis when force is applied along the similar axis. In-plane *E* is typically determined by the M–X bond strength, whereas out-of-plane *E* depends on the organic spacer.[3,24,25] An appropriate choice of organic spacers can lead to a much smaller *E* in the 2D layered perovskites than the 3D analogous,[24,25] suggesting a lower pressure threshold for tuning their optoelectronic and transport properties. The anisotropy of layered hybrid perovskites renders their compression predominant in out-of-plane (*c-axis*) direction under mild pressures.[21,22,26] This is expected to be mainly determined by the organic spacer layer and it could result in different structural changes, including the compression of the organic spacer, its tilting, increased penetration depth or octahedral tilting (**Figure 5.1c**, *left*).[21,22,26] These structural distortions are expected to change the QW structure or the M and X orbital overlaps and, consequently, optical properties. More specifically, the compression of M–X bonds lowers the optical bandgap due to increased antibonding atomic overlap between the metal and halide orbitals, whereas the deviation from the 180° angle (*i.e.* octahedral tilting) leads to an opposite effect.[27] Under higher pressures, the compressed inorganic perovskite lattice relaxes through two competing processes, namely M–X bond tilting or M–X bond

contraction (**Figure 5.1c**, *right*)[7,28] which directly affect the optoelectronic properties.[12,28]

It is of great importance to study effects in mild pressure regimes (< 1 GPa), since induced levels of strain are comparable with polaron effects,[29,30] chemical (*i.e.* conformational) strain[31,32] or strain due to lattice mismatches,[32,33] especially in 2D/3D perovskite composites.[34] In that regard, the behaviour under mild pressure may serve as a powerful tool for controlling the properties of these materials in a manner comparable to other processes inducing internal strain. However, the investigations of layered hybrid perovskites in such mild-pressure ranges are underrepresented and the differences in the pressure-dependent behaviour of RP and DJ phases remain elusive.

In this Chapter, we investigated representative DJ and RP 2D perovskites based on 1,4-phenylenedimethylammonium (PDMA) and benzylammonium (BN) spacers under hydrostatic pressure up to 0.35 GPa. These aromatic spacer moieties are closely comparable, and they have already demonstrated the capacity to form well-defined 2D perovskite phases,[27,35,36] which makes them appropriate models to analyse the differences in compression between RP and DJ type perovskites. We further study the halide effect on their structure-property relationship by comparing systems based on $(BN)_2PbX_4$ and $(PDMA)PbX_4$ compositions for X = I, Br halide counter ions by pressure-dependent optical measurements and X-ray diffraction. One would expect that RP layered perovskites are more compressible and more sensitive to external pressure due to Van der Waals interactions in organic bilayer as opposed to DJ. However, we find that the RP and DJ perovskites behave similarly under pressure, despite the different binding mode of the spacer molecules. In addition, we establish no direct pressure-dependent difference between the Br- and I-based compositions and the differences under pressure are more subtle. For all the compositions we observe that the unit cell monotonically shrinks, which is accompanied by a red shift of the optical absorption of the excitonic feature upon increasing the pressure to 0.35 GPa. $(BN)_2PbBr_4$ shows the most significant red shift of absorption of the excitonic feature (-54.9 meV) as compared to the other compositions where a comparable shift (~ -30 meV) is observed. Density functional theory (DFT) calculations reveal that this is due to the increase in Pb–Br–Pb angle which allows

BN spacers penetrating deeper into the inorganic lattice, translating into a stronger pressure response as compared to its iodide counterpart and the PDMA-based DJ systems.

## 5.2. Pressure-dependent Structural Changes

To gain insights into the pressure response of RP and DJ perovskites, we prepared iodide-based precursor solutions using the monofunctional BN and the bifunctional PDMA as organic spacers.[27,35–38] These aromatic spacers were selected based on their comparable structural features that permit the formation of phase-pure RP and DJ perovskites. While iodide-based 2D layered perovskites have been previously investigated in the GPa pressure range (1–12 GPa),[13,21] pressure studies of the bromide-based analogues are unprecedented. Although less investigated due to their high bandgap energy, a fundamental understanding on the dependence of the mechanical response on the halide species is required for designing materials for new applications.

We therefore fabricated thin films based on $(PDMA)PbX_4$ and $(BN)_2PbX_4$ (X = I, Br) compositions as described in the **Experimental Methods 5.5** section. We focused the analysis on these $n$ =1 2D systems, since they represent the most well-defined layered structures.[2,3,8] Moreover, understanding the behavior of $n$ = 1 layered perovskites provides a limiting case for the analysis of $n$ >1 systems in the future. The monofunctional spacers in RP phases form bilayers interacting via van der Waals interactions,[39] whereas bifunctional spacers in DJ layered perovskites directly connect the neighbouring perovskite slabs.[40] Accordingly, one might expect that the additional degrees of freedom in RP spacer layers would render them more compressible as compared to their DJ analogues. Similarly, the differences in the lattice parameters of iodide and bromide systems are expected to become apparent in their different behavior under pressure.[41]

Layered perovskite structure in the given thin films is confirmed by well-defined periodic diffraction patterns measured by X-ray diffraction (XRD) at ambient pressure, which exhibit the most intense basal plane reflections below 10° that are followed by higher-order reflections at the higher angles (**Figure 5.2**).

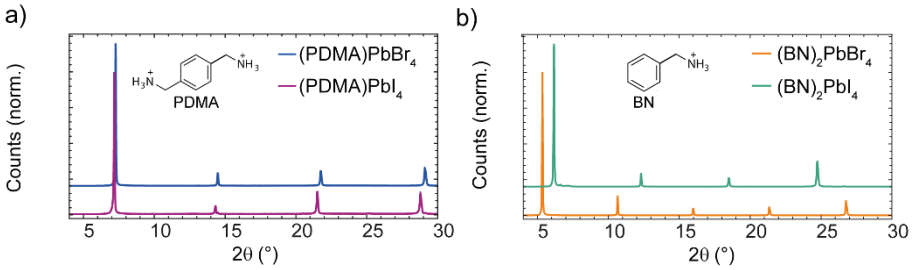


**Figure 5.2.** *Structural differences of layered 2D perovskites with bromide and iodide forming the inorganic framework*. X-Ray diffraction (Cu Kα 1.5406 Å) pattern at ambient pressure of **a)** (PDMA)$PbX_4$ and **b)** $(BN)_2PbX_4$ showing a compression of the unit cell for the PDMA-based systems when the iodide counter ion is replaced with the bromide. The opposite is observed for the BN-systems, where the presence of the bromide in the inorganic framework results in the expansion of the unit cell.

A shift towards higher angles is observed when the iodide in the PDMA-based system is replaced by the bromide (**Figure 5.2a**), in accordance with the smaller halide radius which in turn lead to smaller unit cell. On the contrary, when the iodide is replaced by bromide in the BN-based system, we observe the opposite behavior and a shift toward lower angles, indicating a larger unit cell (**Figure 5.2b**). This could suggest a difference in the packing of the spacer for different halide counter ions.

To understand this peculiar behaviour as a function of halide counter ion and to elucidate the role of the physical pressure on the structural properties of these compositions, we investigated pressure-induced changes in the lattice parameters by pressure-dependent X-ray diffraction. Diffraction data of powders for each composition were acquired using a synchrotron source at several pressure points by using a membrane diamond-anvil cell (see **Experimental Methods 5.5** and **Appendix 5.6.3** for details and the attribution of the diffraction peaks). At low pressures, the monoclinic $P2_1/c$ space group is assigned to (PDMA)$PbI_4$ and (PDMA)$PbBr_4$, the orthorhombic *Pnma* to $(BN)_2PbI_4$ and the orthorhombic $Cmc2_1$ to $(BN)_2PbBr_4$. Despite a compression along all the axes (**Figure 5.3a**), the largest compression is recorded along the *c-axis* for all systems, which is in

accordance with previous reports[21,26]. This trend is significantly more pronounced for the $(BN)_2PbBr_4$ case (**Figure 5.3b**), which shows a larger compression in the out-of-plane *c-axis* direction (-8% relative change) and an elongation of the in-plane *a* and *b axis* followed by a compression (**Figure A5.1** for absolute values of the lattice parameters).

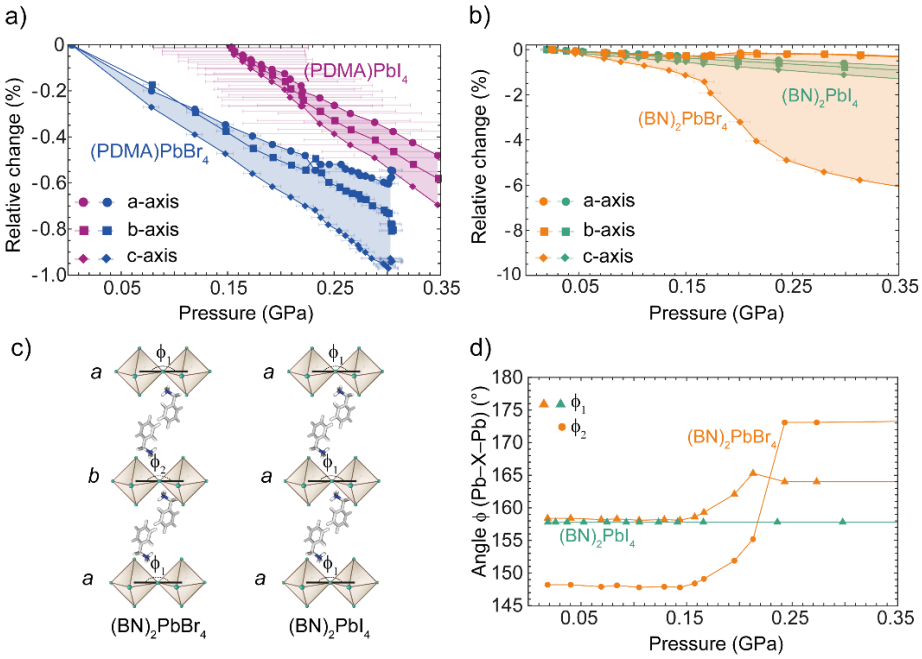


**Figure 5.3.** *Pressure-dependent X-ray diffraction with synchrotron source reveal the changes of the inorganic framework as a function of pressure.* **a)** Relative change of the lattice parameters as a function of pressure for $(PDMA)PbX_4$ and **b)** $(BN)_2PbX_4$ compositions. **c)** Schematic representation of $(BN)_2PbBr_4$ alternating inorganic sheet (*aba*) in comparison with its iodide counterpart (*aaa*) and the corresponding **d)** inter-octahedral tilting angles in $(BN)_2PbBr_4$ and $(BN)_2PbI_4$.

Further structural analysis reveals that there are two distinct values of Pb–X–Pb angles ($\phi_1$ and $\phi_2$) in $(BN)_2PbBr_4$ as compared to $(BN)_2PbI_4$, where only one value of the Pb–X–Pb angle ($\phi_1$) is found (**Figure 5.3c**). Under pressure the angle between two adjacent octahedra hardly changes in the case of $(BN)_2PbI_4$, whereas

the two Pb–Br–Pb angles in $(BN)_2PbBr_4$ both change significantly between 0.15 – 0.20 GPa, the range where also the compression along the *c-axis* is strongest (**Figure 5.3d**). Although these changes are remarkable, the *Cmc2₁* space group is maintained, meaning that $(BN)_2PbBr_4$ undergoes an isostructural phase transition in this pressure range.[42] Furthermore, to quantify at a first approximation the compressibility of the compositions in study, we calculate the isothermal bulk modulus from the pressure-volume relationship assuming mostly isotropic response to pressure by relying on the second order Birch-Murnaghan equation of state (**Appendix 5.6.4**).[43] Two distinct bulk modulus for $(BN)_2PbBr_4$ composition have been identified, which are attributed to low pressure and elevated pressure isostructural phases.[44] In addition, smaller bulk modulus obtained for $(BN)_2PbBr_4$ supports its higher susceptibility to compression.

## 5.3. Local Orientation of The Organic Spacer

Since elucidating the local orientation of the organic spacer molecules remains challenging based on the diffraction experiments, we further investigate the effect of pressure on the organic spacer layer by density functional theory (DFT) calculations. To better account for the thermal expansion of the lattice parameters at the measured temperature, the initial structures obtained from the XRD were relaxed while keeping the cell fixed at the experimentally measured values. The results suggest that the compression along the *c-axis* is due to reduced distance between the two neighboring spacers and their closer packing (**Figure 5.4a**). The initial vertical distance between the two BN spacers, *d(BN-BN),* defined from the center of the benzyl ring, is significantly larger in the case of $(BN)_2PbBr_4$ (4.43 Å) as compared to $(BN)_2PbI_4$ (2.97 Å; **Figure 5.4a**). This distance decreases by 0.4 Å for $(BN)_2PbBr_4$, whereas for the I-based analogue the decrease accounts to only 0.08 Å within the same pressure range, resulting in a larger compression for $(BN)_2PbBr_4$ (**Figure 5.4a**). In accordance with the experimental analysis, DFT calculations reveal the presence of two distinct octahedra tilting angles (calculated to be 141.5° and 154.5°) in $(BN)_2PbBr_4$ (**Figure 5.4b**). These angles are significantly lower than the one in $(BN)_2PbI_4$ (by 4° and 16°, respectively), which leads to higher distortion of the octahedra,

thereby leaving less space for the BN spacers to penetrate. The Pb–X–Pb angles in $(BN)_2PbBr_4$ were found to increase with pressure (**Figure 5.4b**), leading to higher penetration depth of the spacers in the inorganic framework (**Figure 5.4c**). This is in contrast with the comparable octahedral tilting in $(BN)_2PbI_4$ and in PDMA-based systems (**Figure A5.2a**). In addition, the penetration depth of the spacer in the inorganic framework for the other compositions changes continuously upon increasing pressure (**Figure A5.2b**). The difference in the BN-based systems could thus primarily originate from the changes in the orientation of the spacers and the penetration depth[41] into the inorganic framework, which is defined by the distance between the nitrogen atom of the ammonium group of the spacer moiety and the axial halide plane. In addition to the penetration of the spacer layer one might expect also the Pb-X bond length to change under pressure. The equatorial Pb–Br bond lengths in $(BN)_2PbBr_4$ at low pressure (2.98 Å and 3.02 Å; **Figure A5.2c**) are smaller than the ones in $(BN)_2PbI_4$ (3.21 Å and 3.25 Å; **Figure A5.2c**), leading to a denser octahedral packing and, in turn, a significantly lower penetration into the Pb–Br lattice at ambient pressure. These structural differences in the low-pressure structures also translate into different responses to external pressure. However, the axial Pb–X bond lengths (**Figure A5.2c**) remain constant over the entire pressure range. This implies that the measured compressions are not caused by changes in the bond lengths of Pb–X. Instead, the response to mild pressure is the result to changes in the packing in the organic spacer layer (**Figure A5.3**). While $(BN)_2PbI_4$ and $(PDMA)PbX_4$ show no significant change, the two BN spacers in $(BN)_2PbBr_4$ move closer together (**Table 5.2**, **Table 5.3**, **Table 5.4**, **Table 5.5**). Our calculations reveal that in the pressure range between 0.164 GPa to 0.213 GPa the BN spacers penetrate deeper into the inorganic lattice of $PbBr_4$ (**Figure 5.4c**).

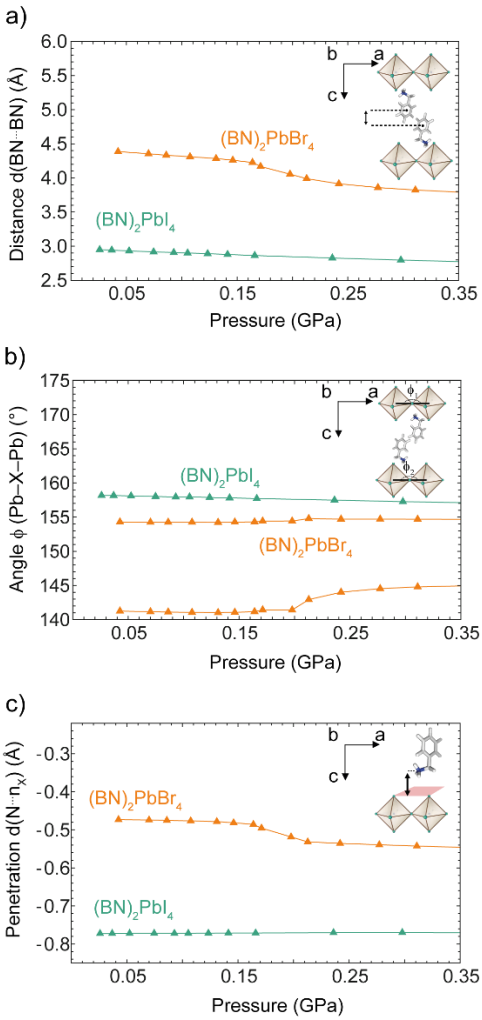


**Figure 5.4.** *Calculated location of the organic spacer and inteoctahedral angles as a function of pressure.* Calculated **a)** average distances of the (vertically) neighboring BN rings *d(BN···BN)* in the RP layer; **b)** average Pb–X–Pb angles in the Pb–X planes *ϕ(Pb–X–Pb)* as a measure of the equatorial tilting of the octahedra; and **c)** nitrogen penetration depth in the halide plane *d(N···nX)* as a measure of the penetration depth from DFT optimized structures (PBEsol).

It is important to note that the zero is set at the halide planes and larger penetration corresponds to more negative values. This process is accompanied by

a decrease in the BN tilting angle, $\phi(BN\cdots n_{PbX})$, defined as the angle between the *c-axis* and the benzyl plane (**Figure A5.2d**). Such a change corresponds to a rearrangement of the BN spacers into a more parallel orientation with respect to the *c-axis* (**Figure A5.2d**). Consequently, the significant change in the distance between the neighbouring BN groups is in accordance with the experimental observation of a larger compression for $(BN)_2PbBr_4$. Such changes in the assembly of the spacer layer in response to pressure are further reflected in their optical properties.

## 5.4. Pressure-dependent Mechanocromism

To assess the mechanochromic properties, we monitored the optical absorption energy of the excitonic feature as a function of applied external stress by measuring pressure-dependent absorption spectra of $(PDMA)PbX_4$ and $(BN)_2PbX_4$ (X = Br, I). The samples were placed inside a hydrostatic pressure cell filled with an inert liquid (tetradecafluorohexane, FC-72, **Experimental Methods 5.5** and schematically depicted in **Figure 5.5a**). We applied pressure from 0 to 0.350 GPa in steps of 0.050 GPa through a manual pump. Quantum and dielectric confinement effects give rise to an intense and narrow excitonic feature (**Figure A5.4**), typical of layered 2D perovskites.[45,46] We observe a continuous shift of the excitonic peak toward lower energies for all analysed layered perovskite compositions (**Figure 5.5b-e**). In addition, the red-shift confirms that a mild external pressure can be sufficient to tune the optical properties in these materials. Similarly, pressure-dependent photoluminescence measurements show a red-shift toward smaller energy upon increasing pressure (**Figure A5.5**). We obtained the excitonic peak energy of the $(PDMA)PbI_4$ and $(BN)_2PbI_4$ as a function of pressure fitting a skewed Gaussian function to optical spectra measured. At ambient pressure, the excitonic peak energy of $(PDMA)PbI_4$ and $(BN)_2PbI_4$ is 2.41 eV and 2.36 eV, respectively.

Upon increasing the pressure, the excitonic-peak shift at 0.30 GPa as compared to ambient pressure is about (-25 ± 0.6) meV for $(PDMA)PbI_4$ and (-27 ± 1) meV for $(BN)_2PbI_4$ (**Figure 5.5f**). We observed a similar linear trend for both RP and DJ perovskites until 0.30 GPa, where the response to external

pressure causes a comparable energy shift. From 0.30 GPa onward, the $(BN)_2PbI_4$ appears to shift to a larger extent in comparison with the $(PDMA)PbI_4$, showing an energy shift of (-33 ± 1) meV and (-27 ± 0.5) meV, respectively.

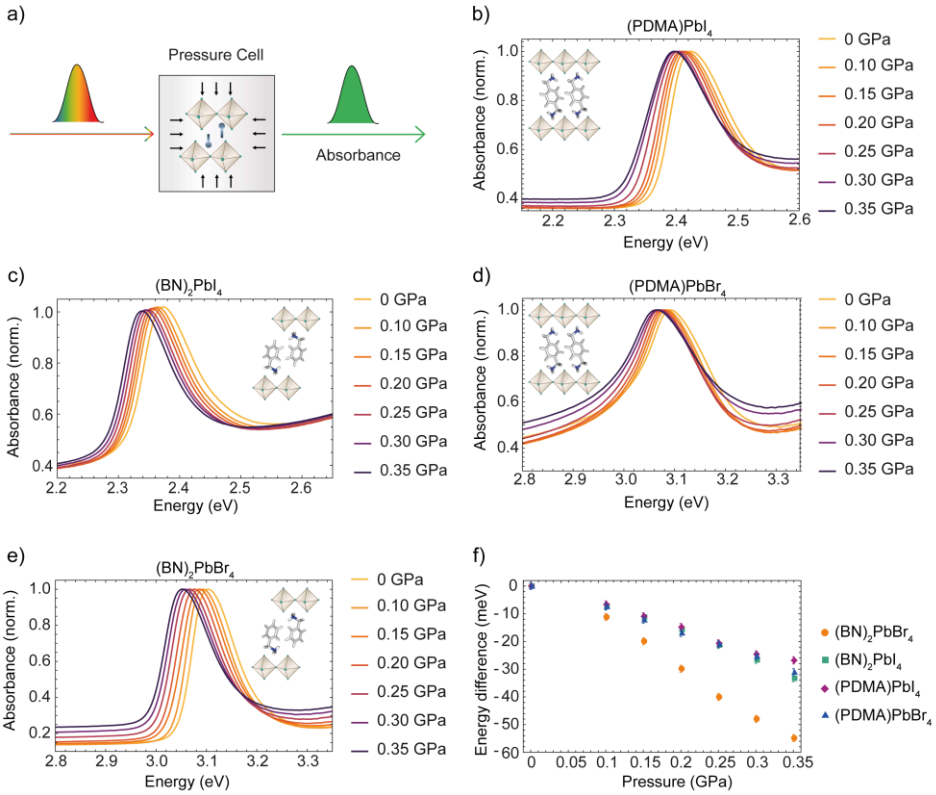


**Figure 5.5.** *Optical measurements reveal a red-shift of the excitonic feature.* Schematic of the **a)** experimental setup for pressure-dependent absorption measurements and **b)** pressure-dependent absorbance collected $(PDMA)PbI_4$, **c)** $(BN)_2PbI_4$, **d)** $(PDMA)PbBr_4$ and **e)** $(BN)_2PbI_4$ from ambient to 0.35 GPa. The inset shows a schematic representation of the layered structures. **f)** Energy difference of the excitonic peak energy as a function of applied pressure.

Further investigations at pressures above 0.35 GPa are not possible with the same experimental setup because of the limitations of the windows of the hydrostatic pressure cell. Moreover, monitoring the shift of the excitonic peak by its maximum intensity reveals the same slope as fitting the skewed Gaussian with a

larger error given by the resolution of the measurement (**Figure A5.6** and **Table 5.6**, **Table 5.7**, **Table 5.8**, **Table 5.9**). Considering the bromide analogues, the excitonic peak energy is 3.06 eV and 3.07 eV for (PDMA)$PbBr_4$ and $(BN)_2PbBr_4$, respectively. Upon increasing the pressure from ambient to 0.35 GPa, the energy shifts for both (PDMA)$PbBr_4$ and $(BN)_2PbBr_4$ by (-31 ± 1) meV and (-55 ± 0.2) meV, respectively. The $(BN)_2PbBr_4$ perovskite, despite showing a red-shift as a function pressure, has a notably larger energy shift than its iodide counterpart and the PDMA-based systems (**Figure 5.5f** and **Table 5.6**, **Table 5.7**, **Table 5.8** and **Table 5.9**). To sum up, the energy shifts in iodide-based samples are closely corresponding to each other, which suggest that pressure-dependent properties are comparable for RP and DJ phases. However, bromide-based systems show contrasting differences, with $(BN)_2PbBr_4$ having remarkably larger shifts than (PDMA)$PbBr_4$ and the I-based systems.

The expected change in the bandgap was calculated for all the compositions by DFT (**Figure A5.7**, **Table 5.10**, **Table 5.11**,

**Table 5.12**, **Table 5.13**) to observe qualitative variations of the bandgaps as a function of pressure, which corroborate with the experimental results. The larger red shift in $(BN)_2PbBr_4$ is in accordance with the significantly larger compressibility of $(BN)_2PbBr_4$ as compared to its iodide-based analogue and the PDMA-based systems (**Figure A5.10**). Furthermore, the isostructural phase transition induced by the reduction of octahedral tilting (*i.e.* the Pb–Br–Pb tilting is closer to 180° at the highest pressure measured) is associated with the change of penetration depth of the BN spacers into the perovskite lattice, which in turn favours a larger red shift of the optical absorption. Finally, we can directly correlate the experimental structural parameters obtained by pressure-dependent XRD measurements with the change in the optical absorption.

The relationship between the shift in the exciton absorption peak and the length of the *c-axis* is linear for both PDMA-based and BN-based samples (**Figure 5.6a,b**), with the exception in $(BN)_2PbBr_4$, where we observe two different regimes which attributed to the isostructural phase transition.

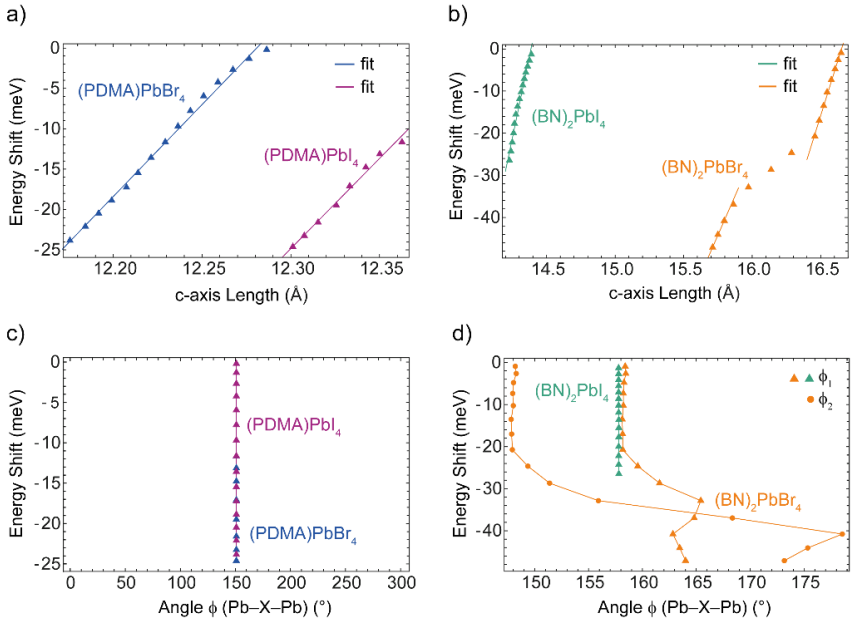


**Figure 5.6.** *Optical properties dependency on the compression of the c-axis and interoctahedral angles.* Optical absorption shift in meV as a function of **a)** the *c-axis* length for PDMA-systems and **b)** BN-systems, and as a function of the Pb–X–Pb angles for **c)** for PDMA-systems and **d)** BN-systems based on the experimental data.

A linear fit of the energy shift as a function of the c-axis length results in a slope of 0.227 eV/Å, 0.223 eV/Å for (PDMA) and $PbBr_4$ $(PDMA)PbI_4$, respectively. We obtain a slope of 0.156 eV/Å for $(BN)_2PbI_4$, 0.104 eV/Å and 0.074 eV/Å for $(BN)_2PbBr_4$ below and above the isostructural phase transition, respectively (**Figure 5.6a,b**). This finding suggests a larger dependency of the PDMA systems on the change of the *c-axis* compared to the BN systems. No correlation is observed between Pb–X–Pb angle and the optical properties (**Figure 5.6c,d**), except in the case of isostructural phase transition regime in $(BN)_2PbBr_4$ (**Figure 5.6d**). Thus, we find that in the representative DJ and RP layered 2D perovskites presented in this study, the bandgap change is largely caused by the compression of the *c-axis* which is expected because of the reduced quantum confinement but no correlation is found with the Pb–X–Pb angles within the same structural phase.

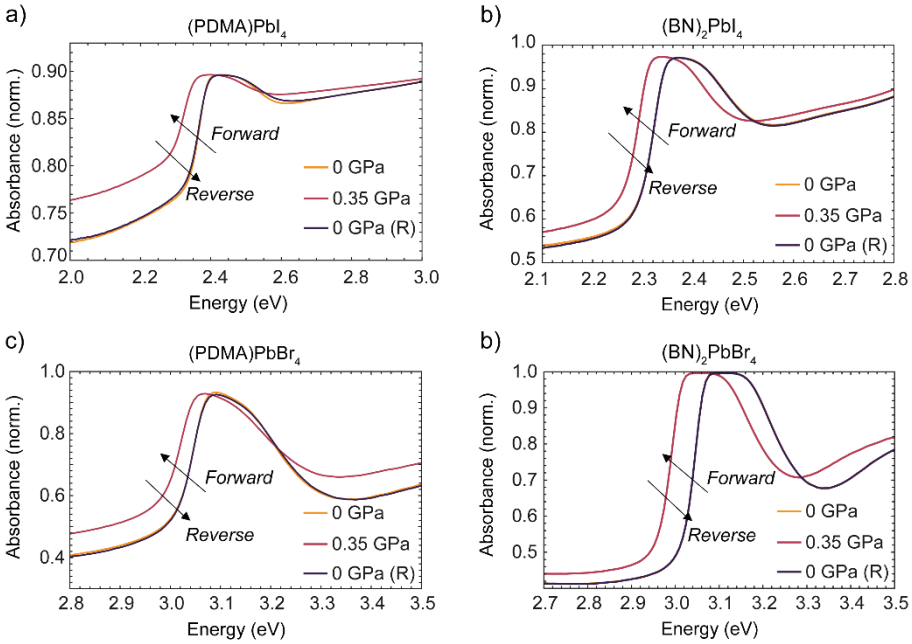


**Figure 5.7.** *Fully reversible mechanochromism.* Pressure-dependent absorption recorded at three characteristic pressures in the upward and downward direction for **a)** $(PDMA)PbI_4$ and **b)** $(BN)_2PbI_4$, **c)** $(PDMA)PbBr_4$ and **d)** $(BN)_2PbBr_4$.

The shift of the excitonic peak is fully recovered for both $I^-$ and $Br^-$ based RP and DJ perovskite samples upon decompression from 0.35 GPa to ambient pressure, implying that the process is reversible in this pressure range. The corresponding absorption spectra of both materials almost perfectly overlap in shape and intensity after decompression (**Figure 5.7**). The reversibility of the optical features strongly suggests structural reversibility, which is in agreement with the DFT predictions and in contrast with the amorphization commonly reported at higher pressures.[47–49] This reversibility of the mechanochromic response of layered hybrid perovskites is of interest to their use as model systems for elucidating structure-property relationships in hybrid layered materials, provides promise for the long-term stability of flexible perovskite devices, but also points towards the use of mechanophores in the development of various smart materials and pressure sensors.[50–52]

# 5.4. Conclusion

In summary, we reported a direct comparison of the response of iodide and bromide-based RP and DJ 2D perovskites to pressure by using comparable aromatic spacer moieties, namely benzylammonium (BN) and 1,4-phenylenedimethylammonium (PDMA), respectively. We applied a mild pressure up to 0.35 GPa to all the compositions and detected a red shift of the excitonic peak upon increasing the pressure. Whereas PDMA-based DJ perovskites were not found to be susceptible to changes associated with the halide ion, BN-based perovskite results in a larger shift of the optical absorption associated with the excitonic feature in bromide-based compositions that is in contrast with their higher expected level of rigidity. Furthermore, X-ray diffraction experiments in conjunction with DFT calculations under pressure suggest that this effect is related to the structural properties of the 2D perovskite phases. Specifically, X-ray diffraction experiments reveal the presence of an isostructural phase transition in $(BN)_2PbBr_4$ that maintain the orthorhombic C$mc2_1$ space group, whereas no phase transition is detected for the other compositions. DFT computations further indicate that this isostructural space group transition is associated with a decrease in the octahedra tilting which leads to an increased penetration depth of the BN spacers into the Pb–Br lattice. These changes explain the large compression of $(BN)_2PbBr_4$ under mild pressures up to 0.350 GPa. This study thereby provides important insights into the mechanochromic properties of layered hybrid perovskites. Finally, the unique reversibility of their mechanochromic response in this mild pressure range opens new perspective towards the utility of layered hybrid perovskites as platforms for amphidynamic materials[53,54] and mechanophores,[50–52] which expands the perspectives for their future applications.

# 5.5. Experimental Methods

### Sample Preparation

Iodide-based solutions were obtained mixing $PbI_2$ and $(PDMA)I_2$ powders in 1:1 stoichiometric ratio for $(PDMA)PbI_4$, whereas 1:2 ratio of $PbI_2$:(BN)I for $(BN)_2PbI_4$. Subsequently, solid mixtures were dissolved in the *N*,*N*-dimethylformamide (DMF) and dimethyl sulfoxide (DMSO) solvent mixture (4:1, v/v) to obtain 0.2 M solution. Bromide-based solutions were made mixing $PbBr_2$:$(PDMA)Br_2$ in 1:1 ratio for $(PDMA)PbBr_4$ and in 1:2 $PbBr_2$:(BN)Br for $(BN)_2PbBr_4$. The mixtures were then dissolved in (DMF:DMSO) (1:1, v/v) solvent to obtain 0.2 M solution. All the films were solution-processed by spin-coating. Before deposition, the glass substrates were ultrasonically cleaned with acetone and ethanol sequentially for 5 min, followed by UV-Ozone cleaning/treatment for 15 min. Precursor solution was dropped on the glass substrate (Assitent 50), which was afterwards spun at 1000 rpm and 4000 rpm for 10 s and 20 s, respectively. Spin-coated films were annealed on a hot plate at 150 °C for 10 min. Solution preparation was carried out in an argon atmosphere glovebox (0.5 ppm < $O_2$ and 0.5 ppm < $H_2O$), whereas sample deposition in the dry air glovebox ( $RH \approx 5\%$). Perovskite powders were prepared using mechanosynthesis by grinding in a ball mill (Retsch Ball Mill MM-200) using a grinding jar (10 ml) and a ball (⌀10 mm) for 30 min at 25 Hz. The molar ratios of all the precursors were stoichiometric and the resulting powders were annealed at 150 °C for 30 min.

### Pressure-dependent absorption

We measured pressure-dependent absorption using a LAMBDA 750 UV/Vis/NIR Spectrophotometer (Perkin Elmer). The samples are placed inside a pressure cell (ISS Inc.) filled with inert liquid (perfluorohexane, FC-72, 3M). The increase in the volume of the liquid inside the pressure cell upon pumping generates high pressure. Measurements are performed from ambient pressure to 0.350 GPa, in steps of 0.050 GPa, and we waited 7 min before measuring at each pressure to ensure equilibration under pressure. Prior to use, the liquid is degassed in a Schlenk line to remove oxygen, responsible for scattering of light above 0.3

GPa and consequent reduction of the transmitted signal. We estimate an error of the reading of 0.020 GPa.

### X-Ray Diffraction

Measurements of perovskite thin films were carried out using PANalytical Empyrean Series 2 instrument in Bragg-Brentano configuration with Cu Kα radiation at 40 kV voltage and 40 mA current. A nickel filter was used to reduce Kβ contribution. X-rays were detected using a PIXcel3d detector.

### Steady-State Photoluminescence

We measured photoluminescence (PL) with a home-built setup equipped with a 405 nm CW laser source (S1FC405, Thorlabs) for the iodide-based perovskite composition (PDMA-I and BN-I). The PL was coupled into a fiber connected to an OceanOptics USB4000 spectrometer. To remove the excitation laser from the acquired signal, a long-pass filter LP500 was mounted before the spectrometer. An integration time of 1 second was used for each measurement. To measure the PL of bromide-based perovskite composition (PDMA-Br and BN-Br), a 375 nm laser was used.

### Density Functional Theory

All computations were done on the DFT level of theory with the software package Quantum ESPRESSO v6.6 using ultrasoft pseudopotentials from the pslibrary 1.0.0, a wavefunction cutoff of 60 Ry, a charge density cutoff of 480 Ry, Gaussian spreading of 0.005 Ry and the semiempirical Grimme‘s DFT-D3 vdW correction.[55–57] Relaxations were performed using the PBEsol functional in which the energies and forces are converged up to $10^{-7}$ Ry and $10^{-6}$ Ry/Bohr, respectively, with the system specific converged at Γ-point centered k-point Monkhorst-Pack grid (**Table 5.1**). For the computations of the bandgap, single point energy computations were done on the relaxed structures using the Perdew-Burke-Ernzerhof (PBE) functional with a wavefunction convergence up to $10^{-8}$ Ry and (apart from $(BN)_2PbBr_4$) at higher k-point Monkhorst-Pack grid (**Table 5.1**). For each pressure, the experimentally obtained structure files are taken and

used for relaxation while keeping the cell fixed. For the PDMA based systems, a 2×2×1 supercell was created prior to relaxation.

**Table 5.1.** *k-point Monkhorst-Pack grid used for the relaxation and SPE of the systems.*

| System | Relaxation | SPE |
|---|---|---|
| $(BN)_2PbBr_4$ | 8×8×2 | 8×8×2 |
| $(BN)_2PbI_4$ | 6×6×2 | 9×10×3 |
| $(PDMA)PbX_4$ (X=Br,I) | 4×4×6 | 6×6×9 |

### High-pressure powder X-Ray diffraction

High-pressure powder X-ray diffraction measurements were performed with synchrotron radiation in the Swiss Light Source (λ= 0.49217Å and Pilatus 6M detector).[58] The samples were compressed in a membrane diamond-anvil cell using DAPHNA oil as medium. Prior to the measurement, the cell is pre-pressurized applying a pressure of 3-4 bars on the membrane to avoid leaks and ensure a good sealing of the cell. This results in a slightly higher value for the first datapoint with respect to ambient pressure. We note that the response of the membrane used to measure the $(PDMA)PbBr_4$ is higher than for the other compositions, resulting in higher starting pressure. We used α-quartz as a pressure calibrant, blended with a sample, and diffraction patterns of the mixture were collected. The equation of state of quartz was used to determine pressure with accuracy of approximately 0.005 GPa.[59] Raw data was processed in Dioptas[60] extracting patterns of the mixtures after masking diffraction spots from the diamonds. PXRD patterns were treated with TOPAS software and unit-cell parameters were determined using Rietveld refinement.[61,62]

# 5.6. Appendix

## 5.6.1. Additional Figures

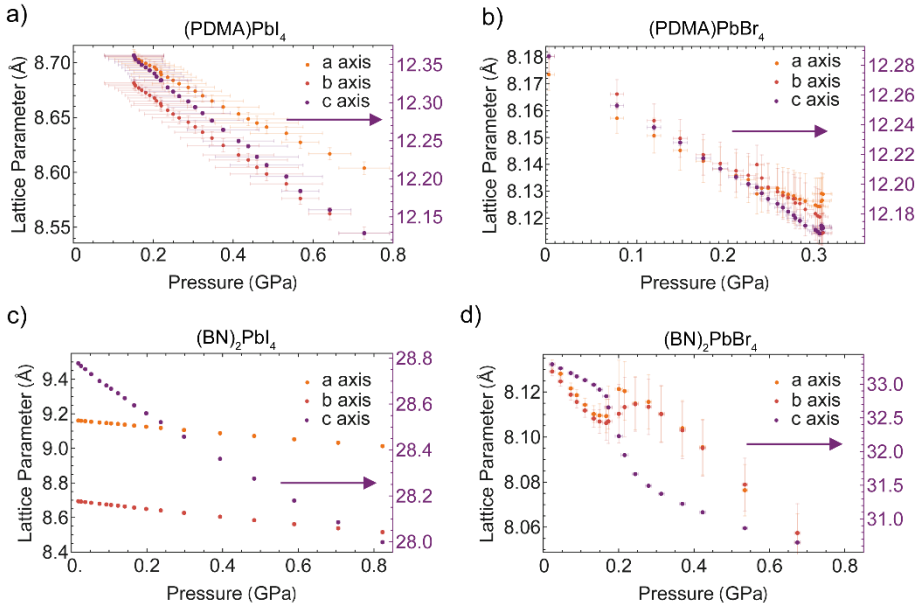


**Figure A5.1**. Lattice parameters as a function of pressure obtained from Rietveld refinements of diffraction patterns for **a)** (PDMA)$PbI_4$, **b)** $(BN)_2PbI_4$, **c)** (PDMA)$PbBr_4$, **d)** $(BN)_2PbBr_4$. The right axis refers to the *c-axis* (in purple).

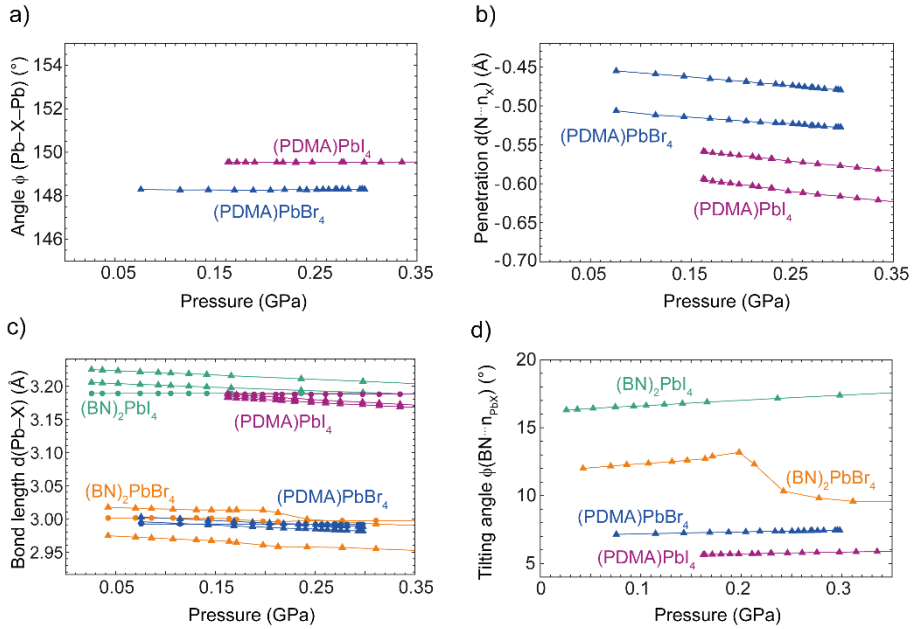


**Figure A5.2.** Computed **a)** *ϕ(Pb–X–Pb)* tilting angle and **b)** nitrogen penetration depth in the plane formed by the halide atoms *d(N···n$_X$)*. The penetration depths of the two nitrogen in the PDMA spacer are not equivalent. Computed **c)** average equatorial (triangle) and axial (disk) Pb–X bond lengths *d(Pb–X)*. The octahedra has two inequivalent equatorial bonds and one axial bond and **d)** average tilting angles of the benzyl ring relative to the *c-axis ϕ(BN···n$_{PbX}$)*.

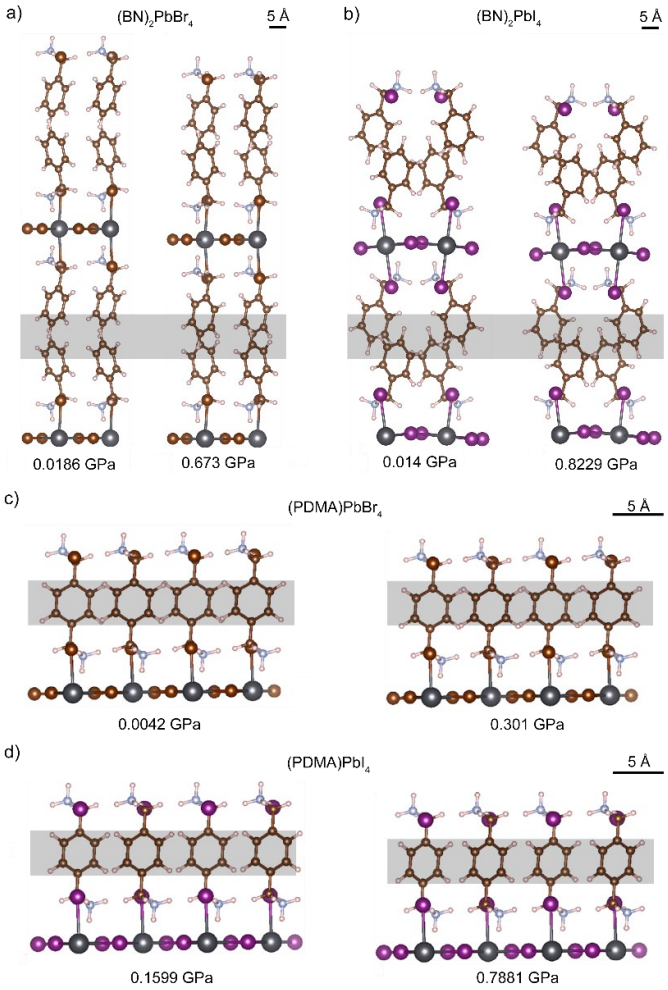


**Figure A5.3.** Relaxed structures of **a)** $(BN)_2PbBr_4$ at 0.014 GPa and at 0.673 GPa, **b)** $(BN)_2PbI_4$ at 0.0186 GPa and at 0.8229 GPa. **c)** $(PDMA)PbBr_4$ at 0.0042 GPa and at 0.3011 GPa, **d)** $(PDMA)PbI_4$ at 0.1598 GPa and 0.7881 GPa. The rectangle in grey highlights the change in the spacers' distance for all the systems at a representative low and high pressure.

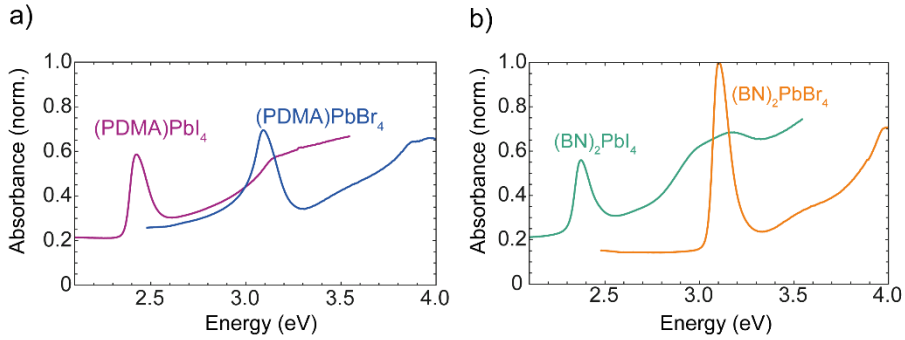


**Figure A5.4.** Normalized absorbance collected at ambient pressure for **a)** $(PDMA)PbI_4$ and $(PDMA)PbBr_4$, **b)** $(BN)_2PbI_4$ and $(BN)_2PbBr_4$ highlighting the presence of the typical excitonic feature observed in layered 2D perovskites.

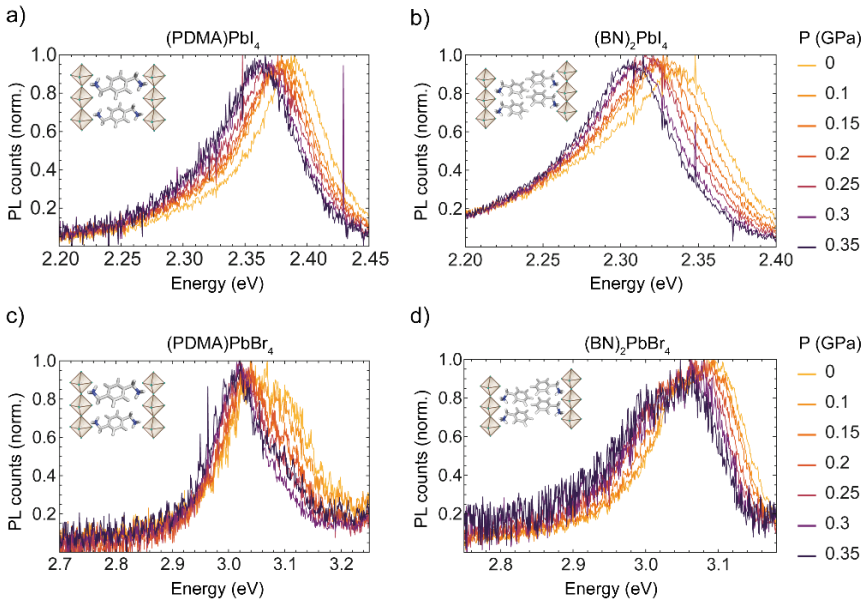


**Figure A5.5.** Pressure-dependent photoluminescence for **a)** $(PDMA)PbI_4$, **b)** $(BN)_2PbI_4$, **c)** $(PDMA)PbBr_4$, **d)** $(BN)_2PbBr_4$. The photoluminescence peak shifts towards smaller energy as a function of pressure for all the compositions studied.

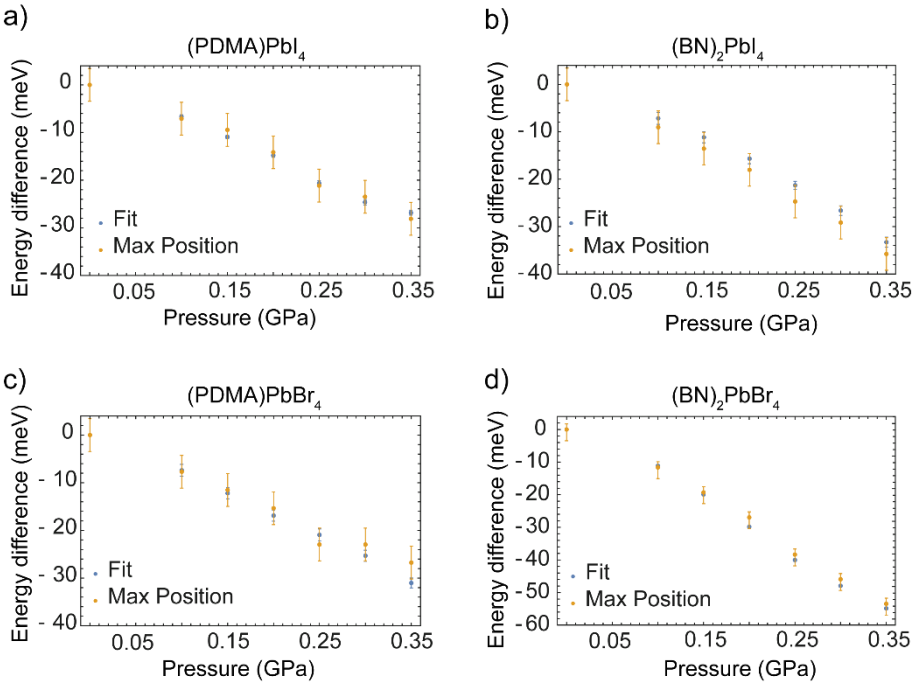


**Figure A5.6.** Excitonic peak estimated using a skewed gaussian fit (blue) and the maximum intensity position of the excitonic feature (in orange) for **a)** (PDMA)$PbI_4$, **b)** $(BN)_2PbI_4$, **c)** (PDMA)$PbBr_4$, **d)** $(BN)_2PbBr_4$. The two methods result in comparable results. The larger error in the second method is given by the resolution of the measurement.

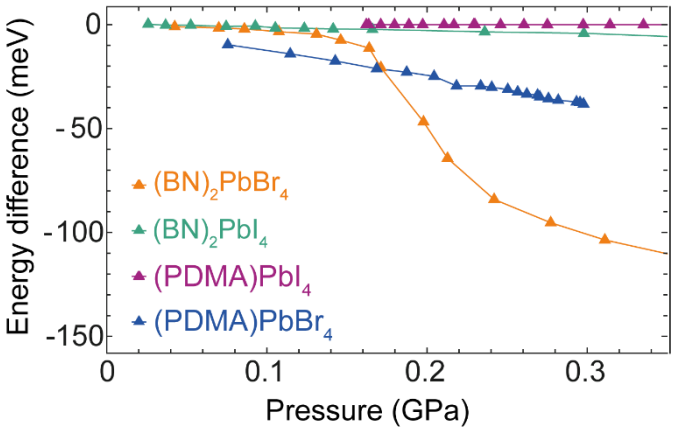


**Figure A5.7.** DFT calculation of the change of bandgap $E_{gap}$ relative to the corresponding structure at low pressure for all the compositions in study.

## 5.6.2. ADDITIONAL TABLES

**Table 5.2.** Absolute values of the DFT calculated equatorial and axial bond length *d(Pb–X)*, bond angle Pb–X–Pb, distance from the nitrogen of each organic spacer to the X plane $d(N^{\cdots}n_X)$, titing angle between the organic spacer the Pb–X plane $\phi(N^{\cdots}Pb–X)$ for (PDMA)$PbI_4$ as a function of pressure.

| *Pressure (GPa)* | *Pb–X–Pb (°)* | $d(Pb–X)_{ax}$ *(Å)* | $d(Pb–X)_{eq}$ *(Å)* | $d(N^{\cdots}n_X)$ *(Å)* | $d(N^{\cdots}n_X)$ *(Å)* | $\phi(N^{\cdots}Pb–X)$ *(°)* |
|---|---|---|---|---|---|---|
| **0.1598** | 149.5329 | 3.1885 | 3.18315 | -0.5933 | -0.55825 | 5.64388 |
| **0.1621** | 149.5348 | 3.18812 | 3.18276 | -0.5949 | -0.5592 | 5.65079 |
| **0.1636** | 149.5361 | 3.18749 | 3.1823 | -0.5965 | -0.56033 | 5.66000 |
| **0.1711** | 149.5376 | 3.18683 | 3.18167 | -0.5979 | -0.56151 | 5.67174 |
| **0.1797** | 149.5426 | 3.18606 | 3.18105 | -0.5992 | -0.56259 | 5.68260 |
| **0.1887** | 149.5367 | 3.1853 | 3.1803 | -0.6007 | -0.56374 | 5.69450 |
| **0.1973** | | | | -0.6025 | -0.56506 | 5.71414 |
| **0.2106** | 149.5398 | 3.18369 | 3.17889 | -0.6040 | -0.56638 | 5.71800 |
| **0.2168** | 149.5377 | 3.18267 | 3.17802 | -0.6056 | -0.56783 | 5.731925 |
| **0.2292** | 149.5198 | 3.18119 | 3.17658 | -0.6059 | -0.56793 | 5.755073 |
| **0.2299** | 149.5434 | 3.18185 | 3.17718 | -0.6095 | -0.57081 | 5.746575 |
| **0.2459** | 149.5398 | 3.17971 | 3.17529 | -0.6113 | -0.57254 | 5.778501 |
| **0.2605** | | | | -0.6135 | -0.5744 | 5.794679 |
| **0.2751** | 149.5377 | 3.17726 | 3.17303 | -0.6159 | -0.57671 | 5.816089 |
| **0.2975** | 149.5439 | 3.17588 | 3.17175 | -0.6185 | -0.57908 | 5.836809 |
| **0.3142** | 149.5448 | 3.17432 | 3.1703 | -0.6209 | -0.58163 | 5.861448 |
| **0.3351** | 149.547 | 3.17257 | 3.16869 | -0.6244 | -0.58475 | 5.883516 |
| **0.3597** | 149.5609 | 3.16817 | 3.16462 | -0.6282 | -0.5886 | 5.916929 |
| **0.3934** | 149.5703 | 3.16518 | 3.16196 | -0.6327 | -0.59339 | 5.953579 |
| **0.4299** | | | | -0.6344 | -0.59578 | 5.999345 |
| **0.4576** | | | | -0.6398 | -0.6000 | 6.021744 |
| **0.4838** | | | | -0.6428 | -0.60357 | 6.066036 |
| **0.5085** | 149.6319 | 3.15907 | 3.15646 | -0.6475 | -0.60857 | 6.100086 |
| **0.5515** | 149.638 | 3.15629 | 3.15385 | -0.6539 | -0.61504 | 6.142101 |
| **0.5994** | 149.6621 | 3.15251 | 3.1504 | -0.6614 | -0.62352 | 6.207654 |
| **0.6734** | | | | -0.6716 | -0.6336 | 6.295497 |
| **0.7881** | | | | | -0.5582 | 6.378513 |

**Table 5.3.** Absolute values of the DFT calculated equatorial and axial bond length *d(Pb–X)*, bond angle Pb–X–Pb, distance from the nitrogen of each organic spacer to the X plane $d(N\cdots n_X)$, titing angle between the organic spacer the Pb–X plane $\phi(N\cdots Pb–X)$ for $(PDMA)PbBr_4$ as a function of pressure.

| *Pressure (GPa)* | *Pb–X–Pb (°)* | $d(Pb–X)_{ax}$ *(Å)* | $d(Pb–X)_{eq}$ *(Å)* | $d(N\cdots n_X)$ *(Å)* | $d(N\cdots n_X)$*(Å)* | $\phi(N\cdots Pb–X)$ *(°)* |
|---|---|---|---|---|---|---|
| **0.0042** | 148.2977 | 3.0086 | 3.00124 | | | |
| **0.0756** | 148.2827 | 3.002715 | 2.99565 | -0.50629 | -0.45516 | 7.024311 |
| **0.1146** | 148.266 | 2.99997 | 2.99308 | -0.51182 | -0.45921 | 7.146059 |
| **0.1427** | 148.2715 | 2.997863 | 2.99308 | -0.51397 | -0.4620 | 7.203226 |
| **0.1686** | 148.2562 | 2.996003 | 2.98911 | -0.51635 | -0.46520 | 7.248788 |
| **0.1873** | 148.248 | 2.994741 | 2.98797 | -0.51803 | -0.46714 | 7.28877 |
| **0.2044** | 148.2498 | 2.993764 | 2.98711 | -0.5197 | -0.46877 | 7.306107 |
| **0.2184** | 148.2777 | 2.992746 | 2.98585 | -0.5211 | -0.47095 | 7.33093 |
| **0.2335** | 148.2772 | 2.992309 | 2.98547 | -0.52171 | -0.47203 | 7.372813 |
| **0.2404** | 148.2706 | 2.991744 | 2.98496 | -0.52207 | -0.47298 | 7.36974 |
| **0.2504** | 148.2782 | 2.991343 | 2.98463 | -0.52297 | -0.47393 | 7.373831 |
| **0.2566** | 148.2928 | 2.990668 | 2.98457 | -0.52350 | -0.47460 | 7.379919 |
| **0.2623** | 148.2872 | 2.990378 | 2.98352 | -0.52395 | -0.47559 | 7.398313 |
| **0.269** | 148.2957 | 2.990151 | 2.9834 | -0.52520 | -0.47630 | 7.405101 |
| **0.2704** | 148.2907 | 2.98981 | 2.98306 | -0.52573 | -0.47670 | 7.410301 |
| **0.2758** | 148.3007 | 2.989559 | 2.98281 | -0.52556 | -0.47733 | 7.417375 |
| **0.2819** | 148.2979 | 2.989176 | 2.98245 | -0.52646 | -0.47822 | 7.421604 |
| **0.2933** | 148.2951 | 2.988621 | 2.98193 | -0.52733 | -0.47895 | 7.430358 |
| **0.2955** | 148.3059 | 2.988262 | 2.9815 | -0.52748 | -0.47934 | 7.437077 |
| **0.2979** | 148.2996 | 3.0086 | 2.98137 | -0.52728 | -0.4798 | 7.445589 |

**Table 5.4.** Absolute values of the DFT calculated equatorial and axial bond length *d(Pb–X)*, bond angle Pb–X–Pb, distance from the nitrogen of each organic spacer to the X plane *d(N···n$_X$)*, titing angle between the organic spacer the Pb–X plane ϕ*(N···Pb–X)* and the distance between the spacer *d(BN···BN)* for $(BN)_2PbI_4$ as a function of pressure.

| ***Pressure (GPa)*** | ***Pb–X–Pb (°)*** | ***d(Pb–X)$_{ax}$ (Å)*** | ***d(Pb–X)$_{eq}$ (Å)*** | ***d(Pb–X)$_{eq}$ (Å)*** | ***d(BN-BN) (Å)*** | ***d(N···n$_X$) (Å)*** | ***ϕ(N···Pb–X) (°)*** |
|---|---|---|---|---|---|---|---|
| **0.0186** | 158.226 | 3.188795 | 3.205568 | 3.225182 | 2.95517 | -0.77249 | 16.26021 |
| **0.0259** | 158.171 | 3.188876 | 3.205345 | 3.224699 | 2.949492 | -0.77237 | 16.30191 |
| **0.0368** | 158.161 | 3.188793 | 3.204526 | 3.224062 | 2.942536 | -0.77207 | 16.35031 |
| **0.0525** | 158.0914 | 3.188814 | 3.203614 | 3.222925 | 2.931349 | -0.77186 | 16.42522 |
| **0.0746** | 158.0189 | 3.188839 | 3.202264 | 3.22139 | 2.916536 | -0.77203 | 16.52653 |
| **0.0928** | 157.9442 | 3.188883 | 3.201589 | 3.220359 | 2.907326 | -0.77192 | 16.58269 |
| **0.1053** | 157.946 | 3.188861 | 3.200642 | 3.219423 | 2.900458 | -0.77165 | 16.62962 |
| **0.1234** | 157.8722 | 3.188865 | 3.199676 | 3.218584 | 2.890662 | -0.77131 | 16.70087 |
| **0.1414** | 157.8064 | 3.18887 | 3.198585 | 3.217279 | 2.879254 | -0.77107 | 16.77728 |
| **0.1659** | 157.7161 | 3.188866 | 3.197197 | 3.21537 | 2.864104 | -0.77016 | 16.88414 |
| **0.236** | 157.4868 | 3.188785 | 3.19345 | 3.210936 | 2.827205 | -0.76990 | 17.15686 |
| **0.2977** | 157.2632 | 3.188675 | 3.19038 | 3.20701 | 2.797149 | -0.77086 | 17.38496 |
| **0.3934** | 156.9954 | 3.188082 | 3.185162 | 3.200705 | 2.755883 | -0.77248 | 17.72018 |
| **0.4831** | 156.7842 | 3.187391 | 3.180165 | 3.19515 | 2.721692 | -0.77495 | 18.02232 |
| **0.5888** | 156.5197 | 3.186379 | 3.174538 | 3.188543 | 2.686233 | -0.7783 | 18.34094 |
| **0.7054** | 156.0185 | 3.185185 | 3.16887 | 3.181604 | 2.654936 | -0.78188 | 18.64073 |

**Table 5.5.** Absolute values of the DFT calculated equatorial and axial bond length *d(Pb–X)*, bond angle Pb–X–Pb, distance from the nitrogen of each organic spacer to the X plane $d(N\cdots n_X)$, titing angle between the organic spacer the Pb–X plane $\phi(N\cdots Pb–X)$ and the distance between the spacer $d(BN\cdots BN)$ for $(BN)_2PbBr_4$ as a function of pressure.

| *Pressure (GPa)* | *Pb–X–Pb (°)* | *Pb–X–Pb (°)* | *$d(Pb–X)_{ax}$ (Å)* | *$d(Pb–X)_{eq}$ (Å)* | *$d(Pb–X)_{eq}$ (Å)* | *d(BN-BN) (Å)* | *$d(N\cdots n_X)$ (Å)* | *$\phi(N\cdots Pb–X)$ (°)* |
|---|---|---|---|---|---|---|---|---|
| **0.0143** | 141.305 | 154.31 | 3.001 | 2.976 | 3.018 | 4.4130 | | 11.88 |
| **0.0425** | 141.251 | 154.288 | 3.0011 | 2.974 | 3.017 | 4.3856 | -0.4730 | 12.00 |
| **0.07** | 141.157 | 154.256 | 3.0013 | 2.9724 | 3.0159 | 4.3545 | -0.4741 | 12.169 |
| **0.086** | 141.111 | 154.252 | 3.0012 | 2.9712 | 3.0152 | 4.3334 | -0.4751 | 12.274 |
| **0.1075** | 141.053 | 154.250 | 3.0012 | 2.9697 | 3.0143 | 4.3105 | -0.4764 | 12.375 |
| **0.131** | 141.025 | 154.231 | 3.0012 | 2.9681 | 3.0134 | 4.2842 | -0.4783 | 12.499 |
| **0.1461** | 141.068 | 154.27 | 3.0007 | 2.9671 | 3.0133 | 4.2598 | -0.4814 | 12.596 |
| **0.1639** | 141.163 | 154.300 | 3.0002 | 2.9659 | 3.0131 | 4.2268 | -0.4857 | 12.710 |
| **0.1712** | 141.426 | 154.414 | 2.9989 | 2.9643 | 3.0135 | 4.1682 | -0.4954 | 12.887 |
| **0.1978** | 141.414 | 154.424 | 2.9962 | 2.9604 | 3.0129 | 4.0554 | -0.5185 | 13.188 |
| **0.2128** | 142.933 | 154.782 | 2.9956 | 2.9582 | 3.0091 | 3.9898 | -0.5317 | 12.310 |
| **0.2419** | 144.009 | 154.701 | 2.9971 | 2.9574 | 2.9993 | 3.9142 | -0.5355 | 10.327 |
| **0.2772** | 144.538 | 154.704 | 2.9972 | 2.9567 | 2.9955 | 3.8591 | -0.5392 | 9.8109 |
| **0.311** | 144.794 | 154.688 | 2.9972 | 2.9547 | 2.9923 | 3.8235 | -0.5426 | 9.5804 |
| **0.3666** | 144.994 | 154.662 | 2.9971 | 2.9515 | 2.9888 | 3.7783 | -0.5474 | 9.5743 |
| **0.4202** | 145.140 | 154.619 | 2.9971 | 2.9481 | 2.9853 | 3.7400 | -0.5517 | 9.5202 |
| **0.5322** | 145.244 | 154.575 | 2.9969 | 2.9410 | 2.9791 | 3.6656 | -0.560 | 9.9320 |

**Table 5.6.** Excitonic peak position and shift obtained from the pressure-dependent optical measurements of $(PDMA)PbI_4$ by tracking the maximum position of the excitonic peak and by fitting the curve to a skewed Gaussian.

| | Max position | | Fit | |
|---|---|---|---|---|
| **Pressure (GPa)** | **Peak energy (eV)** | **Energy shift (meV)** | **Peak energy (eV)** | **Energy shift (meV)** |
| **0** | 2.424±0.002 | 0 | 2.4126±0.0002 | 0 |
| **0.10** | 2.417±0.002 | -7.08±3.44 | 2.406±0.0002 | -6.64±0.37 |
| **0.15** | 2.414±0.002 | -9.44±3.44 | 2.401±0.0002 | -10.94±0.38 |
| **0.20** | 2.411±0.002 | -14.13±3.44 | 2.397±0.0004 | -14.78±0.41 |
| **0.25** | 2.403±0.002 | -21.14±3.44 | 2.391±0.0004 | -20.66±0.54 |
| **0.30** | 2.401±0.002 | -23.46±3.44 | 2.388±0.0003 | -24.61±0.56 |
| **0.35** | 2.396±0.002 | -28.10±3.44 | 2.385±0.0003 | -26.82±0.51 |

**Table 5.7.** Excitonic peak position and shift obtained from the pressure-dependent optical measurements of $(PDMA)PbBr_4$ by tracking the maximum position of the excitonic peak and by fitting the curve to a skewed Gaussian.

| | Max position | | Fit | |
|---|---|---|---|---|
| **Pressure (GPa)** | **Peak energy (eV)** | **Energy shift (meV)** | **Peak energy (eV)** | **Energy shift (meV)** |
| **0** | 3.092±0.002 | 0 | 3.0673±0.0006 | 0 |
| **0.10** | 3.084±0.002 | -7.69±3.44 | 3.0599±0.0006 | -7.38±1.24 |
| **0.15** | 3.081±0.002 | -11.52±3.44 | 3.0551±0.0005 | -12.20±1.17 |
| **0.20** | 3.077±0.002 | -15.34±3.44 | 3.0504±0.0005 | -16.89±1.17 |
| **0.25** | 3.069±0.002 | -22.96±3.44 | 3.0463±0.0006 | -20.94±1.24 |
| **0.30** | 3.069±0.002 | -22.96±3.44 | 3.0420±0.0005 | -25.30±1.15 |
| **0.35** | 3.065±0.002 | -26.75±3.44 | 3.0363±0.0003 | -31.02±1.03 |

**Table 5.8.** Excitonic peak position and shift obtained from the pressure-dependent optical measurements of $(BN)_2PbI_4$ by tracking the maximum position of the excitonic peak and by fitting the curve to a skewed Gaussian.

| | Max position | | Fit | |
|---|---|---|---|---|
| **Pressure (GPa)** | **Peak energy (eV)** | **Energy shift (meV)** | **Peak energy (eV)** | **Energy shift (meV)** |
| **0** | 2.373±0.002 | 0 | 2.3668±0.0007 | 0 |
| **0.10** | 2.364±0.002 | -9.04±3.44 | 2.3596±0.0005 | -7.17±1.25 |
| **0.15** | 2.359±0.002 | -13.54±3.44 | 2.3556±0.0004 | -11.16±1.16 |
| **0.20** | 2.355±0.002 | -18.03±3.44 | 2.3511±0.0004 | -15.66±1.07 |
| **0.25** | 2.348±0.002 | -24.72±3.44 | 2.3455±0.0001 | -21.28±0.82 |
| **0.30** | 2.344±0.002 | -29.16±3.44 | 2.3402±0.0003 | -26.63±1.01 |
| **0.35** | 2.337±0.002 | -35.78±3.44 | 2.3335±0.0003 | -33.29±1.05 |

**Table 5.9.** Excitonic peak position and shift obtained from the pressure-dependent optical measurements of $(BN)_2PbBr_4$ by tracking the maximum position of the excitonic peak and by fitting the curve to a skewed Gaussian.

| | Max position | | Fit | |
|---|---|---|---|---|
| **Pressure (GPa)** | Peak energy (eV) | Energy shift (meV) | Peak energy (eV) | Energy shift (meV) |
| **0** | 3.103±0.002 | 0 | 3.0734±0.0001 | 0 |
| **0.10** | 3.092±0.002 | -11.61±3.44 | 3.0623±0.0001 | -11.15±0.19 |
| **0.15** | 3.084±0.002 | -19.30±3.44 | 3.0535±0.0001 | -19.91±0.18 |
| **0.20** | 3.076±0.002 | -26.95±3.44 | 3.0436±0.0001 | -29.83±0.17 |
| **0.25** | 3.065±0.002 | -38.36±3.44 | 3.0334±0.0001 | -40.03±0.16 |
| **0.30** | 3.057±0.002 | -45.92±3.44 | 3.0355±0.0001 | -47.94±0.16 |
| **0.35** | 3.050±0.002 | -53.44±3.44 | 3.0186±0.0001 | -54.88±0.17 |

**Table 5.10.** Computed $E_{gap}$ for $(PDMA)PbI_4$

| Pressure (GPa) | Bandgap (eV) |
|---|---|
| 0.1598 | 2.1277 |
| 0.1621 | 2.1272 |
| 0.1636 | 2.1264 |
| 0.1711 | 2.1254 |
| 0.1797 | 2.1243 |
| 0.1887 | 2.1235 |
| 0.2106 | 2.1223 |
| 0.2168 | 2.1213 |
| 0.2292 | 2.1202 |
| 0.2299 | 2.1185 |
| 0.2459 | 2.1187 |
| 0.2772 | 2.116 |
| 0.2751 | 2.1143 |
| 0.2975 | 2.1121 |
| 0.3142 | 2.1096 |
| 0.3351 | 2.1068 |
| 0.3934 | 2.1038 |
| 0.4299 | 2.1003 |
| 0.5085 | 2.0957 |
| 0.5511 | 2.0902 |
| 0.5994 | 2.0874 |
| 0.6734 | 2.0824 |
| 0.7881 | 2.078 |

**Table 5.11.** Computed $E_{gap}$ for $(PDMA)PbBr_4$

| Pressure (GPa) | Bandgap (eV) |
|---|---|
| 0.0042 | 2.5925 |
| 0.0756 | 2.5828 |
| 0.1146 | 2.5784 |
| 0.1427 | 2.575 |
| 0.1686 | 2.5713 |
| 0.1873 | 2.5696 |
| 0.2044 | 2.5676 |
| 0.2184 | 2.563 |
| 0.2335 | 2.563 |
| 0.2404 | 2.5623 |
| 0.2504 | 2.5613 |
| 0.2566 | 2.5601 |
| 0.2623 | 2.5591 |
| 0.269 | 2.5586 |
| 0.2704 | 2.5577 |
| 0.2758 | 2.5569 |
| 0.2819 | 2.5561 |
| 0.2933 | 2.5553 |
| 0.2955 | 2.555 |
| 0.2979 | 2.5543 |

**Table 5.12.** Computed $E_{gap}$ for $(BN)_2PbBr_4$

| Pressure (GPa) | Bandgap (eV) |
|---|---|
| 0.0143 | 2.7044 |
| 0.0425 | 2.7034 |
| 0.07 | 2.7028 |
| 0.086 | 2.7023 |
| 0.1075 | 2.701 |
| 0.131 | 2.6998 |
| 0.1461 | 2.6969 |
| 0.1639 | 2.6931 |
| 0.1712 | 2.6837 |
| 0.1978 | 2.6576 |
| 0.2128 | 2.6401 |
| 0.2419 | 2.6203 |
| 0.2772 | 2.6091 |
| 0.311 | 2.6008 |
| 0.3666 | 2.5913 |
| 0.4202 | 2.582 |
| 0.5322 | 2.5681 |
| 0.6733 | 2.5547 |

**Table 5.13.** Computed $E_{gap}$ for $(BN)_2PbI_4$

| Pressure (GPa) | Bandgap (eV) |
|---|---|
| 0 | 1.9504 |
| 0.0259 | 1.9506 |
| 0.0368 | 1.9501 |
| 0.0525 | 1.9501 |
| 0.0746 | 1.9495 |
| 0.0928 | 1.9497 |
| 0.1053 | 1.9488 |
| 0.1234 | 1.9486 |
| 0.1414 | 1.9483 |
| 0.1659 | 1.9481 |
| 0.2128 | 1.9469 |
| 0.3934 | 1.9462 |
| 0.4831 | 1.9434 |
| 0.5888 | 1.9399 |
| 0.7054 | 1.9359 |
| 0.8229 | 1.9316 |

### 5.6.3. Detailed Analysis of Pressure-dependent XRD

The refinement revealed presence of unreacted substrates in all four mechanosynthesized samples (**Figure A5.8**).

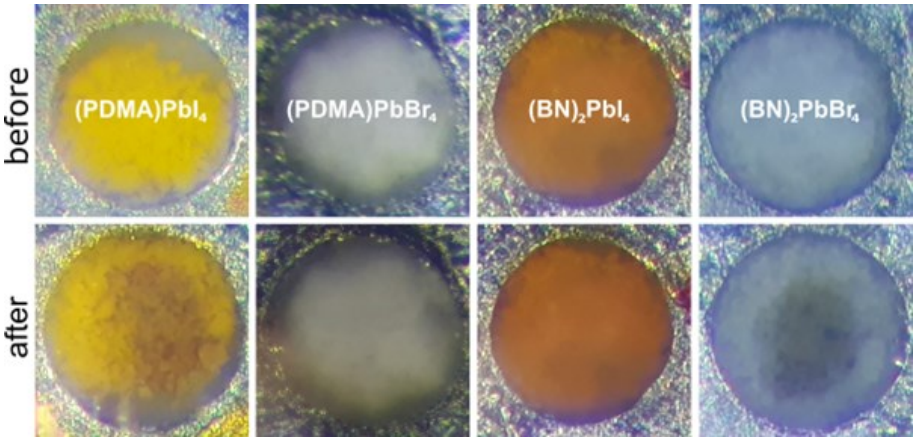


**Figure A5.8.** The samples inside a diamond anvil cell with a visible radiation damage after the experiments.

A detailed description of the XRD patterns for all the four samples (**Figure A5.9**) is reported below. The mechanosynthesis of $(BN)_2PbI_4$ resulted in almost a full conversion of the precursors into the desired product. The fitting of $SiO_2$ (green) and $(BN)_2PbI_4$ (red) patterns left just a few unidentified Bragg peaks (grey plot), which were not assigned neither to $PbI_2$ nor BN-I. The reaction leading to $(BN)_2PbBr_4$ is slower and apart from the product identified (35.9%), the sample contains unreacted precursor BN-Br and $PbBr_2$ (18.4 and 11.5%, respectively) and the remaining 34.2% is quartz. All significant reflections were fitted during the refinement (grey). The scattering of $(PDMA)PbI_4$ sample was weaker, thus no strong high-angle reflections appeared for $2\theta > 26°$. Only the product and quartz were identified, but some remaining Bragg peaks (grey) could come from the phases. Although the fitting of full substrate's patterns was unsuccessful, some of the reflections matched, which shows partial amorphization and/or preferential orientation of the substrate crystals after mechanosynthesis. The reaction yield of $(PDMA)PbBr_4$ within the given

conversion time is not full as $PbBr_2$ (28.8%) and PDMA-Br (18.6%) were identified in the mixture together with the product (21.7%) and the pressure sensor (30.9%). As indicated before, lack of some reflection (*e.g.* 001 2θ~3.7°) may suggest preferential orientation of PDMA-Br crystals. On the other hand, no distinguishable Bragg peaks for 2θ > 12° and broad reflections below may indicate partial amorphisation of the organic precursor. The crystal structure of $(PDMA)PbBr_4$ is unknown and for the research purposes it was assumed isostructural to the I-analogue, which gave good agreement with collected data. Attempts to obtain a single crystal confirming the crystal structure were unsuccessful.

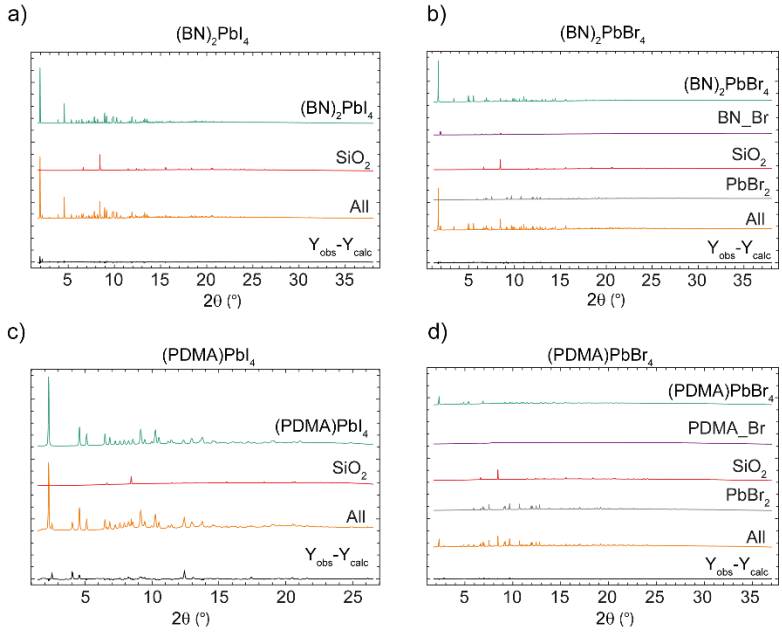


**Figure A5.9.** XRD patterns of **a)** $(BN)_2PbI_4$, **b)** $(BN)_2PbBr_4$, **c)** $(PDMA)PbBr_4$ and **d)** $(PDMA)PbBr_4$ showing the mixtures (orange) and separated patterns of the components, quartz (red), products (green) and unreacted substrates (if present, gray and magenta).

## 5.6.4. Bulk Modulus Calculation

Given the mostly isotropic response to the exertion of pressure, we calculate the isothermal bulk modulus from the pressure-volume (*P-V*) relationship (**Figure A5.10**) using the second order Birch-Murnaghan equation of state[43]

$$P = \frac{3}{2} K_{T0} \left[ \left( \frac{V_0}{V} \right)^{\frac{7}{3}} - \left( \frac{V_0}{V} \right)^{\frac{5}{3}} \right] \tag{5.1}$$

where $K_{T0}$ is the isothermal bulk modulus at standard temperature, $V_0$ is the initial volume, $V$ is the volume at pressure $P$. To account for the isostructural phase transition in $(BN)_2PbBr_4$, the two-phase transition regimes are fitted separately and two $K_{T0}$ are obtained for this composition (**Table 5.14**).

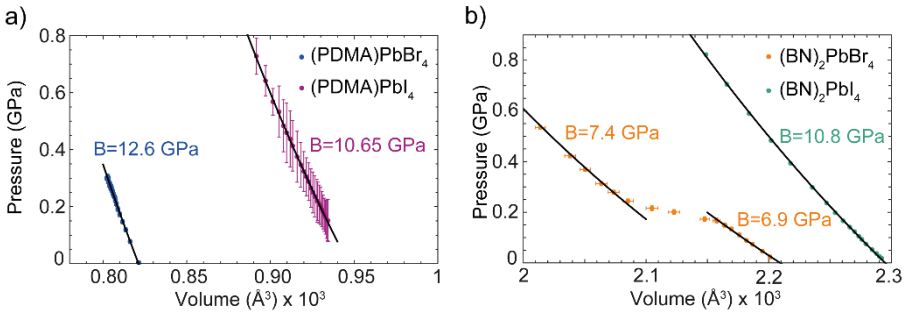


**Figure A5.10.** Pressure-Volume (*P-V*) relationship as a function of pressure fitted with second order Birch-Murnaghan equation of state fit (solid black line) for **a)** $(PDMA)PbX_4$ and **b)** $(BN)_2PbX_4$. Here, *c-axis* is the out-of-plane direction and *a* and *b* axis are the in-plane ones.

**Table 5.14.** Isothermal bulk moduli for the layered 2D perovskites studied.

| Composition | $K_{T0}$ (GPa) |
|---|---|
| $(PDMA)PbI_4$ | 10.65 ± 0.06 |
| $(PDMA)PbBr_4$ | 12.6 ± 0.1 |
| $(BN)_2PbI_4$ | 10.88 ± 0.03 |
| $(BN)_2PbBr_4$ (< 0.14 GPa) | 6.9 ± 0.1 |
| $(BN)_2PbBr_4$ (> 0.14 GPa) | 7.4 ± 0.2 |

A larger bulk modulus suggests a greater stiffness of the material. While one might expect that RP-type layered perovskites should be less rigid and more compressible due to van der Waals interactions in the spacer bilayers, the bulk modulus of (BN)$PbI_4$ is comparable to (PDMA)$PbI_4$. However, the behaviour of the bromide analogues is different; $(BN)_2PbBr_4$ shows a significantly smaller bulk modulus indicating higher compressibility and pressure responsiveness. According to the obtained bulk modulus, we expect a more pronounced effect of the pressure to the optoelectronic properties in the case of $(BN)_2PbBr_4$.

# 5.7. References


(1) Saparov, B.; Mitzi, D. B. Organic − Inorganic Perovskites : Structural Versatility for Functional Materials Design. *Chem. Rev.* **2016**, *116* (7). https://doi.org/10.1021/acs.chemrev.5b00715.

(2) Grancini, G.; Nazeeruddin, M. K. Dimensional Tailoring of Hybrid Perovskites for Photovoltaics. *Nat. Rev. Mater.* **2019**, *4* (1). https://doi.org/10.1038/s41578-018-0065-0.

(3) Blancon, J. C.; Even, J.; Stoumpos, C. C.; Kanatzidis, M. G.; Mohite, A. D. Semiconductor Physics of Organic–Inorganic 2D Halide Perovskites. *Nat. Nanotechnol.* **2020**, *15* (12). https://doi.org/10.1038/s41565-020-00811-1.

(4) Li, X.; Hoffman, J. M.; Kanatzidis, M. G. The 2D Halide Perovskite Rulebook: How the Spacer Influences Everything from the Structure to Optoelectronic Device Efficiency. *Chem. Rev.* **2021**, *121* (4). https://doi.org/10.1021/acs.chemrev.0c01006.

(5) Stoumpos, C. C.; Cao, D. H.; Clark, D. J.; Young, J.; Rondinelli, J. M.; Jang, J. I.; Hupp, J. T.; Kanatzidis, M. G. Ruddlesden − Popper Hybrid Lead Iodide Perovskite 2D Homologous Semiconductors. *Chem. Mater.* **2016**, *28*. https://doi.org/10.1021/acs.chemmater.6b00847.

(6) Mao, L.; Ke, W.; Pedesseau, L.; Wu, Y.; Katan, C.; Even, J.; Wasielewski, M. R.; Stoumpos, C. C.; Kanatzidis, M. G. Hybrid Dion–Jacobson 2D Lead Iodide Perovskites. *J. Am. Chem. Soc.* **2018**, *140*. https://doi.org/10.1021/jacs.8b00542.

(7) Kong, L.; Liu, G.; Gong, J.; Mao, L.; Chen, M.; Hu, Q.; Lü, X.; Yang, W.; Kanatzidis, M. G.; Mao, H. K. Highly Tunable Properties in Pressure-Treated Two-Dimensional Dion–Jacobson Perovskites. *Proc. Natl. Acad. Sci. U. S. A.* **2020**, *117* (28). https://doi.org/10.1073/pnas.2003561117.

(8) Mao, L.; Stoumpos, C. C.; Kanatzidis, M. G. Two-Dimensional Hybrid Halide Perovskites: Principles and Promises. *J. Am. Chem. Soc.* **2018**, *141* (3). https://doi.org/10.1021/JACS.8B10851.

(9) Blancon, J.; Stier, A. V; Tsai, H.; Nie, W.; Stoumpos, C. C.; Traoré, B.; Pedesseau, L.; Kepenekian, M.; Katsutani, F.; Noe, G. T.; et al. Scaling Law for Excitons in 2D Perovskite Quantum Wells. *Nat. Commun.* **2018**, *9*. https://doi.org/10.1038/s41467-018-04659-x.

(10) Sichert, J. A.; Hemmerling, A.; Cardenas-Daw, C.; Urban, A. S.; Feldmann, J. Tuning the Optical Bandgap in Layered Hybrid Perovskites through Variation of Alkyl Chain Length. *APL Mater.* **2019**, *7* (4).

https://doi.org/10.1063/1.5087296.

(11) Zhang, K.; Zhang, M.; Zhu, N.; Yin, H.; Xing, J.; Wang, L. Effects of Organic Ligands on Efficiency and Stability of Perovskite Light-Emitting Diodes. *J. Mater. Sci.* **2021**, *56* (19). https://doi.org/10.1007/s10853-021-06022-w.

(12) Jaffe, A.; Lin, Y.; Karunadasa, H. I. Halide Perovskites under Pressure: Accessing New Properties through Lattice Compression. *ACS Energy Lett.* **2017**, *2* (7). https://doi.org/10.1021/acsenergylett.7b00284.

(13) Liu, S.; Sun, S.; Gan, C. K.; Del Águila, A. G.; Fang, Y.; Xing, J.; Thu Ha Do, T.; White, T. J.; Li, H.; Huang, W.; et al. Manipulating Efficient Light Emission in Two-Dimensional Perovskite Crystals by Pressure-Induced Anisotropic Deformation. *Sci. Adv.* **2019**, *5* (7). https://doi.org/10.1126/sciadv.aav9445.

(14) Jaffe, A.; Lin, Y.; Beavers, C. M.; Voss, J.; Mao, W. L.; Karunadasa, H. I. High-Pressure Single-Crystal Structures of 3D Lead-Halide Hybrid Perovskites and Pressure Effects on Their Electronic and Optical Properties. *ACS Cent. Sci.* **2016**, *2* (4). https://doi.org/10.1021/acscentsci.6b00055.

(15) Szafrański, M.; Katrusiak, A. Photovoltaic Hybrid Perovskites under Pressure. *J. Phys. Chem. Lett.* **2017**, *8* (11). https://doi.org/10.1021/acs.jpclett.7b00520.

(16) Jaffe, A.; Lin, Y.; L. Mao, W.; I. Karunadasa, H. Pressure-Induced Conductivity and Yellow-to-Black Piezochromism in a Layered Cu–Cl Hybrid Perovskite. *J. Am. Chem. Soc.* **2015**, *137* (4). https://doi.org/10.1021/ja512396m.

(17) Umeyama, D.; Lin, Y.; I. Karunadasa, H. Red-to-Black Piezochromism in a Compressible Pb–I–SCN Layered Perovskite. *Chem. Mater.* **2016**, *28* (10). https://doi.org/10.1021/acs.chemmater.6b01147.

(18) Li, Q.; Yin, L.; Chen, Z.; Deng, K.; Luo, S.; Zou, B.; Wang, Z.; Tang, J.; Quan, Z. High Pressure Structural and Optical Properties of Two-Dimensional Hybrid Halide Perovskite (CH3NH3)3Bi2Br9. *Inorg. Chem.* **2019**, *58* (2). https://doi.org/10.1021/acs.inorgchem.8b03190.

(19) Mao, H. K.; Chen, L. C.; Hemley, R. J.; Jephcoat, A. P.; Wu, Y.; Bassett, W. A. Stability and Equation of State of CaSiO3-Perovskite to 134 GPa. *J. Geophys. Res. Solid Earth* **1989**, *94* (B12) https://doi.org/https://doi.org/10.1029/JB094iB12p17889.

(20) Kung, J.; Rigden, S. Oxide Perovskites: Pressure Derivatives of the Bulk and Shear Moduli. *Phys. Chem. Miner.* **1999**, *26* (3). https://doi.org/10.1007/s002690050182.

(21) Liu, G.; Gong, J.; Kong, L.; Schaller, R. D.; Hu, Q.; Liu, Z.; Yan, S.; Yang, W.; Stoumpos, C. C.; Kanatzidis, M. G.; et al. Isothermal Pressure-Derived Metastable States in 2D Hybrid Perovskites Showing Enduring Bandgap Narrowing. *Proc. Natl. Acad. Sci. U. S. A.* **2018**, *115* (32). https://doi.org/10.1073/pnas.1809167115.

(22) Liu, S.; Sun, S.; Kwan Gan, C.; Granados del Águila, A.; Fang, Y.; Xing, J.; Thu Ha Do, T.; White, T. J.; Li, H.; Huang, W.; et al. Manipulating Efficient Light Emission in Two-Dimensional Perovskite Crystals by Pressure-Induced Anisotropic Deformation. *Sci. Adv.* **2019**, *5* (7). https://doi.org/10.1126/sciadv.aav9445.

(23) Tu, Q.; Spanopoulos, I.; Yasaei, P.; Stoumpos, C. C.; Kanatzidis, M. G.; Shekhawat, G. S.; Dravid, V. P. Stretching and Breaking of Ultrathin 2D Hybrid Organic-Inorganic Perovskites. *ACS Nano* **2018**, *12* (10). https://doi.org/10.1021/acsnano.8b05623.

(24) Tu, Q.; Spanopoulos, I.; Hao, S.; Wolverton, C.; Kanatzidis, M. G.; Shekhawat, G. S.; Dravid, V. P. Out-of-Plane Mechanical Properties of 2D Hybrid Organic-Inorganic Perovskites by Nanoindentation. *ACS Appl. Mater. Interfaces* **2018**, *10* (26). https://doi.org/10.1021/acsami.8b05138.

(25) Tu, Q.; Spanopoulos, I.; Vasileiadou, E. S.; Li, X.; Kanatzidis, M. G.; Shekhawat, G. S.; Dravid, V. P. Exploring the Factors Affecting the Mechanical Properties of 2D Hybrid Organic-Inorganic Perovskites. *ACS Appl. Mater. Interfaces* **2020**, *12* (18). https://doi.org/10.1021/acsami.0c02313.

(26) Liu, G.; Kong, L.; Guo, P.; Stoumpos, C. C.; Hu, Q.; Liu, Z.; Cai, Z.; Gosztola, D. J.; Mao, H. K.; Kanatzidis, M. G.; et al. Two Regimes of Bandgap Red Shift and Partial Ambient Retention in Pressure-Treated Two-Dimensional Perovskites. *ACS Energy Lett.* **2017**, *2* (11). https://doi.org/10.1021/acsenergylett.7b00807.

(27) Du, K.-Z. Z.; Tu, Q.; Zhang, X.; Han, Q.; Liu, J.; Zauscher, S.; Mitzi, D. B. Two-Dimensional Lead(II) Halide-Based Hybrid Perovskites Templated by Acene Alkylamines: Crystal Structures, Optical Properties, and Piezoelectricity. *Inorg. Chem.* **2017**, *56* (15). https://doi.org/10.1021/acs.inorgchem.7b01094.

(28) Kong, L.; Liua, G.; Gong, J.; Hu, Q.; Schaller, R. D.; Dera, P.; Zhang, D.; Liu, Z.; Yang, W.; Zhu, K.; et al. Simultaneous Band-Gap Narrowing and Carrier-Lifetime Prolongation of Organic-Inorganic Trihalide Perovskites. *Proc. Natl. Acad. Sci. U. S. A.* **2016**, *113* (32). https://doi.org/10.1073/pnas.1609030113.

(29) Guzelturk, B.; Winkler, T.; Van de Goor, T. W. J.; Smith, M. D.; Bourelle, S. A.; Feldmann, S.; Trigo, M.; Teitelbaum, S. W.; Steinrück, H. G.; de la

Pena, G. A.; et al. Visualization of Dynamic Polaronic Strain Fields in Hybrid Lead Halide Perovskites. *Nat. Mater.* **2021**, *20* (5). https://doi.org/10.1038/s41563-020-00865-5.

(30) Limmer, D. T.; Ginsberg, N. S. Photoinduced Phase Separation in the Lead Halides Is a Polaronic Effect. *J. Chem. Phys.* **2020**, *152* (23). https://doi.org/10.1063/1.5144291.

(31) Zhu, C.; Niu, X.; Fu, Y.; Li, N.; Hu, C.; Chen, Y.; He, X.; Na, G.; Liu, P.; Zai, H.; et al. Strain Engineering in Perovskite Solar Cells and Its Impacts on Carrier Dynamics. *Nat. Commun.* **2019**, *10* (1). https://doi.org/10.1038/s41467-019-08507-4.

(32) Liu, D.; Luo, D.; Iqbal, A. N.; Orr, K. W. P.; Doherty, T. A. S.; Lu, Z. H.; Stranks, S. D.; Zhang, W. Strain Analysis and Engineering in Halide Perovskite Photovoltaics. *Nature Materials*. **2021**, *20* (10). https://doi.org/10.1038/s41563-021-01097-x.

(33) Chen, Y.; Lei, Y.; Li, Y.; Yu, Y.; Cai, J.; Chiu, M. H.; Rao, R.; Gu, Y.; Wang, C.; Choi, W.; et al. Strain Engineering and Epitaxial Stabilization of Halide Perovskites. *Nature* **2020**, *577* (7789). https://doi.org/10.1038/s41586-019-1868-x.

(34) Zhang, C.; Wu, S.; Tao, L.; Arumugam, G. M.; Liu, C.; Wang, Z.; Zhu, S.; Yang, Y.; Lin, J.; Liu, X.; et al. Fabrication Strategy for Efficient 2D/3D Perovskite Solar Cells Enabled by Diffusion Passivation and Strain Compensation. *Adv. Energy Mater.* **2020**, *10* (43). https://doi.org/10.1002/aenm.202002004.

(35) Gélvez-Rueda, M. C.; Ahlawat, P.; Merten, L.; Jahanbakhshi, F.; Mladenović, M.; Hinderhofer, A.; Dar, M. I.; Li, Y.; Dučinskas, A.; Carlsen, B.; et al. Formamidinium-Based Dion-Jacobson Layered Hybrid Perovskites: Structural Complexity and Optoelectronic Properties. *Adv. Funct. Mater.* **2020**, *30* (38). https://doi.org/10.1002/adfm.202003428.

(36) Yu, S.; Yan, Y.; Abdellah, M.; Pullerits, T.; Zheng, K.; Liang, Z. Nonconfinement Structure Revealed in Dion–Jacobson Type Quasi-2D Perovskite Expedites Interlayer Charge Transport. *Small* **2019**, *15* (49). https://doi.org/10.1002/smll.201905081.

(37) Kamminga, M. E.; Fang, H.-H. H.; Filip, M. R.; Giustino, F.; Baas, J.; Blake, G. R.; Loi, M. A.; Palstra, T. T. M. M. Confinement Effects in Low-Dimensional Lead Iodide Perovskite Hybrids. *Chem. Mater.* **2016**, *28* (13). https://doi.org/10.1021/acs.chemmater.6b00809.

(38) Li, Y.; Milić, J. V.; Ummadisingu, A.; Seo, J. Y.; Im, J. H.; Kim, H. S.; Liu, Y.; Dar, M. I.; Zakeeruddin, S. M.; Wang, P.; et al. Bifunctional Organic Spacers for Formamidinium-Based Hybrid Dion-Jacobson Two-Dimensional Perovskite Solar Cells. *Nano Lett.* **2019**, *19* (1).

https://doi.org/10.1021/acs.nanolett.8b03552.

(39) Kamminga, M. E.; Fang, H.-H.; Filip, M. R.; Giustino, F.; Baas, J.; Blake, G. R.; Loi, M. A.; Palstra, T. T. M. Confinement Effects in Low-Dimensional Lead Iodide Perovskite Hybrids. *Chem. Mater* **2016**, *28*, 2. https://doi.org/10.1021/acs.chemmater.6b00809.

(40) Mao, L.; Ke, W.; Pedesseau, L.; Wu, Y.; Katan, C.; Even, J.; Wasielewski, M. R.; Stoumpos, C. C.; Kanatzidis, M. G. Hybrid Dion−Jacobson 2D Lead Iodide Perovskites Sn I 3n+1 (n = 2−3), $(CH_3C_6H_4CH_2NH_3)_2$ ( MA)$Pb_2I_7$, $(HO_2C(CH_2)_3NH_3)_2$(MA)$PbI_7$,$(C_4H_3SCH_2NH_3)_2$(MA)$Pb_2I_7$, $(EA)_4Pb_3X_{10}$ (X = Cl,. *J. Am. Chem. Soc* **2018**, *140*, 47. https://doi.org/10.1021/jacs.8b00542.

(41) Du, K.-Z.; Tu, Q.; Zhang, X.; Han, Q.; Liu, J.; Zauscher, S.; Mitzi, D. B. Two-Dimensional Lead(II) Halide-Based Hybrid Perovskites Templated by Acene Alkylamines: Crystal Structures, Optical Properties, and Piezoelectricity. *Inorg. Chem* **2017**, *56*, 28. https://doi.org/10.1021/acs.inorgchem.7b01094.

(42) Wang, L.; Wang, K.; Xiao, G.; Zeng, Q.; Zou, B. Pressure-Induced Structural Evolution and Band Gap Shifts of Organometal Halide Perovskite-Based Methylammonium Lead Chloride. *J. Phys. Chem. Lett.* **2016**, *7* (24). https://doi.org/10.1021/acs.jpclett.6b02420.

(43) Katsura, T.; Tange, Y. A Simple Derivation of the Birch–Murnaghan Equations of State (EOSs) and Comparison with EOSs Derived from Other Definitions of Finite Strain. *Minerals* **2019**, *9* (12). https://doi.org/10.3390/min9120745.

(44) Liang, A.; Rahman, S.; Saqib, H.; Rodriguez-Hernandez, P.; Muñoz, A.; Nénert, G.; Yousef, I.; Popescu, C.; Errandonea, D. First-Order Isostructural Phase Transition Induced by High Pressure in $Fe(IO_3)_3$. *J. Phys. Chem. C* **2020**, *124* (16). https://doi.org/10.1021/acs.jpcc.0c02080.

(45) Kitazawa, N. Excitons in Two-Dimensional Layered Perovskite Compounds: $(C_6H_5C_2H_4NH_3)_2Pb(Br,I)_4$ and $(C_6H_5C_2H_4NH_3)_2Pb(Cl,Br)_4$. *Mater. Sci. Eng. B* **1997**, *49* (3). https://doi.org/10.1016/S0921-5107(97)00132-3.

(46) Hong, X.; Ishihara, T.; Nurmikko, A. V. Dielectric Confinement Effect on Excitons in $PbI_4$-Based Layered Semiconductors, **1992**. https://doi.org/10.1103/PhysRevB.45.6961.

(47) Chen, Y.; Fu, R.; Wang, L.; Ma, Z.; Xiao, G.; Wang, K.; Zou, B. Emission Enhancement and Bandgap Retention of a Two-Dimensional Mixed Cation Lead Halide Perovskite under High Pressure. *J. Mater. Chem. A* **2019**, *7* (11). https://doi.org/10.1039/c8ta11992a.

(48) Qin, Y.; Lv, Z.; Chen, S.; Li, W.; Wu, X.; Ye, L.; Li, N.; Lu, P. Tuning Pressure-Induced Phase Transitions, Amorphization, and Excitonic Emissions of 2D Hybrid Perovskites via Varying Organic Amine Cations. *J. Phys. Chem. C* **2019**, *123*, 45. https://doi.org/10.1021/acs.jpcc.9b06169.

(49) Zhang, L.; Wu, L.; Wang, K.; Zou, B. Pressure-Induced Broadband Emission of 2D Organic–Inorganic Hybrid Perovskite $(C_6H_5C_2H_4NH_3)_2PbBr_4$. *Adv. Sci.* **2019**, *6* (2). https://doi.org/10.1002/advs.201801628.

(50) Al-Qatatsheh, A.; Morsi, Y.; Zavabeti, A.; Zolfagharian, A.; Salim, N.; Kouzani, A. Z.; Mosadegh, B.; Gharaie, S.; Au, A. Z. K. Blood Pressure Sensors: Materials, Fabrication Methods, Performance Evaluations and Future Perspectives, **2020**, *20* (16). https://doi.org/10.3390/s20164484.

(51) Park, J.; Lee, Y.; Barbee, M. H.; Cho, S.; Cho, S.; Shanker, R.; Kim, J.; Myoung, J.; Kim, M. P.; Baig, C.; et al. A Hierarchical Nanoparticle-in-Micropore Architecture for Enhanced Mechanosensitivity and Stretchability in Mechanochromic Electronic Skins. *Adv. Mater.* **2019**, *31* (25). https://doi.org/10.1002/adma.201808148.

(52) Cho, S.; Kang, S.; Pandya, A.; Shanker, R.; Khan, Z.; Lee, Y.; Park, J.; Craig, S. L.; Ko, H. Large-Area Cross-Aligned Silver Nanowire Electrodes for Flexible, Transparent, and Force-Sensitive Mechanochromic Touch Screens. *ACS Nano* **2017**, *11*, 7. https://doi.org/10.1021/acsnano.7b01714.

(53) Zhang, W.; Ye, H.-Y.; Graf, R.; Spiess, H. W.; Yao, Y.-F.; Zhu, R.-Q.; Xiong, R.-G. Tunable and Switchable Dielectric Constant in an Amphidynamic Crystal. *J. Am. Chem. Soc* **2013**, *135*, 7. https://doi.org/10.1021/ja3110335.

(54) Sun, Y. L.; Shi, C.; Zhang, W. Distinct Roomerature Dielectric Transition in a Perchlorate-Based Organic-Inorganic Hybrid Perovskite. *Dalt. Trans.* **2017**, *46* (48). https://doi.org/10.1039/c7dt03798h.

(55) Giannozzi, P.; Andreussi, O.; Brumme, T.; Bunau, O.; Buongiorno Nardelli, M.; Calandra, M.; Car, R.; Cavazzoni, C.; Ceresoli, D.; Cococcioni, M.; et al. Advanced Capabilities for Materials Modelling with Quantum ESPRESSO. *J. Phys. Condens. Matter* **2017**, *29* (46). https://doi.org/10.1088/1361-648X/aa8f79.

(56) Giannozzi, P.; Baseggio, O.; Bonfà, P.; Brunato, D.; Car, R.; Carnimeo, I.; Cavazzoni, C.; De Gironcoli, S.; Delugas, P.; Ferrari Ruffino, F.; et al. Quantum ESPRESSO toward the Exascale. *J. Chem. Phys.* **2020**, *152* (15). https://doi.org/10.1063/5.0005082.

(57) Giannozzi, P.; Baroni, S.; Bonini, N.; Calandra, M.; Car, R.; Cavazzoni,

C.; Ceresoli, D.; Chiarotti, G. L.; Cococcioni, M.; Dabo, I.; et al. QUANTUM ESPRESSO: A Modular and Open-Source Software Project for Quantum Simulations of Materials. *J. Phys. Condens. Matter* **2009**, *21* (39). https://doi.org/10.1088/0953-8984/21/39/395502.

(58) Willmott, P. R.; Meister, D.; Leake, S. J.; Lange, M.; Bergamaschi, A.; Böge, M.; Calvi, M.; Cancellieri, C.; Casati, N.; Cervellino, A.; et al. The Materials Science Beamline Upgrade at the Swiss Light Source. *J. Synchrotron Radiat.* **2013**, *20* (5). https://doi.org/10.1107/S0909049513018475.

(59) Angel, R. J.; Allan, D. R.; Miletich, R.; Finger, L. W. The Use of Quartz as an Internal Pressure Standard in High-Pressure Crystallography. *J. Appl. Crystallogr.* **1997**, *30* (4). https://doi.org/10.1107/S0021889897000861.

(60) Prescher, C.; Prakapenka, V. B. DIOPTAS: A Program for Reduction of Two-Dimensional X-Ray Diffraction Data and Data Exploration. *http://dx.doi.org/10.1080/08957959.2015.1059835* **2015**, *35* (3). https://doi.org/10.1080/08957959.2015.1059835.

(61) Coelho, A. A.; Evans, J.; Evans, I.; Kern, A.; Parsons, S. The TOPAS Symbolic Computation System. *Powder Diffr.* **2011**, *26*. https://doi.org/10.1154/1.3661087.

(62) Rietveld, H. M. A Profile Refinement Method for Nuclear and Magnetic Structures. *J. Appl. Crystallogr.* **1969**, *2* (2). https://doi.org/10.1107/S0021889869006558.

# SUMMARY

In the last decade, lead-halide perovskites have gathered significant attention due to their fascinating optoelectronic properties which make them suitable for a plethora of applications (*e.g.* solar cells, light-emitting diodes, scintillators, thermoelectric devices, lasers). The versatility of these materials results from the possibility to tune their properties by directly manipulating their chemical composition and structure. To make full use of this tunability we need to be able to understand the relationship between structure and properties. Thus, in this thesis we investigate how variations in structure resulting from different grain growth and mechanical stimuli can manipulate the optical properties of perovskite thin films.

**Chapter 1** starts with an introduction to lead-halide perovskites and to their peculiar electronic structure. After elaborating on how changes in bond length and octahedral tilting can affect the optoelectronic properties of these materials, we compare the bulk moduli of such perovskites with conventional semiconductors. The soft nature of the perovskite lattice paves the way for manipulating the optoelectronic properties by means of external mechanical stimuli such as pressure. Thus, we introduce pressure-dependent transient absorption spectroscopy and pressure-dependent photoluminescence which are the main analysis methods used throughout this thesis. Together with applied external pressure, changes in structural properties can be achieved by using different fabrication methods, which can result in a different size and crystallographic orientation of grains. We introduce Electron Back-Scattered Diffraction (EBSD) as a powerful technique to obtain crystallographic information combined with the high spatial resolution typical of a scanning electron microscope (SEM).

We use EBSD in **Chapter 2** to study the microstructure of methylammonium lead iodide ($MAPbI_3$) thin films fabricated with the conventional antisolvent-dripping (AS) method and flash-infrared annealing (FIRA). EBSD analysis reveals that oftentimes the domains observed in SEM are misidentified with crystallographic grains. Also, we find that despite substantial differences in grain size between the two systems (~100s of nm for

the AS and ~100s of μm for the FIRA), the optoelectronic properties are similar suggesting that the optoelectronic quality is not necessarily related to the orientation and size of crystalline domains.

In **Chapter 3**, we study the hot-carrier cooling process. At the femtosecond timescale, hot electrons generated by high-energy radiation interact with the lattice to dissipate the excess of energy in the form of heat. This process involves interactions between the photogenerated electrons and the vibrations of the lattice. We investigate how manipulating the lattice properties by applying external pressure affects the rate at which the hot electrons cool to the lattice temperature. We find that compressive stress favours fast hot-carrier cooling at high excitation density (> $10^{18}$ photons/$cm^2$) which would be beneficial for light-emitting diodes (LEDs) and laser applications.

The easy bandgap tunability of lead-halide perovskites is one of the most intriguing properties for the manufacture of LEDs, lasers and tandem solar cells. This tunability can be achieved by mixing the halide components in different stoichiometric ratio allowing to tune the bandgap from the UV toward the NIR. However, mixed-halide perovskites suffer from halide migration under light illumination or electrical bias. This halide migration leads to phase segregation in some composition. The formation of halide-rich domains in turn disrupts the homogeneity of the bandgap. The onset of phase segregation coincides with a phase transition from tetragonal to cubic when more than 20% of bromide is incorporated in the composition. However, it is not clear if and how the phase transition affects phase segregation. In **Chapter 4**, we use pressure-dependent transient absorption spectroscopy to verify how changes in the unit cell volume affect the thermodynamics and kinetics of phase segregation. We observe that phase segregation is almost suppressed at an external pressure of 0.3 GPa for several bromide-iodide mixing ratio and also the overall segregation rate is dramatically reduced. Our findings suggest that the process of phase segregation cannot be associated to the presence of a phase transition as the crystal structure of all the compositions studied remain cubic in the pressure range used. In addition, the pressure reveals itself as an effective tool to reduce phase segregation. A similar compression of the unit cell volume can also be induced by change in the chemical composition, specifically replacing the $A^+$ cation with

a smaller ion, exemplified by replacing $MA^+$ with $Cs^+$. Comparably to what is obtained under hydrostatic pressure, the change induced by this "*chemical pressure*" reduces the phase-segregation.

Layered 2D perovskites have attracted considerable interest due to their highly modular structure that can be tailored by altering both organic and inorganic components. Given the presence of organic spacers, this class of materials is more easily compressible across different pressure ranges, demonstrating mechanochromic behaviour. In **Chapter 5**, we investigate the structure-property relationship in Ruddlesden-Popper and Dion-Jacobson 2D layered perovskites fabricated with comparable organic spacers, *i.e.* benzylammonium (BN) and 1,4-phenylenedimethylammonium (PDMA). Combining pressure-dependent absorption, X-ray diffraction with synchrotron radiation and density functional theory calculations, we surprisingly find that Ruddlesden-Popper and Dion-Jacobson layered perovskites behave rather similarly under pressure despite the different forces involved in connecting the two perovskites slabs. In addition, we find no direct difference between the Br- and I- based compositions, in contrast with the higher expected level of rigidity of the bromide-based system in comparison with its iodide counterpart. The most significant shift in the optical absorption is observed in $(BN)_2PbBr_4$ under 0.35 GPa pressure. Density functional theory in combination with pressure-dependent X-ray diffraction reveal that, at mild pressure, $(BN)_2PbBr_4$ shows an isostructural phase transition associated with a change of penetration depth of the BN spacers into the Pb-Br lattice. The isostructural phase transition is associated with a decrease in the octahedra tilting which leads to an increased penetration depth of the BN spacers into the Pb–Br lattice, enabling some relaxation of the spacer tilting. This structural rearrangement can be correlated with the larger susceptibility of the system to pressure which in turn results in a larger redshift of the excitonic feature. These 2D perovskite materials hence show a rich parameter space for structural manipulations and understanding and manipulating the structural properties is pivotal to design new functional materials for targeted applications.

# SAMENVATTING

In het afgelopen decennium hebben lood-halide perovskieten volop in de aandacht gestaan vanwege hun fascinerende opto-elektronische eigenschappen, waardoor ze geschikt zijn voor een overvloed aan toepassingen (zoals zonnecellen, lichtgevende diodes, scintillatoren, thermo-elektrische apparaten, lasers De veelzijdigheid van deze materialen komt voort uit de mogelijkheid hun eigenschappen af te stemmen door direct hun chemische samenstelling en structuur aan te passen. Om deze afstembaarheid volledig te benutten is het begrijpen van de relatie tussen structuur en eigenschappen essentieel. In dit proefschrift onderzoeken we daarom hoe variaties in structuur als gevolg van verschillen in kristalkorrel groei en mechanische stimuli de opto-elektronische eigenschappen van dunne perovskietlagen kunnen veranderen.

**Hoofdstuk 1** begint met een inleiding tot lood-halide perovskieten en hun bijzondere elektronische structuur. Na het uitwerken van de invloed van veranderingen in bindingslengte en octaëdrische kanteling op de opto-elektronische eigenschappen van deze materialen, vergelijken we de compressiemoduli van dergelijke perovskieten met conventionele halfgeleiders. De zachte aard van het perovskietrooster maakt het mogelijk de opto-elektronische eigenschappen aan te passen door middel van externe mechanische stimuli zoals druk. Daarom introduceren we drukafhankelijke tijdsopgeloste absorptiespectroscopie en drukafhankelijke fotoluminescentie, de belangrijkste analysemethoden die in dit proefschrift worden gebruikt. Naast het toepassen van externe druk kunnen structurele eigenschappen worden veranderd door verschillende fabricagemethoden te gebruiken, wat kan resulteren in een verschillende grootte en kristallografische oriëntatie van kristalkorrels. We introduceren elektronen terugverstrooiing diffractie als een krachtige techniek om kristallografische informatie te verkrijgen in combinatie met de hoge ruimtelijke resolutie die typisch is voor een rasterelektronenmicroscoop.

We gebruiken EBSD in **Hoofdstuk 2** om de microstructuur van dunne Methylammonium loodjodide ($MAPbI_3$)-films te vergelijken die zijn gefabriceerd met de conventionele anti-oplosmiddel druppel methode of en met flash infrarood gloeien. EBSD-analyse onthult dat de domeinen die met de SEM

worden waargenomen vaak verkeerd worden geïdentificeerd als kristallografische korrels. Daarnaast demonstreren we dat, ondanks de aanzienlijke verschillen in kristalkorrelgrootte tussen de twee systemen (honderden nanometers voor AS en honderden micrometers voor FIRA) de opto-elektronische eigenschappen vergelijkbaar zijn, wat suggereert dat de opto-elektronische kwaliteit niet noodzakelijk gerelateerd is aan de oriëntatie en grootte van kristallijne domeinen.

In **Hoofdstuk 3** bestuderen we het koelproces van hete ladingdragers in perovskiet halfgeleiders. Op de femtoseconde tijdschaal leidt de interactie tussen hete elektronen en het kristalrooster ertoe dat de overtollige energie wordt afgevoerd in de vorm van warmte. Dit proces omvat interacties tussen de door hoogenergetisch licht aangeslagen elektronen en de trillingen van het rooster. We onderzoeken hoe het aanpassen van de roostereigenschappen door het toepassen van externe druk de snelheid beïnvloedt waarmee de hete elektronen afkoelen tot de roostertemperatuur. We ontdekken dat drukspanning een snelle koeling van de aangeslagen ladingdragers bevordert bij een hoge excitatiedichtheid ($> 10^{18}$ fotonen/cm$^2$), wat gunstig zou zijn voor lichtemitterende diodes (LED's) en lasertoepassingen.

De gemakkelijke afstembaarheid van de bandkloof van lood-halide perovskieten is een van de meest intrigerende eigenschappen voor de productie van LED's, lasers en tandemzonnecellen. Deze afstembaarheid kan worden bereikt door de halidecomponenten in verschillende stoichiometrische verhoudingen te mengen, waardoor de bandkloof van ultraviolet (UV) tot nabij-infrarood (NIR)kan worden afgestemd. Gemengde halideperovskieten hebben echter last van halidemigratie onder invloed van licht of elektrische spanning. Deze halidemigratie leidt tot fasescheiding in een bepaalde samenstelling. De vorming van haliderijke domeinen verstoort op zijn beurt de homogeniteit van de bandkloof. Het begin van de fasescheiding valt samen met een faseovergang van tetragonaal naar kubisch wanneer de samenstelling voor meer dan 20% uit bromide bestaat. Het is echter niet duidelijk of en hoe de faseovergang de fasescheiding beïnvloedt. In **Hoofdstuk 4** gebruiken we drukafhankelijke tijdsopgeloste absorptiespectroscopie om te verifiëren hoe veranderingen in het volume van de eenheidscel de thermodynamica en kinetiek van fasescheiding

beïnvloeden. We zien dat fasescheiding bijna geheel onderdrukt wordt bij een externe druk van 0,3 GPa voor verschillende bromide-jodide mengverhoudingen en dat de algehele segregatiesnelheid drastisch wordt verminderd. Onze bevindingen suggereren dat het proces van fasescheiding niet kan worden geassocieerd met de aanwezigheid van een faseovergang, aangezien de kristalstructuur van alle bestudeerde composities kubisch blijft in het gebruikte drukbereik. Bovendien ontpopt de druk zich als een effectief middel om fasescheiding te verminderen. Een vergelijkbare compressie van het eenheidscelvolume kan ook worden geïnduceerd door verandering in de chemische samenstelling, met name door het $A^+$-kation te vervangen door een kleiner ion, bijvoorbeeld door $MA^+$ te vervangen door $Cs^+$. Vergelijkbaar met wat wordt bevonden onder hydrostatische druk, vermindert de verandering die wordt veroorzaakt door deze "chemische druk" de fasescheiding.

Er is veel belangstelling uitgegaan naar gelaagde 2D perovskieten vanwege hun zeer modulaire structuur die kan worden aangepast door zowel organische als anorganische componenten te veranderen. Gezien de aanwezigheid van organische tussenlagen is deze klasse materialen gemakkelijker samendrukbaar over verschillende drukbereiken, met aantoonbaar mechanochroom gedrag. In **Hoofdstuk 5** onderzoeken we de structuur-eigenschap relatie in Ruddlesden-Popper en Dion-Jacobson 2D gelaagde perovskieten vervaardigd met vergelijkbare organische tussenlagen, namelijk benzylammonium (BN) en 1,4-fenyleendimethylammonium (PDMA). Door drukafhankelijke absorptie, röntgendiffractie met synchrotronstraling en dichtheidsfunctionaaltheorieberekeningen te combineren, ontdekken we dat Ruddlesden-Popper en Dion-Jacobson gelaagde perovskieten zich verrassend genoeg redelijk vergelijkbaar gedragen onder druk ondanks de verschillende bindingsmodus van de organische tussenlaag. Daarnaast vinden we geen direct verschil tussen de op Br- en I-gebaseerde samenstellingen, in tegenstelling tot de hogere verwachte stijfheid van het op bromide gebaseerde systeem in vergelijking met zijn jodide-tegenhanger. De meest significante verschuiving in de optische absorptie wordt waargenomen in $(BN)_2PbBr_4$ onder een druk van 0,35 GPa. Dichtheidsfunctionaaltheorie in combinatie met drukafhankelijke röntgendiffractie onthullen dat $(BN)_2PbBr_4$ bij milde druk een isostructurele

faseovergang vertoont geassocieerd met een verandering van penetratiediepte van de BN-afstandhouders in het Pb-Br-rooster. De isostructurele faseovergang gaat gepaard met een afname van de kanteling van de octaëders, wat leidt tot een grotere penetratiediepte van de BN- tussenlagen in het Pb-Br-rooster, waardoor enige ontspanning van de kanteling van de tussenlaag mogelijk wordt. Deze structurele herschikking kan worden gecorreleerd met de grotere gevoeligheid van het systeem voor druk, wat op zijn beurt resulteert in een grotere roodverschuiving van het excitonische kenmerk. Deze 2D-perovskietmaterialen vertonen dus een rijke parameterruimte voor structurele aanpassingen en het begrijpen en afstemmen van de structurele eigenschappen is cruciaal om nieuwe functionele materialen voor gerichte toepassingen te ontwerpen.

# LIST OF PUBLICATIONS

The Chapters of this thesis are based on the following publications:

1. *Reversible and Pressure-Dependent Mechanochromism in Dion-Jacobson and Ruddlesden-Popper Layered Hybrid Perovskites*
   **Loreta A. Muscarella***, Algirdas Dučinskas*, Mathias Dankl, Michal Andrzejewski, Nicola Pietro Maria Casati, Ursula Rothlisberger, Davide Moia, Joachim Maier, Michael Graetzel, Bruno Ehrler, Jovana Milic
   *Submitted*

2. *Accelerated hot-carrier cooling in $MAPbI_3$ perovskite by pressure-induced lattice compression*
   **Loreta A. Muscarella**, Eline M. Hutter, Jarvist M. Frost, Gianluca G. Grimaldi, Jan Versluis, Huib J. Bakker, Bruno Ehrler.
   J. Phys. Chem. Lett. 2021, 12, 9, 2423–2428
   DOI: 10.1021/acs.jpclett.1c00205

3. *Lattice compression increases the activation barrier for phase segregation in mixed-halide perovskites*
   **Loreta A. Muscarella**, Eline M. Hutter, Francesca Wittmann, Young Won Woo, Young-Kwang Jung, Lucie McGovern, Jan Versluis, Aron Walsh, Huib J. Bakker, and Bruno Ehrler
   ACS Energy Lett. 2020, 5, 10, 3152–3158
   DOI: 10.1021/acsenergylett.0c01474

4. *Thermodynamic stabilization of mixed-halide perovskites against phase segregation*
   Eline M. Hutter, **Loreta A. Muscarella**, Francesca Wittmann, Jan Versluis, Lucie McGovern, Huib Bakker, Young-Won Woo, Young-Kwang Jung, Aron Walsh, Bruno Ehrler
   Cell Reports Physical Science1,100120
   DOI: doi.org/10.1016/j.xcrp.2020.100120

5. *Crystal Orientation and Grain Size: Do They Determine Optoelectronic Properties of $MAPbI_3$ Perovskite?*
   **Loreta A. Muscarella**, Eline M. Hutter , Sandy Sanchez , Christian D. Dieleman , Tom J. Savenije, Anders Hagfeldt, Michael Saliba, Bruno Ehrler
   J. Phys. Chem. Lett. 2019, 10, 20, 6010–6018
   DOI: 10.1021/acs.jpclett.9b02757

**shared authorship*

Other publications by the author:

6. *Reduced Barrier for Ion Migration in Mixed-Halide Perovskites*
   Lucie McGovern, Moritz H. Futscher, Eline M. Hutter, **Loreta A. Muscarella**, Gianluca Grimaldi, Moritz C. Schmidt, Bruno Ehrler
   *Submitted*

7. *Ion Exchange Lithography: Localized Ion Exchange Reactions for Spatial Patterning of Perovskite Semiconductors and Insulators*
   Lukas Helmbrecht, Moritz H Futscher, **Loreta A. Muscarella**, Bruno Ehrler, Willem L Noorduin
   Adv. Mater. 2021, 2005291
   DOI: 10.1002/adma.202005291

8. *Grain Size Influences Activation Energy and Migration Pathways in MAPbBr3 Perovskite Solar Cells*
   Lucie McGovern, Isabel Koschany, Gianluca G. Grimaldi, **Loreta A. Muscarella**, Bruno Ehrler
   J. Phys. Chem. Lett. 2021, 12, 9, 2423–2428
   DOI: 10.1021/acs.jpclett.1c00205

9. *Shaping perovskites: In-situ crystallisation mechanism of rapid-thermally annealed, pre-patterned perovskite films*
   Antonio Gunzler, Esteban Bermúdez-Urena, **Loreta A. Muscarella**, Mario Ochoa, Efraín Ochoa-Martinez, Michael Saliba, Bruno Ehrler, and Ullrich Steiner
   ACS Appl. Mater. Interfaces 2021, 13, 5, 6854–6863
   DOI: 10.1021/acsami.0c20958

10. *Understanding the Stability of $MAPbBr_3$ versus $MAPbI_3$ – Suppression of Methylammonium Migration and Reduction of Halide Migration*
    Lucie Mcgovern, Moritz Hieronymus Futscher, **Loreta A. Muscarella**, Bruno Ehrler
    J. Phys. Chem. Lett. 2020, 11, 17, 7127–7132
    DOI: 10.1021/acs.jpclett.0c01822

11. *Impact of exciton delocalization on exciton-vibration interactions in organic semiconductors*
    Antonios M. Alvertis, Raj Pandya, **Loreta A. Muscarella**, Nipun Sawhney, Malgorzata Nguyen, Bruno Ehrler, Akshay Rao, Richard H. Friend, Alex W. Chin, and Bartomeu Monserrat
    Phys. Rev. B 102, 081122(R)
    DOI: 10.1103/PhysRevB.102.081122

12. *Grain size control of crystalline III-V semiconductors at ambient conditions using electrochemically mediated growth*
Marco Valenti, Yorick Bleiji, Javier Blanco Portals, **Loreta A. Muscarella**, Mark Aarts, Francesca Peiro, Sonia Estrade, Esther Alarcón Lladó
*Journal of Materials Chemistry A*, 2020
DOI: 10.1039/C9TA07410D

13. *Local Crystal Misorientation Influences Non-radiative Recombination in Halide Perovskites*
Sarthak Jariwala, Hongyu Sun, Gede W.P.Adhyaksa, Andries Lof, **Loreta A. Muscarella**, Bruno Ehrler, Erik C. Garnett, David S. Ginger
Joule 3, 3048–3060
DOI: 10.1016/j.joule.2019.09.001

14. *Air-stable and oriented mixed lead halide perovskite (FA/MA) by one-step deposition method using zinc iodide and chloroamine additive*
**Loreta A. Muscarella**, Dina Petrova, Rebecca Jorge Cervasio, Aram Farawar, Olivier Lugier, Charlotte McLure, Martin J Slaman, Junke Wang, Bruno Ehrler, Elizabeth von Hauff, Rene M Williams
ACS Appl. Mater. Interfaces 2019, 11, 19, 17555–17562
DOI: 10.1021/acsami.9b03810

15. *Perovskite Thin Film Materials Stabilized and Enhanced by Zinc (II) Doping*
Arjaan Kooijman, **Loreta A. Muscarella**, René M Williams
Applied Sciences 9 (8), 1678, 2019
DOI: 10.3390/app9081678

16. *Quantification of ion migration in $CH_3NH_3PbI_3$ perovskite solar cells by transient capacitance measurements*
Moritz H Futscher, Ju Min Lee, Lucie McGovern, **Loreta A. Muscarella**, Tianyi Wang, Muhammad Irfan Haider, Azhar Fakharuddin, Lukas Schmidt-Mende, Bruno Ehrler
Mater. Horiz., 2019,6, 1497-1503
DOI: 10.1039/C9MH00445A

17. *Control of Surface Defects in ZnO Nanorod Arrays with thermally-deposited Au nanoparticles for Perovskite Photovoltaics*
Tulus, Selina Olthof, Magdalena Marszalek, Andreas Peukert, **Loreta A. Muscarella**, Bruno Ehrler, Olivera Vukovic, Yulia Galagan, Simon Christian Boehme, Elizabeth von Hauff
ACS Appl. Energy Mater. 2019, 2, 5, 3736–3748
DOI: 10.1021/acsaem.9b00452

# ACKNOWLEDGEMENTS

I would like to start thanking my supervisor and promotor Bruno Ehrler. I am infinitely grateful for the opportunity you have given me to start a PhD in such a fantastic place as AMOLF. Thanks for letting me develop my own identity as young scientist, guiding my choices, supporting my independence in exploring on my own all the possible steps in my career but always being present if I needed to put things in perspective or a good advice.

I want to thank my other supervisor, Albert Polman, for being always very supportive, enthusiastic about my work and sincerely interested not only in my professional life but also in my personal life. You are always an inspiration; you always have a nice word for everyone and you are actively involved in making connections among the students because we are not only co-workers but also a big scientific family.

I wish to thank Prof. Maria Loi, Prof. Ferdinand Grozema, Prof. René Janssen, Prof. Moniek Tromp and Dr. Jovana Milić for carefully reading and evaluating this thesis, the product of a 4 years-long journey. I admire you as scientists and it is for me a great honour to have my thesis assessed by you.

I would also like to thank the other group leaders at AMOLF. In particular, I would like to thank Esther Alarcón-Lladó for your enthusiasm in promoting and supporting the work of young talented women in science, for your empathy and kindness. Thanks to Erik Garnett for your feedback on my works, for great discussions and acute questions that helped me in understanding better my findings. Thanks to Said Rodriguez for the great discussions about the pitfalls of the academic system, for the productive exchange on how we, as scientists, should believe more in our value. Thanks to Wim Noorduin for your endless enthusiasm about chemistry and science, for your supportive attitude even though LEDs were not really working in the lab, for always believing in your students. A big thanks to Hans Zeijlemaker for the support during the early days while using the new EBSD detector, for your enthusiasm and curiosity about the EBSD-perovskite experiments. I will never forget when you were entering in the SEM room every day, 5 minutes before the end of the working day, just to ask if I was

happy about the experiment. And thanks to the cleanroom guys, Dimitry, Igor, Bob and Andries for your support in the toughest cleanroom and SEM days.

I firmly believe that doing science is a team effort and for this reason I do have to thank many of the people I have worked with during the last 4 years. Most of these collaborations resulted in a very nice scientific publications, but this is just the tip of the iceberg. There is much more behind a scientific publication: collaborative discussions, sharing ideas, infinite hours spent on analysing data or correcting a manuscript. All the collaborators I have met during these 4 years taught me something that is now part of my education as a scientist. I want to thank all of them. In particular, Jovana Milić, what a force of the nature you are! Since the first day I met you, I was impressed by your sincere enthusiasm and care not only for science but also for the people who do science, your collaborators. You are not only a great scientist but you are always supportive, grateful, optimistic. I am grateful you could attend my defence, despite online, but I hope to meet you in person soon. I wish you all the best for your brilliant career and I hope we can collaborate again in the future. Thanks to Algirdas Dučinskas for the fantastic collaboration, which is featured in this thesis, in Chapter 5. I wish all my colleagues to have a collaborator like you. We were such a great team, together with Mathias Dankl, in shaping the manuscript and fit all the pieces of the puzzle together. Thanks both for the last-minute meetings, the last-minute changes and discussions and for sharing part of this journey with me. But hey, it is still not over yet, we are still under revision! Thanks to Ilaria Fratoddi and René Williams, you were my Master thesis supervisors, and it is thanks to both of you if I had the chance to start working with these bizarre materials, the perovskites. Thanks to René for being involved in my Master project with curiosity and enthusiasm, for your welcome in your group.

Thanks to Ilaria for trusting me since I started my Bachelor thesis with you, for supporting me and my academic decisions, and thanks for supporting all the students in the chemistry department in doing an experience abroad. I am glad I am still in contact with both of you.

Thanks to all the support staff of AMOLF, to our fantastic receptionists, to all the technicians, to all the people working in the workshop, to the software and electronic engineers, to the design department staff, to the finance and

purchase department staff, to the canteen staff, to all the people who take care of the cleaning of our offices. You are the real pillars of AMOLF, and without you we could not do our daily work in such a great environment.

Thanks to the Hybrid Solar Cells group. In the last 4 years I have seen many people coming and leaving, I started when the group was still small and now it is great to see how many brilliant and talented scientists are part of this group. Acknowledgements here are in completely random order, you are so many that I hope to not forget some of you. Jumin Lee, the first postdoc of the group. I started in the group just two months before the end of your contract, but it was enough to show me how fun and kind you are. Benjamin Daiber, a page with the list of how many times you helped me coding will not be enough to acknowledge you properly. Thanks for teaching me a bit of Mathematica, for answering to all of my questions without being annoyed. You are one of the most precise, meticulous scientists I have ever met. Thanks to Moritz Futscher for being such an inspiration during my start as a PhD. It was great to meet again and see how our lives have changed in these 4 years. You are an excellent scientist and wish you all the success you deserve in academia. My dear mevrouw, Lucie McGovern, thanks for being the best officemate one could wish. We started together, only 6 days of difference, and we are now finishing together this journey. Thanks for sharing our ups and downs during this rollercoaster called PhD. Your optimism and enthusiasm are contagious. And thanks for retrieving my bag all the time with María during the group trip. Thanks to Christian Dieleman for sharing the bad and good days of the PhD, and one of the most exciting conference trips together with Jenny and Lucie in the US. I enjoyed the food-related discussions, and I am glad to see that after 4 years you know how to properly cook Italian food. You still need to work on the salad next to the pasta, an Italian dies everytime you do that! Thanks to Jeroen de Boer and Moritz Schmidt, for me you will always be the magic duo who started together the PhD. You are great, keep up the good work! I am looking forward to reading more science from you. Thanks to Silvia Ferro, the other Sicilian in the group. Thanks for all the efforts you have done to organise together with Jeroen the fantastic group trip that was for me the last big event before finishing my PhD. Thanks to Imme Schuringa for being always supportive, for sharing our good and bad

moments throughout the PhD. I wish I could spend more time together into the lab and collaborating on new projects. You are a brilliant scientist and a caring person; I wish you all the best for the rest of your PhD. Thanks to María Gélvez-Rueda, you are fun and always with a smile for others. Despite the pandemic did not help in letting us work more closely together, I hope we can still work on a collaborative project soon, your project rocks! Good luck with it! Thanks to Gianluca Grimaldi, one of my paranymphs. Gianluca, thanks for bearing with my panic moments just before the submission, when I was questioning my entire PhD. Thanks for always be reassuring, especially when I was listing all the possible dramatic scenarios for the hot-carrier cooling project (ah, that project!). Thanks to our Bachelor and Master students, Isabelle Koschany, Marnix Ackermann, Rens van Roosmalen, Francesca Wittmann, Joris Bodin, Emil Kensington, Oscar van de Water, Floris Blom, Jouke Blum, Toon Maassen, Menke Knol for being such a great and fun group members. Thanks to David Langhorst, the first master student I have supervised for the fun in the lab ad for teaching me what being a supervisor mean. Thanks to Georg Krause, the second student I have ever supervised, for being such a meticulous and independent student. I am impressed how quickly you learnt, and I hope we can finish together this challenging bachelor project. Thanks to the guests who visited our group, Cedric Gonzales, Rowan McQueen, Adrian Callies and Andrew Pun, you brought a refreshing atmosphere in the group. Thanks to our super technician, Marc Duursma. Thanks for keeping the lab a safe place and for taking care of our equipment with such a care. You are not only a super technician but also a very nice person to talk with, always smiling and supporting us.

Here, a special mention goes to Eline Hutter. Eline, you came in the group at the right moment. It was not the best moment of my PhD and I was questioning myself whether this direction was still exciting for me. I learnt so much from you and I regained enthusiasm in what I was doing. Thanks for being an inspiring woman and scientist, you are a role model. And thanks once more for the trust you have in me and my capabilities. I am looking forward to starting this new adventure, as a postdoc, in your group. I would have not imagined, when you left AMOLF to start your position as Assistant Professor, that we would meet again in these new roles!

I also have to thank all the fantastic people I have met during these years at AMOLF: Jenny Kontoleta, the third lady in the volcanic US trip, Nasim Tavakoli, your smile is so calming and reassuring, Anna Capitaine thanks to you we have finally a full girl office. And then Susan Rigter, Tom Veeken, Magda Solà Garcia, Verena Neder, Nika van Nielen, Matthias Liebtrau, Stefan Tabernig, Hongyu Sun, Sven Askes, Lukas Helmbrecht, Yorick Bleiji, Eitan Oksenberg, Carolyn Moll, Daphne Antony, Giorgio Olivieri. It is a pity that I could not spend more time with you all due to the pandemic. You made the work at AMOLF even more special than just a PhD. Thanks to Debapriya Pal, you are great and such a methodical and meticulous scientist. I am glad I had the chance to know you and work with you!

And now the other paranymph and friend, Andrea Meffrrr Cordaro. Meffr, how many joys and sorrows have we faced during these 4 years? Too many. Since the very beginning of the PhD, when I was living in the DUWO, where we spent most of our evenings after work cooking carbonara and baked potatoes (my specialty), while playing playstation and gossiping about the latest news. And every Tuesday was Bella Storia pizza. You are a good friend, and I am glad we could deal with the PhD together, sharing our ups and downs, celebrating our achievements and supporting each other during personal and professional difficult times. You are not only a good friend but a talented scientist, sharp, responsible, accurate and I wish you all the success you deserve.

Maura, my dearest friend. We met 9 years ago, and we would not imagine we would be here today. Our friendship at Ximenes was full of ups and downs, and after we lost each other for some time, we found ourselves back a few years later. You were there during my whole academic path, from the Bachelor to the PhD. You were there also when I moved to Amsterdam and you came visit me for a few weeks. I was still living alone and not yet familiar with the new place. You brought family warmth in a cold spring in Amsterdam. As we always say, we are close even though we are far apart. And you can always count on me as I know I can count on you.

Arianna and Marco, *i pazzi-enti*, thanks for always being present despite being far apart. I am looking forward to seeing you, as always in a different cousine restaurant (so far, the best is the Mexican), updating each other's about our lives

in Rome and in Almere. Thanks for being always supportive and for listening to such long vocal messages, Marco I know how painful is for you! And thanks for being present for the defense, one of the most difficult but also rewarding moment of my life.
Ambra, we started our Bachelor together, and who would have imagined we would meet again in The Netherlands? You will always be my number one source of gossips, binnen and buiten The Netherlands, but also the number one expert on LinkdIn.
Marco and Silvia, how many chances there were we could have Italian neighbours? With you and the real kings of the house, Nicola and Gabri, I feel more home than I have never felt in the last 4 years. Just a coffee or a lunch or dinner makes the difference. Thanks for being such a supportive neighbours and friends and for helping us so much during the first period in the new house. You can always count on us.

My family, such an important piece of this PhD. Luckily for them, they did not have to deal with experiments, perovskites and data analyses but I am sure that dealing with me during this period was as tough as doing a PhD.
Thanks to my grandparents, for raising me as a daughter, for showing me what true love, compassion and dedication are. You are one of a kind. Thanks for being always present despite being far apart. You were a role models together with my parents during my childhood and you still are now that I am an adult. I wish everyone could have grandparents like you.
Thanks to my uncles and my aunts, we are all over the places but every time I see you it seems like that time has never passed. Thanks for all your calls and messages, I am glad I could share with you this piece of my life. Thanks for always being supportive and sincerely interested in my personal and professional life, for your kind words and your smiles.
Thanks to Merita and Mimino for welcoming in your family. Despite the distance, your love reaches this far.
Paolino, looking back in time, how much we have grown up, how many things have changed. But I am truly happy to see how far we got, fighting for our dreams, working hard to become who we are now. I am proud of you, and you know you can always count on me.

Despite your acknowledgement was for long time under debate, Ciki you are the best fratellino ever, no one will take away this from you.
Mom and dad, this whole book would not have been possible without you. I will always be eternally grateful for everything you have done for me, for teaching me that everything can be achieved with discipline and commitment. Thanks for believing in me since I was a little child, for being a role model for my entire life. You always did what was right for me, supporting all my choices and being always present for a good advice or just a silly chat. I hope that today, as yesterday, you are proud of who I am and what I have done so far. In the future, I wish I could be a good parent as you are. I love you.
Last but not least, Valerio. You truly deserve at least half of this PhD. Seriously. We have been through a lot in these years supporting each other's in this rollercoaster called life. We built our life together, brick by brick, without loosing the smile even in toughest moments. Thanks for supporting me every day, for reading my papers and commenting all the figures that I show you ten thousand times until I am fully convinced. Thanks for all the good advice, for bringing rationality when I am faltering. Thanks for always being honest and good hearted, you are the best life companion I could ever desire. I am looking forward to place all the other bricks together with you, and it does not matter how heavy they will be, we will always do it together, smiling. I love you.

# RINGRAZIAMENTI

Vorrei iniziare ringraziando il mio relatore Bruno Ehrler. Ti sono infinitamente grata per l'opportunità che mi hai dato di intraprendere un dottorato in un posto fantastico come AMOLF. Grazie per avermi permesso di sviluppare la mia identità di giovane scienziato, guidando le mie scelte ma senza costrizioni, supportando la mia indipendenza nell'esplorare tutti i possibili scenari nella mia carriera ma essendo sempre nel momento del bisogno.

Voglio ringraziare il mio co-relatore, Albert Polman, per essere sempre di grande supporto, entusiasta del mio lavoro e sinceramente interessato non solo alla mia vita professionale ma anche alla mia vita personale. Sei sempre stato un'ispirazione; hai sempre una bella parola per tutti e sei attivamente coinvolto nel creare connessioni tra gli studenti perché per te non siamo solo colleghi di lavoro ma anche una grande famiglia.

Desidero ringraziare la Prof.ssa Maria Loi, il Prof. Ferdinand Grozema, il Prof. René Janssen, la Prof.ssa Moniek Tromp e la Dott.ssa Jovana Milić per aver letto e valutato con attenzione questa tesi, frutto di un viaggio lungo 4 anni. Vi ammiro come scienziati ed è per me un grande onore aver la tesi valutata da voi.

Vorrei ringraziare gli altri group leaders di AMOLF. In particolare, vorrei ringraziare Esther Alarcón-Lladó per il tuo entusiasmo nel promuovere e sostenere il lavoro di giovani donne di talento nella scienza, per la tua empatia e gentilezza. Grazie a Erik Garnett per i feedback sui miei lavori, per le interessanti discussioni e le domande acute che mi hanno aiutato a comprendere meglio le mie scoperte scientifiche. Grazie a Said Rodriguez per le interessanti discussioni sulle insidie del sistema accademico, per sostenere fortemente il valore di noi scienziati nella comunità. Grazie a Wim Noorduin per il tuo infinito entusiasmo per la chimica e la scienza, per il tuo supporto anche nei periodi in cui gli esperimenti erano in stallo, per aver sempre creduto nei tuoi studenti. Un grande ringraziamento a Hans Zeijlemaker per il supporto durante i primi periodi in cui utilizzavamo il nuovo detector EBSD, per il tuo entusiasmo e curiosità riguardo gli esperimenti di EBSD sulla perovskite. Non dimenticherò mai quando ti vedevo entrare nella stanza del SEM ogni giorno, 5 minuti prima della fine della

giornata lavorativa, solo per chiedere se fossi felice dell'esperimento. E grazie ai ragazzi della cleanroom, Dimitry, Igor, Bob e Andries per il vostro supporto nei giorni più difficili.

Credo fermamente che fare scienza sia un lavoro di squadra e per questo motivo devo ringraziare molte delle persone con cui ho lavorato negli ultimi 4 anni. La maggior parte di queste collaborazioni ha portato a pubblicazioni scientifiche di cui sono molto orgogliosa, ma questa è solo la punta dell'iceberg. C'è molto di più dietro una pubblicazione scientifica: discussioni, condivisione di idee, infinite ore trascorse ad analizzare dati o correggere un manoscritto. Tutti i collaboratori che ho incontrato in questi 4 anni mi hanno insegnato qualcosa che ormai fa parte del mio background di scienziato. Voglio ringraziarvi tutti. In particolare, Jovana Milić, che forza della natura che sei! Fin dal primo giorno che ti ho incontrato, sono rimasto colpito dal tuo sincero entusiasmo e attenzione non solo per la scienza ma anche per le persone che fanno scienza, i tuoi collaboratori. Non sei solo un grande scienziato, ma sei anche solidale, grata, ottimista. Sono grato che tu faccia parte della commissione alla mia difesa, nonostante online, e spero di incontrarti presto di persona. Ti auguro tutto il meglio per la tua brillante carriera e spero che potremo collaborare di nuovo in futuro. Grazie ad Algirdas Dučinskas per la fantastica collaborazione, che è inclusa in questa tesi, nel capitolo 5. Auguro a tutti i miei colleghi di avere un collaboratore come te. Siamo stati una grande squadra, insieme a Mathias Dankl, nel dare forma al paper e mettere insieme tutti i pezzi del puzzle. Grazie per tutti i meeting, i cambiamenti dell'ultimo minuto e il vostro incredibile entusiasmo. Ma ehi, non è ancora finita, siamo ancora in fase di revisione!

Grazie a Ilaria Fratoddi e René Williams, siete stati i relatori della mia tesi magistrale, ed è grazie ad entrambi se ho avuto la possibilità di iniziare a lavorare con questi materiali bizzarri, le perovskiti. Grazie a René per essere stato coinvolto nel mio progetto magistrale con curiosità ed entusiasmo e per la tua accoglienza nel tuo gruppo. Grazie a Ilaria per avermi dato fiducia fin da quando ho iniziato con te la mia tesi di laurea triennale, per aver supportato me e le mie scelte accademiche, e grazie per supportare costantemente tutti gli studenti del dipartimento di chimica nel fare un'esperienza all'estero. Sono felice di essere ancora in contatto con entrambi.

Grazie a tutto il personale di supporto ad AMOLF, ai nostri fantastici receptionists, a tutti i tecnici, a tutte le persone che lavorano in officina, agli ingegneri software ed elettronici, al personale dell'ufficio di progettazione, al personale dell'ufficio finanza e acquisti, al personale della mensa, a tutte le persone che si occupano della pulizia dei nostri uffici. Siete i veri pilastri di AMOLF e senza di voi non potremmo svolgere il nostro lavoro in un ambiente così tranquillo.

Grazie al gruppo Hybrid Solar Cells. Negli ultimi 4 anni ho visto molte persone andare e venire. Ho iniziato il mio dottorato quando il gruppo era ancora piccolo e ora è bello vedere quanti scienziati brillanti e talentuosi fanno parte di questo gruppo. I ringraziamenti qui sono in ordine del tutto casuale, siete così tanti che spero di non dimenticare nessuno di voi. Jumin Lee, il primo postdoc del gruppo. Ho iniziato il mio dottorato solo due mesi prima della scadenza del tuo contratto, ma è stato sufficiente per farmi vedere quanto sei divertente e gentile. Benjamin Daiber, una pagina con l'elenco di quante volte mi hai aiutato a programmare non sarà sufficiente per ringraziarti adeguatamente. Grazie per avermi insegnato un po' di Mathematica, per aver risposto a tutte le mie domande senza mai esserne scocciato. Sei uno degli scienziati più precisi e meticolosi che abbia mai incontrato. Grazie a Moritz Futscher per essere stata un'ispirazione fin dall'inizio come dottorando. È stato bello incontrarci di nuovo e vedere come sono cambiate le nostre vite in questi 4 anni. Sei un eccellente scienziato e ti auguro tutto il successo che meriti nel mondo accademico. Mia cara mevrouw, Lucie McGovern, grazie per essere la migliore collega che si possa desiderare. Abbiamo iniziato insieme, con solo 6 giorni di differenza, e ora stiamo finendo insieme questo viaggio. Grazie per aver condiviso i nostri alti e bassi durante queste montagne russe chiamate dottorato. Il tuo ottimismo ed entusiasmo sono contagiosi. Grazie a Christian Dieleman per aver condiviso i giorni brutti e buoni di questo percorso, e aver fatto parte di uno dei viaggi più incredibili insieme a Jenny e Lucie negli Stati Uniti. Sono felice di vedere che dopo 4 anni sai come cucinare correttamente il cibo italiano. Devi ancora lavorare sull'insalata accanto alla pasta, un italiano muore ogni volta che lo fai! Grazie a Jeroen de Boer e Moritz Schmidt, per me sarete sempre il duo magico che ha iniziato insieme il dottorato. Siete grandi, continuate così! Non vedo l'ora di leggere i vostri lavori.

Grazie a Silvia Ferro, l'altra siciliana del gruppo. Grazie per tutti gli sforzi che hai fatto per organizzare insieme a Jeroen il fantastico viaggio di gruppo che è stato per me l'ultimo grande evento prima di finire il mio dottorato. Grazie a Imme Schuringa per essere sempre di supporto, per aver condiviso tanti momenti insieme. Avrei voluto trascorrere più tempo insieme in laboratorio e collaborare a nuovi progetti. Sei uno scienziato brillante e una persona premurosa. Ti auguro il meglio. Grazie a María Gélvez-Rueda, sei divertente e sempre con il sorriso per gli altri. Nonostante la pandemia non sia stata d'aiuto nel farci lavorare più a stretto contatto, spero che potremmo farlo in futuro, il tuo progetto è formidabile! Buona fortuna! Grazie a Gianluca Grimaldi, uno dei miei paraninfi, si dice così in italiano? Gianluca, grazie per aver sopportato i miei momenti di panico poco prima della sottomissione, quando stavo mettendo in discussione il mio intero dottorato. Grazie per essere sempre rassicurante, specialmente nel momento in cui ho cominciato ad elencare tutti i possibili scenari drammatici per la fine del progetto del cooling (ah, quel progetto!). Grazie ai nostri studenti triennali e magistrali, Isabelle Koschany, Marnix Ackermann, Rens van Roosmalen, Francesca Wittmann, Joris Bodin, Emil Kensington, Oscar van de Water, Floris Blom, Jouke Blum, Toon Maassen, Menke Knol per essere stati membri del gruppo così fantastici e divertenti. Grazie a David Langhorst, il primo studente magistrale che ho supervisionato, per il divertimento in laboratorio e per avermi insegnato cosa significa essere un relatore. Grazie a Georg Krause, il secondo studente che abbia mai supervisionato, per essere uno studente così meticoloso e indipendente. Sono impressionato dalla rapidità con cui hai imparato e spero di poter finire insieme questo impegnativo progetto di laurea. Grazie agli ospiti che hanno visitato il nostro gruppo, Cedric Gonzales, Rowan McQueen, Adrian Callies e Andrew Pun, avete portato un'atmosfera nuova nel gruppo. Grazie al nostro super tecnico, Marc Duursma. Grazie per mantenere sicuro il nostro laboratorio e per esserti preso cura delle nostre apparecchiature. Non sei solo un super tecnico ma anche una persona molto simpatica con cui parlare, sempre sorridente.

Qui, una menzione speciale va a Eline Hutter. Eline, sei entrata nel gruppo al momento giusto. Non era il momento migliore del mio dottorato e mi chiedevo se questo percorso fosse per me ancora entusiasmante. Ho imparato tanto da te e

ho ritrovato entusiasmo in quello che stavo facendo. Grazie per essere una donna e una scienziata fantastica, sei un modello. E grazie ancora per la fiducia che hai in me e nelle mie capacità. Non vedo l'ora di iniziare questa nuova avventura, come postdoc, nel tuo gruppo. Non avrei immaginato, quando hai lasciato AMOLF per iniziare la tua posizione professoressa, che ci saremmo incontrati di nuovo in questi nuovi ruoli!

Devo anche ringraziare tutte le persone fantastiche che ho incontrato in questi anni ad AMOLF: Jenny Kontoleta, la terza donna nel vulcanico viaggio negli Stati Uniti, Nasim Tavakoli, il tuo sorriso è così calmante e rassicurante, Anna Capitane grazie a te abbiamo finalmente un ufficio completamente al femminile. E poi Susan Rigter, Tom Veeken, Magda Solà Garcia, Verena Neder, Nika van Nielen, Matthias Liebtrau, Stefan Tabernig, Hongyu Sun, Sven Askes, Lukas Helmbrecht, Yorick Bleiji, Eitan Oksenberg, Carolyn Moll, Daphne Antony, Giorgio Olivieri. È un peccato non aver potuto passare più tempo con tutti voi a causa della pandemia. Avete reso il lavoro in AMOLF ancora più speciale di un semplice dottorato. Grazie a Debapriya Pal, sei uno scienziato eccezionale e metodico. Sono felice di aver avuto la possibilità di conoscerti e lavorare con te!

E ora l'altro paraninfo e amico, Andrea Meffrrr Cordaro. Meffr, quante gioie e dolori abbiamo affrontato in questi 4 anni? Troppi. Fin dall'inizio del dottorato, quando vivevo al DUWO, dove passavamo la maggior parte delle serate dopo il lavoro a cucinare carbonara e patate al forno (la mia specialità), giocando alla playstation e spettegolando sulle ultime novità. E ogni martedì c'era la pizza da Bella Storia. Sei un buon amico e sono contenta che abbiamo potuto affrontare insieme il dottorato, condividendo i nostri alti e bassi, celebrando i nostri successi e supportandoci a vicenda durante i momenti difficili, personali e professionali. Non sei solo un buon amico ma uno scienziato di talento, acuto, responsabile, accurato e ti auguro tutto il successo che meriti. E pure l'abilitazione!

Maura, mia carissima amica. Ci siamo conosciuti 9 anni fa e probabilmente non avremmo immaginato di essere qui oggi. La nostra amicizia allo Ximenes è stata piena di alti e bassi, ci siamo perse per un po' di tempo e poi ci siamo ritrovate. Ci sei stata durante tutto il mio percorso accademico, dalla

laurea triennale al dottorato. C'eri anche tu quando mi sono trasferito ad Amsterdam venendomi a trovare per qualche settimana. Vivevo ancora da solo e non avevo ancora familiarità con il nuovo posto. Hai portato il calore familiare in una fredda primavera olandese. Come ci diciamo sempre, siamo vicine anche se lontane. E puoi sempre contare su di me come so che posso contare su di te.
Arianna e Marco, i *pazzi-enti*, grazie per essere sempre presenti pur essendo così distanti. Non vedo l'ora di vedervi, come sempre in un ristorante di cucina diversa (finora, il migliore è il messicano però eh), aggiornandoci a vicenda sulla nostra vita a Roma e ad Almere. Grazie per essere stati sempre di supporto e per aver ascoltato messaggi vocali infiniti, Marco, so quanto ti faccia soffrire! Sto ancora aspettando il matrimonio. Grazie per essere presenti a questo evento cosí importante, significa molto per me.
Ambra, abbiamo iniziato il nostro corso di laurea insieme, e chi avrebbe immaginato che ci saremmo incontrati di nuovo in Olanda? Sarai sempre la mia fonte numero uno di pettegolezzi, dentro e fuori ai Paesi Bassi, ma anche l'esperto numero uno su LinkdIn.
Marco e Silvia, quante possibilità c'erano di avere vicini italiani? Con voi e i veri re di casa, Nicola e Gabri, mi sento più a casa di quanto non mi sia mai sentita negli ultimi 4 anni. Solo un caffè o un pranzo o una cena fa la differenza. Grazie per essere stati vicini e amici così solidali e per averci aiutato così tanto durante il primo periodo nella nuova casa. Sapete che potete sempre contare su di noi.
La mia famiglia, un pezzo così importante di questo dottorato. Fortunatamente per loro, non hanno avuto a che fare con esperimenti, perovskiti e analisi dei dati, ma sono sicura che avere a che fare con me in questo periodo è stato difficile come fare un dottorato. Grazie ai miei nonni, per avermi cresciuto come una figlia, per avermi mostrato cosa sono il vero amore, la compassione e la dedizione. Siete unici. Grazie per essere sempre presenti. Siete stati un modello insieme ai miei genitori durante la mia infanzia e lo siete ancora adesso che sono un'adulta. Auguro a tutti di avere nonni come voi.
Grazie ai miei zii e alle mie zie, siamo sparsi dappertutto ma ogni volta che vi vedo sembra che il tempo non sia mai passato. Grazie per tutte le vostre chiamate e messaggi, sono felice di poter condividere con voi questo pezzo della mia vita, significa molto per me. Grazie per essere sempre di supporto e sinceramente

interessato alla mia vita personale e professionale, per la vostra presenza e i vostri sorrisi.
Grazie a Merita e Mimino per avermi accolta nella vostra famiglia. Nonostante la distanza, il vostro affetto arriva fin qui.
Paolino, guardando indietro nel tempo, quanto siamo cresciuti, quante cose sono cambiate. Ma sono davvero felice di vedere fino a che punto siamo arrivati, lottando per i nostri sogni, lavorando duramente per diventare quello che siamo ora. Sono orgogliosa di te e sai che puoi sempre contare su di me.
Nonostante l'aggiungerti tra i ringraziamenti sia stato a lungo oggetto di discussione, Ciki sei il miglior fratellino o sorellino di sempre, nessuno te lo puó negare.
Mamma e papà, questo libro non sarebbe stato possibile senza di voi. Sarò sempre eternamente grata per tutto ciò che avete fatto per me, per avermi insegnato che tutto può essere raggiunto con disciplina e impegno. Grazie per aver creduto in me sin da quando ero una bambina pazzerella, per essere stati un modello per tutta la mia vita. Avete sempre fatto quello che era giusto per me, assecondando tutte le mie scelte ed essendo sempre presente per un buon consiglio o solo una chiacchierata. Spero che oggi, come ieri, voi siate orgogliosi di chi sono e di quello che ho fatto finora. In futuro, vorrei poter essere un buon genitore come lo siete voi per me. Vi voglio bene.
Ultimo ma non meno importante, Valerio. Ti meriti davvero almeno la metà di questo dottorato. Sul serio. Ne abbiamo passate tante in questi anni sostenendoci a vicenda in queste montagne russe chiamate vita. Abbiamo costruito la nostra vita insieme, mattone su mattone, senza perdere il sorriso anche nei momenti più difficili. Grazie per avermi sostenuto ogni giorno, per aver letto i miei papers e aver commentato tutte le figure che ti ho mostrato fino all'esasperazione. Grazie per tutti i buoni consigli, per portare la razionalità quando la mia sta vacillando. Grazie per essere sempre onesto e buono, sei il miglior compagno di vita che potessi desiderare. Non vedo l'ora di mettere insieme tutti gli altri mattoni, e non importa quanto saranno pesanti, lo faremo sempre insieme, sorridendo. Ti amo.

# About the Author

Loreta Angela Muscarella was born in Palermo, Italy on January 15, 1994. In 2012, after completing her high school studies with major in humanities, she moved to Rome where she started a bachelor in chemistry at "La Sapienza" University of Rome. From 2014 to 2016, she was lab assistant for the class of "Applied and Instrumental Analytical Chemistry" at "La Sapienza" University of Rome. In 2016, she started a MSc in inorganic and physical chemistry at "La Sapienza" University of Rome. During her Master's studies, she spent seven months at the University of Amsterdam under the supervision of Dr. René Williams to write her thesis on the effect of metallic ions in mixed-halide perovskites to improve stability and optoelectronic properties. She received her MSc degree *cum laude* (with honors). In 2018, Loreta joined the group of Prof. Dr. Bruno Ehrler at AMOLF as a PhD student. Here, she investigated the structure-optoelectronic properties relation in 3D and layered 2D lead-halide perovskites by monitoring the optoelectronic properties of mechanically compressed perovskites. The results of these scientific investigations are presented in this thesis. In 2022, she will join the group of Dr. Eline Hutter at Utrecht University to study photochemical processes using lead-free perovskites.